A COMPREHENSIVE PROTECTION SCHEME FOR DISTRIBUTION SYSTEMS

A Dissertation
Presented to
The Academic Faculty

By

Yonghee Lee

In partial fulfillment
Of the requirements for the Degree
Doctor of Philosophy in Electrical and Computer Engineering

Georgia Institute of Technology

December 2014

A COMPREHENSIVE PROTECTION SCHEME FOR DISTRIBUTION SYSTEMS

Approved by:

Dr. A. P. Meliopoulos, Advisor
School of Electrical Computer Engineering
Georgia Institute of Technology

Dr. Maryam Saeedifard
School of Electrical Computer Engineering
Georgia Institute of Technology

Dr. Ronald Harley
School of Electrical Computer Engineering
Georgia Institute of Technology

Dr. Andy Sun
School of Industrial & Systems Engineering
Georgia Institute of Technology

Dr. Thomas Habetler
School of Electrical Computer Engineering
Georgia Institute of Technology

Date Approved: October 27, 2014

ACKNOWLEDGEMENTS

I would like to thank Bomi Park, Aiden Lee, and my mother and father.

TABLE OF CONTENTS

LIST OF TABLES

LIST OF FIGURES

NOMENCLATURE

- DG: Distributed Generation
- CB: Circuit Breaker
- TCC: Time Current Curve
- IED: Intelligent Electronic Devices
- PMU: Phasor Measurement Unit
- MU: Merging Unit
- GPS: Global Positioning System
- PDC: Phasor Data Concentrator
- SE: State Estimation
- DSE: Dynamic State Estimation
- VIT: Voltage, Current, and Time
- NVC: No Voltage Counter
- FCC: Fault Current Counter
- AQCF: Algebraic Quadratic Companion Form
- COMTRADE: Common Format for Transient Data Exchange (IEEE standard C37.111)
- ASDU: Application Service Data Unit (ASDU)
- HIF: High Impedance Fault

SUMMARY

The objective of the proposed work is to formulate and demonstrate protection schemes for radial and loop system, an active distribution system, and microgrid. The proposed schemes are composed of (a) A new loop scheme by utilizing voltage, current, and time (VIT) reclosers and sectionalizers and (b) A new protection scheme, the dynamic state estimation (DSE) based protection, for active distribution systems and microgrids.

First, most of the radial distribution systems have one source, and many loads are attached to the only source. For many entities with critical loads such as hospitals, prisons, and airports, which cannot tolerate loss of power, an automatic load transfer scheme is required. When one of the distribution-feeder circuits loses the primary source during a fault recovery scheme, a normally open tie recloser closes to provide an alternative power source. A three-recloser or a five-recloser loop sectionalizing scheme has been used for automatic load transfers. However, a well known issue during the conventional loop sectionalizing scheme is a close-in fault. This nuisance trip damages apparatus connected to the feeder.

The close-in fault problem is solved using the proposed VIT scheme. The main concept of the VIT scheme is to detect a Fault on source side and load side as well mainly by utilizing counter and timer coordination between the VIT recloser and the VIT sectionalizers. The name VIT is formed from the fact that this algorithm uses voltage, current, and timer information to coordinate protection devices. One component of the VIT scheme is the traditional fault current counter (FCC) and time current curve (TCC) coordination. An additional feature is proposed, no-voltage counter (NVC), to confirm the fault condition from load side, to isolate the fault location, and eventually to prevent

the close-in fault. The NVC counts no-voltage condition of the feeder that results from backup device operation.

Second, an increased number of alternative sources for supplying power referred to as distributed generations (DGs) are installed along passive distribution systems. As significant levels of DG penetration have been achieved, several protection issues arise because DG connections invalidate traditional protection schemes. The protection problem resulted from DG connections is that most of the existing coordination of protection devices will fail. To solve the issue, the state of recent technological advances (PMU capability, merging units (MUs), process bus, station bus and interoperability) are thoroughly studied so that the technological advances can be accompanied with commensurate advances on the protection coordination.

A new fault detection scheme, setting-less protection scheme, is proposed in this proposal based on synchronized measurements. The proposed method uses dynamic state estimation, based on the dynamic model of the component that accurately reflects the characteristics of the component as well as the loading and thermal state of the component. The dynamic state estimation is used to continuously monitor the dynamic model of the component (zone) under protection. If any of the physical laws for the component under protection is violated, the dynamic state estimation will capture this condition.

The immediate benefit of the VIT schemes is a reduction of the nuisance trips because of the close-in fault. Other benefits include (a) Cheap and easy installation throughout the distribution systems and (b) More number of protection zones compared to traditional schemes. Moreover, using the DSE based protections system that fully uses PMU data, it

is expected that the protection of active distribution systems and microgrid is feasible in real time.

1 Introduction

Traditionally, the distribution system has been a passive system in the sense that the distribution system delivers power from transmission systems to loads. Most of the distribution systems have one source, and many loads are attached to the only source. Such a distribution network is called a radial system. Regardless of its configuration, most of the traditional distributions have one source, and loads are attached to the source along the lines. For many entities with critical loads such as hospitals, prisons, and airports, which cannot tolerate loss of power, an automatic load transfer scheme is required. When one of the distribution-feeder circuits loses the primary source during a fault-recovery scheme, a normally open tie recloser closes to provide an alternative power. A three-recloser or a five-recloser loop sectionalizing scheme has been used for the automatic load transfer and are explained in detail [1, 2]. In the following Section 2.3, a well-known issue during the conventional loop sectionalizing scheme, close-in fault operation, is reviewed. The solution to the issue is explained in the Section 4.2.

Recently, an increased number of alternative sources for supplying power referred to as distributed generations (DGs) are installed along the passive distribution system. As significant levels of DG penetration have been achieved, several protection issues arise because DG connections invalidate traditional protection schemes. The protection problem resulted from DG connections is that most of the existing coordination of protection devices will fail. To solve the issue, the state of recent technological advances (PMU capability, merging units (MUs), process bus, station bus and interoperability) are

thoroughly studied so that the technological advances can be accompanied with commensurate advances on the protection coordination.

A new fault detection scheme, dynamic state estimation-based protection scheme, is developed in this thesis based on synchronized measurements. The new protection method uses dynamic state estimation, based on the dynamic model of the component that accurately reflects the characteristics of the component as well as the loading and thermal state of the component. The dynamic state estimation is used to continuously monitor the dynamic model of the component (zone) under protection. If any of the physical laws for the component under protection is violated, the dynamic state estimation will capture this condition.

The immediate benefit of the VIT schemes is a reduction of the nuisance trips because of the close-in fault. Other benefits include (a) Cheap and easy installation throughout the distribution systems and (b) More number of protection zones compared to traditional schemes. Moreover, using the DSE-based protections system that fully uses sampled data, it is expected that the protection of active distribution systems and microgrid is feasible in real time.

The focus of this thesis is to address the issues of (a) A loop scheme in distribution systems and (b) Protection schemes in an active distribution system and a low voltage (LV) microgrid. The first scheme uses voltage, current measurement, and time information. The second scheme is based on synchronized measurement data from every terminal of equipment under protection. The objectives of this work are to develop a feasible and comprehensive protection schemes for DGs connected active distribution

and LV microgrid system using a dynamic state estimator (DSE) and a three-phase, asymmetric, and breaker-oriented power system model.

2 Literature Review and Background Information

2.1 Introduction

The background information of currently available technologies related to the researches along with literature reviews of the issues and related research efforts on these topics is provided in this section. The VIT scheme for the protection of a distribution system integrates traditional overcurrent [1] and voltage-based [3] schemes. In particular, Section 2.2 reviews basic operation principles of reclosers and sectionalizers. An operation of traditional loop schemes and associated problems is illustrated in Section 2.3.

In addition, the DSE-based protection scheme for the protection of an active distribution and a LV microgrid system is introduced by utilizing the state of the art technology adopted for the modern power system protection. Section 2.6 roughly introduces requirements for the protection schemes for an active distribution and a LV microgrid system with or without communication channels. The advantages and disadvantages of the existing methods are discussed along with the basic requirements for the protection of an active distribution and a LV microgrid. In Section 2.7, the state of the art technology applied in power systems to integrate and exploit powerful microprocessor technologies are explained. Section 2.8 briefly introduces a MU and process bus concept that achieves full observability of the feeder by merging available information based on the IEC 61580 standard.

2.2 Basic Operation Principles of Reclosers and Sectionalizers

A brief review of protection devices such as reclosers and sectionalizers that are commonly used in the distribution automation is provided in this chapter. An example of a distribution system protected by circuit breakers (CBs), reclosers, and sectionalizers is given in Figure 1.

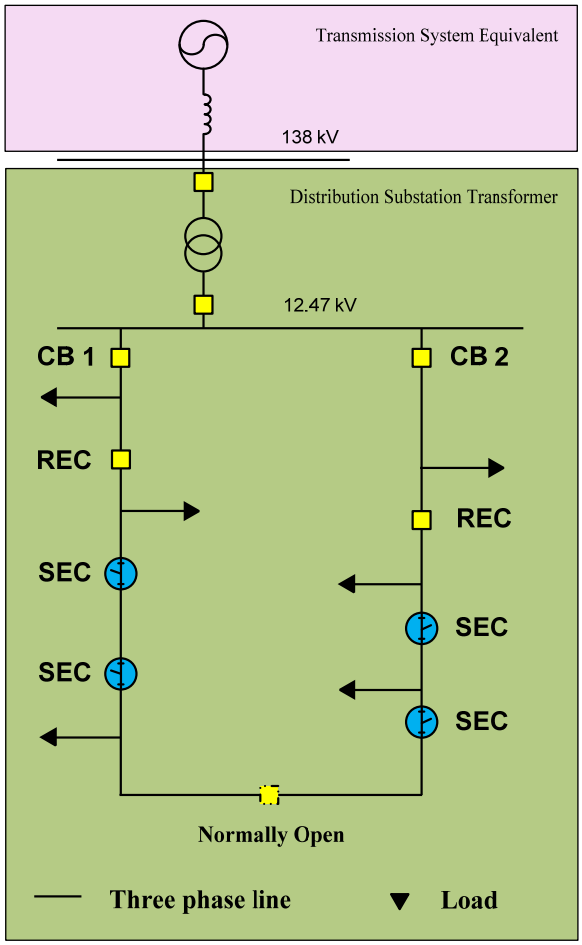

Figure 1: Distribution system architecture.

CBs by themselves have no capability to detect a fault, and in general, relays provide the intelligence for controlling the operation of the circuit breakers. In this thesis, circuit

breakers and relays are considered as one device that comes together. A circuit breaker is usually installed at the substation level of the distribution system to clear a high fault current. A circuit breaker is capable of making, carrying, and breaking during normal operating conditions and during the system transients resulted from fault conditions. One of the more applicable types of a relay for sensing and responding to a fault condition is an overcurrent relay. According to the IEEE standard C37.112 [4], the trip time of an overcurrent relay is determined by a family of curves as shown in Figure 2.

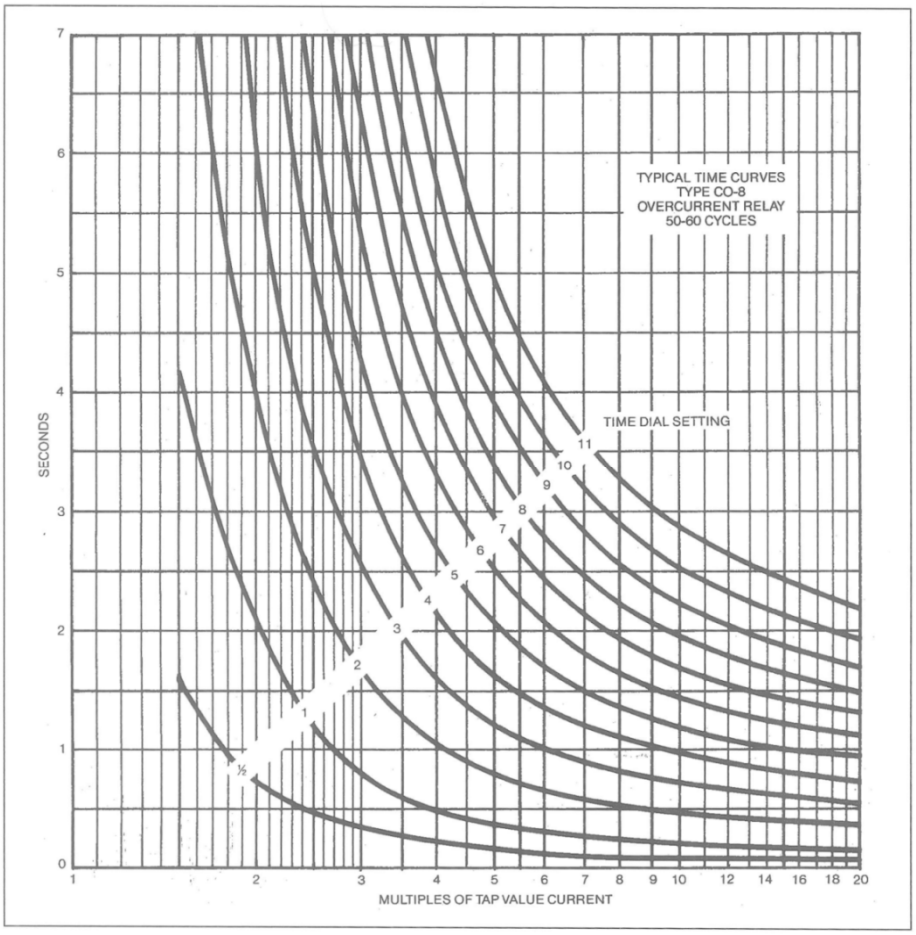

Figure 2: A typical overcurrent relay TCC [1].

Typical reclosers are coordinated with other protection devices based on the time-current curve (TCC) to isolate faults within minimal service outage region. The basic idea of the TCC coordination is that a device closer to the fault location activates faster to minimize the impact of a fault to a distribution system. Another common protection schemes for a distribution line is a distance relay scheme. A distance relay responds to current and voltage input and determines the fault location from the relay by monitoring fundamental frequency impedance of the line. When the ratio of a voltage to a current is within an operating zone of a distance relay, it trips. If the fault is detected, then reclosers interrupt the circuit by opening on faults to remove temporary or permanent faults. Most of faults, 80~85%, including semi-permanent faults in overhead distribution systems, are temporary faults and can be removed by reclosing operations of the recloser [5, 6]. On the other hand, when faults persist after several reclosing operations (usually up to four times), reclosers open to lockout so that engineering personnel can remove and fix permanent fault section.

Sectionalizers are normally coordinated with the operation of backup devices such as CBs or reclosers to determine if a permanent fault is inside of the protection zone. The coordination of hydraulic controlled reclosers is tight and difficult. On the contrary to this, microprocessor based relays are more flexible and easier to coordinate. Recent transition from hydraulic to electronically controlled sectionalizers has led to sectionalizers with versatile functions that can be used for protection schemes [7]. Sectionalizers count the number of operations of the backup device during a fault condition. Two conditions are required to count the fault condition: (a) A measured fault current larger than a threshold and (b) Zero voltage or current after trip of the backup

device as in Figure 3. In this thesis, it is called a fault-current counter (FCC). The sectionalizers will not count the operation of a backup device when a source voltage is present at the sectionalizer. In this case, a downstream protection device has already removed the fault condition. This feature is called a voltage restraint. And a current count restraint feature that blocks the count operation as long as a load current of five amperes or more flows through the sectionalizer also is a standard feature of sectionalizers [1].

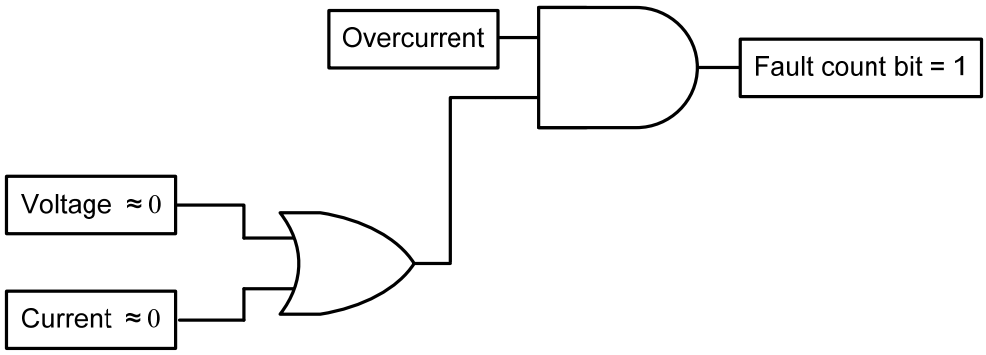

Figure 3: Symbolic logic circuit for traditional sectionalizer count operation.

A typical example of these restraint features for count operation is illustrated in Figure 4. For a fault on the load side of the system beyond the recloser, F2, the recloser trips before the backup CB trips, and the sectionalizer does not count because of the voltage or current restraint feature. For a fault on F1, the backup CB first trips, and the sectionalizer increases FCC. And the sectionalizer trips open when the FCC meets the number selected beforehand while the backup device is open because sectionalizers are not capable of interrupting a fault current.

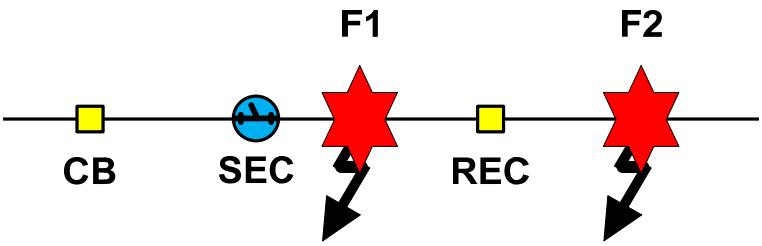

Figure 4: Sectionalizer between a CB and a recloser.

Coordination practices for reclosers and sectionalizers applied on radial system are explained in the remaining of this chapter using simplified illustration of the system with a fault between sectionalizers as depicted in Figure 5.

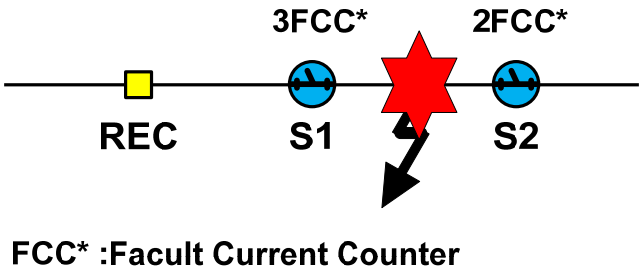

Figure 5: Fault between two sectionalizers.

A typical sequence of a recloser is a four-time reclosing. The counter setting of sectionalizer is three FCCs for S1 and two FCCs for S2. The backup device trips to clear the fault. A temporary fault would be extinguished by the first tripping operation, and the sectionalizers will remain closed because only S1 has counted one FCC followed by zero voltage or current. So, when it is desirable to clear temporary fault with one time tripping and reclosing operation, setting sectionalizers to have two or three FCCs is a feasible option. If the fault persists after the first trip and the reclosing operation, the backup

device opens and recloses after a reclosing interval, and only S1 counts two FCCs. The backup device trips and recloses again, and the fault current condition followed by zero voltage or current increases the FCC of S1 from two to three. After the count of three FCCs, S1 opens to isolate the faulted section of the system while the backup device is open. The fault location is isolated by opening S1. And then the counters of the sectionalizers are reset to zero while current flows from a minimum five amperes to the minimum pickup current without interruption for longer than a time setting after a successful reclosing operation or whenever the sectionalizer is opened [1]. The counter reset setting selected for the sectionalizers must be coordinated with the trip and reclosing times of the backup device. To successfully coordinate with a backup device, the memory time of sectionalizers must be longer than the total time of recloser tripping and reclosing. The count sequence of sectionalizers according to the reclosing operation of a recloser is illustrated in Figure 6.

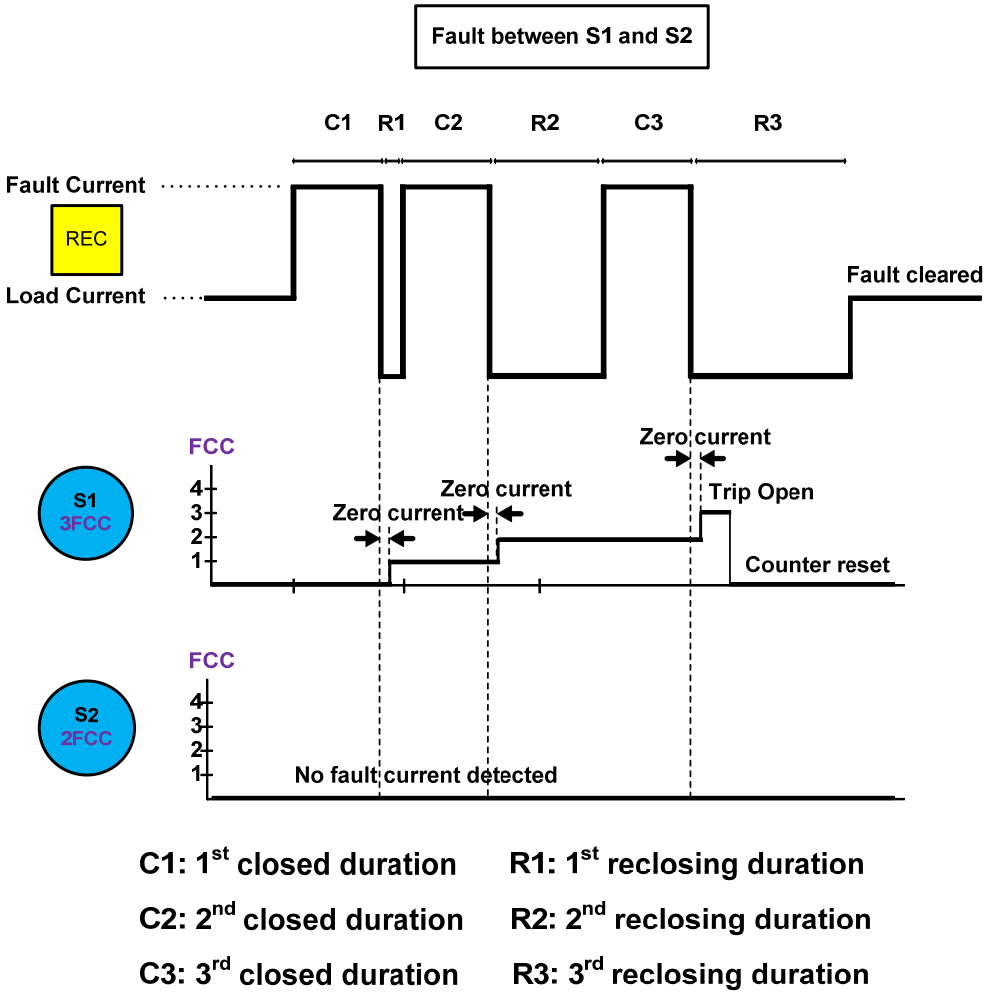

Figure 6: A count sequence of sectionalizers.

Strategically located sectionalizers provide better solution for tight or improper recloser coordination [7, 8]. When it is desirable to have more sections along the distribution lines, it is more economical and feasible to deploy sectionalizers than reclosers [8]. For example, if two reclosers are installed too close each other, then engineers have difficulties in coordinating two closely placed TCCs, while sectionalizers provide better coordination margins [7, 8].

2.3 Loop Scheme

A brief review on a five-recloser loop scheme follows. In a classical five-recloser loop control scheme, each feeder circuit is connected at a normally open tie recloser, and a mid-recloser is located between an upstream recloser and a tie recloser as shown in Figure 7.

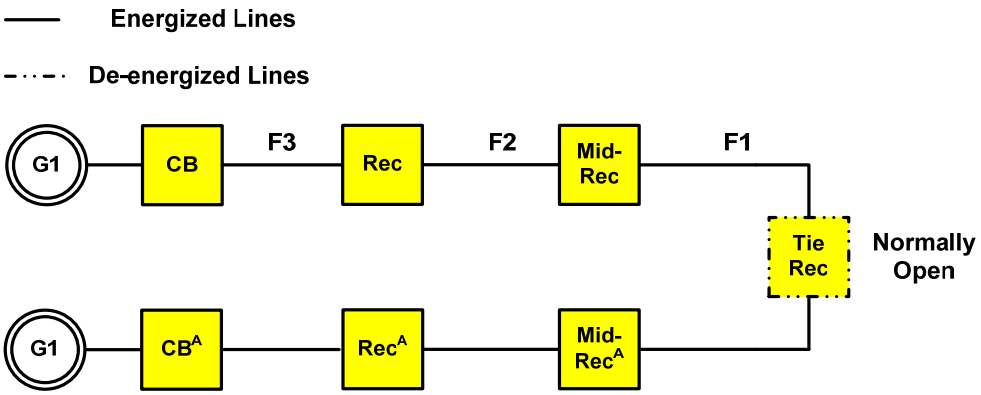

Figure 7: Traditional five-recloser loop scheme.

During a normal operation, the conventional five-recloser scheme involves a radial coordination of one CB with two reclosers as shown in Figure 7. For a fault on F2, the recloser operates and locks out. The mid-recloser and the tie recloser sense voltage loss. Then the mid-recloser times out first, changes its minimum trip current to a lower value (580 to 280 amperes), and changes to the one-shot lockout mode. After the time delay of the tie recloser, which is longer than the time delay of the mid-recloser, the tie recloser closes onto the fault, and the mid-recloser trips to lockout [1] as shown in Figure 8.

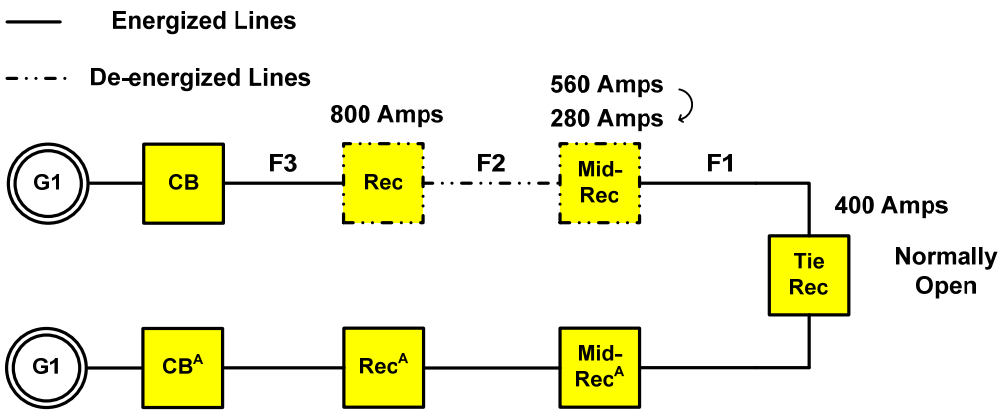

Figure 8: Restoration result of traditional five-recloser loop scheme, fault on F2.

Although every utility wants to prevent closing the tie switch onto a fault, this problem is considered unsolvable unless communication devices are installed on each protection device. Another defect of traditional coordination is that the alternative direction TCC coordination of the CB^A, the $recloser^A$, the $mid\text{-}recloser^A$, the tie recloser, and the mid-recloser could be difficult if these devices are in close proximity and have limited selectivity for the TCC coordination.

Some papers utilize remotely controlled switches from a control center for distribution-system automation [9-14]. Some of the existing automatic loop control schemes based on the distributed intelligent devices so that loop control can be done locally [2], [8], [15, 16]. In contrast to communication-based schemes, a pulse closing method was introduced by McCarthy et al. to reduce the mechanical and thermal stresses on a system [17, 18]. The method requires the installation of a point-on-wave controller, a pulse-generating mechanism, and a rather complex energy-calculating algorithm to each phase of every protection device. While the method reduces mechanical and thermal stresses, the problem of closing tie recloser onto a fault is not eliminated. Butts et al. and Taylor et al.

suggested to embed sectionalizer logic in a recloser relay [19, 20]. They showed that using sectionalizers instead of reclosers may provide a better solution without the need for TCC coordination. The scheme becomes difficult to implement for long feeders with quite big differences in fault currents at the start and end of the feeder. At the same time, the scheme does not eliminate the problem of closing onto a fault.

2.4 High Impedance Fault (HIF)

The range of a phase to ground fault current can vary from zero to significant level according to the electrical contact of downed conductor. An HIF occurs when a power system conductor is being contacted with non-conducting materials, so the fault current is limited and resulted in undetectable level of current by utilizing conventional protection devices. When the conductors broken and fallen to the ground still remains energized, there are hazards for public and unsafe condition for utilities, for example fire because of arcing current or direct human contact to the sagging conductor. For this reason, detecting the HIF accurately and removing it from power system has been the main subject of power system engineers. Table 1 shows typical field data of currents level on different surfaces which resulted from HIF [21].

Table 1: Typical Fault Currents on Various Surfaces

Surface	Current (A)
Dry asphalt or sand	0
Wet sand	15
Dry sand	20
Dry grass	25
Wet sand	40
Wet grass	50
Reinforced concrete	75

A number of researcher proposed HIF detection schemes in recent years and these detection schemes can be categorized into three groups: (1) methods using ground relay concept (2) methods using harmonic and non-harmonic component resulted from arc fault (3) methods using voltage unbalance and communication device to detect open conductor.

Ground relaying on distribution system is governed by the ground fault current level and the normal unbalance load ratio of the system [22]. In specific, ground relaying protection scheme creates a trip signal when the ground fault level exceeds pickup current level. Ground relays that can monitor residual current, 3I0, of the system are favored on three phase three wire systems because normal unbalance load ratio of the system is very small, and so good sensitivity of the ground relaying setting can be acquired. Ground relays on the three phase three wire systems are able to monitor small increment of the residual current value using a certain type of zero CT and generate a trip signal if monitored residual current value is larger than a threshold. However, solidly grounded three phase four wire systems are difficult to protect against HIF. That's because the 4th wire, neutral wire, provides a return path of load unbalance current and the normal load unbalance current value is relatively high. Several schemes have been suggested for the detection of HIF using ground relaying concept. For example, ratio ground relay (RGR) algorithm by Pennsylvania Power and Light Company (PP&L) [23] and proportional ground relay (PGR) algorithm by Carr et al. [24] are developed and tested on several different sites. RGR algorithm adjusts setting value of ground overcurrent relay according to load level changes. On the other hand, neutral and ground currents are measured to separate load current from fault current for PGR algorithm.

These methods might increase the possibility of detection of HIF somewhat extent. The application of ground relaying on solidly grounded three phase four wire systems will be reemphasized in the next section.

Meanwhile, Russell et al. have shown from their field test results that most of HIFs are accompanied with arcing current that shows randomness [25] and proposed several HIF detection algorithms based on this phenomenon [26-28]. And several other researchers used even order or third harmonic of fault current to detect arcing current resulted from HIF [29, 30]. Some researchers proposed multi criteria algorithms using artificial neural network (ANN), wavelet transform, fuzzy systems, and so on to provide better security of HIF detection algorithm [31-33]. Several ideas have been made into commercial products [34, 35]. From the experience of utilities with these algorithms, it can be concluded that those extensive researches have brought a certain level of confidence in HIF detection by providing arcing current detection technologies.

Detection methods in the third group have been proposed by Meliopoulos et al and other researchers [36-38]. The researchers proposed that voltage unbalance monitored at the load side of the fault location is a positive proof of fault occurrence. The voltage unbalance techniques require certain form of a transmitter to send the fault occurrence confirm signal and a receiver at adjacent protective device to trip the device. Once the line opened and voltage unbalance is detected by a sensor, then any open conductor fault will be cleared by tripping the closet protection device and the service will be restored.

2.5 Active Distribution Systems Related Protection Issues and State-of-the-Art Schemes

As significant levels of DG penetration have been achieved, the passive distribution system evolved into an active distribution system. The active distribution system can provide capacity relief of transmission and distribution lines, energy efficiency, improved reliability, and so on [39]. Although the increased number of DG connections provides many benefits, several protection issues will arise because DG connections invalidate a traditional protection scheme. The first protection problem resulted from DG connections is that the increment of short-circuit fault current level will exceed the operation current level of existing distribution protection devices. In general, the short-circuit fault current level contribution of DGs depends on various factors, such as the distance between a DG and the fault location, the fault impedance, and the employed connection method [40, 41]. The output of a DG can be connected to the system via three different forms: synchronous generators, induction generators, and power electronics [42]. Directly connected synchronous generators contribute highest level of a fault current among them. Induction generators come next but the fault current decays to a negligible level within 10 cycles. Moreover, inverters produce no remarkable fault current contribution because inverters limit the fault current about 25% higher than the current available at the maximum power point [43, 44]. A solution to the problem that requires an extensive reinforcement of the system is to calculate each fault current contribution and replace old devices with greater fault current rating protection devices to ensure that the monitored fault current is lower than the interruption capability of devices. On the other hand, Meliopoulos et al. and other researchers propose to implement fault current limiting (FCL)

devices to reduce the fault current contribution of DGs [45-48]. In the report [48], Meliopoulos et al. proposed online fault current assessment of the system with inverter-connected DGs.

Another issue resulted from the proliferation of DG connections is that most of the existing coordination of protection devices will fail. Because of the increased short circuit current level and changed direction of the fault current fed by DGs, a previously tuned protection coordination that assumes the single generator attached system might be lost [49]. In the paper [50], the authors show some examples of coordination between fuses and relays with and without DGs. The authors conclude that the coordination in presence of DGs can be obtained only after all DGs are disconnected before the reclosing operation.

The third issue is s a back-feeding problem. Most faults on the overhead lines on the passive distribution systems are a temporary fault and can be removed by one or two reclosing operations. Fast reclosing devices trip when the monitored fault current exceeds the trip setting value and reclose within few cycles to minimize power outage duration. If the fault is temporary, the reclosing is successful. However, with DGs, multiple power sources support the voltage level required to sustain arc at the fault location. As a result, the fault will not be cleared, and the temporary fault may evolve into a permanent fault unless disconnect DGs before the reclosing. So, utilities need to prevent an unintentional operation of DGs by disconnecting all the DGs during the trip and reclosing operation as recommended in the IEEE standard 1547.2 [51].

Whenever a fault occurs, current standards state that utilities need to disconnect all the DGs before reclosing operation to recover the traditional protection coordination [51]. By

disconnecting all the DGs, traditional coordination can be easily obtained again. However, when the active distribution system with high penetration of DGs looses all the connections simultaneously, the voltage stability of the system is not secure any more. The main grid generator might not be able to keep up supporting the increased load amount, and wide range voltage sag might be followed. So, the amended IEEE standard 1547.4 encourages ride-though operation during a fault condition. As a result, a promising operation philosophy of the distributed system with widespread DGs is to deploy the DGs and local area loads in such a way that they have stable balance between load and generator capacity, and making several DGs load frequency controllable [50]. Such a configuration of power system is called a microgrid, and the microgrid operation results in better stability and reliability [52].

The final issue is that the microgrid protection must ensure a safe operation during the island mode and grid connected mode. When a fault occurred in the microgrid during the island mode, the fault current level contributed by the microgrid generator is so small that the traditional overcurrent coordination is not applicable. Moreover, because of the relatively small size of the microgrid, the fault current in the microgrid does not change much with the fault location. As a result, the traditional overcurrent relay coordinated scheme based on current selectivity has the potential of a slow or unsuccessful fault detection [53]. Consequently, the conventional overcurrent protection scheme is not enough for the protection of a microgrid.

2.6 Microgrid Protection Issues and State-of-the-Art Schemes

In this section, microgrid protection issues are summarized, and the state of the art schemes are explained. The fault protection scheme for the internal fault should work seamlessly while the microgrid is connected or disconnected to the main [54]. The issues are how to coordinate protection devices against the fault on the main lines and internal of the microgrid during the grid-connected and the island operation. The inverse time overcurrent or time definite overcurrent relays are used vastly in distribution systems where the distinctive fault current level enables the closest relay to clear the fault. However, the conventional overcurrent protection scheme is not valid anymore because of the changed fault current level and direction. A fault current level is limited when the inverter or a fault current limiter (FCL) connected generator is powering the microgrid during the island operation. Moreover, the direction of a fault current is different from the radial systems.

Recently, many researchers proposed protection schemes for the protection of a microgrid. The protection schemes can be categorized into three groups: non-communication-based schemes, centralized schemes, and peer-to-peer schemes. The centralized schemes and peer-to-peer schemes are relying on a communication channel between protection equipment.

The first method, several non-communication-based schemes are proposed by researchers. In the paper [55], a scheme that uses a state-detection algorithm is proposed. Under a fault condition, the number of lost generators is identified by the fault current level and corresponding relay settings are loaded. However, it requires extensive system study to obtain the time overcurrent characteristics of all the downstream relays. Since this

scheme is not a communication-based scheme, it again requires a fault-current study whenever a new device is implemented to the system. Moreover, protection strategies proposed in [55] do not offer a method for an island mode fault detection. Several approaches detect a limited-current fault by voltage disturbance using Park transformation [56, 57]. The three-phase AC voltage output of a microgrid are monitored and then transformed into DC quantities using the Park transformation. Afterwards, the disturbance signal is extracted by representing the difference between the three-phase balanced voltages and the transformed DC quantities. Under normal conditions, the disturbance signal should be almost zero. Otherwise, the disturbance signal will be a DC value that shows distinctive characteristics according to the fault type. Using similar concepts, in [58], a fault detection method for the system in an island operation based on the direction of a fault current has been proposed. The proposed strategy aims to clear the fault on DGs connected systems without requiring communications. However, in the paper [58], the fault direction determine scheme uses per-phase or quadrature polarizing quantity. Problems pertinent to each directional element entry proposed in [58, 59] are well described in [60]. To overcome a false decision of direction to a fault, [61] proposes that merging all different types of directional element into one relay function allows the numerical relay to determine which of the directional decisions is the best. Moreover, the reduced voltage and current level during the island mode operation might invalidate traditional directional element [62].

The second method, centralized control scheme, uses a control center to monitor and protect the system. In [63], the control system that already has the network configuration information monitors protection devices and finds the fault location by assigning

numbers on each device. Reference [64] presents one central master unit based protection scheme. The master unit adaptively changes the coordination between protection devices according to the operation mode, either a normal or island operating mode. Brahma et al. [65] proposed a strategy based on communication among the zones, but the strategy does not accommodate the island operation case. Under the assumption that smart grid monitoring devices are widely deployed, the centralized protection schemes offer an integrated protection and control of an active distribution and a microgrid.

Finally, peer-to-peer and plug-and-play mode should be applied for the protection schemes [64] to enhance the reliability and to clear a fault immediately. The peer-to-peer concept enables continuous operation of the system even with loss of any component. And the time required for the decision of a fault condition is quite short when compared to the centralized method. The plug-and-play concept expands the coordination between the protection devices limitlessly without reconfiguration of the settings of newly implemented protection devices. For the peer-to-peer method, in [66, 67], an interlocking signal that blocks the operation of upstream device is sent to the upstream devices to deliver fault information. The paper [67] introduces a directional interlocking signal to avoid the shortcomings of a non-directional-interlocking signal [68]. The non-directional interlocking scheme installed on radial distribution feeders sends an interlocking signal to the source side. And a corresponding recloser that the interlocking signal has not been reached trips and isolate the faulted portion.

2.7 Synchrophasor and Synchronized Sampling

This chapter provides an overview of the technology on present day intelligent electronic devices (IEDs) such as a phasor measurement unit (PMU) and a phasor data concentrator (PDC). The need to achieve synchronized measurements for a state estimation (SE) has been long recognized. To achieve synchronized measurements, a clock with accuracy better than one micro second is required at every key location of power systems. The first device capable of performing synchronized measurements with accuracy comparable to the global positioning system (GPS) clock accuracy was developed by Macrodyne and was released in the market in 1992 [69]. The PMU device is capable of performing GPS synchronized measurements with GPS accuracy. A time reference provided by the GPS can provide a very accurate time reference of which accuracy better than one micro second anywhere on earth. Specifically, the phase of voltage and current can be calculated on almost absolute basis by use of a highly accurate GPS clock. This time reference allows the measurement of the phase angle of the fundamental signal with an accuracy of 0.02 degrees on a system-wide common reference. Commercial PMUs were installed throughout the eastern and western power systems of the United States [70]. Use of synchronized measurements simplifies the SE problem. Most of the cases, PMUs are deployed with several other PMUs to back up other PMUs that might be out of order and so deteriorate the computation of the SE. Generally, these PMUs will be integrated with a number of other functions to build fully networked and automated power systems.

In addition, a phasor data concentrator (PDC) collects data from multiple PMUs, manages the data including time alignment and provides the sum of the data to other entities for various applications. Because of the differences in latency and reporting rate

of various PMUs, the synchrophasor data measured in time usually will not arrive at the same time. PDCs may buffer data for short time duration to produce a validated and time-aligned output stream. Each measurement carries a precise time stamp taken from the GPS so that the entire electric grid can be analyzed at any moment in time. The PDC will complete the process when all relevant data have arrived or when the maximum waiting time has collapsed. If some of the data are not processed, then it will discard the data and move on to the next process because the PDC does not store the data [71]. Real-time data broadcasting capability of the PDC enables other utilities to make use of the time aligned data. The PDC supports the synchrophasor standard, 37.118, IEEE1344, PDC stream, and object linking and embedding (OLE) for process control (OPC) for real-time data transmission. OPC and extensible markup language (XML) formatted historical data access options enables us to store and access massive amount of data.

The numerical relay enabled increased automation. Two major approaches as evolved in the past decade are shown in Figure 9. To the right of the figure, the approach of connecting numerical relays to the instrument transformers and control circuits on one side and to a station bus on the other side for easy communications and managing relay settings is shown. To the left of the figure, the introduction of the MUs and the process bus is shown. These arrangement lead to the capability to use the relays as an integral part of the SCADA system and eliminates the need for remote terminal units (RTUs) since relays or the station bus provides the functionality of the RTUs. It also leads to the integration of protection and control.

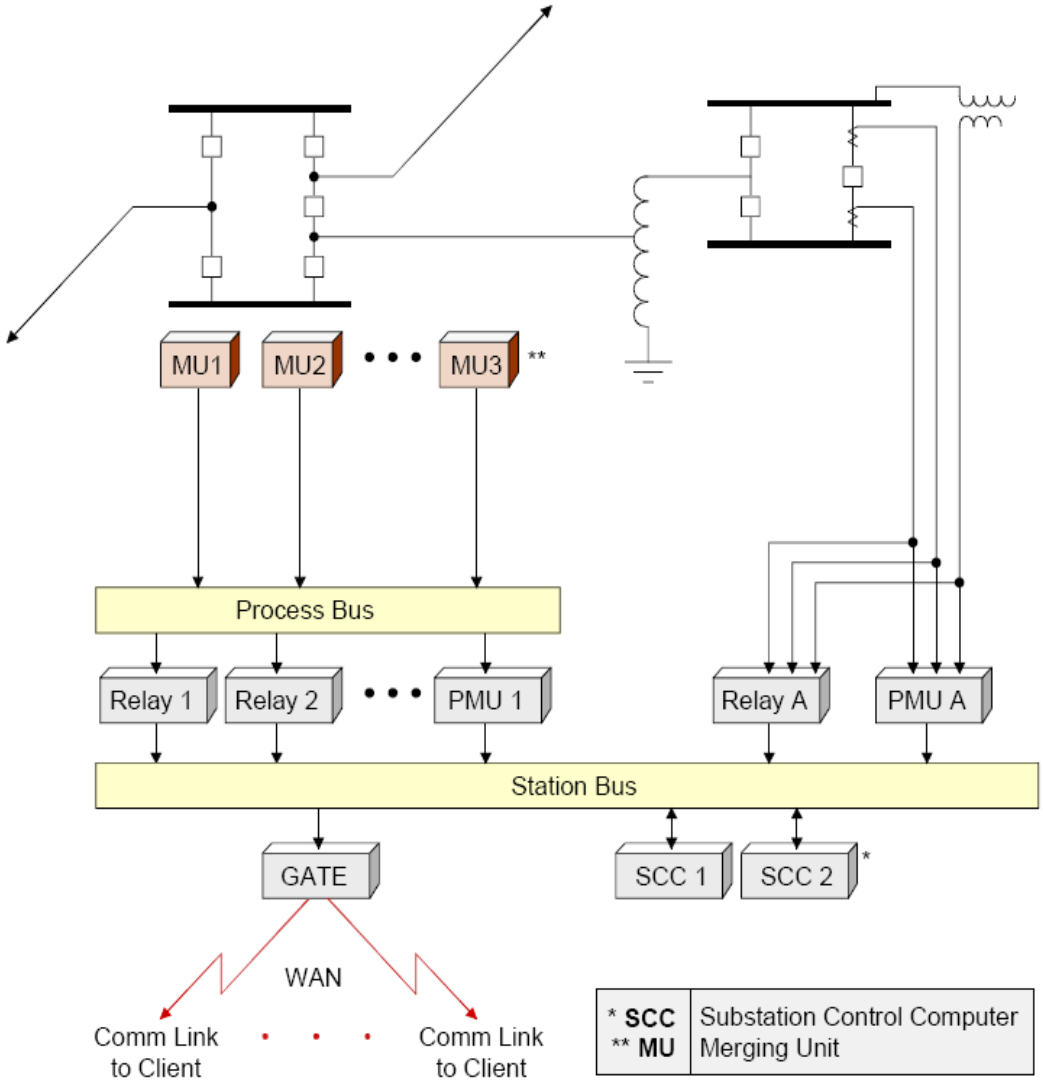

Figure 9: Data collection at a substation [69].

2.8 IEC 61850 Process Bus Application for Protection of Power Systems

In this section, a novel communication standard for substation automation, IEC 61850, and its application for protection of power system is introduced. The possibilities of a fully automated, self organized, reliable and secure protection are huge considering that

present state of technology in monitoring, protection and control of power systems is advanced. To achieve these goals, the first step is to recognize that the presently fragmented approach to protection and control of the systems can be easily integrated with present day technology. It is required to achieve full observability of the feeder, potentially at every bus of an active distribution system and a LV microgrid. Thus to achieve the full observability, merging units (MUs) are deployed. MUs collect data directly at the instrument transformers, data is digitized, time tagged, and the processed data are transmitted to the process bus or via concentrator to the process bus by communication channels according to IEC 61850-9 standard [72].

The major expected benefit of using the MUs for the protection applications is the savings on the equipment and process wiring with increased flexibility by replacing traditional IEDs with simple sensors with all protection and control schemes performed on a PC. The architecture of such a system is show in Figure 10.

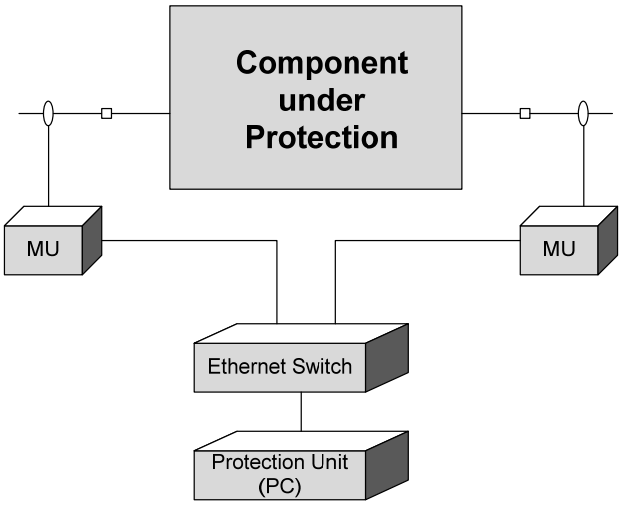

Figure 10: IEC 61850 process bus based unit protection.

2.9 A Novel Smart Metering Device

To achieve the possibilities of a fully automated, self organized, reliable and secure protection, the deployment of a novel smart metering device which will be referred to as a universal GPS synchronized meter (UGPSSM) is assumed. The UGPSSM are deployed on the poles of feeder lines, along active distribution and LV microgrid feeders. The major characteristics of the UGPSSM are the following: a) low cost, b) power autonomous, c) synchronized voltage and current phasor computation capability, and d) two way communications capability.

The major components of the UGPSSM are illustrated in Figure 11. It consists of an energy harvester, a voltage and a current sensor, a GPS sensor, a microprocessor, and a communication component. Overall, this component is an advanced meter that performs the role of MUs. MUs collect data directly at the instrument transformers, data is digitized, time tagged, and the processed data are transmitted to the process bus or via concentrator to process bus by communication channels according to IEC 61850-9 standard [72].

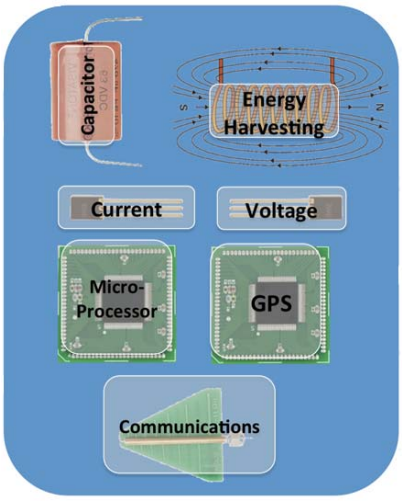

Figure 11: Conceptual view of self powered GPS synchronized, communications enabled smart meter [73].

3 Motivation of the Research

The main objective of this thesis is to formulate and demonstrate protection schemes for loop systems, an active distribution system, and a LV microgrid. The protection schemes are composed of (a) A new loop scheme that uses the VIT reclosers and sectionalizers and (b) A new protection scheme, the DSE-based protection, for an active distribution system and a LV microgrid controlled by means of DSE information.

The close-in fault problem of a traditional loop scheme can be solved by the use of the VIT devices. Although every utility wants to prevent the close-in fault, the problem is considered unsolvable unless communication devices are installed on each protection device. The first objective of this thesis is to suggest a practical and reliable technology that solves this problem. The best solution is source- and load-side fault confirmation without communication devices.

On the other hand, the state of recent technological advances (PMU capability, MUs, process bus, station bus and interoperability) has not been accompanied with commensurate advances on the protection coordination. The settings of protective devices still utilize the same principles of many decades ago. These principles rely on distinct separations and characteristics between "fault conditions" and "normal and tolerable conditions". Even for the classical power system without renewable energies and a plethora of power electronic interfaced components, the separation and identification of "fault conditions" and "normal and tolerable conditions" is in many circumstances difficult, for example, short lines, weak/strong feeds, HIF, etc. In the presence of renewable energies with power electronic interfaces, these issues multiply.

The end result is that it becomes extremely difficult to develop a secure, reliable, dependable, speedy, safe and low cost protection system based on the conventional principles.

Despite the advanced status of numerical relays, gaps in protection and settings may lead to compromised solutions. The challenges arise with the presence of renewable energies on distribution systems and microgrids are reduced fault current level and changed fault direction. Moreover, bidirectional power flow systems with many generating resources along the distribution system also arise numerous protection issues.

The second objective of this thesis is to solve the problems related to the active distribution system and the microgrid by using the DSE-based protection scheme. It is expected that the DSE-based protection scheme will maximize the recent technological advances. It is feasible by utilizing the protection logic that acts on the basis of the operating condition and health of the system.

4 Research

4.1 The Research Description

Two protection schemes are as follows: (a) The VIT scheme and (b) The DSE-based protection scheme. The protection schemes are briefly described here.

4.1.1 The VIT Scheme

The VIT scheme offers a solution to the close-in fault operation. The VIT scheme provides fault detection algorithm at source side and load side as well mainly by utilizing counter and timer coordination between the VIT recloser and the VIT sectionalizers. The name VIT is formed from the fact that this algorithm uses voltage, current, and timer information to coordinate protection devices. The VIT technology involves traditional FCC and TCC coordination. The VIT scheme introduces an additional feature, no-voltage counter (NVC), to confirm the fault condition from load side, to isolate the fault location, and eventually to prevent the close-in fault operation. The NVC counts no-voltage condition of the feeder that results from backup device operation. The VIT scheme is described in greater detail in Section 4.2. Simulation results are provided in Section 5.1 and Section 5.2.

4.1.2 The DSE-based protection scheme

For the DSE-based protection scheme, DSE is used to continuously monitor the dynamic model of the component (zone) under protection. If any of the physical laws for the component under protection is violated, the DSE will capture this condition. The method requires a time-synchronized monitoring system of the component under protection that

continuously measures terminal data (such as the terminal voltage magnitude and angle, the frequency, and the rate of frequency change) and component status data (such as tap setting (if transformer) and temperature). The DSE processes these measurement data with the dynamic model of the component yielding the operating conditions of the component. Afterwards, the chi-square value (see Section 4.3.1.5) of measurement data is computed to check the consistency between the measurement and the quadratic model. If the confidence level is low, then an internal fault is detected, and the relay will trip the CB to protect the system. The DSE-based protection approach is described in more detail in Section 4.3. Simulation results are demonstrated for the DSE-based distribution line protection scheme case on an active distribution in Section 0, 5.3.2, and 5.3.3 and on a LV microgrid, in Section 5.3.4, 5.3.5, and 5.3.6.

4.2 The VIT Scheme

A new self-healing loop scheme that prevents the close-in fault problem is illustrated in this chapter. The VIT technology coordinates CBs, reclosers, and sectionalizers at every critical node of a distribution system to provide more selectivity and confirms fault condition at both source side and load side without communication devices. The VIT scheme measures RMS values of current and voltage at the relay installation as illustrated in Figure 12.

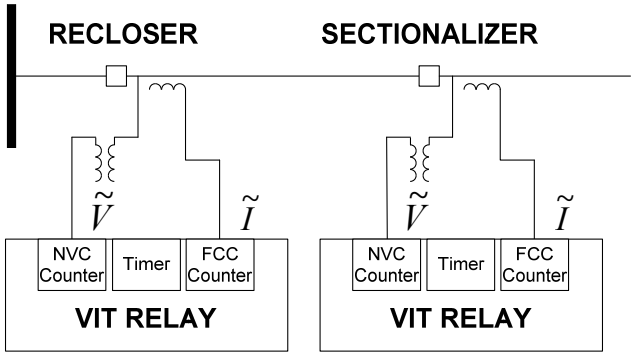

Figure 12: System configuration for the VIT relays.

From the current and voltage measurements, the VIT relays can monitor FCC and/or NVC. After that, the VIT scheme uses counters to count the number of FCC and/or NVC. When the counted number of FCC or NVC is equal to the pre-selected setting values, then the VIT relays get ready for an instant or a time-delayed trip operation. The trip command isolates the fault condition by tripping source and load side recloser or sectionalizers. As a result, the fault location is removed from the system before the normally open recloser closes onto the fault, and nuisance trip of the normally open recloser can be prevented. Note that the VIT scheme only requires local information. The detailed operating conditions and setting values are explained in the next section.

4.2.1 VIT Scheme Description

The overall implementation of the VIT scheme is described in this section. For the loop scheme, the VIT scheme composes of the following counters and timers:

- FCC – A VIT device counts the number of trip of a back up device. For a fault condition on a grounded system, the first recloser located at the upstream of the fault location trips before other backup devices. A VIT device trips instantly when the

counted number of fault current is equal to the FCC setting value. If the fault is a temporary fault, then the backup device attempts to clear the temporary fault by reclosing. In this thesis, one-time reclosing for temporary fault is assumed. Therefore, a VIT device has FCC setting value larger than one to guarantee the temporary fault removal. If the temporary fault is not cleared after the first reclosing of a backup device, then the fault is a permanent fault. To isolate a fault condition by tripping a fault-upstream device, a VIT device is set to open lockout when the VIT device counts one less operation of an upstream device. The details of the FCC setting values are explained in the later example.

- No-voltage counter (NVC) – The VIT scheme introduces a new feature, the NVC, to confirm the fault condition from the load side of the fault. A VIT device counts the number of no-voltage condition followed by a trip of a backup device. A VIT device trips after a close time delay when the counted number is equal to the NVC setting value. As a result, the VIT scheme enables an isolation of the fault location before the tie recloser closes onto the fault. The details of the NVC setting values are explained in the later example.

- Close timer – A close time starts when the counted number of no-voltage conditions is equal to the NVC setting value. The close timer is programmed in such a way that the NVC of a downstream VIT device does not initiate a trip signal while NVC value is increasing. Finishing the close timer without monitoring a fault condition indicates that the fault is on the source side; so the VIT device closes. A close lockout timer starts after the successful closing.

- Counter and timer reset – The FCC and NVC counters are reset after the trip signal is generated, and the timers are reset when it finishes.

- Normally open close timer – For a normally open sectionalizer, voltage measurement data at two sides of the device is required. When voltage measurements at one side of the normally open sectionalizer disappear, the normally open sectionalizer closes into an alternative source after finishing the normally open close time.

The instrumentation of the VIT scheme, which measures three-phase voltage and current, is shown in Figure 13. Three current transformers and three resistive voltage sensors are integrated inside the VIT recloser or sectionalizer. Note that for a normally open sectionalizer, voltages are measured at both sides. The current transformers monitor the fault current level, and the voltage sensors monitor the voltage level. Note that any of the phases can be utilized for the VIT scheme.

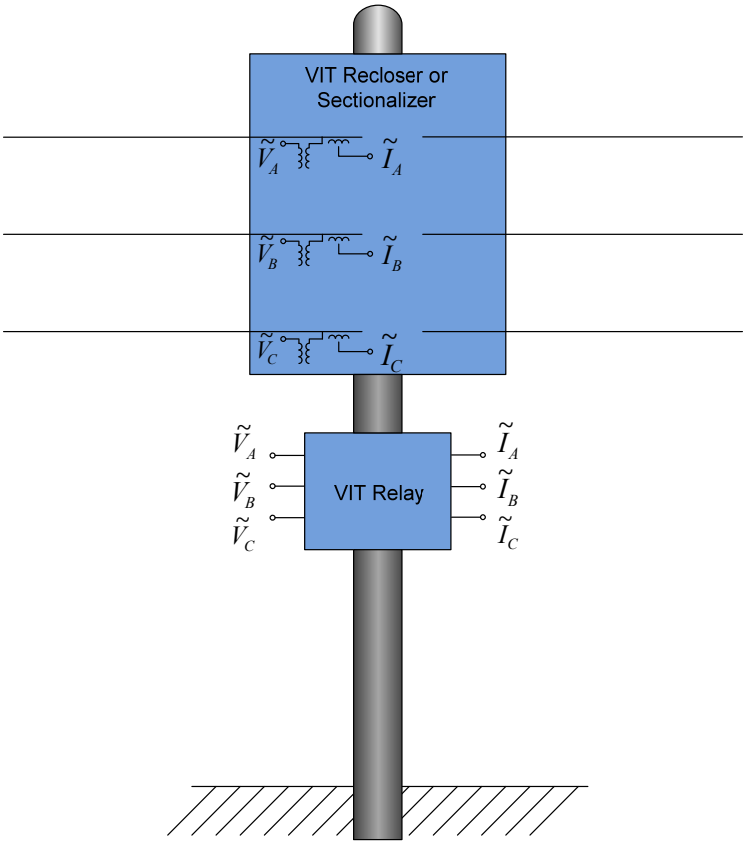

Figure 13: Voltage and current measurement for the VIT scheme.

The FCC and the NVC setting value of a VIT device is selected as shown in Figure 14. For the FCC setting, a downstream VIT device has one less operation of an upstream device. For example, an upstream recloser with four reclosing is coordinated with a downstream sectionalizer, which has three FCC setting value. For the NVC setting, a downstream VIT device has same FCC or same operation of an upstream device. For example, an upstream recloser with four reclosing is coordinated with a downstream sectionalizer, which has four NVC setting value.

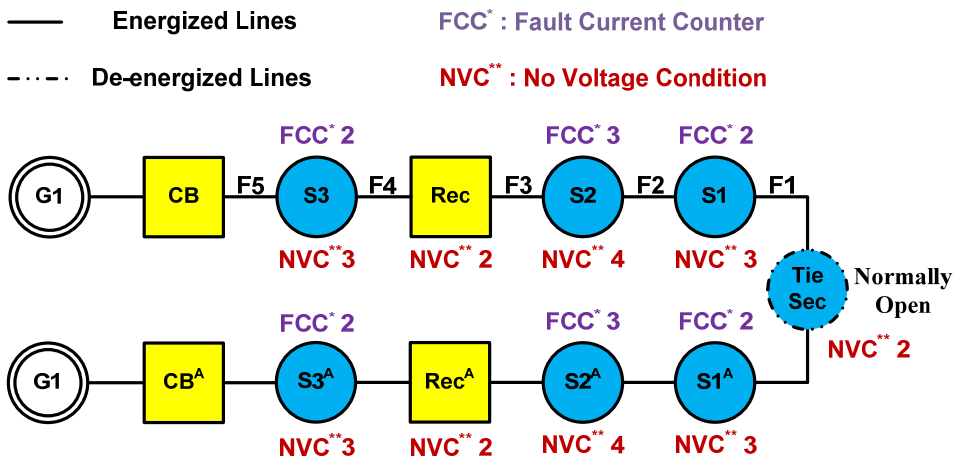

Figure 14: FCC and NVC settings of the VIT reclosers and sectionalizers.

In fact, a VIT device opens to lockout if either the FCC or NVC condition is satisfied. A simplified logic diagram of the VIT scheme is illustrated in Figure 15. The VIT device located at the closest upstream of a fault section completes the FCC first and opens to lockout instantly while the VIT device located at the nearest downstream of a fault section completes the NVC and opens to lockout after a time delay.

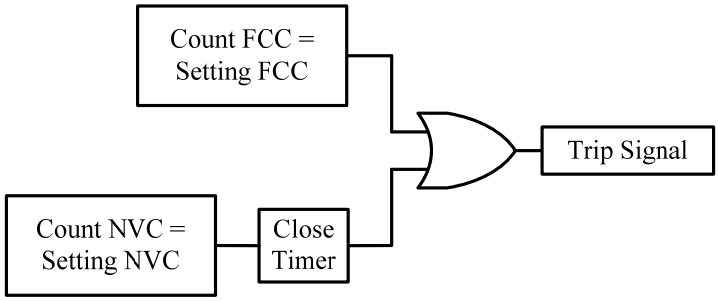

Figure 15: Symbolic logic diagram for the VIT scheme trip operation.

The FCC and NVC counters reset when the trip signal is generated, and the timers reset when it finishes. In the next following Section 4.2.2, more detailed example of fault isolation operation of the VIT scheme is illustrated.

4.2.2 An Examples of Device Coordination, Fault on F2

A fault occurs between S2 and S1, on F2 of Figure 14.

First Open and Reclosing Operation

The primary feeder recloser senses the fault current and opens circuit on the first fast trip curve (first operation). S2 detects both fault current and no-voltage condition, and then S2 increases its FCC and NVC values from zero to one. On the other hand, both S1 and the tie sectionalizer do not experience fault current because no power sources other than main source supply the fault current. Instead, S1 and the tie sectionalizer experience no-voltage condition when the backup recloser is open and count one NVC.

Second Open and Reclosing Operation

S2 again detects both fault current and no-voltage condition and advances both FCC and NVC values from one to two. S1 and the tie sectionalizer detect no-voltage condition and count two NVCs. The close timer of the tie sectionalizer starts since the counted no-voltage condition is equal to the programmed NVC setting value (two no-voltage conditions = two NVCs). However, this close timer is canceled by the third no-voltage condition.

Third Open and Reclosing Operation

S2 counts three FCCs and three NVCs and then trips to a lockout because the counted FCC is equal to the programmed FCC value (three fault current conditions = three FCCs).

And the FCC of S2 resets. The reset of FCC of S2 initiates reset of NVC of S2. S1 detects three NVCs and the close timer starts because the cumulated NVCs are same with the pre-selected NVC value (three no-voltage conditions = three NVCs). S1 trips after the close time delay, and the S1 NVC resets after the trip. On the other hand, the tie sectionalizer also counts three NVC but the tie sectionalizer does not trip because the NVC setting value is two. As soon as the NVC value is not equal to the NVC setting value, the close timer stops. As a result, both upstream and downstream fault nearest sectionalizers, S2 and S1, trip to isolate the fault. The increment of FCC and NVC values along the operation of a recloser for a fault on F2 case is illustrated in Figure 16.

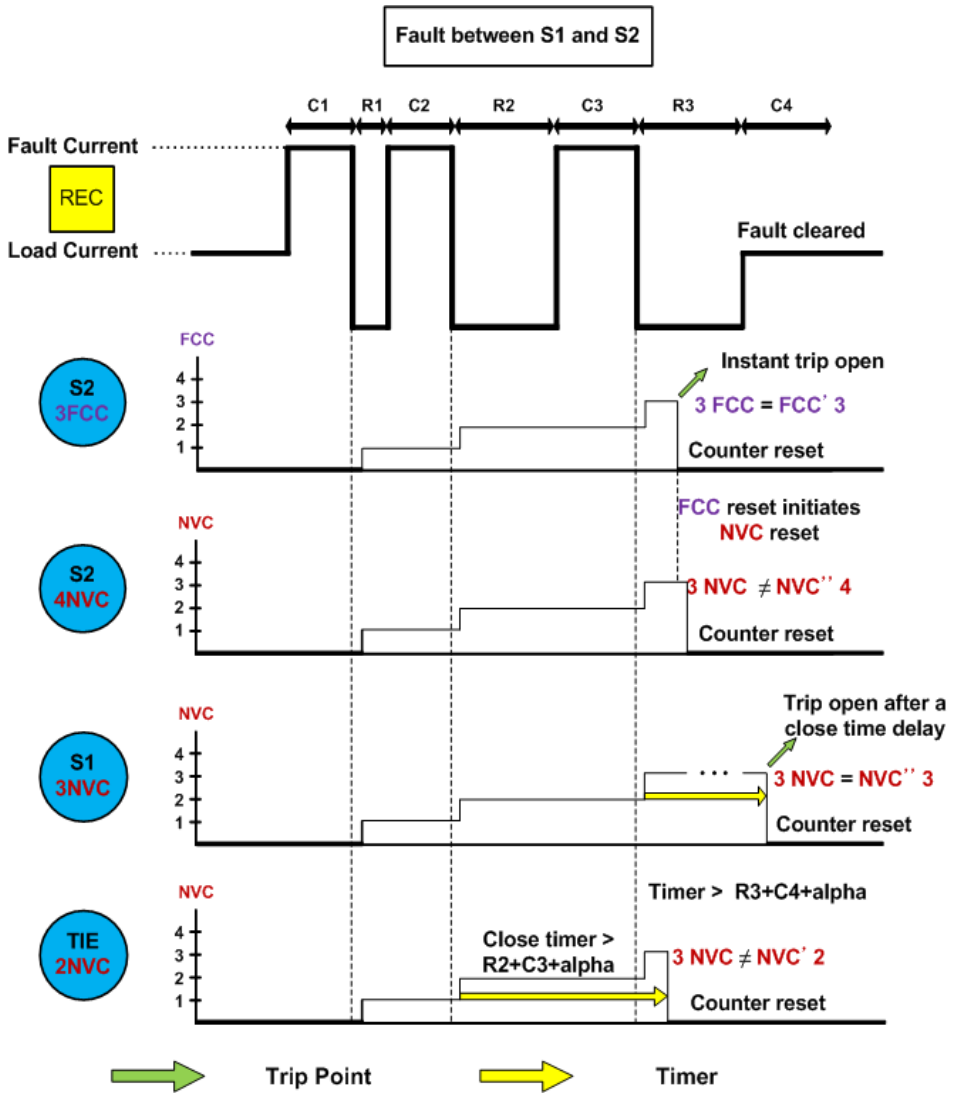

Figure 16: Sectionalizer counters operation sequence as related to recloser operation.

After the isolation of the fault by tripping S2 and S1, the tie sectionalizer closes after the normally open close timer to recover the power of the system from an alternative source. The tie sectionalizer senses loss of voltage from one feeder, changes setting to a closed switch mode, and closes to the secondary feeder after a time delay. During the closed switch mode, the corresponding protection device is closed with no specific setting values. When the tie sectionalizer connects to an alternative source, no nuisance trip is

occurred. To see how the loop system is reconfigured after the fault detection and isolation, refer to Figure 17, which shows that nine tenths of the restored loop system are healthy and protected by coordinated devices.

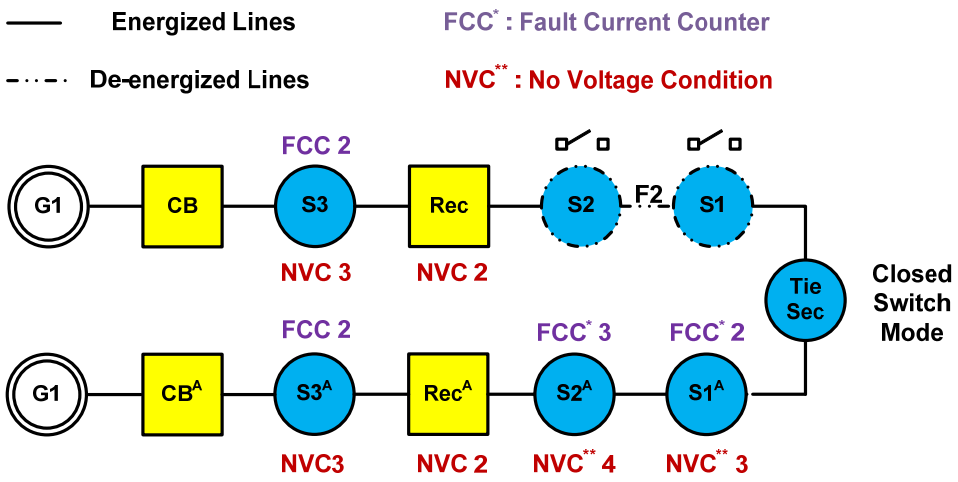

Figure 17: A loop system restoration after a fault on F2.

For a fault on F2 section, the primary feeder protection devices supplies power to the section F3, and the secondary feeder protection devices provide power to F1 section through the tie sectionalizer.

4.2.3 An Examples of Device Coordination, Fault on F3

When fault occurs between recloser and S2, at F3, recloser finishes its four time tripping sequence and S2 counts "4" NVC during the process. S1 and tie sectionalizer also count "4" NVC. Both upstream recloser and downstream fault nearest sectionalizers S2 succeeded in detection and isolation of the fault.

To coordinate S1 and tie sectionalizer with alternative source, a closed switch mode is utilized. The closed switch mode sectionalizers have no FCC or NVC setting. Since both

S1 and tie sectionalizer knows that the fault section is F3 ("4" NVC), these devices prepare closed switch mode to coordinate with the secondary feeder protection devices such as CB^{A}, S3^{A}, recloser^{A}, S2^{A}, and S1^{A}. S1 and tie sectionalizer sense loss of voltage from both feeders, changes setting to closed switch mode, and closes to the secondary feeder after a time delay. To see how the looped distribution system is reconfigured, refer to Figure 18, which shows that nine tenths of the restored loop system are still energized and protected by coordinated devices.

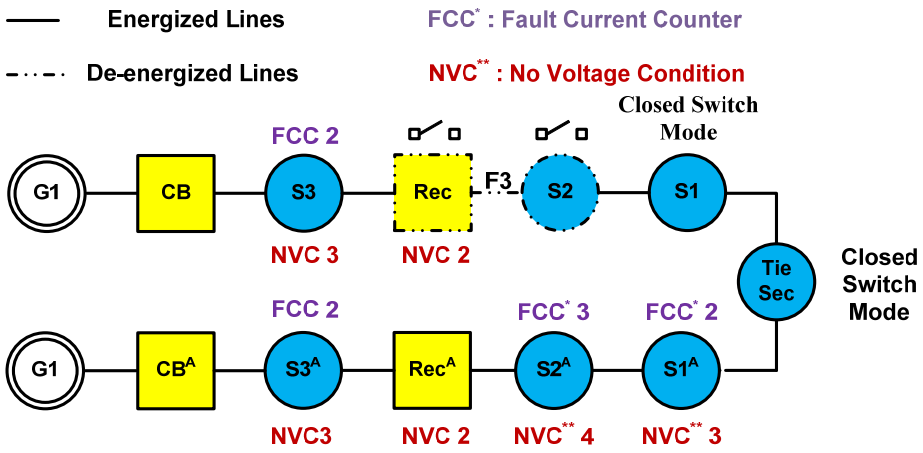

Figure 18: Looped distribution system restoration after Fault on F3.

For a fault on F3 section, the primary feeder protection devices supplies power to the section F4 and the secondary feeder protection devices provide power to F2 section through the tie sectionalizer.

4.2.4 An Examples of Device Coordination, Fault on F4

When fault occurs at F4, the primary feeder backup CB detects fault current and closes on its fast curve. However, when fault occurs upstream of recloser, VIT scheme requires

one more restraint to discriminate fault between CB and recloser from fault between recloser and tie sectionalizer. In more detail, although recloser, S2, and S1 do not monitor fault current, recloser, S2, and S1 count NVCs. Therefore they have potential hazard of a false tripping. For example, S3 and S1 have same NVC setting value and will trip on counting "3" NVCs. The method in this theis, called temporary open method, is that the recloser also opens to desensitize downstream devices as soon as recloser detects source voltage loss. More specifically, if fault condition still exists after CB's fast trip, then the microprocessor let the recloser be opened so that S2 and S1 do not have a chance to count NVC more than "1". Along the sequence of VIT scheme, S3 opens on counting "2" FCC and recloser opens on counting "2" NVC. And the fault section is removed.

Since S2, S1 and tie sectionalizer knows that the fault section is somewhere upstream of recloser ("1" NVC), these devices prepare closed switch mode to coordinate with the secondary feeder protection devices such as CB^{A}, $S3^{A}$, $recloser^{A}$, $S2^{A}$, and $S1^{A}$. S2, S1 and tie sectionalizer sense loss of voltage from both feeders, changes setting to closed switch mode, and closes to the secondary feeder after a time delay. Consequently, the Fault on F4 is cleared by S3 and recloser as in Figure 19 and nine tenths of the entire circuit are still energized and protected by coordinated devices after recovering secondary feeder.

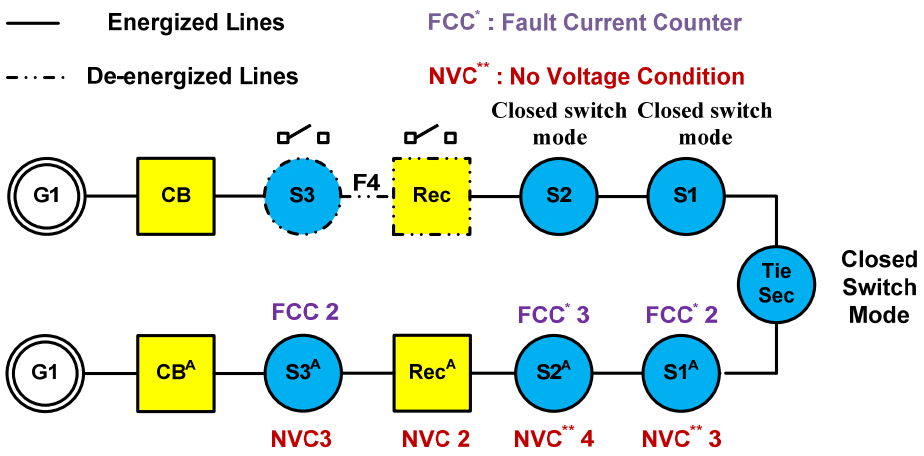

Figure 19: Restored looped distribution system after Fault on F4.

For a fault on F4 section, the primary CB supplies power to the section F5. Radial coordination between CB^A, $S3^A$, $recloser^A$, S1, and S2 makes it possible to provide power to F3 section through the tie sectionalizer.

4.3 The DSE-based protection scheme

A new fault-detection scheme relies on synchronized sampling is explained in this chapter. The protection scheme uses DSE (see Section 4.3.1.3), based on the dynamic model of the component that accurately reflects the nonlinear characteristics of the component as well as the loading and thermal state of the component. The method has been inspired from the fact that differential protection is one of the more secure protection schemes, and it does not require coordination with other protection function. Differential protection simply monitors the validity of Kirchoff's current law in a device, i.e. the weighted sum of the currents going into a device must be equal to zero. This concept can be generalized into monitoring the validity of all other physical laws that the

device must satisfy, such as Kirchoff's voltage law, Faraday's law, etc. This monitoring can be done in a systematic way by the use of the DSE. Specifically, all the physical laws that a component must obey are expressed in the dynamic model of the component. The DSE is used to continuously monitor the dynamic model of the component (zone) under protection. If any of the physical laws for the component under protection is violated, the DSE will capture this condition. Thus, the dynamic state estimator is used to extract the dynamic model of the component under protection [74-78] and to determine whether the physical laws for the component are satisfied. The dynamic model of the component accurately reflects the condition of the component and the decision to trip or not to trip the component is based on the condition of the component only irrespectively of the condition (faults, etc.) of other system components. As described in Figure 20, the protection scheme requires a monitoring system at the component under protection that continuously measures terminal data (such as the terminal voltage magnitude and angle, the frequency, and the rate of frequency change) and component status data (such as the tap setting and the temperature). And then the DSE processes these measurement inputs with the dynamic model of the unit to yield operating conditions. A quadratic modeling has been used to improve the convergence of the algorithm.

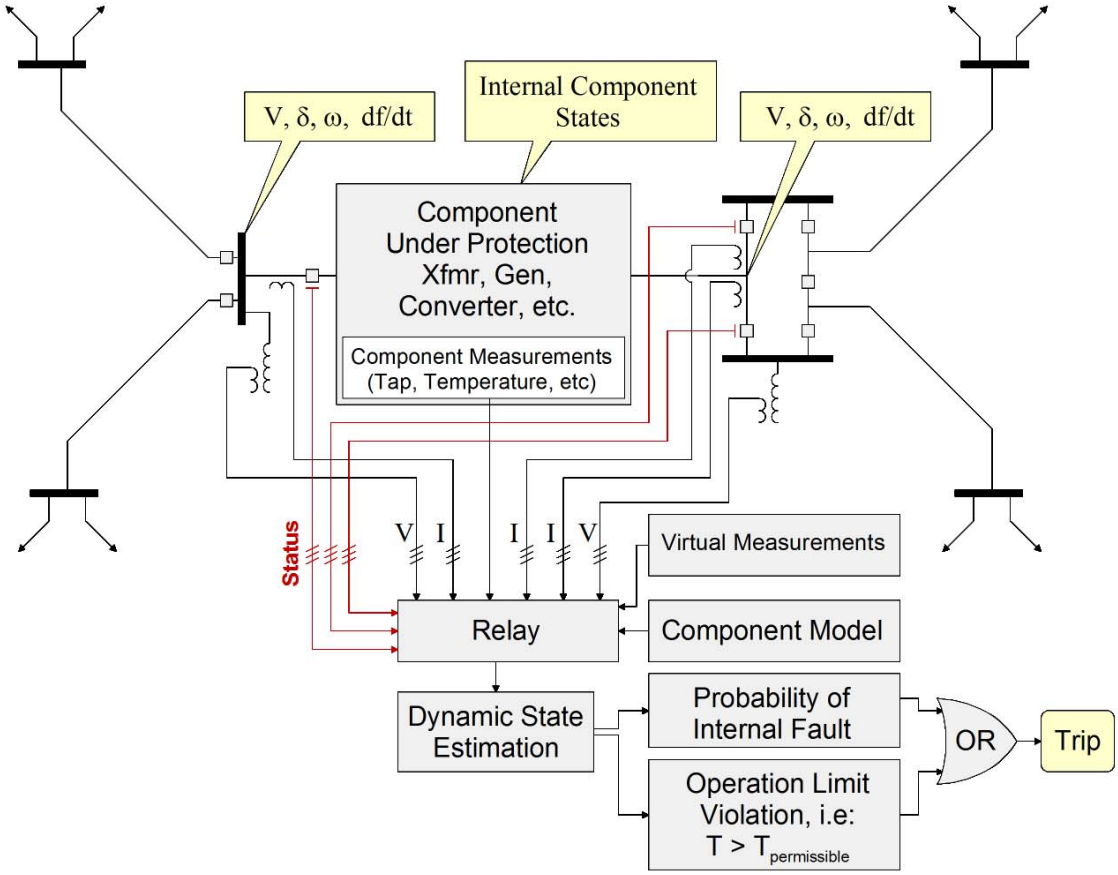

Figure 20: System configuration for the component protection [69].

After estimating the operating conditions, the well known chi-square test calculates the probability that the measurement data are consistent with the protected unit model (see Figure 21). In other words, this probability, which indicates the confidence level of the goodness of fit of the protected unit model to the measurements, can be used to assess the health of the protected unit (see Section 4.3.1.5). This probability shows the confidence level of the goodness of fit of the measurement data to the protected unit. The high confidence level implies a good fit between measurements data and protected unit. As long as a fault occurs outside of the unit protected element, the DSE results in a high

confidence level. On the contrary, any fault condition occurred inside of the protection zone will lead to a reduced confidence level. So, the units are well protected by the DSE-based protection scheme. The protection scheme can identify any internal abnormality of the power system apparatus such as transformers, capacitor banks, generators, and feeder lines within a cycle and trip the circuit breaker immediately. Only the simulation result of a distribution system and microgrid are suggested in this thesis.

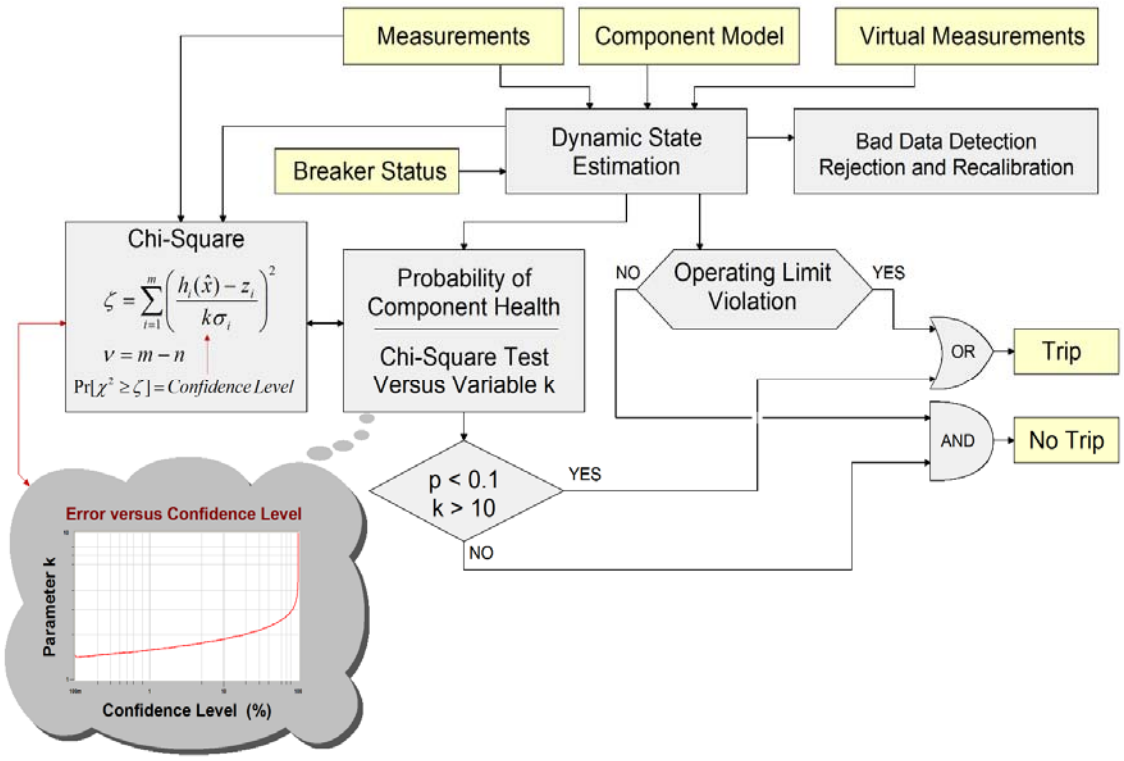

Figure 21: The DSE-based protection scheme [69].

4.3.1 DSE-based Relay Description

The overall implementation of the DSE-based protective relay is described in this section. The architecture of this relay is shown in Figure 22. Note that the relay requires the model of the zone to be protected and the actual (physical) measurements from the data acquisition system. The model must be provided in the AQCF syntax, which is defined in this thesis. Then the remaining analytics are automatically constructed and executed. The remaining analytics are as follows: the pointers that provide the interrelationship of the actual measurements to the zone model, the creation of the measurement models for the actual, virtual, derived, pseudo measurements, the DSE, the bad data detection and identification, and the protection logic.

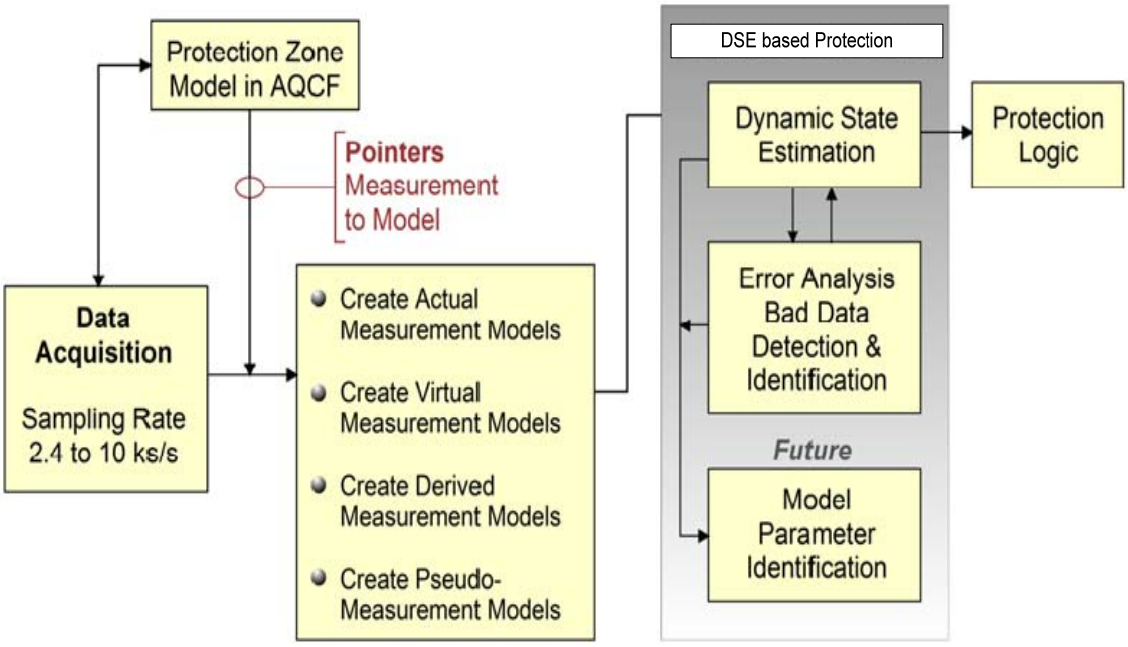

Figure 22: Architecture of a DSE-based relay.

Note that the data acquisition system is continuously streaming measurement into the relay with a specific rate. Typical rates are 2,000 to 5,000 samples per second. As it will be seen later, the model of the component to be protected is derived in the AQCF by using the quadratic integration. The AQCF model is expressed in terms of the values of the various variables at two consecutive time instances (two consecutive samples) and

past history samples. This means that the analytics of the DSE-based protective relay operate on samples of two consecutive time instances. This is illustrated in Figure 23. The samples (measurements) at the two consecutive time instances t and ($t-t_s$) are used. Note that t_s defines the sampling period. For the typical sampling rates referenced above the mining sampling period will be 200 microseconds (5,000 samples per second). This means that the analytics of the DSE-based relay must be performed within the time interval of 400 microseconds (before the next set of data arrive). Obviously, there should be a margin. For this reason the goal for the DSE-based relay is to perform the analytics in time less than 200 microseconds. Numerical experiments have been performed and the performance is documented in Section 5.

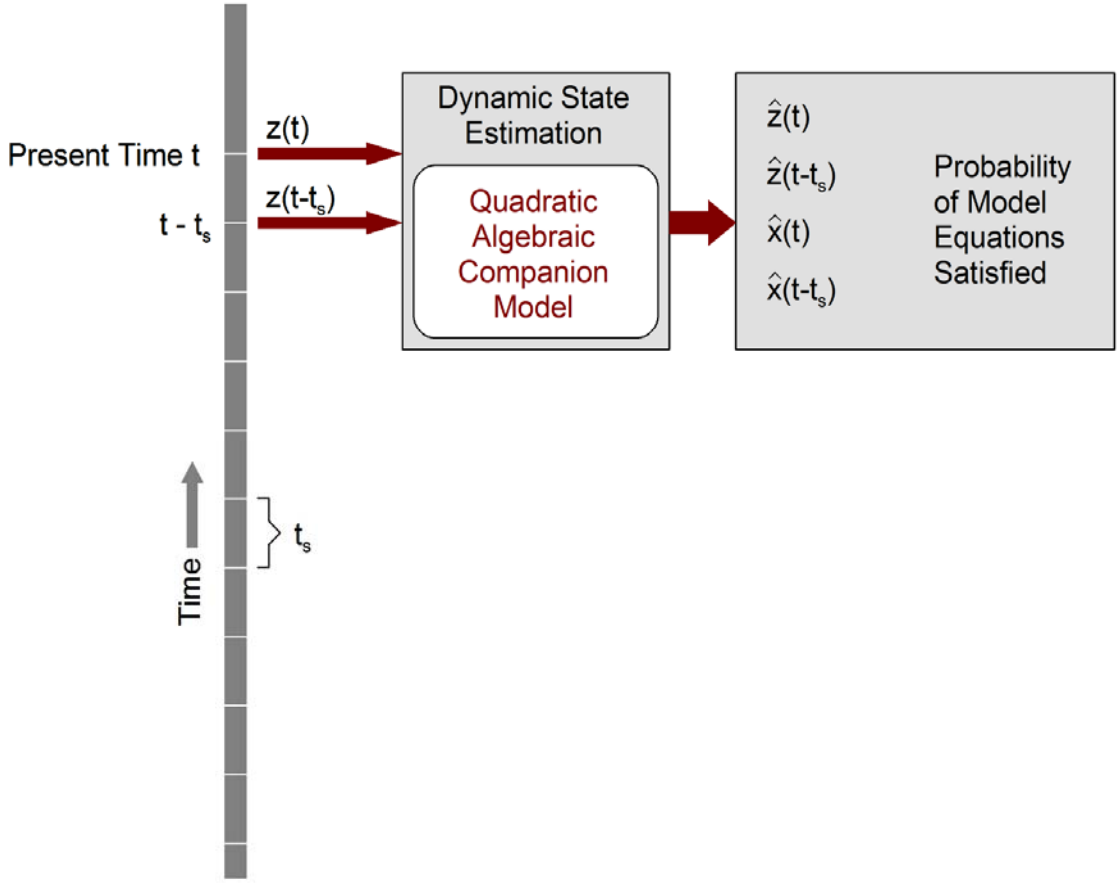

Figure 23: Illustration of time samples utilized at each iteration of the DSE-based relay analytics.

The components of the DSE-based relay are briefly described next.

4.3.1.1 Protection Zone Mathematical Model

The protection zone mathematical model is required in a standard form. A standard has been defined in the form of the algebraic quadratic companion form (AQCF) and in a specified syntax to be defined later. The AQCF for a specific protection zone is derived with three computational procedures. Specifically, the dynamic model of a protection zone consists of a set of algebraic and differential equations. We refer to this model as the compact model of the protection zone. Subsequently this model is quadratized, i.e. in case the nonlinearities of the model is greater than order two, additional state variables are introduced so that at the end the mathematical model consists of a set of linear and quadratic equations. This model is the quadratized model. Finally, the quadratized model is integrated using the quadratic integration method that converts the quadratized model of the protection zone into a set of algebraic (quadratic) function. This model is cast into a generalized Norton form. This model is the AQCF.

The standard algebraic companion form is obtained with two procedures as follows: (a) Model quadratization and (b) Quadratic integration. The model quadratization reduces the model nonlinearities so that the dynamic model will consist of a set of linear and quadratic equations. The quadratic integration is a numerical integration method that is applied to the quadratic model assuming that the functions vary quadratically over the integration time step. The end result is an algebraic companion form that is a set of linear and quadratic algebraic equations that are cast in the following standards form:

$$\begin{bmatrix} i(t) \\ 0 \\ i(t_m) \\ 0 \end{bmatrix} = Y_{eq} \begin{bmatrix} v(t) \\ y(t) \\ v(t_m) \\ y(t_m) \end{bmatrix} + \begin{bmatrix} \begin{bmatrix} v(t) \\ y(t) \\ v(t_m) \\ y(t_m) \end{bmatrix}^T \cdot F_{eq,1} \cdot \begin{bmatrix} v(t) \\ y(t) \\ v(t_m) \\ y(t_m) \end{bmatrix} \\ \vdots \end{bmatrix} - b_{eq},$$

where *i(t)* is the through variable (current) vector, *t* is present time, t_m is the midpoint between the present and previous time, *v(t) is* the across variable (voltage) vector, *y* is the internal state variables vector, Y_{eq} admittance matrix, $F_{eq,i}$ nonlinear matrices, and

$$b_{eq} = \sum_i A_i \cdot \begin{bmatrix} v(t - i \cdot h) \\ y(t - i \cdot h) \end{bmatrix} + \sum_i B_i \cdot \begin{bmatrix} i(t - i \cdot h) \\ 0 \end{bmatrix} + C.$$

This standardization allows the object oriented handling of measurements in state estimation; in addition it converts the DSE into a state estimation that has the form of a static state estimation.

4.3.1.2 Object Oriented Measurements

Any measurement, i.e. current, voltage, temperature, etc. can be viewed as an object that consists of the measured value and a corresponding function that expresses the measurement as a function of the state of the component. This function can be directly obtained (autonomously) from the Algebraic Quadratic Companion Form of the component. Because the algebraic companion form is quadratic at most, the measurement model will be also quadratic at most. Thus, the object-oriented measurement model can be expressed as the following standard equation:

$$z_k(t) = \sum_i a_{i,t}^k \cdot x_i(t) + \sum_i a_{i,tm}^k \cdot x_i(t_m) + \sum_{i,j} b_{i,j,t}^k \cdot x_i(t) \cdot x_j(t) + \sum_{i,j} b_{i,j,tm}^k \cdot x_i(t_m) \cdot x_j(t_m) + c_k(t) + \eta_k \ ,$$

where z is the measured value, t the present time, t_m the midpoint between the present and previous time, x the state variables, a the coefficients of linear terms, b the coefficients of nonlinear terms, c the constant term, and η the measurement error.

The measurements can be identified as follows: (a) Actual measurements, (b) Virtual measurements, and (c) Pseudo measurements. The types of measurements will be discussed next.

Actual measurements – In general the actual measurements can be classified as across and through measurements. The across measurements has a simple model as follows:

$$z_j(t) = x_j(t) + \eta_j \ .$$

The through measurement model is extracted from the algebraic companion form. The measurement model is simply one equation of the ACF model as follows:

$$z_j(t) = Y_{eq}{}^{(k)} \begin{bmatrix} v(t) \\ y(t) \\ v(t_m) \\ y(t_m) \end{bmatrix} + \begin{bmatrix} v(t) \\ y(t) \\ v(t_m) \\ y(t_m) \end{bmatrix}^T \cdot F_{eq,k} \cdot \begin{bmatrix} v(t) \\ y(t) \\ v(t_m) \\ y(t_m) \end{bmatrix} - b_{eq}{}^{(k)} \ ,$$

where the superscript k means the k^{th} row of the matrix or the vector.

Virtual measurements – The virtual measurements represent a physical law that must be satisfied. For example, at a node the sum of the currents must be zero by Kirchoff's current law. In this case a measurement (sum of the currents) can be defined; note that the value of the measurement (zero) is known with certainty. This is a virtual measurement.

The model can provide virtual measurements in the form of equations that must be satisfied. Consider for example the k^{th} AQCF model equation as follows:

$$0 = Y_{eq}^{(k)} \begin{bmatrix} v(t) \\ y(t) \\ v(t_m) \\ y(t_m) \end{bmatrix} + \begin{bmatrix} v(t) \\ y(t) \\ v(t_m) \\ y(t_m) \end{bmatrix}^T \cdot F_{eq,k} \cdot \begin{bmatrix} v(t) \\ y(t) \\ v(t_m) \\ y(t_m) \end{bmatrix} - b_{eq}^{(k)} .$$

This equation is simply a relationship among the states the component that must be satisfied. Therefore the zero value is a measurement with certainty. This is a virtual measurement.

Pseudo measurements – Pseudo measurements are hypothetical measurements for which their expected values are known but actual measurement data are not obtained. For example, a pseudo measurement can be the voltage at the neutral; and this voltage will be very small. In this case a measurement of value zero can be determined with a very high uncertainty.

Eventually, all the measurement objects form the following measurement set:

$$z = h(x,t) + \eta = c + a^T x(t) + b^T x(t_m) + \begin{bmatrix} x^T(t) & x^T(t_m) \end{bmatrix} F \begin{bmatrix} x(t) \\ x(t_m) \end{bmatrix} + \eta ,$$

where z is the measurement vector, x the state vector, h the known function of the model,

a, b are constant vectors, F are constant matrices, and η the vector of measurement errors.

4.3.1.3 Object Oriented DSE

The weighted least squares approach will be used for the state estimator. The algorithm is defined as follows.

$$Minimize \quad J = \sum_{i=1}^{m} \left(\frac{h_i(x) - z_i}{\sigma_i} \right)^2 = \sum_{i=1}^{m} s_i^2 = \eta^T W \eta ,$$

where $s_i = \frac{\eta_i}{\sigma_i}$, $W = diag\left\{ \frac{1}{\sigma_1^2}, \frac{1}{\sigma_2^2}, ..., \frac{1}{\sigma_m^2} \right\}$.

The solution is given with the following iterative algorithm:

$$x^{\nu+1} = x^{\nu} - (H^T W H)^{-1} H^T W (h(x^{\nu}) - z) ,$$

where H is the Jacobean matrix $H = \frac{\partial h(x)}{\partial x}$, $computed\ at\ x = x^{\nu}$.

At each time step of the estimation algorithm, the contributions of each measurement to the information matrix $H^T W H$ and the vector $H^T W (h(x^{\nu}) - z)$ must be computed.

The flow chart of the state estimation is shown in Figure 24.

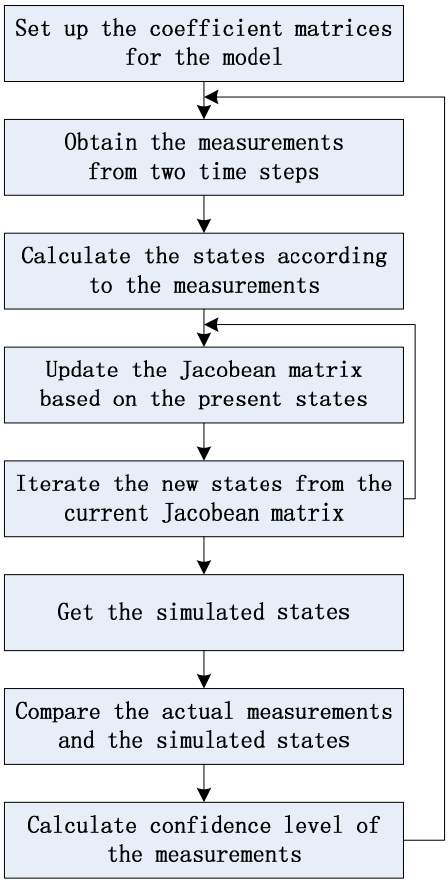

Figure 24: Flow chart for state estimation.

4.3.1.4 Bad Data Detection and Identification

It is possible that the streaming measurements may include bad data. If the confidence level is not satisfying, bad data identification and removal techniques follow. Identification of bad data normally consists of two steps. In the first step, bad data are identified by consistency rules. For example, measurements are known to have specific ranges. If measurements are out of this range, they will be classified as bad data. In the second step, bad data are identified with their effects on confidence level. In case of the least square solution, the possible bad data are identified with their large residuals. A

rather secure but computationally demanding way to identify a bad datum is by means of hypothesis testing. Since detection and identification of the bad data is not the main subject of this thesis, it is not illustrated in detail.

4.3.1.5 Protection Logic and Component Health Index

After DSE, the well known chi-square test performed to quantify the goodness of fit between the model and measurements (i.e., confidence level). The goodness of fit is expressed as the probability that the measurement errors are distributed within their expected range (chi-square distribution). The chi-square test requires two parameters as follows: (a) The degree of freedom (v) and (b) The chi-square critical value (ζ).

$$v = m - n, \qquad \zeta = \sum_{i=1}^{m} \left(\frac{h_i(\hat{x}) - z_i}{\sigma_i} \right)^2 ,$$

where m is the number of measurements, n the number of states, and $\hat{x}$ the best estimate of states. The goodness of fit (confidence level) can be finally obtained as follows:

$$\Pr[\chi^2 \geq \zeta] = 1.0 - \Pr[\chi^2 \leq \zeta] = 1.0 - \Pr(\zeta, v).$$

The curve of confidence level versus chi-square critical value is depicted in Figure 25.

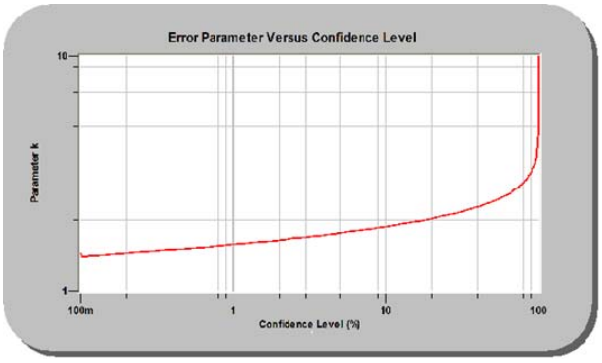

Figure 25: Confidence level (%).

Finally, the protection scheme uses the confidence level as the health index of a component. The high confidence level indicates the good fit between the measurement and the model, and thus it is concluded that the feeder line has no internal fault. The low confidence level, however, implies inconsistency between the measurement and the model, and therefore it is obvious that any internal fault of the feeder line has occurred.

5 Demonstrating Examples

5.1 Application Example of the VIT Scheme – Distribution Feeder

The VIT protection scheme is demonstrated in this chapter. An example test system is illustrated in Figure 26. The test system is composed two feeders that are connected through a normally open sectionalizer, and each feeder is protected by the CB, the VIT recloser, and the VIT sectionalizers. For one feeder, the blue area in Figure 26 depicts the protection zone. The CB and the VIT recloser is coordinated by means of TCC. Moreover, F1, F2, ⋯, and F5 represent the sections separated by CB, the VIT recloser, and the VIT sectionalizers.

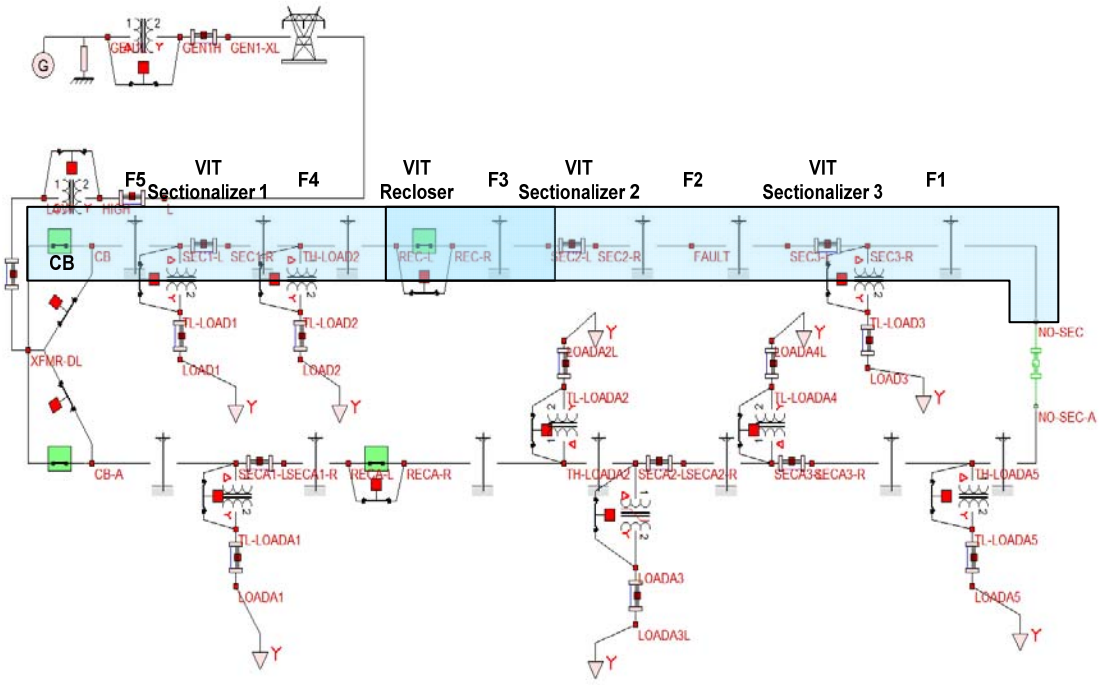

Figure 26: Test system diagram for the distribution feeder protection zone – the VIT loop scheme.

Event Description – A Three-Phase Fault on F2

The intention here is to generate waveforms that represent an internal fault condition, for example, one fault condition is initiated inside of the protection zone. Note that only three VIT relays are monitored because of the page limitation. The following specific fault is employed as shown in Figure 27.

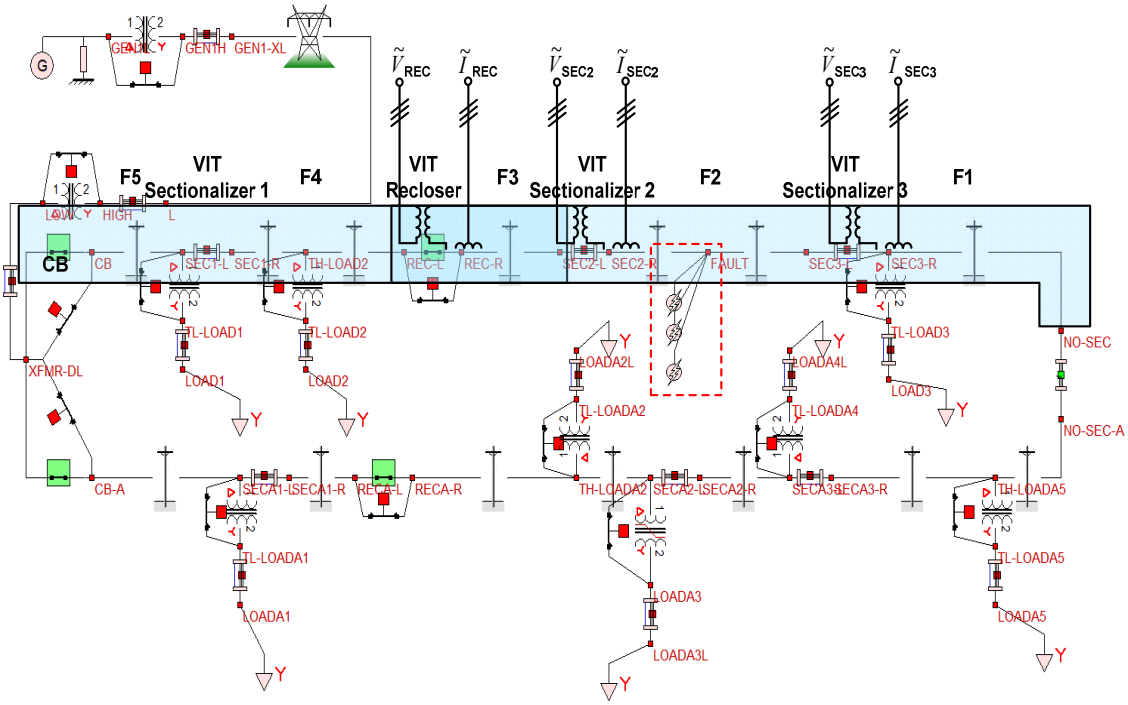

Figure 27: An internal fault simulation on the distribution feeder – the VIT scheme.

At FAULT node on the distribution feeder, a permanent three-phase to ground fault (ABCG) initiates at time 1.3 seconds. The fault is cleared by the first "fast" trip operation (within 0.05 seconds) of the VIT recloser. The VIT recloser operates before the CB on the source side according to the TCC coordination. After 0.3 seconds of delay, the VIT recloser recloses and the fault current initiates the second "fast" trip operation (within

0.05 seconds). After two seconds of delay, the VIT recloser recloses and the fault current initiates the third "delay" trip operation (within 0.5 seconds). Finally the fault is removed by the trip to lockout operation of VIT sectionalizer two and three. A result common format for transient data exchange (COMTRADE, IEEE standard C37.111) data file is generated by measuring voltage and current at the VIT relays. Using the simulated COMTRADE data file, protection of the distribution feeder is tested. Voltage and current measurements are obtained from the local measuring devices, and examples of measurements at the VIT recloser when a fault is on the distribution feeder are shown in Figure 28.

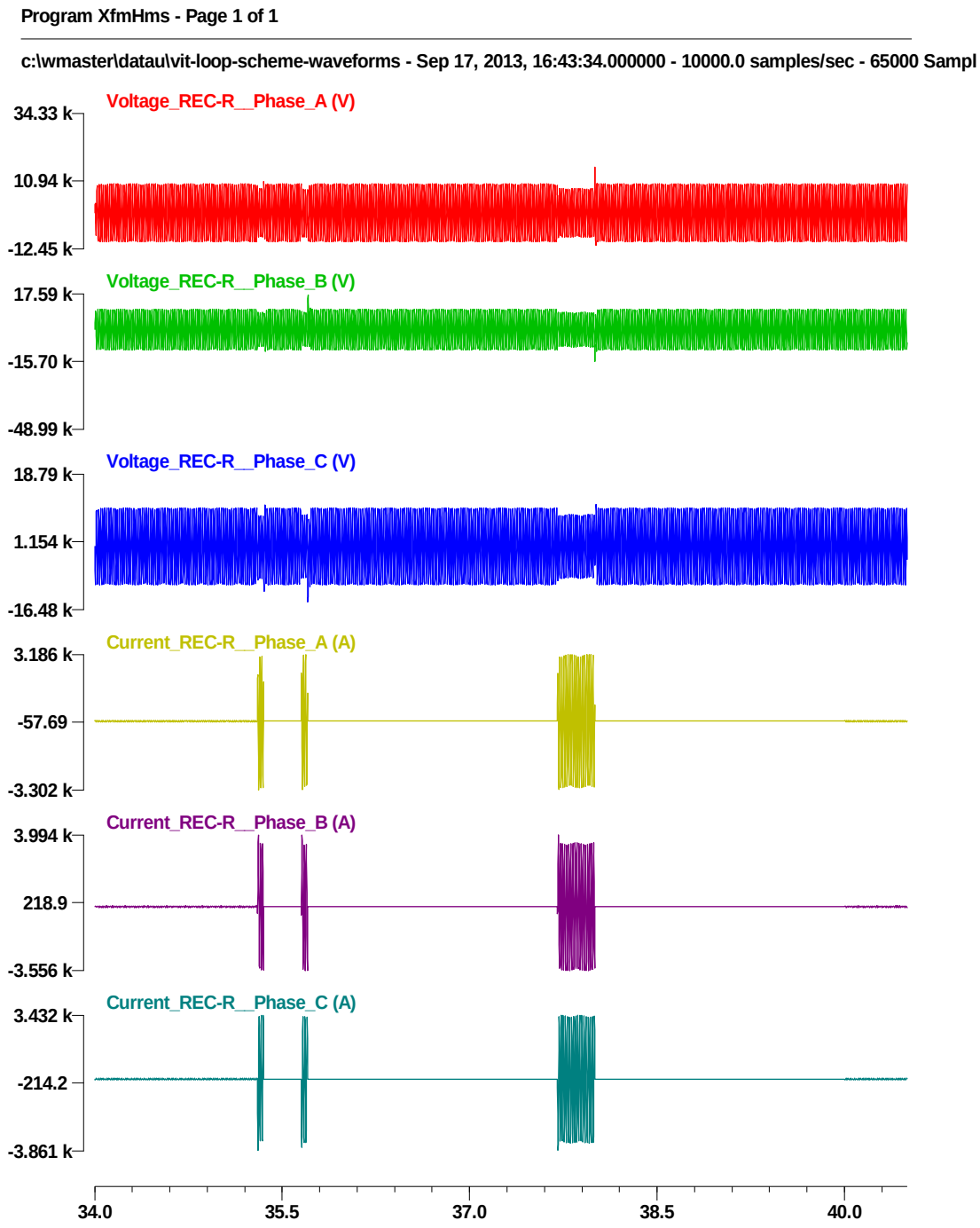

Figure 28: The waveforms of the fault scenario – a fault condition measured at the VIT recloser on the distribution feeder.

5.2 Result Description – Distribution Feeder – VIT Scheme

The resulting waveforms are illustrated in Figure 29, Figure 30, and Figure 31. In more detail, the voltage and current measurements, computed RMS values, and counted NVC and FCC of the VIT recloser are depicted in Figure 29. In Figure 30 and Figure 31, the voltage and current measurements, computed RMS values, and counted NVC and FCC of the VIT sectionalizer two and three are illustrated, respectively.

As the fault initiates at time 0.32 seconds, the VIT recloser trips first on its fast trip. This fault current level increases the FCC of the VIT recloser and the VIT sectionalizer two as shown in Figure 29 and Figure 30. On the other hand, the FCC of the VIT sectionalizer three is not increased because the VIT sectionalizer three is located behind the fault location. After the trip, the no-voltage condition is counted by the NVC of the VIT sectionalizer two and the VIT sectionalizer three as shown in Figure 30 and Figure 31.

The second reclosing operation of the VIT recloser increases the FCC of the VIT recloser and the VIT sectionalizer two to two as shown in Figure 29 and Figure 30. The NVC of the VIT sectionalizer two and the VIT sectionalizer three are two as shown in Figure 30 and Figure 31.

The third operation of the VIT recloser increases the FCC of the VIT recloser and the VIT sectionalizer two to three as shown in Figure 29 and Figure 30. The NVC of the VIT sectionalizer two and the VIT sectionalizer three are three as shown in Figure 30 and Figure 31.

After the third operation, the counted number of FCC of the VIT sectionalizer two is equal to the setting value three, and the VIT sectionalizer two trips to open instantly as

shown in Figure 30. Moreover, the counted number of NVC of the VIT sectionalizer three is equal to the setting value three, and the VIT sectionalizer two trips to open after a time delay as shown in Figure 31. As a result, the fault condition is isolated by tripping the VIT sectionalizer two and three, and the close-in fault problem is prevented.

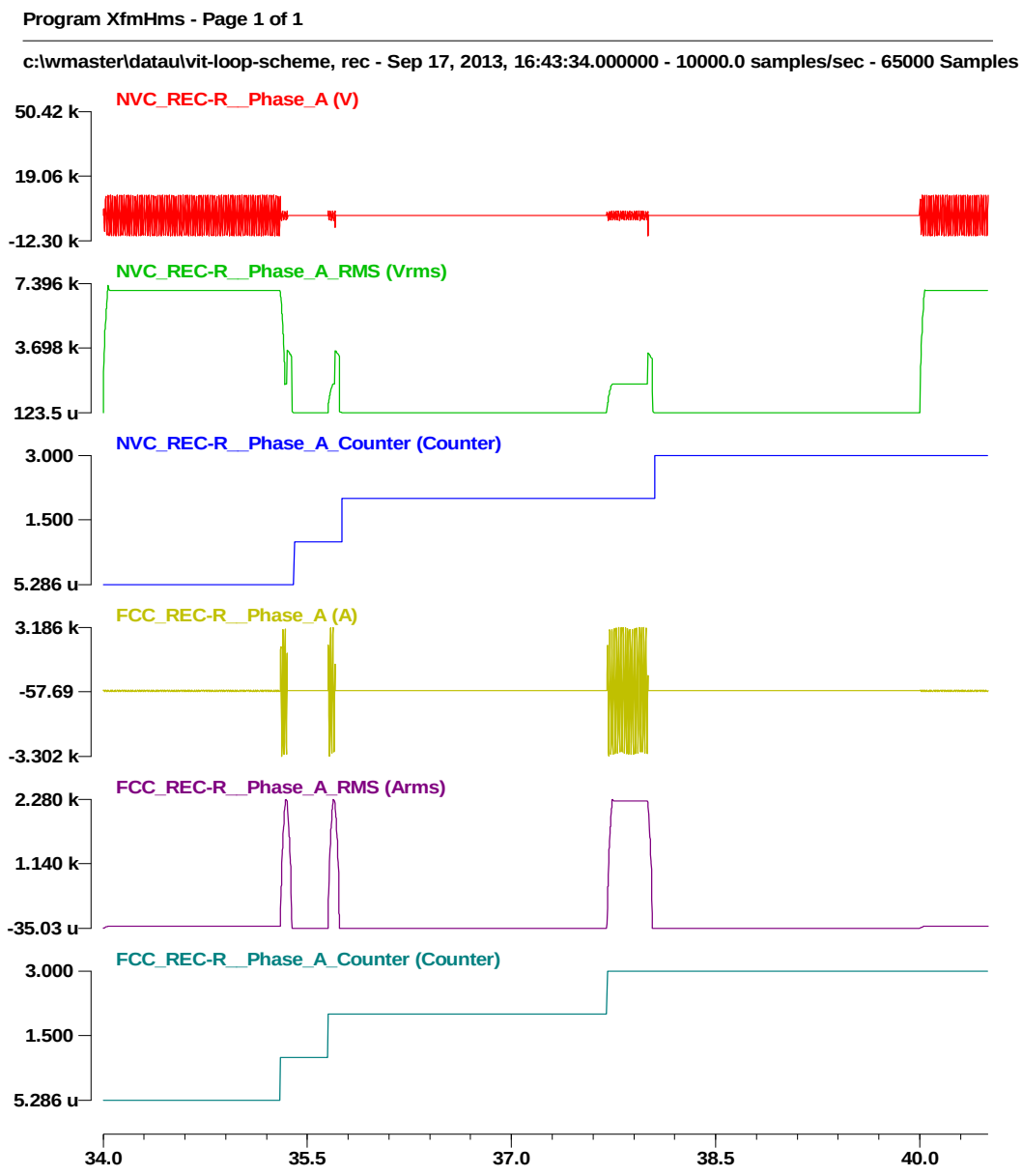

Figure 29: Result graphs for the permanent three-phase fault scenario on the distribution feeder – the VIT recloser.

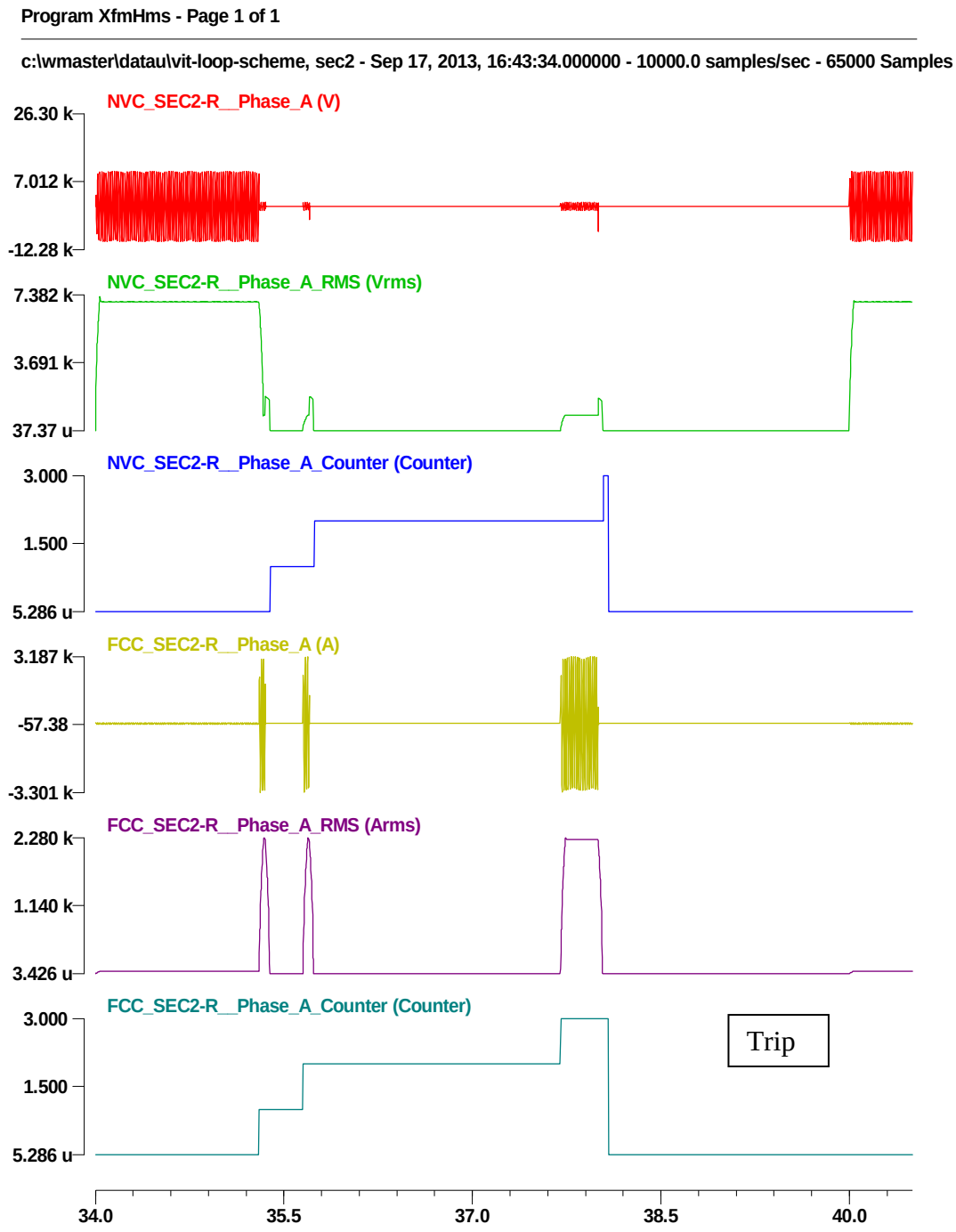

Figure 30: Result graphs for the permanent three-phase fault scenario on the distribution feeder – the VIT sectionalizer two.

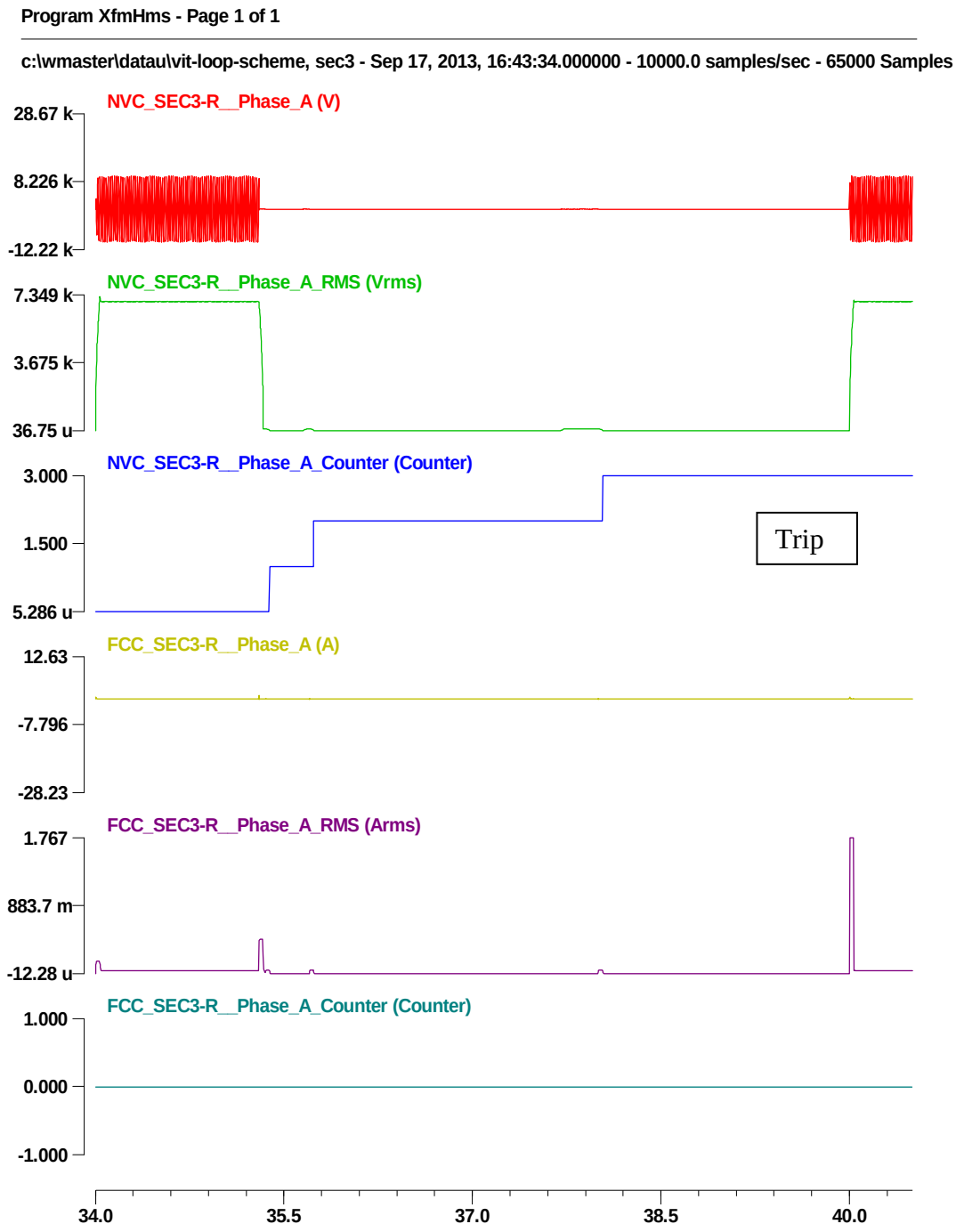

Figure 31: Result graphs for the permanent three-phase fault scenario on the distribution feeder – the VIT sectionalizer three.

5.3 Experimental Setup for the DSE-based Protection

A laboratory test environment has been established as shown in Figure 32 to simulate the DSE-based protection scheme using IEDs and PCs. The experimental setup comprises one PC driven D/A hardware (NI cDAQ-9188, 32 channels), one Omicron amplifier (one CMS 156), one Reason MU (MU320), one waveform generation PC (WinXFM software), one DSE-based protection PC (WinXFM software), and one Arbiter GPS (Arbiter 1093) clock with IRIG-B output. The time synchronization signal is provided by a GPS antenna installed on the roof of Van Leer building. The Omicron amplifier, CMS 156, has three current outputs and three current outputs. The PCs have Windows 7 operating system with eight-core CPU.

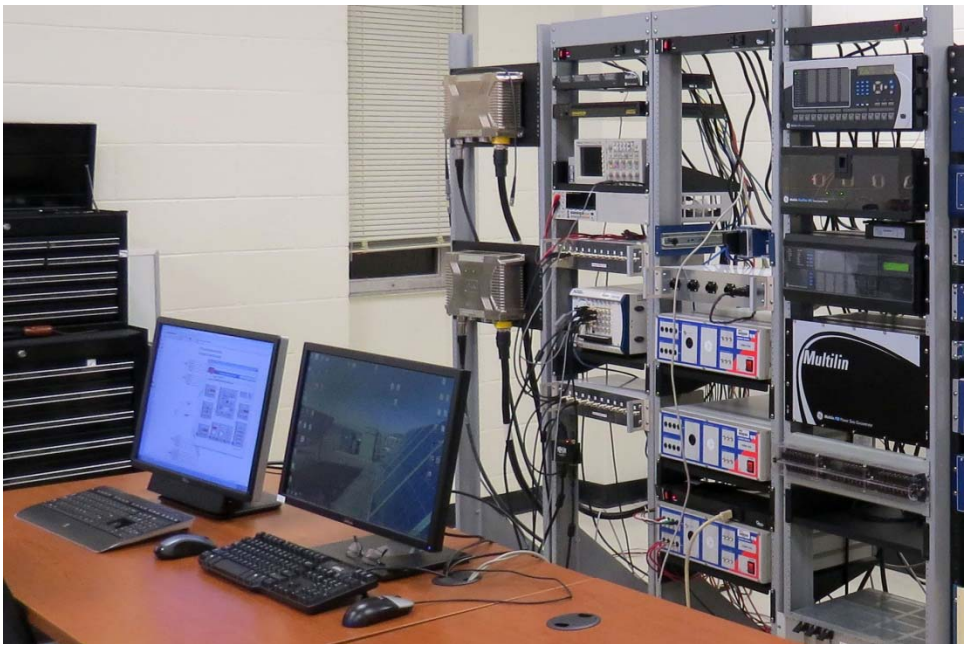

Figure 32: Laboratory setup for the DSE-based protection scheme.

The laboratory instrumentation of the DSE-based protection scheme is shown in Figure 33.

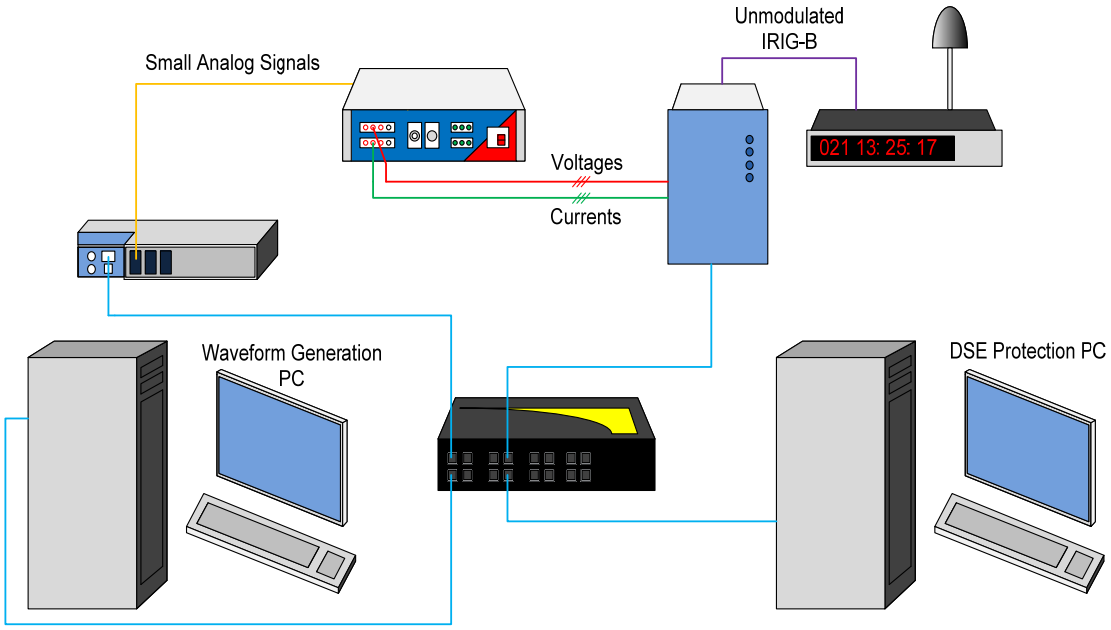

Figure 33: A schematic of the laboratory setup for the DSE-based protection scheme.

For the test of the DSE-based protection scheme, two different tests are performed. One test is based only on the computer simulation and the other test is based on the utilization of the above laboratory setup.

For the computer simulation, the waveform generation PC simulates fault scenarios on a distribution system and a microgrid. The DSE-based protection scheme has been tested using the Win-XFM program.

For the test using the laboratory setup, the simulated waveforms (for a distribution system and a microgrid) are converted into small analog waveforms using the NI cDAQ-9188 unit. The small analog signals are amplified using the Omicron CMS 156 amplifier. Then, the amplified voltage and current signals are measured using the Reason MU. For the time synchronization, Arbiter 1093 unit provides IRIG-B signal which is synched to the GPS signal from the GPS antenna. Note that the Reason MU in our lab can provide only three voltage and three current measurements.

5.3.1 An Application Example of the DSE-based Protection – Distribution Circuit

The DSE-based protection scheme for the distribution circuit is demonstrated in this chapter. The description of the DSE-based protection for an active distribution circuit is provided in from Appendix B to Appendix G. In detail, the AQCF model of the single distribution line and the transformer is derived in Appendix B and Appendix C, respectively. The states and measurement data of the distribution system are defined in Appendix D, Appendix E, and Appendix F. In Appendix G, the measurement data are derived from each model and a set of the point that merges each model into the combined model.

A test system has been used for numerical experiments that include a distribution circuit under protection and a grid connected to the distribution system. The example test system is shown in Figure 34. The distribution circuit protection zone is defined in the blue area as shown in Figure 34.

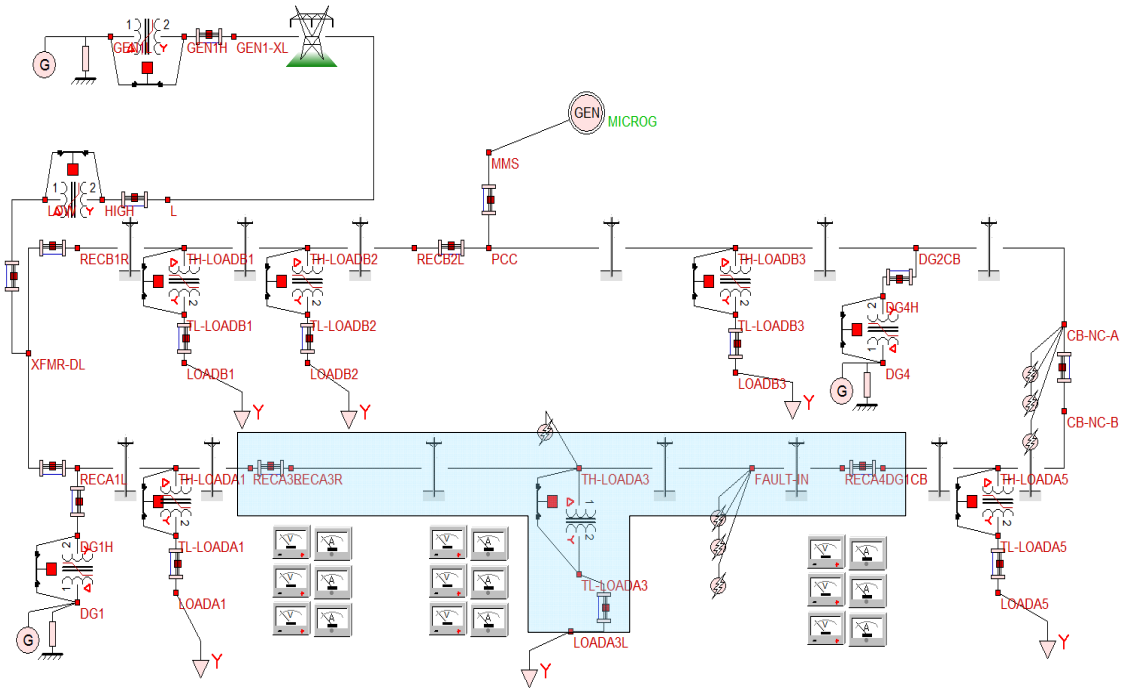

Figure 34: Test system diagram for the distribution circuit protection zone – the DSE-based protection scheme.

Event Description – Fault Conditions on the Distribution System

The intention here is to generate waveforms that represent the fault conditions, for example, three-phase faults and a HIF. Specifically, three-phase fault and HIF on phase A with 10 ohm fault resistance initiated inside of the protection zone at FAULT-IN node and TH-LOADA3 node, respectively, and an external three-phase fault occurred at FAULT-EXT node. The following specific fault is employed as shown in Figure 35. The internal fault starts at 0.32 seconds and ends at 0.35 seconds and the external fault starts at 0.36 seconds and ends at 0.39 seconds. The HIF starts at 0.46 seconds and ends at 0.49 seconds, and note that the fault current is so small to be detected by ordinary relay schemes. A result COMTRADE data file is generated by measuring voltage and current at each terminal of the protection zone. Using the simulated COMTRADE data file, protection of the distribution circuit is tested.

An example test system, measurement, and the faults are illustrated in Figure 35. The blue area in Figure 35 indicates the distribution circuit protection zone. The red boxes indicate the fault conditions.

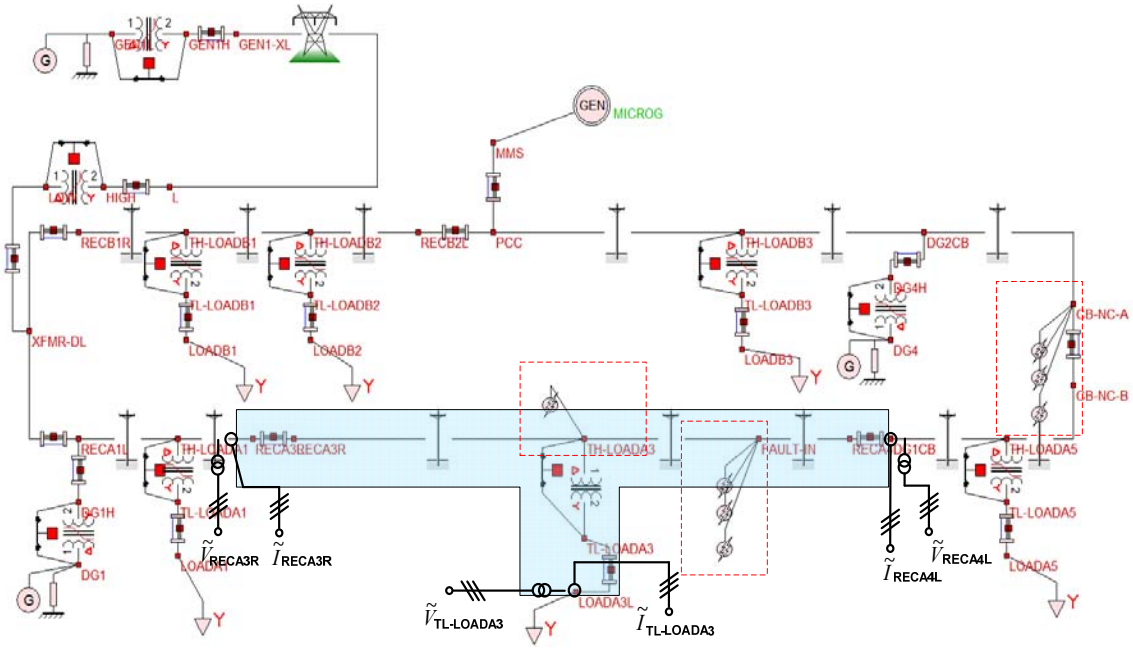

Figure 35: Test system diagram for the distribution circuit protection zone with measurements and faults – the DSE-based protection scheme.

Measurement Data Acquisition

This section describes how the measurement data are obtained, and how the protection scheme can be economically justified.

In the above Figure 35, the active distribution system has only one load tap point in the protection zone. However, it is highly likely that there are multiple of load connections along the feeder lines. Since the protection scheme requires voltage and current digital data, the UGPSSM should be installed at every interface to provide the measurement. Installation of metering devices at every load tap should not involve excessive investments that might deter the implementation of the protection scheme. Excessive economical burden can be minimized by applying the metering devices on the low side of the transformers on the active distribution system. The voltage ratings of low side of the transformers are 480V, which means that the building cost of each metering device can be significantly reduced.

The UGPSSM senses voltage and current data with high sampling rate and converts the measured data from analog to digital (sampled values) according to the IEC 61850 standard. Then the sampled values are sent to the process bus via a concentrator with high data rates. Wireless communication can be used between the UGPSSM and the process bus.

Measurement data of the internal and external fault on the distribution system are shown in Figure 36.

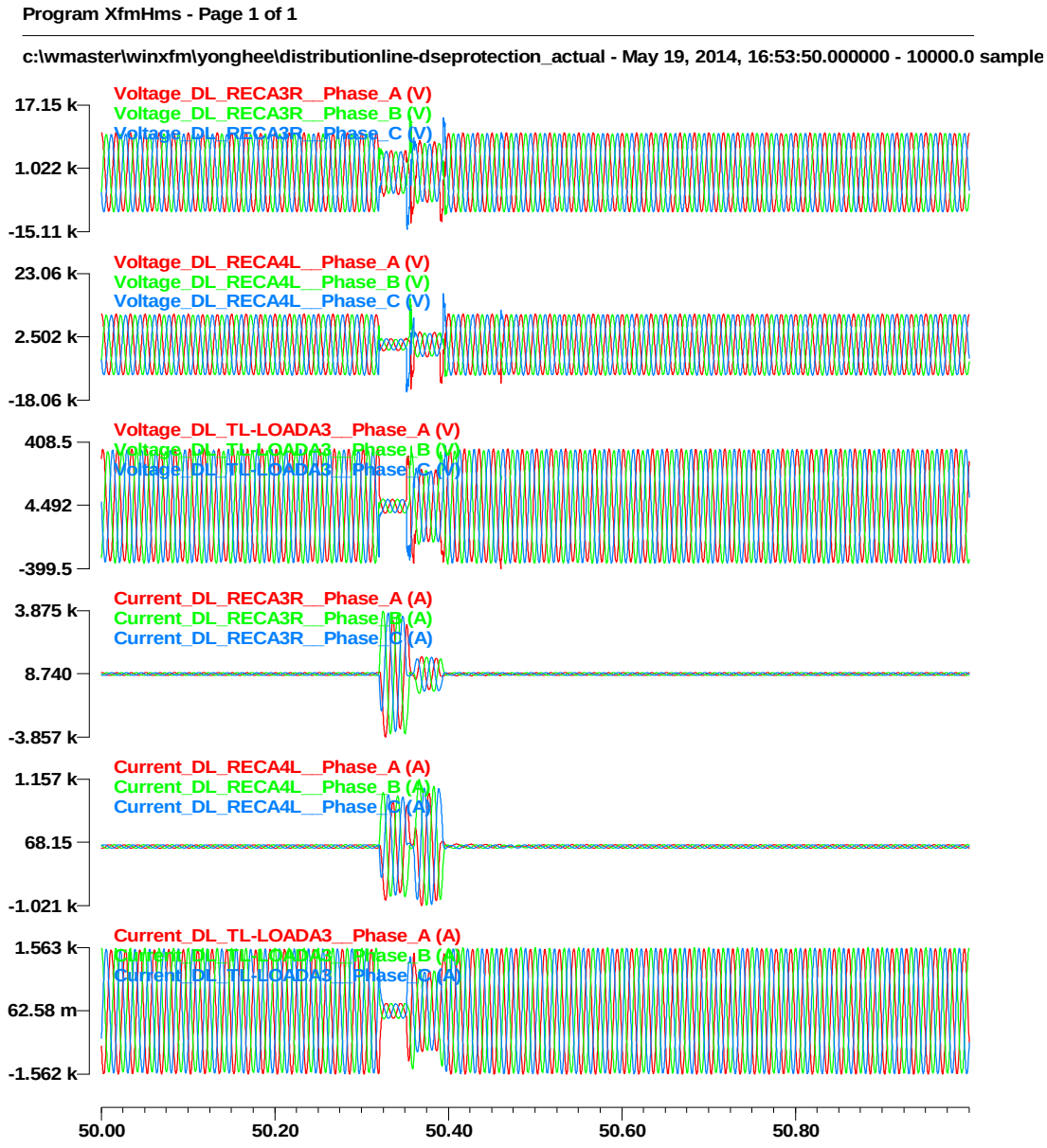

Figure 36: The waveforms of the fault scenario – voltage and current measurement at five terminals of the feeder line on the distribution system.

5.3.2 Result Description for the Computer-based Simulation– Distribution System

Some of the resulting waveforms are shown in Figure 37. Based on the result graphs in Figure 37, it can be concluded that the DSE-based DSE-based protection is able to protect the distribution circuits with 100 % confidence level regardless of the operating condition. More specifically, during the normal operation time, the confidence level is 100%, which means that measurements are consistent with the model and the distribution circuit is in the normal operating condition. For the internal three-phase fault starting from 0.32 seconds in Figure 37, the confidence level is 0%, which means that a fault condition is on the distribution circuit. Moreover, for the internal HIF starting from 0.46 seconds in Figure 37, the confidence level is 0%, which means that a fault condition is on the distribution circuit. On the other hand, for the external fault starting from 0.36 seconds, the confidence level is 100%, which means that a fault condition is outside of the protection zone. The computation time for each step is also depicted in Figure 37. The average computation time is 0.109 ms. More result graphs, for example, states, actual measurement, virtual measurement, pseudo measurement, and resulting error and normalized error for the internal fault and the external fault are provided in Appendix N.

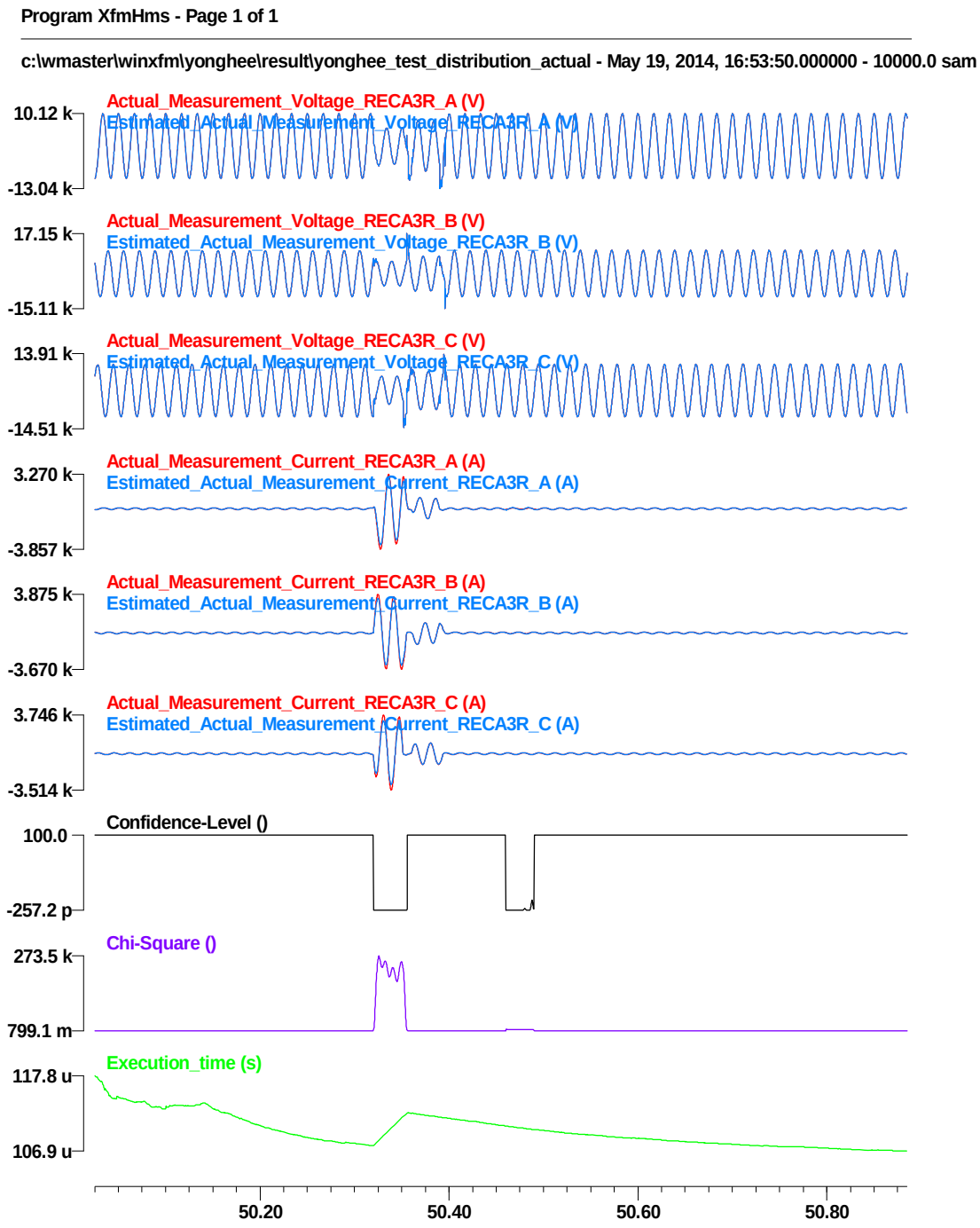

Figure 37: Result graphs for the fault scenario on the distribution system, simulation result.

5.3.3 Result Description for the Laboratory Test – Distribution System

Some of the resulting waveforms are shown in Figure 37. Based on the result graphs in Figure 37, it can be concluded that the DSE-based DSE-based protection is able to protect the distribution circuits with 100 % confidence level regardless of the operating condition. More specifically, during the normal operation time, the confidence level is 100%, which means that measurements are consistent with the model and the distribution circuit is in the normal operating condition. Moreover, for the internal HIF starting from 0.46 seconds in Figure 37, the confidence level is 0%, which means that a fault condition is on the distribution circuit. On the other hand, for the external fault starting from 0.36 seconds, the confidence level is 100%, which means that a fault condition is outside of the protection zone. The computation time for each step is also depicted in Figure 37. The average computation time is 0.107 ms. More result graphs, for example, states, actual measurement, derived measurement, virtual measurement, pseudo measurement, and resulting error and normalized error for the internal fault and the external fault are provided in Appendix O.

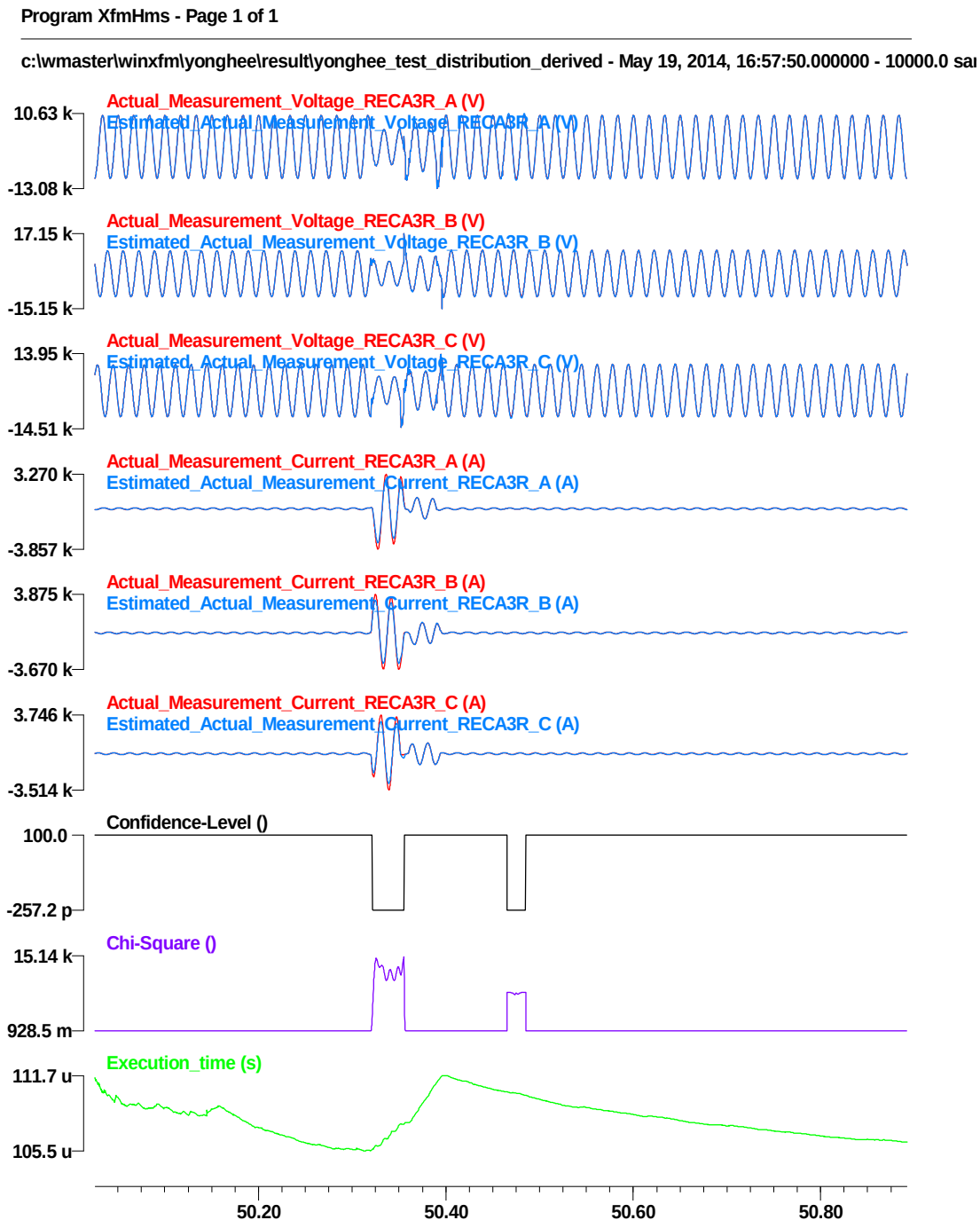

Figure 38: Result graphs for the fault scenario on the distribution system, experimental result.

5.3.4 An Application Example of the DSE-based Protection for the Microgrid – Grid-connected Operation

The DSE-based protection scheme for the microgrid during the grid-connected operation mode is demonstrated in this chapter. The description of the DSE-based protection for the microgrid is provided in Appendix C, Appendix H, Appendix I, Appendix J, and Appendix M. In detail, the AQCF model of the multi phase cable is derived in Appendix C. Note that the multi phase cable model is same with the distribution line model. The states and measurement data of the microgrid are defined in Appendix H and Appendix I, respectively. The measurement data are derived from each model and a set of the point that merges each model into the combined mode in Appendix M. An internal and an external fault cases are simulated.

A test system has been used for numerical experiments that include the microgrid under protection and an integrated system around it. The example test system is shown in Figure 39. The microgrid protection zone is defined in the blue area as shown in Figure 39. To simulate the grid-connected operation mode, the circuit breaker is closed (red) to the distribution system as shown in red oval in Figure 39.

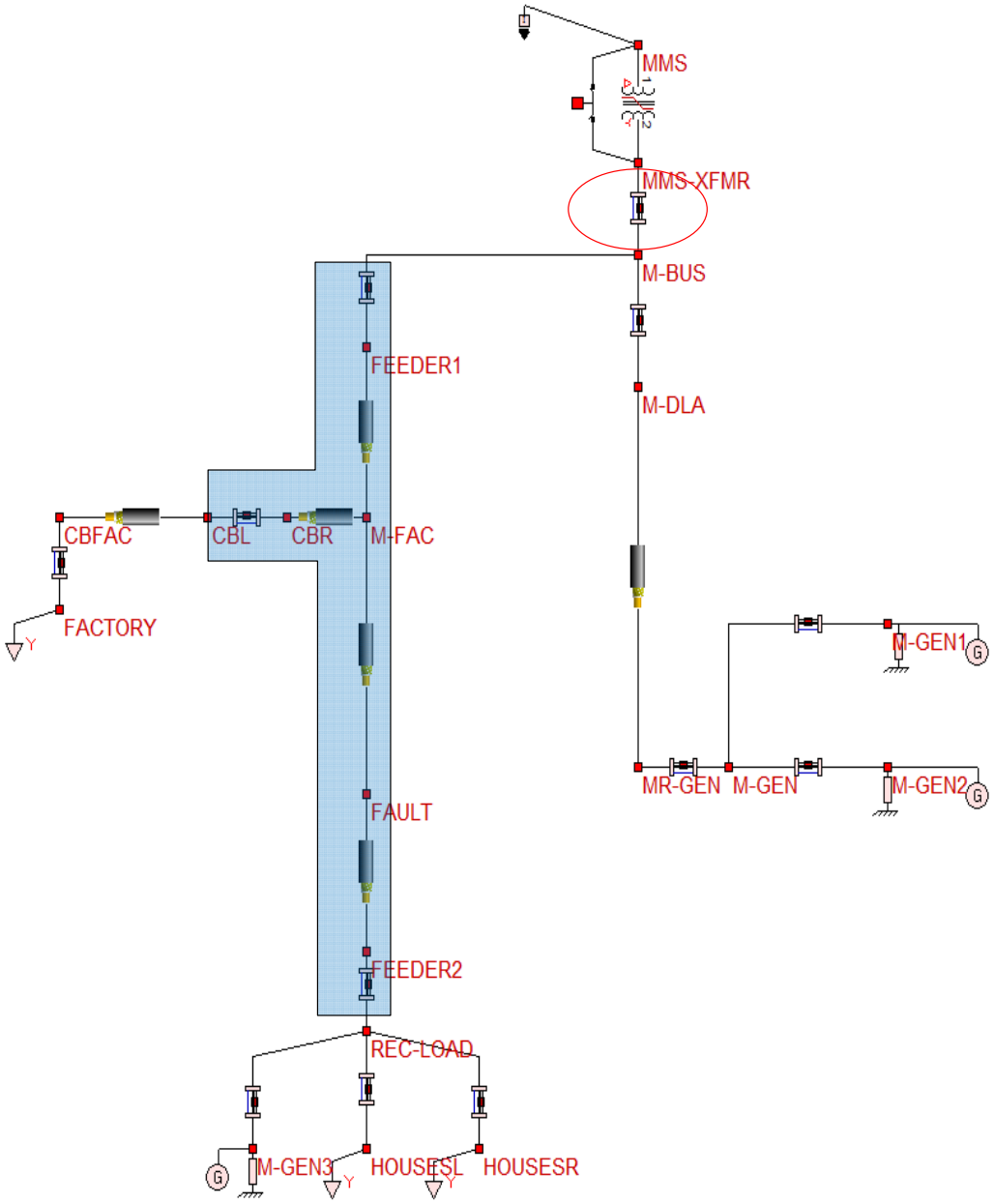

Figure 39: Test system diagram for the microgrid protection zone during the grid-connected operation – the DSE-based protection scheme.

Event Description – An Internal Fault on the Microgrid during the Grid-connected Operation

The following specific faults are employed as shown in Figure 40. The intention here is to generate waveforms that represent the fault condition, for example, three-phase faults are initiated inside and outside of the protection zone at FAULT-IN and at FAULT-EXT node, respectively. The following specific fault is employed as shown in Figure 40. The internal fault starts at 0.32 seconds and ends at 0.35 seconds, and the external fault starts at 0.36 seconds and ends at 0.39 seconds. Note that the fault current level is less than 1.5 times of the normal current level which is very small for the internal fault case. A result COMTRADE data file is generated by measuring voltage and current at each terminal of the protection zone. Using the simulated COMTRADE data file, protection of the distribution circuit is tested.

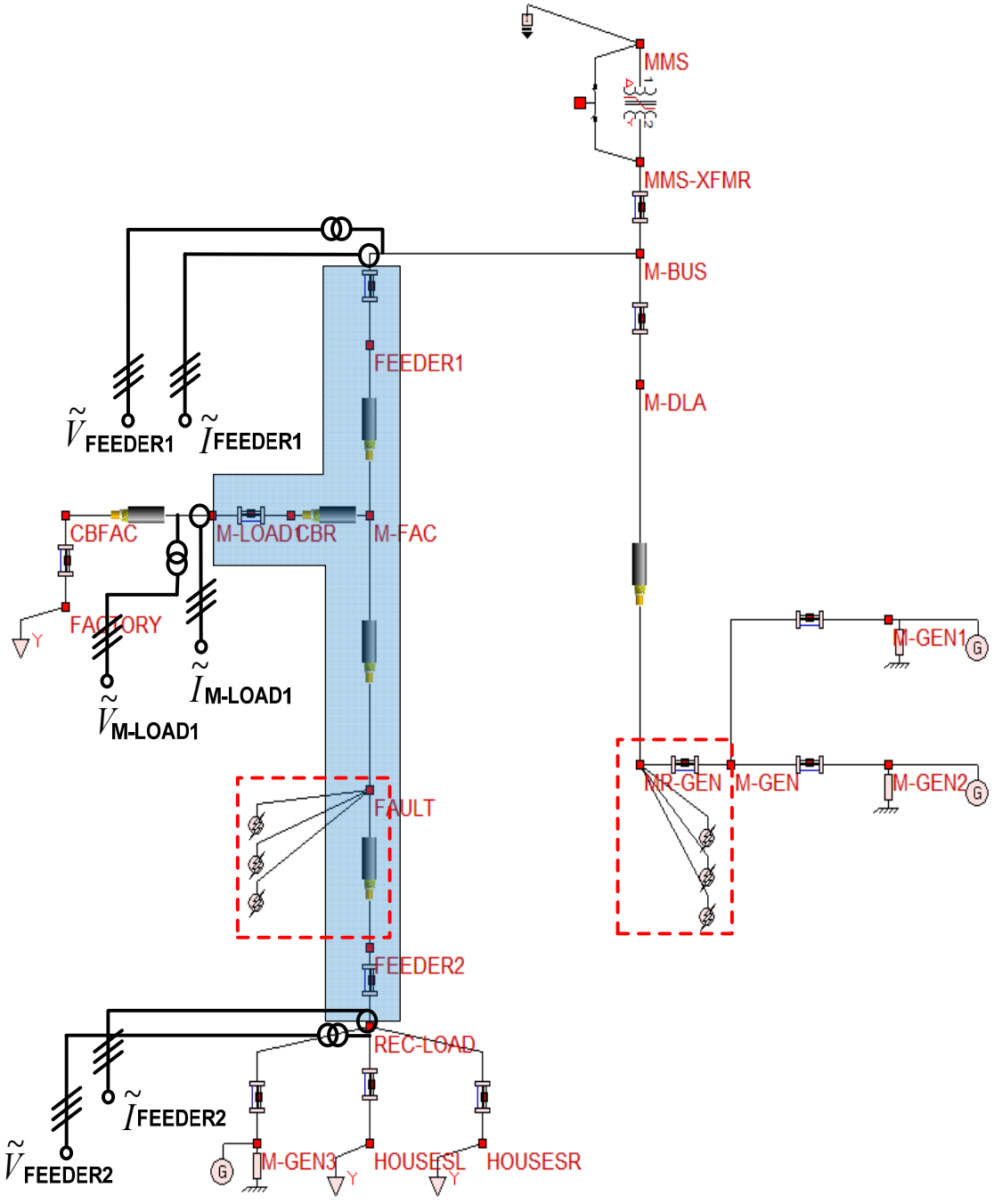

Figure 40: An internal fault simulation on the microgrid with measurements and faults – the DSE-based protection scheme.

Measurement data of the internal fault on the microgrid during the grid-connected operation are shown in Figure 41.

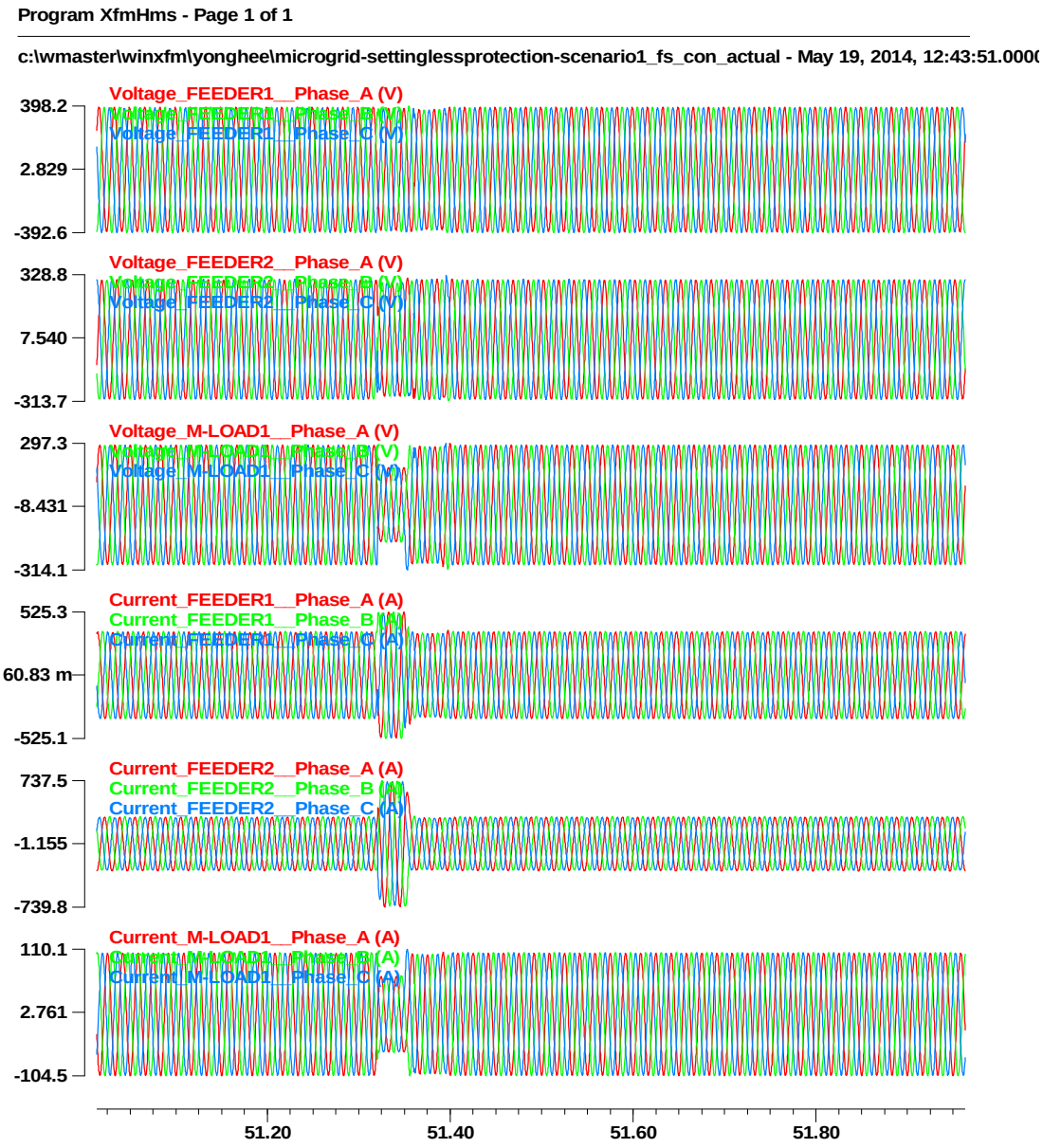

Figure 41: The waveforms of the fault scenario – voltage measurement at three terminals of the feeder line on the microgrid during the grid-connected operation.

5.3.5 Result Description for the Computer-based Simulation – Microgrid during the Grid-connected Operation

The resulting waveforms are shown in Figure 42. Based on the result graphs of the test scenario shown in Figure 42, it can be concluded that the DSE-based protection is able to protect the microgrid circuits with 100 % confidence level regardless of the operating condition. More specifically, during the normal operation time, the confidence level is 100%, which means that measurements are consistent with the model and the microgrid circuit is in the normal operating condition. Moreover, for the internal fault starting from 0.32 seconds in Figure 42, the confidence level is 0%, which means that a fault condition is on the microgrid. On the other hand, for the external fault starting from 0.36 seconds, the confidence level is 100%, which means that a fault condition is outside of the protection zone. The computation time for each step is also depicted in Figure 42. The average computation time is 0.149 ms. More result graphs, for example, states, actual measurement, virtual measurement, pseudo measurement, and resulting error and normalized error for the internal fault and the external fault are provided in Appendix P.

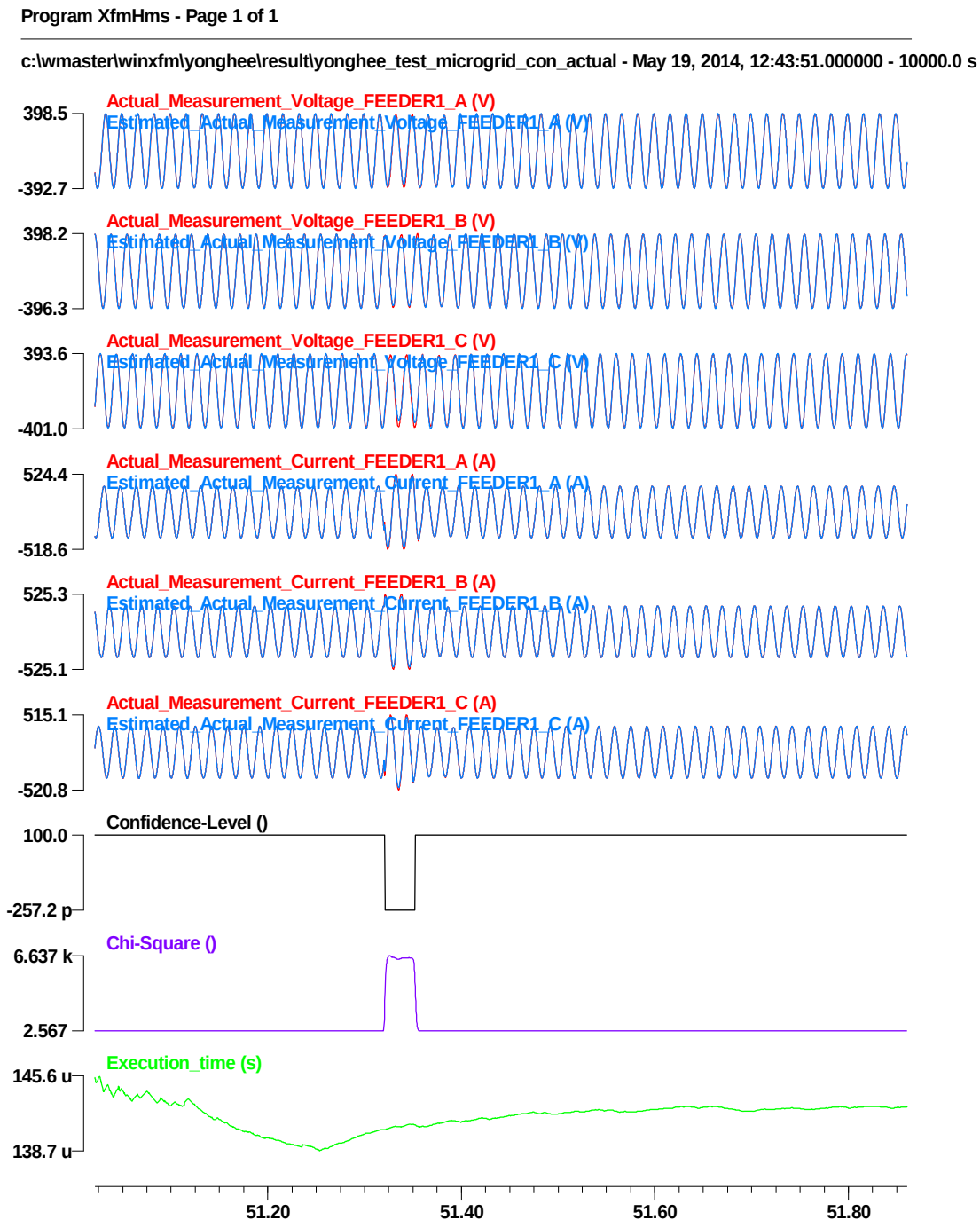

Figure 42: Result graphs for the fault scenario on the microgrid during the grid-connected operation, simulation result.

5.3.6 Result Description for the Laboratory Test – Microgrid during the Grid-connected Operation

The resulting waveforms are shown in Figure 42. Based on the result graphs of the test scenario shown in Figure 42, it can be concluded that the DSE-based protection is able to protect the microgrid circuits with 100 % confidence level regardless of the operating condition. More specifically, during the normal operation time, the confidence level is 100%, which means that measurements are consistent with the model and the microgrid circuit is in the normal operating condition. Moreover, for the internal fault starting from 0.32 seconds in Figure 42, the confidence level is 0%, which means that a fault condition is on the microgrid. On the other hand, for the external fault starting from 0.36 seconds, the confidence level is 100%, which means that a fault condition is outside of the protection zone. The computation time for each step is also depicted in Figure 42. The average computation time is 0.141 ms. More result graphs, for example, states, actual measurement, derived measurement, virtual measurement, pseudo measurement, and resulting error and normalized error for the internal fault and the external fault are provided in Appendix Q.

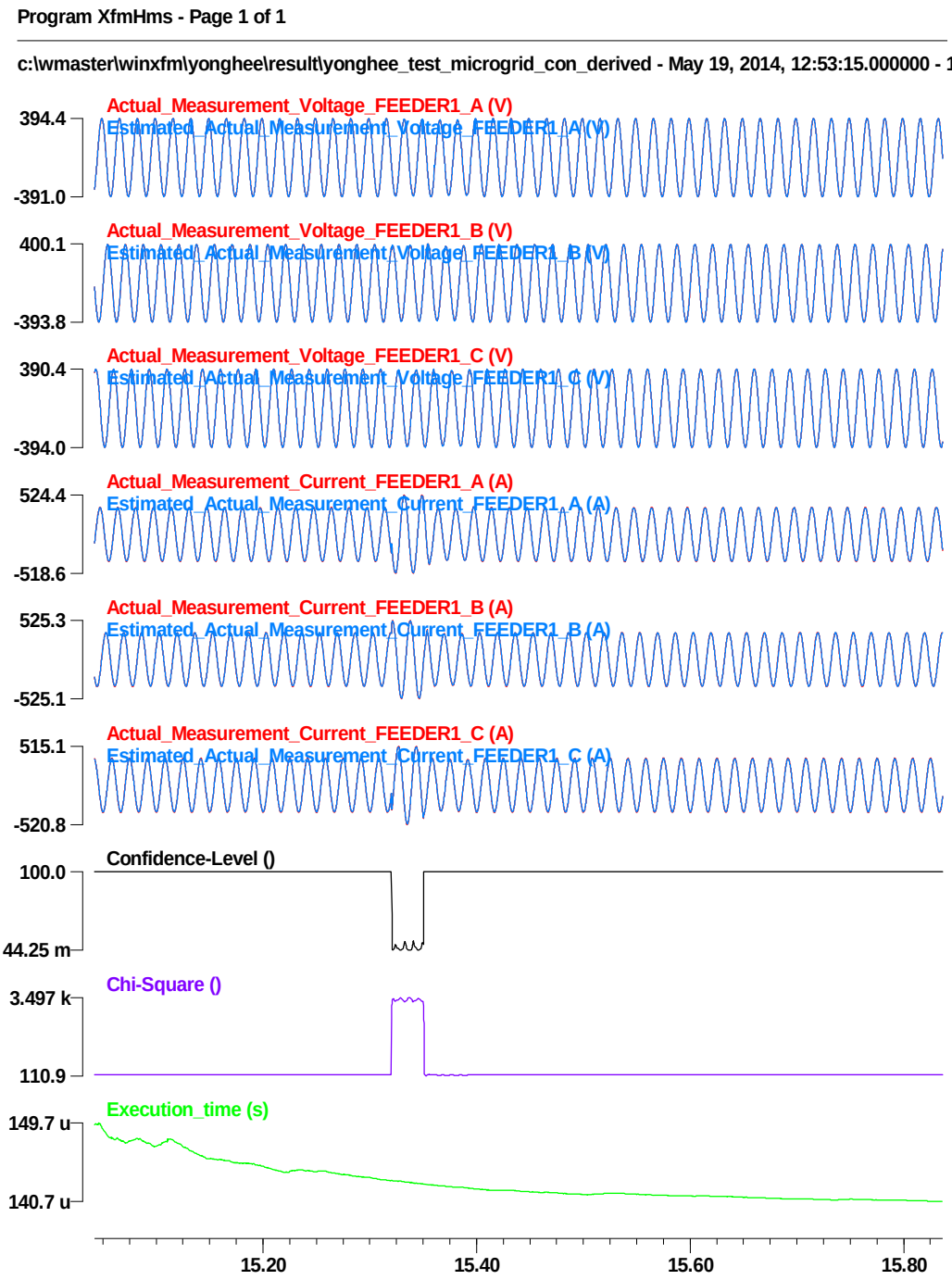

Figure 43: Result graphs for the fault scenario on the microgrid during the grid-connected operation, experimental result.

5.3.7 An Application Example of the DSE-based Protection for the Microgrid – Island Operation

The DSE-based protection scheme for the microgrid during the island operation mode is demonstrated in this chapter. The description of the DSE-based protection for the microgrid is provided in Appendix C, Appendix H, Appendix K, Appendix L, and Appendix M. In detail, the AQCF model of the multi phase cable is derived in Appendix C. Note that the multi phase cable model is same with the distribution line model. The states and measurement data of the microgrid are defined in Appendix H and Appendix I, respectively. The measurement data are derived from each model and a set of the point that merges each model into the combined mode in Appendix M. An internal and an external fault cases are simulated.

A test system has been used for numerical experiments that include the microgrid under protection and an integrated system around it. The example test system is shown in Figure 44. The microgrid protection zone is defined in the blue area as shown in Figure 44. To simulate the island operation mode, the circuit breaker at the PCC has set to open position (green) as shown in the red circle shown in Figure 44.

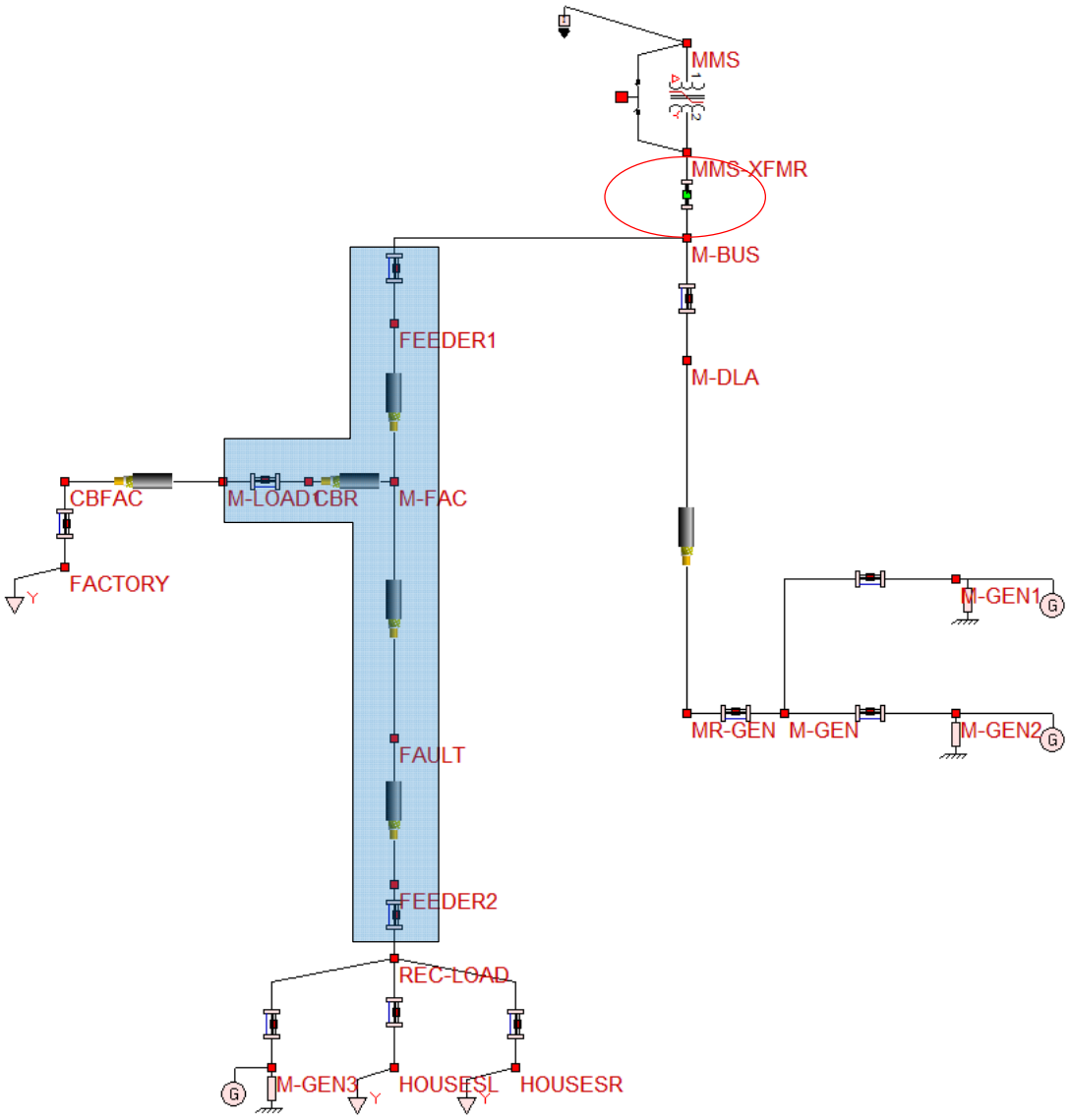

Figure 44: Test system diagram for the microgrid protection zone during the island operation – the DSE-based protection scheme.

Event Description – An Internal Fault on the Microgrid – Island Operation

The following specific faults are employed as shown in Figure 45. The intention here is to generate waveforms that represent the fault condition, for example, three-phase faults are initiated inside and outside of the protection zone at FAULT-IN and at FAULT-EXT node, respectively. The following specific fault is employed as shown in Figure 45. The internal fault starts at 0.32 seconds and ends at 0.35 seconds, and the external fault starts at 0.36 seconds and ends at 0.39 seconds. Note that the fault current level is less than 1.5 times of the normal current level which is very small for the internal fault case. A result COMTRADE data file is generated by measuring voltage and current at each terminal of the protection zone. Using the simulated COMTRADE data file, protection of the distribution circuit is tested.

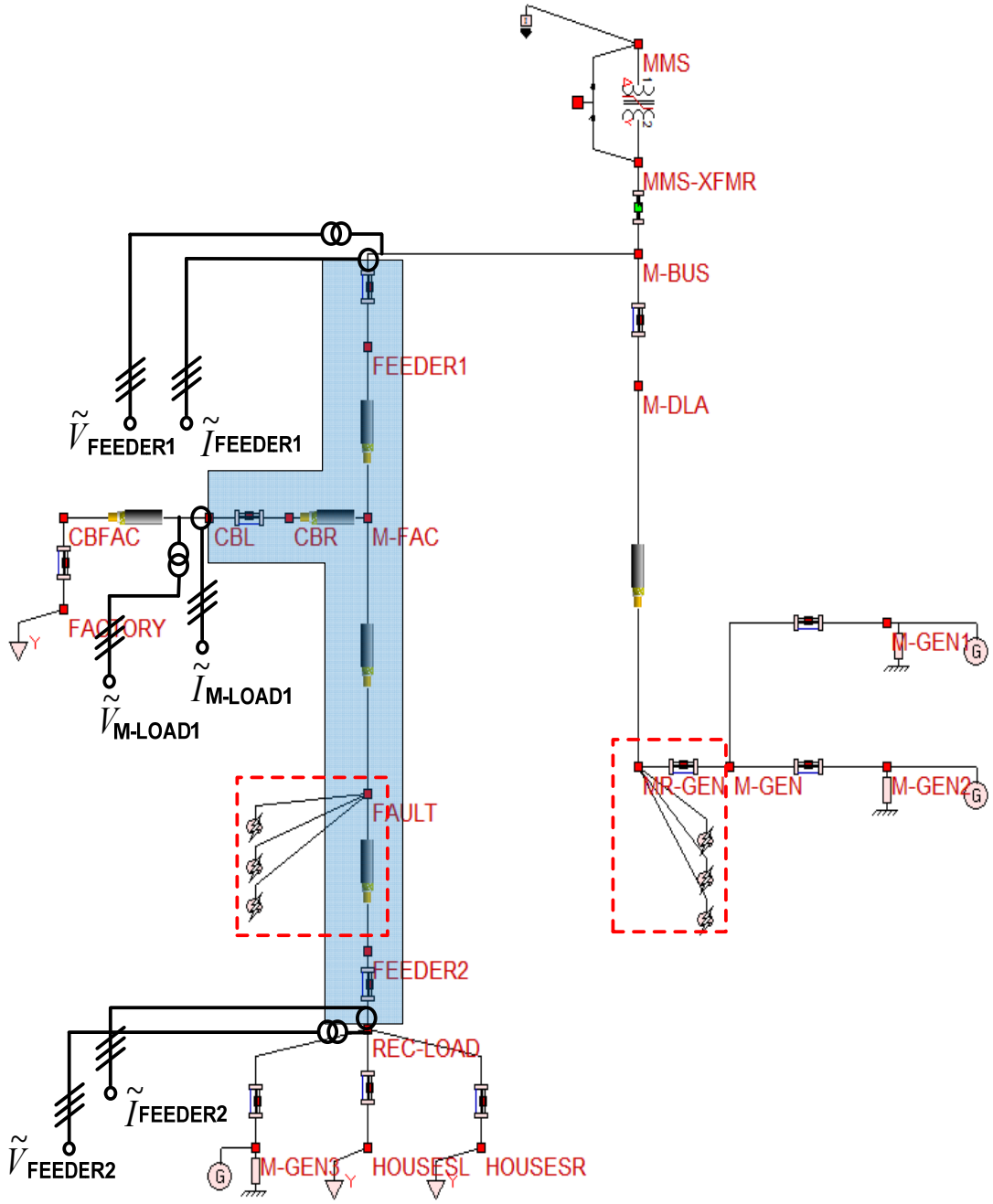

Figure 45: An internal fault simulation on the microgrid with measurements and faults – the DSE-based protection scheme.

Measurement data of the internal fault on the microgrid during the island operation are shown in Figure 46.

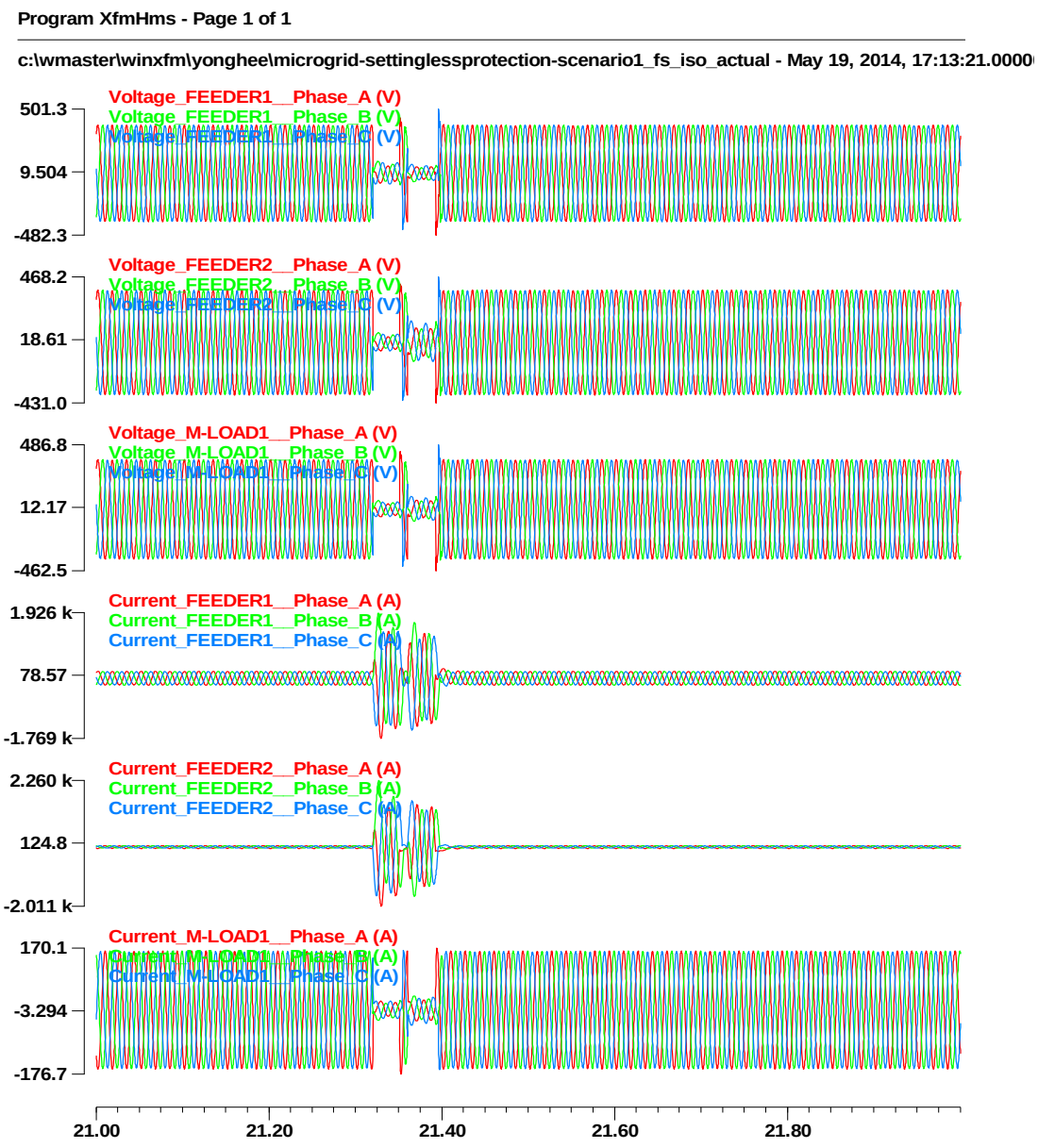

Figure 46: The waveforms of the fault scenario – voltage measurement at three terminals of the feeder line on the microgrid during the island operation.

5.3.8 Result Description for the Computer-based Simulation – Microgrid during the Island Operation

The resulting waveforms are shown in Figure 47. Based on the result graphs of the test scenario shown in Figure 47, it can be concluded that the DSE-based protection is able to protect the microgrid circuits with 100 % confidence level regardless of the operating condition. More specifically, during the normal operation time, the confidence level is 100%, which means that measurements are consistent with the model and the microgrid circuit is in the normal operating condition. Moreover, for the internal fault starting from 0.32 seconds in Figure 47, the confidence level is 0%, which means that a fault condition is on the microgrid. On the other hand, for the external fault starting from 0.36 seconds, the confidence level is 100%, which means that a fault condition is outside of the protection zone. The computation time for each step is also depicted in Figure 47. The average computation time is 0.141 ms. More result graphs, for example, states, actual measurement, virtual measurement, pseudo measurement, and resulting error and normalized error for the internal fault and the external fault are provided in Appendix R

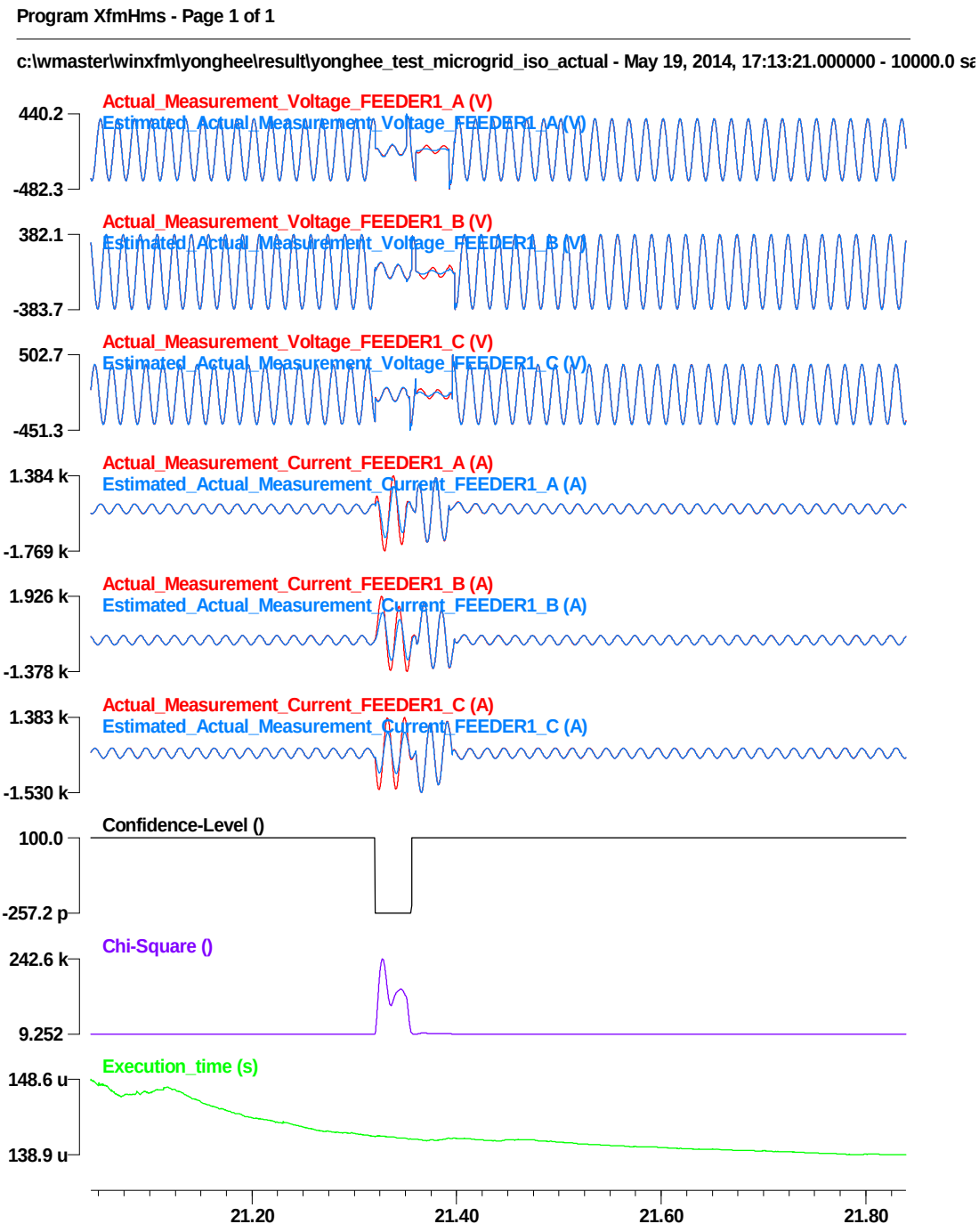

Figure 47: Result graphs for the fault scenario on the microgrid during the island operation, simulation result.

5.3.9 Result Description for the Laboratory Test – Microgrid during the Island Operation

The resulting waveforms are shown in Figure 48. Based on the result graphs of the test scenario shown in Figure 48, it can be concluded that the DSE-based protection is able to protect the microgrid circuits with 100 % confidence level regardless of the operating condition. More specifically, during the normal operation time, the confidence level is 100%, which means that measurements are consistent with the model and the microgrid circuit is in the normal operating condition. Moreover, for the internal fault starting from 0.32 seconds in Figure 48, the confidence level is 0%, which means that a fault condition is on the microgrid. On the other hand, for the external fault starting from 0.36 seconds, the confidence level is 100%, which means that a fault condition is outside of the protection zone. The computation time for each step is also depicted in Figure 48. The average computation time is 0.143 ms. More result graphs, for example, states, actual measurement, derived measurement, virtual measurement, pseudo measurement, and resulting error and normalized error for the internal fault and the external fault are provided in Appendix S.

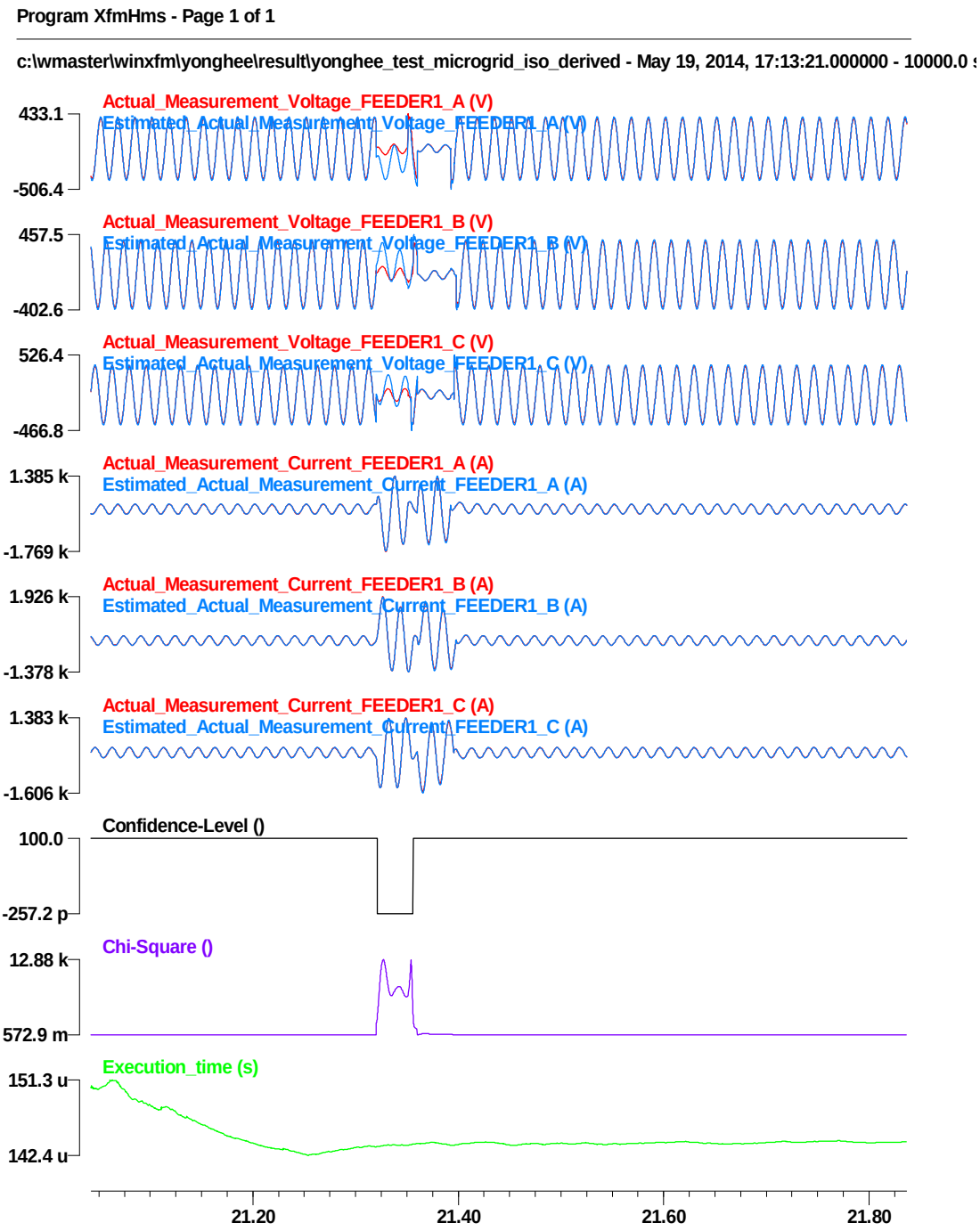

Figure 48: Result graphs for the fault scenario on the microgrid during the island operation, experimental result.

6 Conclusions & Contributions

The VIT Scheme

The application of reclosers and sectionalizers with the VIT scheme provides improved distribution feeder automation with minimum investment. The VIT sectionalizers are easy to coordinate with the VIT reclosers, even under tight coordination condition and provide a flexible operation scheme. The coordination between the VIT sectionalizers is more flexible because they only count the number of fault conditions, and the VIT sectionalizers are not TCC coordinated. The sectionalizers can operate only when the system is de-energized by the operation of the reclosers. Moreover, the VIT scheme does not require communications or expensive controllers to provide an enhanced automatic load transfer function. The VIT scheme engages simple counters and timers to fully utilize the voltage and current measurement. The FCC helps to confirm the fault condition from the source side of the fault, and the NVC helps to confirm the fault condition from the load side of the fault. The VIT scheme helps utilities to minimize unnecessary outages and minimize the number of affected customers in the event of a fault.

This thesis demonstrates the VIT protection scheme for a traditional distribution system and presents numerical experiments using various test scenarios with various fault locations. In all of these test scenarios, the simulation results verify that the protection scheme successfully performs the automatic load transfer scheme for a loop system.

The contributions of the VIT schemes are as follows: (a) the coordination between the VIT reclosers and the VIT sectionalizers provide more selective protection by increasing

the number of protection zones, (b) the VIT scheme requires no additional communication channels, and (c) the VIT scheme can be added to the existing protection schemes easily by installing a set of current and power transformers, and the VIT relay.

The DSE-based protection scheme

The DSE-based protection scheme provides a solution to issues related with large installations of DGs on active distribution systems and LV microgrids. This protection scheme can differentiate the internal fault of the component from normal operating conditions. The protection scheme is based on the dynamic state estimation using real-time measurement data and component's dynamic model; the real-time measurement data are continuously provided by online monitoring system. From these measurements and the dynamic model, the dynamic state estimation produces the real-time dynamic states of the component as well as the confidence level that indicates the goodness of fit of the component model to the measurements. The confidence level is used to assess the health of the component; if the confidence level is almost zero, then we can conclude that an internal fault has occurred inside the component.

The thesis demonstrates the DSE-based protection scheme for active distribution systems and microgrids and presents numerical experiments using a test set with multiple fault scenarios: (a) External fault, (b) HIF, and (c) Internal fault. In all of these fault scenarios, the simulation results verify that the protection scheme successfully discriminate the internal fault from other conditions (e.g., normal operation, external fault, and HIF).

The contributions of the DSE-based protection scheme are as follows: (a) The protection scheme provides a systematic way of utilizing the plethora of MU data, (b) The protection scheme can protect active distribution systems even if DGs provide fault

current, (c) The protection scheme can protect active distribution systems even if fault current level is limited (HIF) (d) The protection scheme can protect microgrid during grid-connected and island operation mode, and (e) The protection scheme can be used as a real-time protection scheme because the protection scheme detects fault conditions from sampled values unlike traditional protection schemes that require phasors to detect fault conditions.

7 Future Work Directions

The VIT Scheme

The thesis has demonstrated the feasibility of the VIT scheme on loop systems. Basically, the loop system tested in the thesis is two radial feeder lines connected through a normally-open sectionalizer. One remaining protection challenge is to modify the VIT scheme in such a way that it can also protect an active distribution system with distributed generation and distributed microgrids. Based on the recent IEEE standard, the DGs will still power the grid while there is a fault on the active distribution system. As a result, the NVC will not work as expected for active distributions systems. For success, the NVC should be revised in such a way that it can detect several conditions that happens when the main grid power is temporarily de-energized by the operation of the reclosing operation: (a) A sudden change in system frequency, (b) A sudden change in system voltage, and (c) A sudden change in df/dt. It is conceptually identical with the protection scheme of anti-islanding. Instead of counting the number of zero-voltage condition, the new NVC component should increase its counter when it detects above

conditions. A thorough investigation through numerous numerical experiments should be performed to assess the performance of the modified VIT scheme in protecting active distribution systems.

The DSE-based protection scheme

The thesis has demonstrated the feasibility of the DSE-based protection of the active distribution systems and the LV microgrid. While a demonstration on an actual system is not illustrated, the challenges of an actual demonstration are well understood. In field demonstrations, any model discrepancies may affect the performance of the scheme. A critical research issue is to develop the ability to assess under field conditions the impact of model accuracy and to develop methodologies for fine tuning the model. For example if the mathematical model of the component does not represent the nonlinear characteristics of the component, then the DSE-based protection scheme may not protect the component with 100% confidence. The modeling issue is fundamental in this approach. For success, the model must be high fidelity so that the component state estimator will reliably determine the operating status (health) of the component. The utilization of the model by the relay in real time could provide the validation of the model. For example the state estimation method may be extended to include the estimation for some key parameters of the mode and therefore the relay itself could be used to fine tune the model. This research can be first performed with power system scale models. Specifically, the method can be tested on the scaled model of a three-substation, three-phase power system in the Power System Control and Automation Laboratory (PSCAL) at Georgia Institute of Technology; the scaled model consists of, a synchronous generator, transformers, lines, and loads. Another important issue is the interoperability of the DSE-based relay at the process bus level. This is mainly coming from the fact that the transmitted data organization varies among manufactures, for example GE vs Reason,

since IEC 61850 does not specify application service data unit (ASDU) format. For success, an MU should work seamlessly with MUs from different manufactures.

8 Publications

Journal

[1] Meliopoulos, A.P.S.; Cokkinides, G.J.; Huang, R.; Farantatos, E.; Sungyun Choi; Yonghee Lee; Xuebei Yu, "Smart Grid Technologies for Autonomous Operation and Control," *Smart Grid, IEEE Transactions on* , vol.2, no.1, pp.1,10, March 2011

Conference

[1] Yonghee Lee, Meliopoulos, A.P., Ju-uk Lee, "New feeder automation scheme using VIT reclosers and VIT sectionalizers, "*PowerTech (POWERTECH), 2013 IEEE Grenoble*, vol., no., pp.1,6, 16-20 June 2013

[2] Meliopoulos, A.P.Sakis; Cokkinides, George J.; Tan, Zhenyu; Choi, Sungyun; Lee, Yonghee; Myrda, Paul, "Setting-Less Protection: Feasibility Study," *System Sciences (HICSS), 2013 46th Hawaii International Conference on*, vol., no., pp.2345,2353, 7-10 Jan. 2013

[3] A. P. Sakis Meliopoulos, George J. Cokkinides, Sungyun Choi, Yonghee Lee, "Setting-Less Transformer Protection Scheme using Dynamic State Estimation" Fault and Disturbance Analysis Conference

[4] Meliopoulos, A.P.S.; Cokkinides, G.J.; Sungyun Choi; Farantatos, E.; Renke Huang; Yonghee Lee; "Symbolic integration and autonomous state estimation: Building blocks for an intelligent power grid," *Intelligent System Application to Power Systems (ISAP), 2011 16th International Conference on* , vol., no., pp.1-6, 25-28 Sept. 2011

[5] Meliopoulos, S.; Cokkinides, G.; Huang, R.; Farantatos, E.; Sungyun Choi; Yonghee Lee; Xuebei Yu; "Smart Grid Infrastructure for Distribution Systems and Applications," *System Sciences (HICSS), 2011 44th Hawaii International Conference on* , vol., no., pp.1-11, 4-7 Jan. 2011

[6] A. P. Sakis Meliopoulos, George J. Cokkinides, Renke Huang, Evangelos Farantatos, Sungyun Choi, Yonghee Lee; "Advances in Disturbance Recording and PlayBack" Fault and Disturbance Analysis Conference, May 2011

[7] Meliopoulos, S.; Cokkinides, G.; Renke Huang; Farantatos, E.; Sungyun Choi; Yonghee Lee; , "Wide area dynamic monitoring and stability controls," *Bulk Power System Dynamics and Control (iREP) - VIII (iREP), 2010 iREP Symposium* , vol., no., pp.1-8, 1-6 Aug. 2010

Appendix A Quadratic Integration Method

In an attempt to facilitate DSE, a dynamic model that contains differential equations can be simplified by the quadratic integration method. This integration method, which is a special case of the class of methods known as collocation methods, is a fourth-order accurate method. Therefore, this method is more accurate than the traditional trapezoidal integration method and free from artificial numerical oscillations. For example, the feeder line model also contains several differential equations, from which the quadratic integration method can generate the ACF, thereby simplifying the DSE.

The basic concept of quadratic integration method is that functions vary quadratically over the time period of one integration step, *h* (see Figure 49).

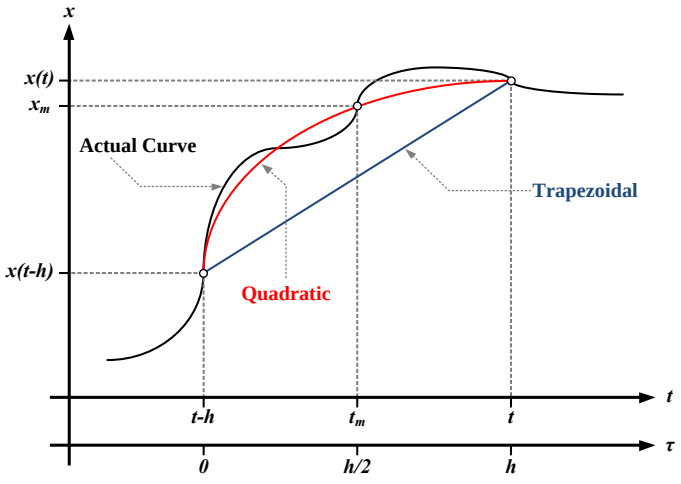

Figure 49: Quadratic-integration method [75].

The quadratic function *x(τ)* in one time step [*t-h* to *t*] can be expressed as follows:

$$x(\tau) = a + b\tau + c\tau^2,$$

where $a = x(t-h)$, $b = \frac{1}{h}\left(-3x(t-h) + 4x_m - x(t)\right)$, $c = \frac{2}{h^2}\left(x(t-h) - 2x_m + x(t)\right)$.

For example, if the dynamic system is represented as follows:

$$\frac{dx(t)}{dt} = Ax(t),$$

where *A* is the coefficient matrix. If this equation is integrated from *t-h* to *t* and from *t-h* to (*t-h)/2*, then the following matrix equation is obtained as follows:

$$\begin{bmatrix} \frac{h}{24}A & I - \frac{h}{3}A \\ I - \frac{h}{6}A & \frac{2h}{3}A \end{bmatrix} \cdot \begin{bmatrix} x(t) \\ x_m \end{bmatrix} = \begin{bmatrix} I + \frac{5h}{24}A \\ I + \frac{h}{6}A \end{bmatrix} \cdot x(t-h),$$

where *I* is the identity matrix.

Appendix B Transformer Mathematical Model – AQCF Model

The AQCF of a three-phase transformer is described in this appendix. The derived three-phase transformer AQCF model is used as a building block of the distribution circuit described in Section 5.3.

Single-Phase Transformer Compact Model Description

The state equations for a three-phase, two-winding transformer is provided in this section. The development proceeds as follows. First one phase of the transformer is modeled and the equations are integrated. Subsequently, the models of each phase are interconnected to provide the overall model.

State space equations for the single-phase model are derived from Figure 50.

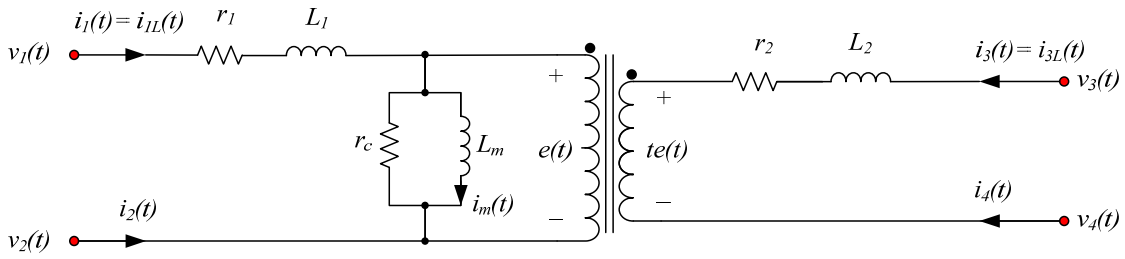

Figure 50: Single-phase transformer.

The state is defined with

$$x(t) = \begin{bmatrix} v_1(t) & v_2(t) & v_3(t) & v_4(t) & i_m(t) & e(t) & \lambda(t) & i_{1L}(t) & i_{3L}(t) \end{bmatrix}^T .$$

The following equations describe the single-phase transformer in Figure 50:

$$i_1(t) = i_{1L}(t),\ i_1(t) + i_2(t) = 0,\ i_3(t) = i_{3L}(t),\ i_3(t) + i_4(t) = 0,$$

$$r_c i_1(t) + r_c t\, i_3(t) = r_c i_m(t) + e(t),\ 0 = L_m i_m(t) - \lambda(t),$$

$$0 = v_1(t) - v_2(t) - e(t) - r_1 i_{1L}(t) - L_1 \frac{d}{dt} i_{1L}(t),$$

$$0 = v_3(t) - v_4(t) - t\, e(t) - r_2 i_{3L}(t) - L_2 \frac{d}{dt} i_{3L}(t),\ 0 = e(t) - \frac{d}{dt}\lambda(t).$$

Above equations can be written in the following compact matrix form as follow:

$$A_1 i_{1\phi}(t) = B_1 v_{1\phi}(t) + B_2 \frac{d}{dt} v_{1\phi}(t),$$

where $i_{1\phi}(t) = \begin{bmatrix} i_1(t) & i_2(t) & i_3(t) & i_4(t) & 0 & 0 & 0 & 0 & 0 \end{bmatrix}^T$,

$$v_{1\phi}(t) = \begin{bmatrix} v_1(t) & v_2(t) & v_3(t) & v_4(t) & i_m(t) & e(t) & \lambda(t) & i_{1L}(t) & i_{3L}(t) \end{bmatrix}^T,$$

$$A_1 = \begin{bmatrix} 1 & 0 & 0 & 0 & 0 & 0 & 0 & 0 & 0 \\ 1 & 1 & 0 & 0 & 0 & 0 & 0 & 0 & 0 \\ 0 & 0 & 1 & 0 & 0 & 0 & 0 & 0 & 0 \\ 0 & 0 & 1 & 1 & 0 & 0 & 0 & 0 & 0 \\ r_c & 0 & r_c t & 0 & 0 & 0 & 0 & 0 & 0 \\ 0 & 0 & 0 & 0 & 0 & 0 & 0 & 0 & 0 \\ 0 & 0 & 0 & 0 & 0 & 0 & 0 & 0 & 0 \\ 0 & 0 & 0 & 0 & 0 & 0 & 0 & 0 & 0 \\ 0 & 0 & 0 & 0 & 0 & 0 & 0 & 0 & 0 \end{bmatrix},$$

$$B_1 = \begin{bmatrix} 0 & 0 & 0 & 0 & 0 & 0 & 0 & 1 & 0 \\ 0 & 0 & 0 & 0 & 0 & 0 & 0 & 0 & 0 \\ 0 & 0 & 0 & 0 & 0 & 0 & 0 & 0 & 1 \\ 0 & 0 & 0 & 0 & 0 & 0 & 0 & 0 & 0 \\ 0 & 0 & 0 & 0 & r_c & 1 & 0 & 0 & 0 \\ 0 & 0 & 0 & 0 & L_m & 0 & -1 & 0 & 0 \\ 1 & -1 & 0 & 0 & 0 & -1 & 0 & -r_1 & 0 \\ 0 & 0 & 1 & -1 & 0 & -t & 0 & -r_2 & 0 \\ 0 & 0 & 0 & 0 & 0 & 1 & 0 & 0 & 0 \end{bmatrix},$$

$$B_2 = \begin{bmatrix} 0 & 0 & 0 & 0 & 0 & 0 & 0 & 0 & 0 \\ 0 & 0 & 0 & 0 & 0 & 0 & 0 & 0 & 0 \\ 0 & 0 & 0 & 0 & 0 & 0 & 0 & 0 & 0 \\ 0 & 0 & 0 & 0 & 0 & 0 & 0 & 0 & 0 \\ 0 & 0 & 0 & 0 & 0 & 0 & 0 & 0 & 0 \\ 0 & 0 & 0 & 0 & 0 & 0 & 0 & 0 & 0 \\ 0 & 0 & 0 & 0 & 0 & 0 & 0 & -L_1 & 0 \\ 0 & 0 & 0 & 0 & 0 & 0 & 0 & 0 & -L_2 \\ 0 & 0 & 0 & 0 & 0 & 0 & -1 & 0 & 0 \end{bmatrix},$$

when integrated over time interval [t-h, t],

$$0 = B_1\left(\frac{h}{6}v_{1\phi}(t-h) + \frac{2h}{3}v_{1\phi}(t_m) + \frac{h}{6}v_{1\phi}(t)\right) + B_2\left(v_{1\phi}(t) - v_{1\phi}(t-h)\right),$$

when integrated over time interval [t-h, t_m],

$$0 = B_1\left(\frac{5h}{24}v_{1\phi}(t-h) + \frac{h}{3}v_{1\phi}(t_m) - \frac{h}{24}v_{1\phi}(t)\right) + B_2\left(v_{1\phi}(t_m) - v_{1\phi}(t-h)\right),$$

where

$$i_{1\phi}(t) = \begin{bmatrix} i_1(t) & i_2(t) & i_3(t) & i_4(t) & 0 & 0 & 0 & 0 & 0 \end{bmatrix}^T$$

,

$$i_{1\phi}(t_m) = \begin{bmatrix} i_1(t_m) & i_2(t_m) & i_3(t_m) & i_4(t_m) & 0 & 0 & 0 & 0 & 0 \end{bmatrix}^T$$

,

$$v_{1\phi}(t) = \begin{bmatrix} v_1(t) & v_2(t) & v_3(t) & v_4(t) & i_m(t) & e(t) & \lambda(t) & i_{1L}(t) & i_{3L}(t) \end{bmatrix}^T$$

,

$$v_{1\phi m} = \begin{bmatrix} v_{1(t_m)} & v_2(t_m) & v_3(t_m) & v_4(t_m) & i_m(t_m) & e(t_m) & \lambda(t_m) & i_{1L}(t_m) & i_{3L}(t_m) \end{bmatrix}^T.$$

Express above equations in a compact matrix form as follows:

$$\begin{bmatrix} A_1 & 0 \\ 0 & 0 \\ 0 & A_1 \\ 0 & 0 \end{bmatrix}\begin{bmatrix} i_{1\phi}(t) \\ i_{1\phi}(t_m) \end{bmatrix} = \begin{bmatrix} B_1 & 0 \\ \frac{h}{6}B_1 + B_2 & \frac{2h}{3}B_1 \\ 0 & B_1 \\ -\frac{h}{24}B_1 & \frac{h}{3}B_1 + B_2 \end{bmatrix}\begin{bmatrix} v_{1\phi}(t) \\ v_{1\phi}(t_m) \end{bmatrix} - \begin{bmatrix} 0 \\ -\frac{h}{6}B_1 + B_2 \\ 0 \\ -\frac{5h}{24}B_1 + B_2 \end{bmatrix}\begin{bmatrix} v_{1\phi}(t-h) \end{bmatrix}.$$

For simplicity rewrite above equation

$$G_d \begin{bmatrix} i_{1\phi}(t) \\ i_{1\phi}(t_m) \end{bmatrix} = H_d \begin{bmatrix} v_{1\phi}(t) \\ v_{1\phi}(t_m) \end{bmatrix} - J\left[v_{1\phi}(t-h)\right],$$

(B.1)

where $G_d = \begin{bmatrix} A_1 & 0 \\ 0 & 0 \\ 0 & A_1 \\ 0 & 0 \end{bmatrix}$, $H_d = \begin{bmatrix} B_1 & 0 \\ \frac{h}{6}B_1 + B_2 & \frac{2h}{3}B_1 \\ 0 & B_1 \\ -\frac{h}{24}B_1 & \frac{h}{3}B_1 + B_2 \end{bmatrix}$, $J = \begin{bmatrix} 0 \\ -\frac{h}{6}B_1 + B_2 \\ 0 \\ -\frac{5h}{24}B_1 + B_2 \end{bmatrix}$.

The algebraic companion form of the transformer is obtained by solving Equation B.1 for $i_{1\phi}(t)$ as follows:

$$\begin{bmatrix} i_{1\phi}(t) \\ i_{1\phi}(t_m) \end{bmatrix} = L \begin{bmatrix} v_{1\phi}(t) \\ v_{1\phi}(t_m) \end{bmatrix} - N\left[v_{1\phi}(t-h)\right],$$

(B.2)

where $L = G_d^+ H_d$, $N = G_d^+ J$, G_d^+ is row operations defined with

$$G_d^+ G_d = diag\{[1 \;\; 1 \;\; 1 \;\; 1 \;\; 0 \;\; 0 \;\; 0 \;\; 0 \;\; 0 \;\; 1 \;\; 1 \;\; 1 \;\; 1 \;\; 0 \;\; 0 \;\; 0 \;\; 0 \;\; 0]\}.$$

Three-Phase Transformer Compact Model Description

Using the algebraic companion form for the single-phase transformer, the algebraic companion form is derived for the three-phase transformer. Three single-phase transformer admittances matrices are combined to form a three-phase transformer admittance matrix. Four phase connections are supported as follows: (a) Wye-wye, (b)

Wye-delta, (c) Delta-wye, and (d) Delta-delta. For this thesis, delta-wye transformer is used.

The AQCF of the three-phase, delta-wye-connected transformer can be derived by integrating three AQCFs of the single-phase transformer model. In order to integrate three AQCFs, the pointers of the single-phase AQCF need to be re-assigned to those of three-phase AQCF. The pointer mapping of external and internal states between single-phase AQCF and three-phase, delta-wye connected AQCF are shown in Figure 51.

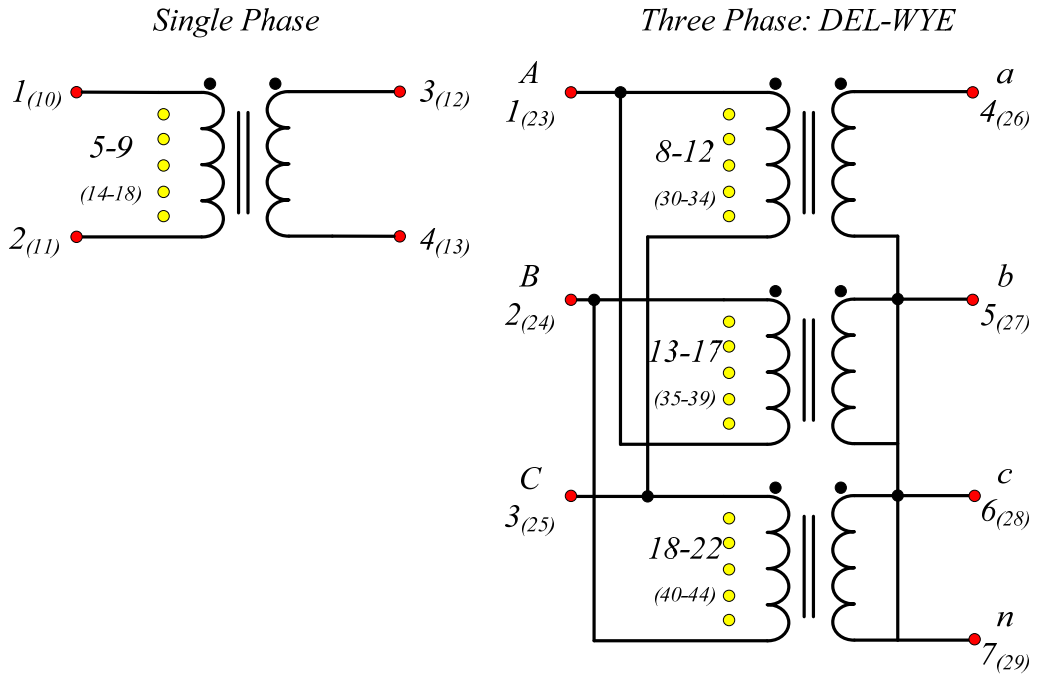

Figure 51: Delta-wye connection indices (quadratic).

The device matrices *L* and *N*, which are described in the single-phase AQCF, (B.2), are integrated based on the following algorithm, thereby providing the integrated matrices Y_{eq} and N_{eq}.

For PHASE = 1:3

```
For     I = 1:18
        K1 = POINTER_PHASE (I)
        For     J = 1:26
                K2 = POINTER_PHASE (J)
                Yeq(K1,K2) = Yeq(K1,K2) + L(I,J)
        End
        For     J = 1:9
                K2 = POINTER_PHASE (J)
                Neq(K1,K2) = Neq(K1,K2) + N(I,J)
        End
End
```

Here, PHASE is the index for each single-phase transformer. POINTER is changed according to the terminal to which each single-phase transformer is connected. They are shown in Table 2. For instance, $POINTER_1(3)$ is four.

Table 2: Pointer elements for delta-wye connection.

Single-Phase Transformer	Pointer Elements ($POINTER_{PHASE}$)
PHASE = 1	1, 3, 4, 7, 8, 9, 10, 11, 12, 23, 25, 26, 28, 30, 31, 32, 33, 34
PHASE = 2	2, 1, 5, 7, 13, 14, 15, 16, 17 24, 23, 27, 29, 35, 36, 37, 38, 39

PHASE = 3	3, 2, 6, 7, 18, 19, 20, 21 25, 27, 28, 29, 40, 41, 42, 43

The model is expressed in terms of the following equations.

$$\begin{bmatrix} i_{3\phi}(t) \\ i_{3\phi}(t_m) \end{bmatrix} = Y_{eq,XFMR} \begin{bmatrix} x_{3\phi}(t) \\ x_{3\phi}(t_m) \end{bmatrix} - N_{eq,XFMR} \cdot x_{3\phi}(t-h),$$

where

$$i_{3\phi}(t) = [i_A(t), i_B(t), i_C(t), i_a(t), i_b(t), i_c(t), i_n(t), 0,0,0,0,0,0,0,0,0,0,0,0,0,0,0]^T,$$

$$\begin{aligned} x_{3\phi}(t) = [&v_A(t), v_B(t), v_C(t), v_a(t), v_b(t), v_c(t), v_n(t), \\ &i_{mA}(t), e_A(t), \lambda_A(t), i_{1LA}(t), i_{3LA}(t), \\ &i_{mB}(t), e_B(t), \lambda_B(t), i_{1LB}(t), i_{3LB}(t), \\ &i_{mC}(t), e_C(t), \lambda_C(t), i_{1LC}(t), i_{3LC}(t)]^T, \end{aligned}$$

$$i_{3\phi}(t) = [i_A(t_m), i_B(t_m), i_C(t_m), i_a(t_m), i_b(t_m), i_c(t_m), i_n(t_m), 0,0,0,0,0,0,0,0,0,0,0,0,0,0,0]^T,$$

$$\begin{aligned} x_{3\phi}(t) = [&v_A(t_m), v_B(t_m), v_C(t_m), v_a(t_m), v_b(t_m), v_c(t_m), v_n(t_m), \\ &i_{mA}(t_m), e_A(t_m), \lambda_A(t_m), i_{1LA}(t_m), i_{3LA}(t_m), \\ &i_{mB}(t_m), e_B(t_m), \lambda_B(t_m), i_{1LB}(t_m), i_{3LB}(t_m), \\ &i_{mC}(t_m), e_C(t_m), \lambda_C(t_m), i_{1LC}(t_m), i_{3LC}(t_m)]^T, \end{aligned}$$

In this thesis, $B_{eq} = N_{eq,XFMR}[x(t-h)]$. So, the final equation is as follows:

$$\begin{bmatrix} i_{3\phi}(t) \\ i_{3\phi}(t_m) \end{bmatrix} = Y_{eq,XFMR} \begin{bmatrix} x_{3\phi}(t) \\ x_{3\phi}(t_m) \end{bmatrix} - B_{eq,XFMR}.$$

Appendix C Distribution Line Mathematical Model – AQCF Model

The AQCF of the distribution line model using quadratic integration is presented in this appendix. Note that the AQCF of the multi phase cable also can be derived from the line AQCF model. We present the AQCF for one section. The derived AQCF model is used as a building block of the distribution system and the microgrid described in Section 5.3 and Section 5.3.4, respectively.

Single-Phase Line Model - Single Section

The physical model of the single-phase distribution line model or the multi phase cable model is illustrated in Figure 52.

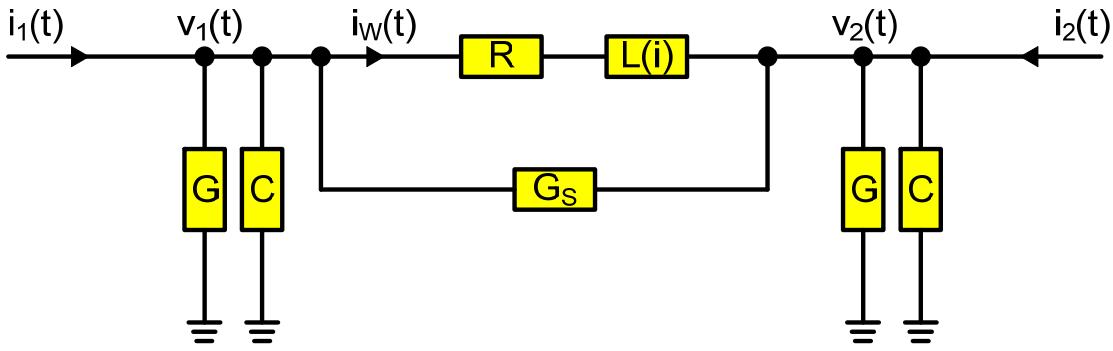

Figure 52: Physical model of one phase of the distribution line – single section.

The pi-equivalent circuit is used for the multiple conductor distribution line. If the length of the section is l and the per unit length parameter are r, L, g, c (all matrices) then

$R = l\,r, \qquad L = l\,L, \qquad C = (l/2)\,c, \qquad G = (l/2)\,g.$

The G_s is a matrix used for numerical purposes only and is not a part of the physical model. It is used as a stabilizer for the numerical integration. In the above four

parameters, L is changing with currents in the conductors, therefore is current dependent in the model. In later sections, this is denoted as L(i). G is the conductance to ground. It can be considered zero in this model.

Model Circuit Equations of Single-Phase Model- One Section

$$i_1(t) = i_W(t) + (G + G_S)v_1(t) - G_S v_2(t) + C\frac{dv_1(t)}{dt},$$

$$i_2(t) = -i_W(t) - G_S v_1(t) + (G + G_S)v_2(t) + C\frac{dv_2(t)}{dt},$$

$$0 = -v_1(t) + v_2(t) + R \cdot i_W(t) + L\frac{di_W(t)}{dt}.$$

Above equations can be rewritten in the following matrix form:

$$A_{11}i(t) + A_{12}\frac{d}{dt}i(t) = B_{11}x(t) + B_{12}\frac{d}{dt}x(t),$$

where

$$i(t) = \begin{bmatrix} i_1(t) & i_2(t) & 0 \end{bmatrix}^T,$$

$$x(t) = \begin{bmatrix} v_1(t) & v_2(t) & i_W(t) \end{bmatrix}^T,$$

$$A_{11} = \begin{bmatrix} 1 & 0 & 0 \\ 0 & 1 & 0 \\ 0 & 0 & 0 \end{bmatrix},$$

$$A_{12} = 0,$$

$$B_{11} = \begin{bmatrix} G+G_S & -G_S & 1 \\ -G_S & G+G_S & -1 \\ -1 & 1 & R \end{bmatrix},$$

$$B_{12} = \begin{bmatrix} C & 0 & 0 \\ 0 & C & 0 \\ 0 & 0 & L \end{bmatrix}.$$

Three-Phase Line Model - Single Section

The physical model of the three-phase distribution line model or the multi phase cable model is shown in Figure 53.

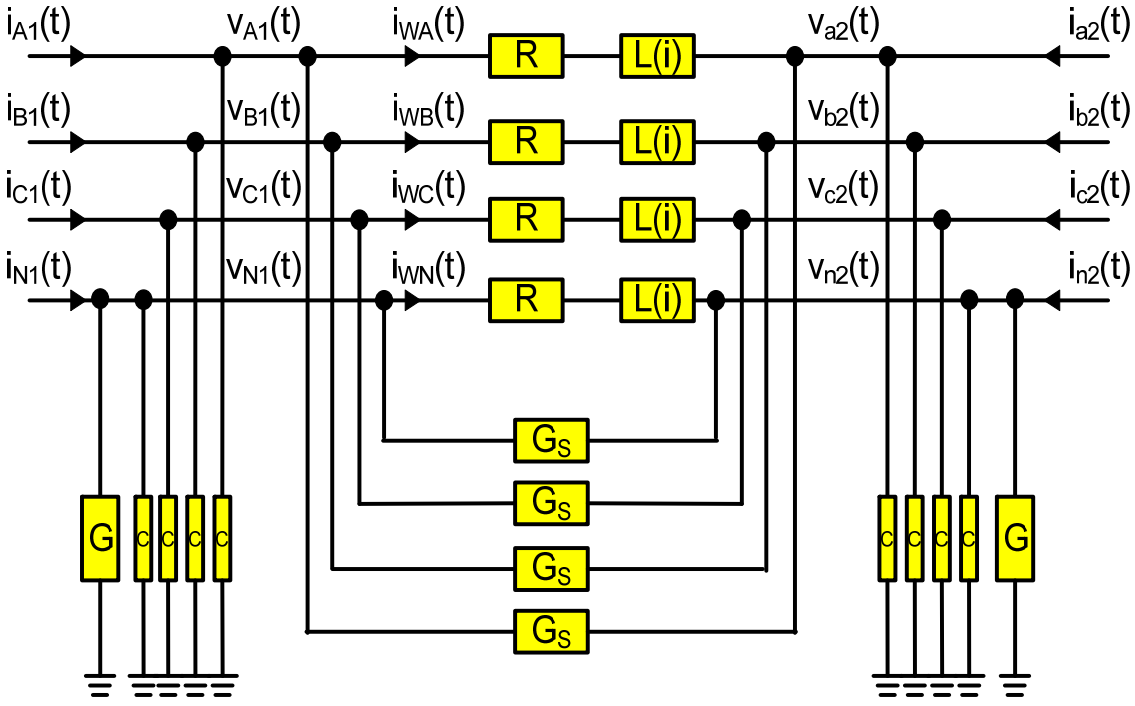

Figure 53: Physical model of three phase distribution line model – single section.

Model Circuit Equations of Three-Phase Model- One Section

$$i_{A1}(t) = i_{AW}(t) + (G + G_S)v_{A1}(t) - G_S v_{a2}(t) + C\frac{dv_{A1}(t)}{dt},$$

$$i_{B1}(t) = i_{BW}(t) + (G + G_S)v_{B1}(t) - G_S v_{b2}(t) + C\frac{dv_{B1}(t)}{dt},$$

$$i_{C1}(t) = i_{CW}(t) + (G + G_S)v_{C1}(t) - G_S v_{c2}(t) + C\frac{dv_{C1}(t)}{dt},$$

$$i_{N1}(t) = i_{NW}(t) + (G + G_S)v_{N1}(t) - G_S v_{n2}(t) + C\frac{dv_{N1}(t)}{dt},$$

$$i_{a2}(t) = -i_{AW}(t) - G_S v_{A1}(t) + (G + G_S)v_{a2}(t) + C\frac{dv_{a2}(t)}{dt},$$

$$i_{b2}(t) = -i_{BW}(t) - G_S v_{B1}(t) + (G + G_S)v_{b2}(t) + C\frac{dv_{b2}(t)}{dt},$$

$$i_{c2}(t) = -i_{CW}(t) - G_S v_{C1}(t) + (G + G_S)v_{c2}(t) + C\frac{dv_{c2}(t)}{dt},$$

$$i_{n2}(t) = -i_{NW}(t) - G_S v_{N1}(t) + (G + G_S)v_{n2}(t) + C\frac{dv_{n2}(t)}{dt},$$

$$0 = -v_{A1}(t) + v_{a2}(t) + R \cdot i_{AW}(t) + L\frac{di_{AW}(t)}{dt},$$

$$0 = -v_{B1}(t) + v_{b2}(t) + R \cdot i_{BW}(t) + L\frac{di_{BW}(t)}{dt},$$

$$0 = -v_{C1}(t) + v_{c2}(t) + R \cdot i_{CW}(t) + L\frac{di_{CW}(t)}{dt},$$

$$0 = -v_{N1}(t) + v_{n2}(t) + R \cdot i_{NW}(t) + L\frac{di_{NW}(t)}{dt},$$

where

$$R = \begin{bmatrix} R11 & R12 & R13 & R14 \\ R21 & R22 & R23 & R24 \\ R31 & R32 & R33 & R34 \\ R41 & R42 & R43 & R44 \end{bmatrix}, \qquad L = \begin{bmatrix} L11 & L12 & L13 & L14 \\ L21 & L22 & L23 & L24 \\ L31 & L32 & L33 & L34 \\ L41 & L42 & L43 & L44 \end{bmatrix},$$

$$C = \begin{bmatrix} C11 & -C12 & -C13 & -C14 \\ -C21 & C22 & -C23 & -C24 \\ -C31 & -C32 & C33 & -C34 \\ -C41 & -C42 & -C43 & C44 \end{bmatrix},$$

$$G_s = \begin{bmatrix} G_s 11 & 0 & 0 & 0 \\ 0 & G_s 22 & 0 & 0 \\ 0 & 0 & G_s 33 & 0 \\ 0 & 0 & 0 & G_s 44 \end{bmatrix}, \quad G = \begin{bmatrix} 0 & 0 & 0 & 0 \\ 0 & 0 & 0 & 0 \\ 0 & 0 & 0 & 0 \\ 0 & 0 & 0 & G44 \end{bmatrix}.$$

Above equations can be rewritten in the following matrix form:

$$A_1 i(t) + A_2 \frac{d}{dt} i(t) = B_1 x(t) + B_2 \frac{d}{dt} x(t),$$

where:

$$i(t) = \begin{bmatrix} i_{A1}(t) & i_{B1}(t) & i_{C1}(t) & i_{N1}(t) & i_{a1}(t) & i_{b1}(t) & i_{c1}(t) & i_{n1}(t) & 0 & 0 & 0 & 0 \end{bmatrix}^T,$$

$$x(t) = \begin{bmatrix} v_{A1}(t) & v_{B1}(t) & v_{C1}(t) & v_{N1}(t) & v_{a2}(t) & v_{b2}(t) & v_{c2}(t) & v_{n2}(t) & i_{AW}(t) & i_{BW}(t) & i_{CW}(t) & i_{NW}(t) \end{bmatrix}^T,$$

$$A_1 = \begin{bmatrix} 1 & 0 & 0 & 0 & 0 & 0 & 0 & 0 & 0 & 0 & 0 & 0 \\ 0 & 1 & 0 & 0 & 0 & 0 & 0 & 0 & 0 & 0 & 0 & 0 \\ 0 & 0 & 1 & 0 & 0 & 0 & 0 & 0 & 0 & 0 & 0 & 0 \\ 0 & 0 & 0 & 1 & 0 & 0 & 0 & 0 & 0 & 0 & 0 & 0 \\ 0 & 0 & 0 & 0 & 1 & 0 & 0 & 0 & 0 & 0 & 0 & 0 \\ 0 & 0 & 0 & 0 & 0 & 1 & 0 & 0 & 0 & 0 & 0 & 0 \\ 0 & 0 & 0 & 0 & 0 & 0 & 1 & 0 & 0 & 0 & 0 & 0 \\ 0 & 0 & 0 & 0 & 0 & 0 & 0 & 1 & 0 & 0 & 0 & 0 \\ 0 & 0 & 0 & 0 & 0 & 0 & 0 & 0 & 0 & 0 & 0 & 0 \\ 0 & 0 & 0 & 0 & 0 & 0 & 0 & 0 & 0 & 0 & 0 & 0 \\ 0 & 0 & 0 & 0 & 0 & 0 & 0 & 0 & 0 & 0 & 0 & 0 \\ 0 & 0 & 0 & 0 & 0 & 0 & 0 & 0 & 0 & 0 & 0 & 0 \end{bmatrix},$$

$$A_2 = 0,$$

$$B_1 = \begin{bmatrix} G_S11 & 0 & 0 & 0 & -G_S11 & 0 & 0 & 0 & 1 & 0 & 0 & 0 \\ 0 & G_S22 & 0 & 0 & 0 & -G_S22 & 0 & 0 & 0 & 1 & 0 & 0 \\ 0 & 0 & G_S33 & 0 & 0 & 0 & -G_S33 & 0 & 0 & 0 & 1 & 0 \\ 0 & 0 & 0 & G44+G_S44 & 0 & 0 & 0 & -G_S44 & 0 & 0 & 0 & 1 \\ -G_S11 & 0 & 0 & 0 & G_S11 & 0 & 0 & 0 & -1 & 0 & 0 & 0 \\ 0 & -G_S22 & 0 & 0 & 0 & G_S22 & 0 & 0 & 0 & -1 & 0 & 0 \\ 0 & 0 & -G_S33 & 0 & 0 & 0 & G_S33 & 0 & 0 & 0 & -1 & 0 \\ 0 & 0 & 0 & -G_S44 & 0 & 0 & 0 & G_S44 & 0 & 0 & 0 & -1 \\ -1 & 0 & 0 & 0 & 1 & 0 & 0 & 0 & R11 & R12 & R13 & R14 \\ 0 & -1 & 0 & 0 & 0 & 1 & 0 & 0 & R21 & R22 & R23 & R24 \\ 0 & 0 & -1 & 0 & 0 & 0 & 1 & 0 & R31 & R32 & R33 & R34 \\ 0 & 0 & 0 & -1 & 0 & 0 & 0 & 1 & R41 & R42 & R43 & R44 \end{bmatrix},$$

$$B_2 = \begin{bmatrix} C11 & -C12 & -C13 & -C14 & 0 & 0 & 0 & 0 & 0 & 0 & 0 & 0 \\ -C21 & C22 & -C23 & -C24 & 0 & 0 & 0 & 0 & 0 & 0 & 0 & 0 \\ -C31 & -C32 & C33 & -C34 & 0 & 0 & 0 & 0 & 0 & 0 & 0 & 0 \\ -C41 & -C42 & -C43 & C44 & 0 & 0 & 0 & 0 & 0 & 0 & 0 & 0 \\ 0 & 0 & 0 & 0 & C11 & -C12 & -C13 & -C14 & 0 & 0 & 0 & 0 \\ 0 & 0 & 0 & 0 & -C21 & C22 & -C23 & -C24 & 0 & 0 & 0 & 0 \\ 0 & 0 & 0 & 0 & -C31 & -C32 & C33 & -C34 & 0 & 0 & 0 & 0 \\ 0 & 0 & 0 & 0 & -C41 & -C42 & -C43 & C44 & 0 & 0 & 0 & 0 \\ 0 & 0 & 0 & 0 & 0 & 0 & 0 & 0 & L11 & L12 & L13 & L14 \\ 0 & 0 & 0 & 0 & 0 & 0 & 0 & 0 & L21 & L22 & L23 & L24 \\ 0 & 0 & 0 & 0 & 0 & 0 & 0 & 0 & L31 & L32 & L33 & L34 \\ 0 & 0 & 0 & 0 & 0 & 0 & 0 & 0 & L41 & L42 & L43 & L44 \end{bmatrix}$$

,

when integrated over time interval [t-h,t],

$$A_1\left(\frac{h}{6}i_{1\phi}(t-h)+\frac{2h}{3}i_{1\phi m}+\frac{h}{6}i_{1\phi}(t)\right)+A_2\left(i_{1\phi}(t)-i_{1\phi}(t-h)\right)=B_1\left(\frac{h}{6}v_{1\phi}(t-h)+\frac{2h}{3}v_{1\phi m}+\frac{h}{6}v_{1\phi}(t)\right)+B_2\left(v_{1\phi}(t)-v_{1\phi}(t-h)\right).$$

when integrated over time interval [t-h,t_m],

$$A_1\left(\frac{5h}{24}i_{1\phi}(t-h)+\frac{h}{3}i_{1\phi m}-\frac{h}{24}i_{1\phi}(t)\right)+A_2\left(i_{1\phi m}-i_{1\phi}(t-h)\right)=B_1\left(\frac{5h}{24}v_{1\phi}(t-h)+\frac{h}{3}v_{1\phi m}-\frac{h}{24}v_{1\phi}(t)\right)+B_2\left(v_{1\phi m}-v_{1\phi}(t-h)\right).$$

Express above equations in a compact matrix form.

$$\begin{bmatrix} \frac{h}{6}A_1+A_2 & \frac{2h}{3}A_1 \\ -\frac{h}{24}A_1 & \frac{h}{3}A_1+A_2 \end{bmatrix}\begin{bmatrix} i(t) \\ i(t_m) \end{bmatrix}=\begin{bmatrix} \frac{h}{6}B_1+B_{12} & \frac{2h}{3}B_1 \\ -\frac{h}{24}B_1 & \frac{h}{3}B_1+B_2 \end{bmatrix}\begin{bmatrix} x(t) \\ x(t_m) \end{bmatrix}-\begin{bmatrix} \frac{h}{6}A_1-A_2 \\ \frac{5h}{24}A_1-A_2 \end{bmatrix}\left[i(t-h)\right]-\begin{bmatrix} -\frac{h}{6}B_1+B_2 \\ -\frac{5h}{24}B_1+B_2 \end{bmatrix}\left[x(t-h)\right]$$

.

For simplicity rewrite above equation

$$G_d\begin{bmatrix} i(t) \\ i(t_m) \end{bmatrix}=H_d\begin{bmatrix} x(t) \\ x(t_m) \end{bmatrix}-I_d\left[i(t-h)\right]-J_d\left[x(t-h)\right]$$

,

where

$$G_d = \begin{bmatrix} \frac{h}{6}A_1 + A_2 & \frac{2h}{3}A_1 \\ -\frac{h}{24}A_1 & \frac{h}{3}A_1 + A_2 \end{bmatrix},$$

$$H_d = \begin{bmatrix} \frac{h}{6}B_1 + B_2 & \frac{2h}{3}B_1 \\ -\frac{h}{24}B_1 & \frac{h}{3}B_1 + B_2 \end{bmatrix},$$

$$I_d = \begin{bmatrix} \frac{h}{6}A_1 - A_2 \\ \frac{5h}{24}A_1 - A_2 \end{bmatrix},$$

$$J_d = \begin{bmatrix} -\frac{h}{6}B_1 + B_2 \\ -\frac{5h}{24}B_1 + B_2 \end{bmatrix}.$$

The algebraic companion form is obtained by solving the above equation for $\begin{bmatrix} i(t) \\ i(t_m) \end{bmatrix}$ as follows:

$$\begin{bmatrix} i(t) \\ i(t_m) \end{bmatrix} = Y_{eq,LINE}\begin{bmatrix} x(t) \\ x(t_m) \end{bmatrix} - M_{eq,LINE}[i(t-h)] - N_{eq,LINE}\left[x(t-h)\right],$$

where $Y_{eq_{LINE}} = G_d^+ H_d$, $M_{eq_{LINE}} = G_d^+ I_d$, $N_{eq_{LINE}} = G_d^+ J_d$.

And G_d^+ is row operations defined with $G_d^+ G = \begin{bmatrix} A_1 & 0 \\ 0 & A_1 \end{bmatrix}$.

In this thesis $B_{eq} = M_{eq_{LINE}}[i(t-h)] + N_{eq_{LINE}}\left[x(t-h)\right]$. So, the final equation is as follows:

$$\begin{bmatrix} i_{3\phi}(t) \\ i_{3\phi}(t_m) \end{bmatrix} = Y_{eq,LINE} \begin{bmatrix} x_{3\phi}(t) \\ x_{3\phi}(t_m) \end{bmatrix} - B_{eq,LINE} \cdot$$

Appendix D Distribution Circuit States Definition

In this appendix, the states of the distribution circuit are defined. The distribution circuit is highlighted in a blue area as depicted in Figure 34. The distribution circuit is composed four line models and three transformer models. For the distribution circuit, states of the model are composed of 24 external states (12 external states for time t and 12 external states for t_m) and 52 internal states (26 internal states for time t and 26 internal states for time t_m). The total number of states is 76.

The external states, part of the internal states, and currents are illustrated in Figure 54. Internal states of the transformers are same as explained in Appendix B.

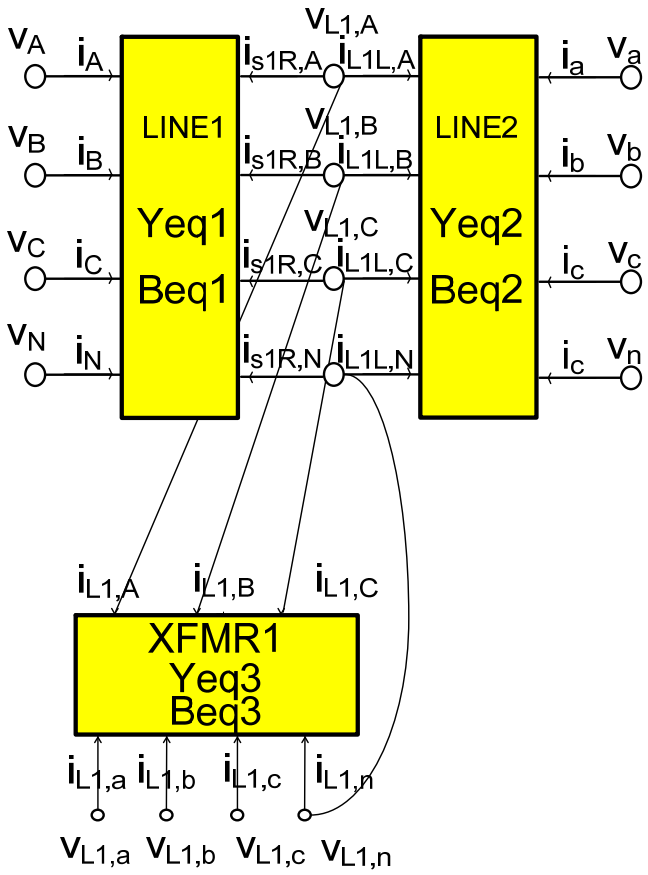

Figure 54: The distribution circuit model representation including states, and currents.

For time t, the states are listed in Table 3. For time t_m, the states are the same.

Table 3: States for three-phase distribution circuit at time t and t_m.

State	type
v_A	External State
v_B	External State
v_C	External State
v_N	External State
v_a	External State
v_b	External State
v_c	External State
v_n	External State
$v_{L1,a}$	External State
$v_{L1,b}$	External State
$v_{L1,c}$	External State
$v_{L1,n}$	External State
$i_{W1,A}$	Internal State
$i_{W1,B}$	Internal State
$i_{W1,C}$	Internal State
$i_{W1,N}$	Internal State
$i_{W2,A}$	Internal State
$i_{W2,B}$	Internal State
$i_{W2,C}$	Internal State
$i_{W2,N}$	Internal State
$v_{L1,A}$	Internal State
$v_{L1,B}$	Internal State
$v_{L1,C}$	Internal State

$i_{L1,L1A}$	Internal State
$i_{L1,L3A}$	Internal State
$i_{L1,mA}$	Internal State
$e_{L1,A}$	Internal State
$\lambda_{L1,A}$	Internal State
$i_{L1,L1B}$	Internal State
$i_{L1,L3B}$	Internal State
$i_{L1,mB}$	Internal State
$e_{L1,B}$	Internal State
$\lambda_{L1,B}$	Internal State
$i_{L1,L1C}$	Internal State
$i_{L1,L3C}$	Internal State
$i_{L1,mC}$	Internal State
$e_{L1,C}$	Internal State
$\lambda_{L1,C}$	Internal State

The states are defined as follows:

$$x(t) = \begin{bmatrix} V(t) \\ v_a(t) \end{bmatrix},\ x(t_m) = \begin{bmatrix} V(t_m) \\ v_a(t_m) \end{bmatrix},$$

where $V(t)$ and $V(t_m)$ are external states, and $v_a(t)$ and $v_a(t_m)$ are internal states as defined above.

Appendix E Distribution Circuit Measurement Data Definition for the Computer Simulation

The measurement data of the distribution circuit depicted in Figure 34 are defined in this appendix. Note that in the actual implementation data will not be coming from the COMTRADE but rather streaming from the data acquisition system. The COMTRADE file is used for offline events simulation and offline DSE-based protection analytics. The measurement number should be changed depending on the number of terminals and load connections. Generally, the number of actual measurement at time t and t_m is determined by 2*(3*(number of terminals) + 3*(number of loads)). For this case, two terminals and one load connection are combined. The number of virtual measurement and pseudo measurement at time t and t_m is dependent on the line and transformer AQCF model. For the computer based simulation, the following measurements of the distribution system could be obtained from the COMTRADE file.

Actual across measurements – Nine voltage measurements at time t and nine voltage measurements at time t_m = (t-h+t)/2 (phase A-N, phase B-N, phase C-N, phase a-n, phase b-n, and phase c-n, phase L1a-N, phase L1b-N, and phase L1c-N). For these measurements assume a measurement error with standard deviation equal to 0.05 p.u.

The model of this measurement type is as follows:

$$V^m(t) = v_i(t) - v_n(t) + \eta \ ,$$

where $V^m(t)$ are the measurement values.

Actual through measurements – Nine current measurements at time t and nine current measurements at time t_m = (t-h+t)/2 (phase A, phase B, phase C, phase a, phase b, phase c,

phase L1a, phase L1b, and phase L1c). For these measurements assume a measurement error with standard deviation equal to 0.01 p.u.

The model of this measurement type is i[th] row of the combined model equation as explained in Appendix G:

$$I^m(t) = yeq\_real \times x(t) - beq\_real + \eta,$$

where $I^m(t)$ are the measurement values.

Virtual measurements – 54 virtual measurements at time t and 54 virtual measurements at time $t_m=(t-h+t)/2$. The virtual measurements can be classified into three groups as follows: (a) Internal measurements of transformers (15 at time t), (b) Internal measurements of single section lines (8 at time t), and (c) Summation of current at each connection (KCL measurement, 4 at time t). The summation of current at each connection is zero according to the KCL. For these measurements assume a measurement error with standard deviation equal to 0.01 p.u.

The model of this measurement type is i[th] row of the combined model equation as explained in Appendix G, simply $0 = yeq\_real \times x(t) - beq\_real + \eta$.

Pseudo measurements – six pseudo measurements at time t and six pseudo measurements at time $t_m=(t-h+t)/2$ (voltage N, voltage n, voltage L1N, current N, current n, and current L1N,). These measurements represent quantities that have a certain value with a relatively large measurement error; in this case normally not measured, such as current in the neutral, or voltage at the neutral. For these measurements assume a measurement error with standard deviation equal to 0.01 p.u.

The pseudo measurements of the distribution model can be divided into two groups as follows:

(a) Six across neutral voltage measurements as follows:

$$0 = v_n(t) + \eta.$$

(b) Six through neutral current measurements as follows:

i^{th} row of the combined model equation $0 = yeq\_real \times x(t) - beq\_real + \eta$,

where i^{th} row are selected as explained in Appendix G.

In summary, the measurement data for three-phase distribution circuit are composed of 36 actual measurements, 58 virtual measurements, eight pseudo measurements, and the total numbers of measurement data are 102. Since the number of states are 76, the degree of freedom, v, is = m-n=102-76=26. It will provide a redundancy of 34.21% (= (102-76)/76*100). The measurements are listed in Table 4.

Table 4: Measurements for three-phase distribution circuit for the computer simulation.

Type	Name	Measurement Model	Standard
Across	voltage_AN	$z_1 = v_A(t) - v_N(t)$	0.05(p.u.)*Vrating
Across	voltage_BN	$z_2 = v_B(t) - v_N(t)$	0.05(p.u.)*Vrating
Across	voltage_CN	$z_3 = v_C(t) - v_N(t)$	0.05(p.u.)*Vrating
Pseudo	voltage_N	$z_4 = 0 = v_N(t)$	0.01(p.u.) *Vrating
Across	voltage_an	$z_5 = v_a(t) - v_n(t)$	0.05(p.u.)*Vrating
Across	voltage_bn	$z_6 = v_b(t) - v_n(t)$	0.05(p.u.)*Vrating
Across	voltage_cn	$z_7 = v_c(t) - v_n(t)$	0.05(p.u.)*Vrating
Pseudo	voltage_n	$z_8 = 0 = v_n(t)$	0.01(p.u.) *Vrating
Across	voltage_AN	$z_9 = v_A(t_m) - v_N(t_m)$	0.05(p.u.)*Vrating

Across	voltage_BNm	$z_{10} = v_B(t_m) - v_N(t_m)$	0.05(p.u.)*Vrating
Across	voltage_CNm	$z_{11} = v_C(t_m) - v_N(t_m)$	0.05(p.u.)*Vrating
Pseudo	voltage_Nm	$z_{12} = 0 = v_N(t_m)$	0.01(p.u.) *Vrating
Across	voltage_anm	$z_{13} = v_a(t_m) - v_n(t_m)$	0.05(p.u.)*Vrating
Across	voltage_bnm	$z_{14} = v_b(t_m) - v_n(t_m)$	0.05(p.u.)*Vrating
Across	voltage_cnm	$z_{15} = v_c(t_m) - v_n(t_m)$	0.05(p.u.)*Vrating
Pseudo	voltage_nm	$z_{16} = 0 = v_n(t_m)$	0.01(p.u.) *Vrating
Across	voltage_L1an	$z_{17} = v_{L1a}(t) - v_{L1n}(t)$	0.05(p.u.)*Vrating
Across	voltage_L1bn	$z_{18} = v_{L1b}(t) - v_{L1n}(t)$	0.05(p.u.)*Vrating
Across	voltage_L1cn	$z_{19} = v_{L1c}(t) - v_{L1n}(t)$	0.05(p.u.)*Vrating
Pseudo	voltage_L1n	$z_{20} = 0 = v_{L1n}(t)$	0.01(p.u.) *Vrating
Across	voltage_L1an	$z_{21} = v_{L1a}(t_m) - v_{L1n}(t_m)$	0.05(p.u.)*Vrating
Across	voltage_L1bn	$z_{22} = v_{L1b}(t_m) - v_{L1n}(t_m)$	0.05(p.u.)*Vrating
Across	voltage_L1cn	$z_{23} = v_{L1c}(t_m) - v_{L1n}(t_m)$	0.05(p.u.)*Vrating
Pseudo	voltage_L1n	$z_{24} = 0 = v_{L1n}(t_m)$	0.01(p.u.) *Vrating
Through	current_A	$z_{25} = i_A(t) = yeq\_real \times x(t) - beq\_real + \eta$	0.01(p.u.)*Irating
Through	current_B	$z_{26} = i_B(t) = yeq\_real \times x(t) - beq\_real + \eta$	0.01(p.u.)*Irating
Through	current_C	$z_{27} = i_C(t) = yeq\_real \times x(t) - beq\_real + \eta$	0.01 (p.u.)*Irating
Pseudo	current_N	$z_{28} = 0 = yeq\_real \times x(t) - beq\_real + \eta$	0.01(p.u.) *Irating
Through	current_a	$z_{29} = i_a(t) = yeq\_real \times x(t) - beq\_real + \eta$	0.01(p.u.)*Irating
Through	current_b	$z_{30} = i_b(t) = yeq\_real \times x(t) - beq\_real + \eta$	0.01(p.u.)*Irating
Through	current_c	$z_{31} = i_c(t) = yeq\_real \times x(t) - beq\_real + \eta$	0.01 (p.u.)*Irating
Pseudo	current_n	$z_{32} = 0 = yeq\_real \times x(t) - beq\_real + \eta$	0.01(p.u.) *Irating
Through	current_Am	$z_{33} = i_A(t_m) = yeq\ real \times x(t_m) - beq\ real + \eta$	0.01(p.u.)*Irating
Through	current_Bm	$z_{34} = i_B(t_m) = yeq\ real \times x(t_m) - beq\ real + \eta$	0.01(p.u.)*Irating
Through	current_Cm	$z_{35} = i_C(t_m) = yeq\ real \times x(t_m) - beq\ real + \eta$	0.01 (p.u.)*Irating
Pseudo	current_Nm	$z_{36} = 0 = yeq\ real \times x(t_m) - beq\ real + \eta$	0.01(p.u.) *Irating
Through	current_am	$z_{37} = i_a(t_m) = yeq\ real \times x(t_m) - beq\ real + \eta$	0.01(p.u.)*Irating
Through	current_bm	$z_{38} = i_b(t_m) = yeq\ real \times x(t_m) - beq\ real + \eta$	0.01(p.u.)*Irating

Through	current_cm	$z_{39} = i_c(t_m) = yeq\ \ real \times x(t_m) - beq\ \ real + \eta$	0.01 (p.u.)*Irating
Pseudo	current_nm	$z_{40} = 0 = yeq\ \ real \times x(t_m) - beq\ \ real + \eta$	0.01(p.u.) *Irating
Through	current_L1a	$z_{41} = i_{L1,a}(t) = yeq\_real \times x(t) - beq\_real + \eta$	0.01(p.u.)*Irating
Through	current_L1b	$z_{42} = i_{L1,b}(t) = yeq\_real \times x(t) - beq\_real + \eta$	0.01(p.u.)*Irating
Through	current_L1c	$z_{43} = i_{L1,c}(t) = yeq\_real \times x(t) - beq\_real + \eta$	0.01 (p.u.)*Irating
Pseudo	current_L1n	$z_{44} = 0 = yeq\_real \times x(t) - beq\_real + \eta$	0.01(p.u.) *Irating
Through	current_L1am	$z_{45} = i_{L1,a}(t_m) = yeq\ \ real \times x(t_m) - beq\ \ real + \eta$	0.01(p.u.)*Irating
Through	current_L1b	$z_{46} = i_{L1,b}(t_m) = yeq\ \ real \times x(t_m) - beq\ \ real + \eta$	0.01(p.u.)*Irating
Through	current_L1cm	$z_{47} = i_{L1,c}(t_m) = yeq\ \ real \times x(t_m) - beq\ \ real + \eta$	0.01 (p.u.)*Irating
Pseudo	current_L1n	$z_{48} = 0 = yeq\_real \times x(t) - beq\_real + \eta$	0.01(p.u.) *Irating
Virtual	0	$z_{49} \sim z_{75} = 0 = yeq\_real \times x(t) - beq\_real + \eta$	0.01(p.u.)*Irating
Virtual	0	$z_{76} \sim z_{102} = 0 = yeq\ \ real \times x(t_m) - beq\ \ real + \eta$	0.01(p.u.)*Irating

Appendix F Distribution Circuit Measurement Data Definition for the Laboratory Test

For the laboratory test, since the Reason MU has three voltage inputs and three current inputs, the test system with nine voltage measurements and nine current measurements requires derived measurements. In this thesis, three actual voltage and current measurements (for time t and t_m) are obtained at bus "RECA_3R" and the derived voltage and current measurements (for time t and t_m) are computed for the bus "RECA_4L" and "TL–LOADA3". Basically, the derived measurements are obtained by calculating the ratio between the bus "RECA_3R" and "RECA_4L" or "RECA_3R" and "TL–LOADA3".

Note that explanations about the duplicated measurements (actual measurements, virtual measurements, and pseudo measurements) are not repeated, although they have different standard deviation values as shown in Table 5.

Derived across measurements for the laboratory test –Six voltage measurements at time t and six voltage measurements at time t_m = (t-h+t)/2 (phase a-n, phase b-n, and phase c-n, phase L1a-N, phase L1b-N, and phase L1c-N). For these measurements assume a measurement error with standard deviation equal to 0.08 p.u.

The model of this measurement type is as follows:

$$V^m(t) = v_i(t) - v_n(t) + \eta \ ,$$

where $V^m(t)$ are the measurement values.

Derived through measurements for the laboratory test – Six current measurements at time t and six current measurements at time t_m = (t-h+t)/2 (phase a, phase b, phase c,

phase L1a, phase L1b, and phase L1c). For these measurements assume a measurement error with standard deviation equal to 0.08 p.u.

The model of this measurement type is i^{th} row of the combined model equation as explained in Appendix G:

$$I^m(t) = yeq\_real \times x(t) - beq\_real + \eta,$$

where $I^m(t)$ are the measurement values.

Table 5: Measurements for three-phase distribution circuit for the laboratory test.

Type	Name	Measurement Model	Standard
Across	voltage_AN	$z_1 = v_A(t) - v_N(t)$	0.01(p.u.)*Vrating
Across	voltage_BN	$z_2 = v_B(t) - v_N(t)$	0.01(p.u.)*Vrating
Across	voltage_CN	$z_3 = v_C(t) - v_N(t)$	0.01(p.u.)*Vrating
Pseudo	voltage_N	$z_4 = 0 = v_N(t)$	0.08(p.u.) *Vrating
Derived	voltage_an	$z_5 = v_a(t) - v_n(t)$	0.08(p.u.)*Vrating
Derived	voltage_bn	$z_6 = v_b(t) - v_n(t)$	0.08(p.u.)*Vrating
Derived	voltage_cn	$z_7 = v_c(t) - v_n(t)$	0.08(p.u.)*Vrating
Pseudo	voltage_n	$z_8 = 0 = v_n(t)$	0.08(p.u.) *Vrating
Across	voltage_ANm	$z_9 = v_A(t_m) - v_N(t_m)$	0.01(p.u.)*Vrating
Across	voltage_BNm	$z_{10} = v_B(t_m) - v_N(t_m)$	0.01(p.u.)*Vrating
Across	voltage_CNm	$z_{11} = v_C(t_m) - v_N(t_m)$	0.01(p.u.)*Vrating
Pseudo	voltage_Nm	$z_{12} = 0 = v_N(t_m)$	0.08(p.u.) *Vrating
Derived	voltage_anm	$z_{13} = v_a(t_m) - v_n(t_m)$	0.08(p.u.)*Vrating
Derived	voltage_bnm	$z_{14} = v_b(t_m) - v_n(t_m)$	0.08(p.u.)*Vrating
Derived	voltage_cnm	$z_{15} = v_c(t_m) - v_n(t_m)$	0.08(p.u.)*Vrating
Pseudo	voltage_nm	$z_{16} = 0 = v_n(t_m)$	0.08(p.u.) *Vrating
Derived	voltage_L1an	$z_{17} = v_{L1a}(t) - v_{L1n}(t)$	0.08(p.u.)*Vrating
Derived	voltage_L1bn	$z_{18} = v_{L1b}(t) - v_{L1n}(t)$	0.08(p.u.)*Vrating

Derived	voltage_L1cn	$z_{19} = v_{L1c}(t) - v_{L1n}(t)$	0.08(p.u.)*Vrating
Pseudo	voltage_L1n	$z_{20} = 0 = v_{L1n}(t)$	0.08(p.u.) *Vrating
Derived	voltage_L1anm	$z_{21} = v_{L1a}(t_m) - v_{L1n}(t_m)$	0.08(p.u.)*Vrating
Derived	voltage_L1bnm	$z_{22} = v_{L1b}(t_m) - v_{L1n}(t_m)$	0.08(p.u.)*Vrating
Derived	voltage_L1cnm	$z_{23} = v_{L1c}(t_m) - v_{L1n}(t_m)$	0.08(p.u.)*Vrating
Pseudo	voltage_L1nm	$z_{24} = 0 = v_{L1n}(t_m)$	0.08(p.u.) *Vrating
Through	current_A	$z_{25} = i_A(t) = yeq\_real \times x(t) - beq\_real + \eta$	0.03(p.u.)*Irating
Through	current_B	$z_{26} = i_B(t) = yeq\_real \times x(t) - beq\_real + \eta$	0.03(p.u.)* Irating
Through	current_C	$z_{27} = i_C(t) = yeq\_real \times x(t) - beq\_real + \eta$	0.03(p.u.)* Irating
Pseudo	current_N	$z_{28} = 0 = yeq\_real \times x(t) - beq\_real + \eta$	0.08(p.u.) * Irating
Derived	current_a	$z_{29} = i_a(t) = yeq\_real \times x(t) - beq\_real + \eta$	0.05(p.u.)* Irating
Derived	current_b	$z_{30} = i_b(t) = yeq\_real \times x(t) - beq\_real + \eta$	0.05(p.u.)* Irating
Derived	current_c	$z_{31} = i_c(t) = yeq\_real \times x(t) - beq\_real + \eta$	0.05(p.u.)* Irating
Pseudo	current_n	$z_{32} = 0 = yeq\_real \times x(t) - beq\_real + \eta$	0.08(p.u.) * Irating
Through	current_Am	$z_{33} = i_A(t_m) = yeq\_real \times x(t_m) - beq\_real + \eta$	0.03(p.u.)*Irating
Through	current_Bm	$z_{34} = i_B(t_m) = yeq\_real \times x(t_m) - beq\_real + \eta$	0.03(p.u.)* Irating
Through	current_Cm	$z_{35} = i_C(t_m) = yeq\_real \times x(t_m) - beq\_real + \eta$	0.03(p.u.)* Irating
Pseudo	current_Nm	$z_{36} = 0 = yeq\_real \times x(t_m) - beq\_real + \eta$	0.08(p.u.) * Irating
Derived	current_am	$z_{37} = i_a(t_m) = yeq\_real \times x(t_m) - beq\_real + \eta$	0.05(p.u.)* Irating
Derived	current_bm	$z_{38} = i_b(t_m) = yeq\_real \times x(t_m) - beq\_real + \eta$	0.05(p.u.)* Irating
Derived	current_cm	$z_{39} = i_c(t_m) = yeq\_real \times x(t_m) - beq\_real + \eta$	0.05(p.u.)* Irating
Pseudo	current_nm	$z_{40} = 0 = yeq\_real \times x(t_m) - beq\_real + \eta$	0.08(p.u.) * Irating
Derived	current_L1a	$z_{41} = i_{L1,a}(t) = yeq\_real \times x(t) - beq\_real + \eta$	0.05(p.u.)* Irating
Derived	current_L1b	$z_{42} = i_{L1,b}(t) = yeq\_real \times x(t) - beq\_real + \eta$	0.05(p.u.)* Irating
Derived	current_L1c	$z_{43} = i_{L1,c}(t) = yeq\_real \times x(t) - beq\_real + \eta$	0.05(p.u.)* Irating
Pseudo	current_L1n	$z_{44} = 0 = yeq\_real \times x(t) - beq\_real + \eta$	0.08(p.u.) * Irating
Derived	current_L1am	$z_{45} = i_{L1,a}(t_m) = yeq\_real \times x(t_m) - beq\_real + \eta$	0.05(p.u.)* Irating
Derived	current_L1bm	$z_{46} = i_{L1,b}(t_m) = yeq\_real \times x(t_m) - beq\_real + \eta$	0.05(p.u.)* Irating
Derived	current_L1cm	$z_{47} = i_{L1,c}(t_m) = yeq\_real \times x(t_m) - beq\_real + \eta$	0.05(p.u.)* Irating

Pseudo	current_L1nm	$z_{48} = 0 = yeq\_real \times x(t) - beq\_real + \eta$	0.08(p.u.) * Irating
Virtual	0	$z_{49} \sim z_{75} = 0 = yeq\_real \times x(t) - beq\_real + \eta$	0.08(p.u.)*Irating
Virtual	0	$z_{76} \sim z_{102} = 0 = yeq\_real \times x(t_m) - beq\_real + \eta$	0.08(p.u.)*Irating

Appendix G Creation of Measurement Models – Distribution System

The creation of the mathematical models of the measurements for the distribution circuit depicted in Figure 34 is described in this appendix. For the distribution circuit, the transformer model and the single section distribution circuit model are combined. The derivation of these models is documented in Appendix B and Appendix C. Measurements are composed of actual, virtual, and pseudo measurements. Among them, actual measurement can be obtained from streaming data or saved COMTRADE data. For online protection scheme, streaming data is required. For this thesis, offline protection scheme is applied, so COMTRADE data are utilized. The relationship between measurement data and system states for time t can be obtained from the single device model and pointers as shown in Figure 55. Note that for time t_m, the same logic can be applied. The $Y_{eq,k,i}$ represents the i^{th} line of the admittance matrix of the k^{th} device, the x_k represents the states of the k^{th} device, and the $B_{eq,k,i}$ represents the i^{th} line of the past history value of the k^{th} device.

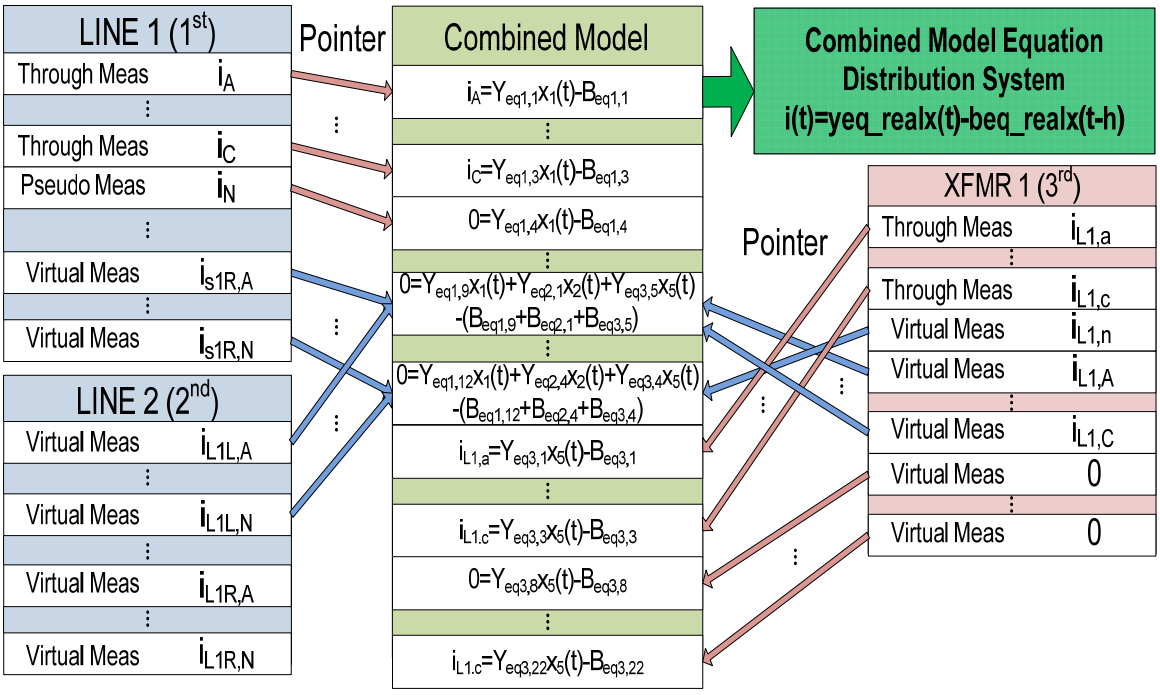

Figure 55: Measurement data and AQCF mapping using pointers – distribution system.

Actual across measurements – For actual across measurements, the model of this measurement type is as follows:

$$V^m(t) = v_i(t) - v_n(t) + \eta ,$$

where $V^m(t)$ are the measurement values.

Actual through measurements – For actual through measurements, the model of this measurement type is i[th] row of the combined model equation as follows:

$$I^m(t) = yeq\_real \times x(t) - beq\_real + \eta ,$$

where $I^m(t)$ are the measurement values.

Derived across measurements – For derived across measurements, the model of this measurement type is as follows:

$V^m(t) = v_i(t) - v_n(t) + \eta$,

where $V^m(t)$ are the derived measurement values.

Derived through measurements – For derived through measurements, the model of this measurement type is ith row of the combined model equation as follows:

$I^m(t) = yeq\_real \times x(t) - beq\_real + \eta$,

where $I^m(t)$ are the derived measurement values.

Pseudo measurements – The pseudo measurements of the distribution circuit model can be divided into two groups as follows:

(a) Five across neutral voltage measurements as follows:

$0 = v_n(t) + \eta$.

(b) Two through neutral current measurements as follows:

ith row of the combined model equation.

$I^m(t) = yeq\_realV(t) - beq\_real + \eta$,

Virtual measurements – The model of this measurement type is ith row of the combined model equation

$0 = yeq\_real \times x(t) - beq\_real + \eta$.

The virtual measurement can be divided in two groups;

(a) Internal measurement of lines

The internal measurement model can be obtained by selecting proper i^{th} row of the line model equation.

(b) Internal measurement of transformers

The internal measurement model can be obtained by selecting proper i^{th} row of the transformer model equation.

(c) Current summation measurement at each node (KCL measurement)

For a composite node that two or more devices are connected, the virtual measurement model is obtained by application of the connectivity constraints among component objects. For electrical circuits, the connectivity constraints are obtained by applying Kirchoff's current law at each node of the system. For example, the row of virtual measurement model that represents the first transformer connection node is obtained by summing the i^{th} row of the combined model equation of the connected single device, line one, line two, and transformer one as shown in Figure 55.

Appendix H Microgrid States Definition

The states of the microgrid depicted in Figure 39 are illustrated in this appendix. The microgrid is composed three multi phase cable models. For the microgrid, states of the model are composed of 24 external states (12 external states for time t and 12 external states for t_m) and 32 internal states (16 internal states for time t and 16 internal states for time t_m). The total number of states is 56.

The external states, the internal states, and currents are illustrated in Figure 56.

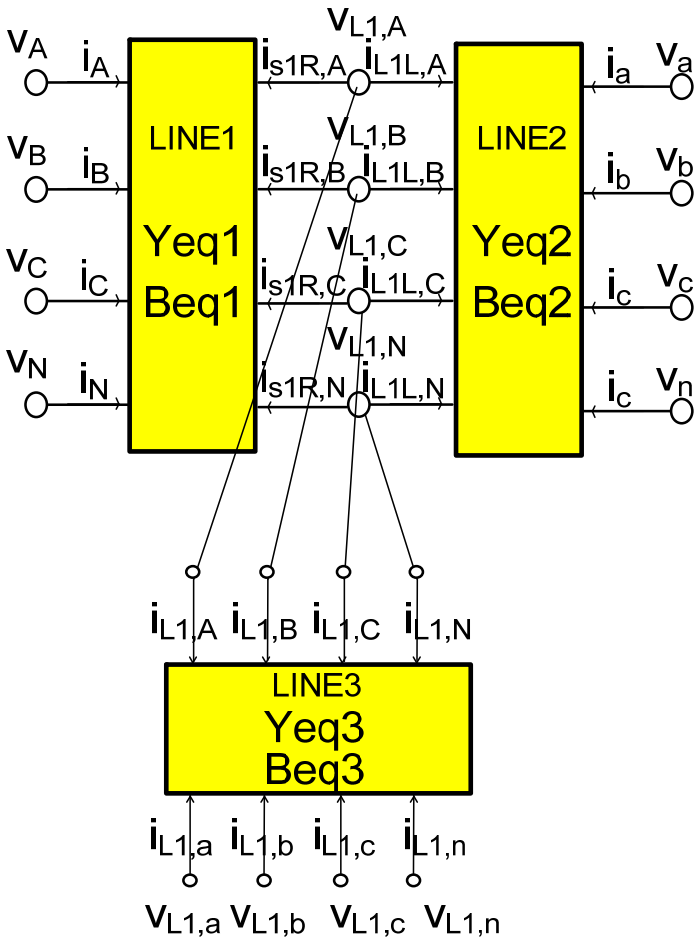

Figure 56: The microgrid circuit model representation including states, and currents.

For time t, the states are listed in Table 6. For time t_m, the states are the same.

Table 6: States for three-phase microgrid at time t and t_m.

State	type
v_A	External State
v_B	External State
v_C	External State
v_N	External State
v_a	External State
v_b	External State
v_c	External State
v_n	External State
$v_{L1,a}$	External State
$v_{L1,b}$	External State
$v_{L1,c}$	External State
$v_{L1,n}$	External State
$i_{W1,A}$	Internal State
$i_{W1,B}$	Internal State
$i_{W1,C}$	Internal State
$i_{W1,N}$	Internal State
$i_{W2,A}$	Internal State
$i_{W2,B}$	Internal State
$i_{W2,C}$	Internal State
$i_{W2,N}$	Internal State
$i_{W3,A}$	Internal State
$i_{W3,B}$	Internal State
$i_{W3,C}$	Internal State
$i_{W3,N}$	Internal State
$v_{L1,A}$	Internal State
$v_{L1,B}$	Internal State

$v_{L1,C}$	Internal State
$v_{L1,N}$	Internal State

The states are defined as follows:

$$x(t) = \begin{bmatrix} V(t) \\ v_a(t) \end{bmatrix},\ x(t_m) = \begin{bmatrix} V(t_m) \\ v_a(t_m) \end{bmatrix},$$

where $V(t)$ and $V(t_m)$ are external states, and $v_a(t)$ and $v_a(t_m)$ are internal states as defined above.

Appendix I Microgrid Measurement Data Definition for the Computer Simulation – Grid-connected Operation

The measurement data of the microgrid depicted in Figure 39 are defined in this appendix. Note that in the actual implementation data will not be coming from the COMTRADE but rather streaming from the data acquisition system. The COMTRADE file is used for offline events simulation and offline DSE-based protection analytics. The measurement number should be changed depending on the number of terminals and load connections. Generally, the number of actual measurement at time t and t_m is determined by 2*(3*(number of terminals) + 3*(number of loads)). For this case, two terminals and one load connections are combined. The number of virtual measurement and pseudo measurement at time t and t_m is dependent on the line AQCF model. For the computer simulation, the following actual measurements of the microgrid could be obtained from the COMTRADE file.

Actual across measurements – nine voltage measurements at time t and nine voltage measurements at time t_m = (t-h+t)/2 (phase A-N, phase B-N, phase C-N, phase a-n, phase b-n, and phase c-n, phase L1a-N, phase L1b-N, and phase L1c-N). For these measurements assume a measurement error with standard deviation equal to 0.05 p.u.

The model of this measurement type is as follows:

$$V^m(t) = v_i(t) - v_n(t) + \eta \ ,$$

where $V^m(t)$ are the measurement values.

Actual through measurements – nine current measurements at time t and nine current measurements at time t_m = (t-h+t)/2 (phase A, phase B, phase C, phase a, phase b, phase c, phase L1a, phase L1b, and phase L1c). For these measurements assume a measurement error with standard deviation equal to 0.01 p.u.

The model of this measurement type is i^{th} row of the combined model equation as follows:

$$I^m(t) = yeq\_real \times x(t) - beq\_real + \eta,$$

where $I^m(t)$ are the measurement values and i^{th} row are selected as explained in Appendix M.

Virtual measurements – eight virtual measurements at time t and eight virtual measurements at time $t_m=(t-h+t)/2$. The virtual measurements can be classified into two groups as follows: (a) Internal measurements of lines (four at time t) and (b) Summation of current at each connection (KCL measurement, four at time t). The summation of current at each connection is zero according to the KCL. For these measurements, assume a measurement error with standard deviation equal to 0.01 p.u.

The model of this measurement type is i^{th} row of the combined model equation as follows:

$$0 = yeq\_real \times x(t) - beq\_real + \eta.$$

where i^{th} row are selected as explained in Appendix M.

Pseudo measurements – six pseudo measurements at time t and six pseudo measurements at time $t_m=(t-h+t)/2$ (voltage N, voltage n, voltage L1n, current N, current n, current L1n). These measurements represent quantities that have a certain value with a relatively large measurement error; in this case normally not measured, such as current in

the neutral, or voltage at the neutral. For these measurements, assume a measurement error with standard deviation equal to 0.01 p.u.

The pseudo measurements of the microgrid model can be divided into two groups as follows:

(a) Three across neutral voltage measurements as follows:

$$0 = v_n(t) + \eta .$$

(b) Three through neutral current measurements as follows:

i^{th} row of the combined model equation

$$0 = yeq\_real \times x(t) - beq\_real + \eta .$$

In summary, the measurement data for the three-phase microgrid are composed of 36 actual measurements, 16 virtual measurements, 12 pseudo measurements, and the total numbers of measurement data are 64. Since the number of states are 56, the degree of freedom, v, is = m-n=64-56=8. It will provide a redundancy of 14.28 % (= (64-56)/56*100). The measurements are listed in Table 7.

Table 7: Measurements for three-phase microgrid during the grid-connected operation for the computer simulation.

Type	Name	Measurement Model	Standard Deviation
Across	voltage_AN	$z_1 = v_A(t) - v_N(t)$	0.05(p.u.)*Vrating
Across	voltage_BN	$z_2 = v_B(t) - v_N(t)$	0.05(p.u.)*Vrating
Across	voltage_CN	$z_3 = v_C(t) - v_N(t)$	0.05(p.u.)*Vrating
Pseudo	voltage_N	$z_4 = 0 = v_N(t)$	0.01(p.u.) *Vrating
Across	voltage_an	$z_5 = v_a(t) - v_n(t)$	0.05(p.u.)*Vrating
Across	voltage_bn	$z_6 = v_b(t) - v_n(t)$	0.05(p.u.)*Vrating

Across	voltage_cn	$z_7 = v_c(t) - v_n(t)$	0.05(p.u.)*Vrating
Pseudo	voltage_n	$z_8 = 0 = v_n(t)$	0.01(p.u.) *Vrating
Across	voltage_ANm	$z_9 = v_A(t_m) - v_N(t_m)$	0.05(p.u.)*Vrating
Across	voltage_BNm	$z_{10} = v_B(t_m) - v_N(t_m)$	0.05(p.u.)*Vrating
Across	voltage_CNm	$z_{11} = v_C(t_m) - v_N(t_m)$	0.05(p.u.)*Vrating
Pseudo	voltage_Nm	$z_{12} = 0 = v_N(t_m)$	0.01(p.u.) *Vrating
Across	voltage_anm	$z_{13} = v_a(t_m) - v_n(t_m)$	0.05(p.u.)*Vrating
Across	voltage_bnm	$z_{14} = v_b(t_m) - v_n(t_m)$	0.05(p.u.)*Vrating
Across	voltage_cnm	$z_{15} = v_c(t_m) - v_n(t_m)$	0.05(p.u.)*Vrating
Pseudo	voltage_nm	$z_{16} = 0 = v_n(t_m)$	0.01(p.u.) *Vrating
Across	voltage_L1an	$z_{17} = v_{L1a}(t) - v_{L1n}(t)$	0.05(p.u.)*Vrating
Across	voltage_L1bn	$z_{18} = v_{L1b}(t) - v_{L1n}(t)$	0.05(p.u.)*Vrating
Across	voltage_L1cn	$z_{19} = v_{L1c}(t) - v_{L1n}(t)$	0.05(p.u.)*Vrating
Pseudo	voltage_L1n	$z_{20} = 0 = v_{L1n}(t)$	0.01(p.u.) *Vrating
Across	voltage_L1anm	$z_{21} = v_{L1a}(t_m) - v_{L1n}(t_m)$	0.05(p.u.)*Vrating
Across	voltage_L1bnm	$z_{22} = v_{L1b}(t_m) - v_{L1n}(t_m)$	0.05(p.u.)*Vrating
Across	voltage_L1cnm	$z_{23} = v_{L1c}(t_m) - v_{L1n}(t_m)$	0.05(p.u.)*Vrating
Pseudo	voltage_L1nm	$z_{24} = 0 = v_{L1n}(t_m)$	0.01(p.u.) *Vrating
Through	current_A	$z_{25} = i_A(t) = yeq\_real \times x(t) - beq\_real + \eta$	0.01(p.u.)*Irating
Through	current_B	$z_{26} = i_B(t) = yeq\_real \times x(t) - beq\_real + \eta$	0.01(p.u.)*Irating
Through	current_C	$z_{27} = i_C(t) = yeq\_real \times x(t) - beq\_real + \eta$	0.01(p.u.)*Irating
Pseudo	current_N	$z_{28} = 0 = yeq\_real \times x(t) - beq\_real + \eta$	0.01(p.u.) *Irating
Through	current_a	$z_{29} = i_a(t) = yeq\_real \times x(t) - beq\_real + \eta$	0.01(p.u.)*Irating
Through	current_b	$z_{30} = i_b(t) = yeq\_real \times x(t) - beq\_real + \eta$	0.01(p.u.)*Irating
Through	current_c	$z_{31} = i_c(t) = yeq\_real \times x(t) - beq\_real + \eta$	0.01(p.u.)*Irating
Pseudo	current_n	$z_{32} = 0 = yeq\_real \times x(t) - beq\_real + \eta$	0.01(p.u.) *Irating
Through	current_Am	$z_{33} = i_A(t_m) = yeq\_real \times x(t_m) - beq\_real + \eta$	0.01(p.u.)*Irating
Through	current_Bm	$z_{34} = i_B(t_m) = yeq\_real \times x(t_m) - beq\_real + \eta$	0.01(p.u.)*Irating
Through	current_Cm	$z_{35} = i_C(t_m) = yeq\_real \times x(t_m) - beq\_real + \eta$	0.01(p.u.)*Irating
Pseudo	current_Nm	$z_{36} = 0 = yeq\_real \times x(t_m) - beq\_real + \eta$	0.01(p.u.) *Irating

Through	current_am	$z_{37} = i_a(t_m) = yeq\_real \times x(t_m) - beq\_real + \eta$	0.01(p.u.)*Irating
Through	current_bm	$z_{38} = i_b(t_m) = yeq\_real \times x(t_m) - beq\_real + \eta$	0.01(p.u.)*Irating
Through	current_cm	$z_{39} = i_c(t_m) = yeq\_real \times x(t_m) - beq\_real + \eta$	0.01(p.u.)*Irating
Pseudo	current_nm	$z_{40} = 0 = yeq\_real \times x(t_m) - beq\_real + \eta$	0.01(p.u.) *Irating
Through	current_L1a	$z_{41} = i_{L1,a}(t) = yeq\_real \times x(t) - beq\_real + \eta$	0.01(p.u.)*Irating
Through	current_L1b	$z_{42} = i_{L1,b}(t) = yeq\_real \times x(t) - beq\_real + \eta$	0.01(p.u.)*Irating
Through	current_L1c	$z_{43} = i_{L1,c}(t) = yeq\_real \times x(t) - beq\_real + \eta$	0.01(p.u.)*Irating
Through	current_L1n	$z_{44} = i_{L1,n}(t) = yeq\_real \times x(t) - beq\_real + \eta$	0.01(p.u.)*Irating
Through	current_L1am	$z_{45} = i_{L1,a}(t_m) = yeq\_real \times x(t_m) - beq\_real + \eta$	0.01(p.u.)*Irating
Through	current_L1bm	$z_{46} = i_{L1,b}(t_m) = yeq\_real \times x(t_m) - beq\_real + \eta$	0.01(p.u.)*Irating
Through	current_L1cm	$z_{47} = i_{L1,c}(t_m) = yeq\_real \times x(t_m) - beq\_real + \eta$	0.01(p.u.)*Irating
Through	current_L1nm	$z_{48} = i_{L1,n}(t_m) = yeq\_real \times x(t_m) - beq\_real + \eta$	0.01(p.u.)*Irating
Virtual	0	$z_{49} \sim z_{56} = 0 = yeq\_real \times x(t) - beq\_real + \eta$	0.01(p.u.)*Irating
Virtual	0	$z_{57} \sim z_{64} = 0 = yeq\_real \times x(t_m) - beq\_real + \eta$	0.01(p.u.)*Irating

Appendix J Microgrid Measurement Data Definition for the Laboratory Test – Grid-connected Operation

For the laboratory test, since the Reason MU has three voltage inputs and three current inputs, the test system with nine voltage measurements and nine current measurements requires derived measurements. In this thesis, three actual voltage and current measurements (for time t and t_m) are obtained at bus "FEEDER1" and the derived voltage and current measurements (for time t and t_m) are computed for the bus "FEEDER2" and "M–LOAD". Basically, the derived measurements are obtained by calculating the ratio between the bus "FEEDER1" and "FEEDER2" or "FEEDER1" and "M–LOAD". Note that explanations about the duplicated measurements (actual measurements, virtual measurements, and pseudo measurements) are not repeated.

Derived across measurements for the laboratory test –Six voltage measurements at time t and six voltage measurements at time t_m = (t-h+t)/2 (phase a-n, phase b-n, and phase c-n, phase L1a-N, phase L1b-N, and phase L1c-N). For these measurements assume a measurement error with standard deviation equal to 0.05 p.u.

The model of this measurement type is as follows:

$$V^m(t) = v_i(t) - v_n(t) + \eta \ ,$$

where $V^m(t)$ are the measurement values.

Derived through measurements for the laboratory test – Six current measurements at time t and six current measurements at time t_m = (t-h+t)/2 (phase a, phase b, phase c,

phase L1a, phase L1b, and phase L1c). For these measurements assume a measurement error with standard deviation equal to 0.06 p.u.

The model of this measurement type is i^{th} row of the combined model equation as explained in Appendix M:

$$I^m(t) = yeq\_real \times x(t) - beq\_real + \eta,$$

where $I^m(t)$ are the measurement values.

Table 8: Measurements for three-phase microgrid during the grid-connected operation for the laboratory test.

Type	Name	Measurement Model	Standard Deviation
Across	voltage_AN	$z_1 = v_A(t) - v_N(t)$	0.05(p.u.)*Vrating
Across	voltage_BN	$z_2 = v_B(t) - v_N(t)$	0.05(p.u.)*Vrating
Across	voltage_CN	$z_3 = v_C(t) - v_N(t)$	0.05(p.u.)*Vrating
Pseudo	voltage_N	$z_4 = 0 = v_N(t)$	0.05(p.u.) *Vrating
Derived	voltage_an	$z_5 = v_a(t) - v_n(t)$	0.07(p.u.)*Vrating
Derived	voltage_bn	$z_6 = v_b(t) - v_n(t)$	0.07(p.u.)*Vrating
Derived	voltage_cn	$z_7 = v_c(t) - v_n(t)$	0.07(p.u.)*Vrating
Pseudo	voltage_n	$z_8 = 0 = v_n(t)$	0.05(p.u.)*Vrating
Across	voltage_ANm	$z_9 = v_A(t_m) - v_N(t_m)$	0.05(p.u.)*Vrating
Across	voltage_BNm	$z_{10} = v_B(t_m) - v_N(t_m)$	0.05(p.u.)*Vrating
Across	voltage_CNm	$z_{11} = v_C(t_m) - v_N(t_m)$	0.05(p.u.)*Vrating
Pseudo	voltage_Nm	$z_{12} = 0 = v_N(t_m)$	0.05(p.u.) *Vrating
Derived	voltage_anm	$z_{13} = v_a(t_m) - v_n(t_m)$	0.07(p.u.)*Vrating
Derived	voltage_bnm	$z_{14} = v_b(t_m) - v_n(t_m)$	0.07(p.u.)*Vrating
Derived	voltage_cnm	$z_{15} = v_c(t_m) - v_n(t_m)$	0.07(p.u.)*Vrating
Pseudo	voltage_nm	$z_{16} = 0 = v_n(t_m)$	0.05(p.u.)*Vrating
Derived	voltage_L1an	$z_{17} = v_{L1a}(t) - v_{L1n}(t)$	0.07(p.u.)*Vrating

Derived	voltage_L1bn	$z_{18} = v_{L1b}(t) - v_{L1n}(t)$	0.07(p.u.)*Vrating
Derived	voltage_L1cn	$z_{19} = v_{L1c}(t) - v_{L1n}(t)$	0.07(p.u.)*Vrating
Pseudo	voltage_L1n	$z_{20} = 0 = v_{L1n}(t)$	0.05(p.u.)*Vrating
Derived	voltage_L1anm	$z_{21} = v_{L1a}(t_m) - v_{L1n}(t_m)$	0.07(p.u.)*Vrating
Derived	voltage_L1bnm	$z_{22} = v_{L1b}(t_m) - v_{L1n}(t_m)$	0.07(p.u.)*Vrating
Derived	voltage_L1cnm	$z_{23} = v_{L1c}(t_m) - v_{L1n}(t_m)$	0.07(p.u.)*Vrating
Pseudo	voltage_L1nm	$z_{24} = 0 = v_{L1n}(t_m)$	0.05(p.u.)*Vrating
Through	current_A	$z_{25} = i_A(t) = yeq\_real \times x(t) - beq\_real + \eta$	0.06(p.u.)*Irating
Through	current_B	$z_{26} = i_B(t) = yeq\_real \times x(t) - beq\_real + \eta$	0.06(p.u.)*Irating
Through	current_C	$z_{27} = i_C(t) = yeq\_real \times x(t) - beq\_real + \eta$	0.06(p.u.)*Irating
Pseudo	current_N	$z_{28} = 0 = yeq\_real \times x(t) - beq\_real + \eta$	0.05(p.u.)*Irating
Derived	current_a	$z_{29} = i_a(t) = yeq\_real \times x(t) - beq\_real + \eta$	0.07(p.u.)*Irating
Derived	current_b	$z_{30} = i_b(t) = yeq\_real \times x(t) - beq\_real + \eta$	0.07(p.u.)*Irating
Derived	current_c	$z_{31} = i_c(t) = yeq\_real \times x(t) - beq\_real + \eta$	0.07(p.u.)*Irating
Pseudo	current_n	$z_{32} = 0 = yeq\_real \times x(t) - beq\_real + \eta$	0.05(p.u.)*Irating
Through	current_Am	$z_{33} = i_A(t_m) = yeq\_real \times x(t_m) - beq\_real + \eta$	0.06(p.u.)*Irating
Through	current_Bm	$z_{34} = i_B(t_m) = yeq\_real \times x(t_m) - beq\_real + \eta$	0.06(p.u.)*Irating
Through	current_Cm	$z_{35} = i_C(t_m) = yeq\_real \times x(t_m) - beq\_real + \eta$	0.06(p.u.)*Irating
Pseudo	current_Nm	$z_{36} = 0 = yeq\_real \times x(t_m) - beq\_real + \eta$	0.05(p.u.)*Irating
Derived	current_am	$z_{37} = i_a(t_m) = yeq\_real \times x(t_m) - beq\_real + \eta$	0.07(p.u.)*Irating
Derived	current_bm	$z_{38} = i_b(t_m) = yeq\_real \times x(t_m) - beq\_real + \eta$	0.07(p.u.)*Irating
Derived	current_cm	$z_{39} = i_c(t_m) = yeq\_real \times x(t_m) - beq\_real + \eta$	0.07(p.u.)*Irating
Pseudo	current_nm	$z_{40} = 0 = yeq\_real \times x(t_m) - beq\_real + \eta$	0.05(p.u.)*Irating
Derived	current_L1a	$z_{41} = i_{L1,a}(t) = yeq\_real \times x(t) - beq\_real + \eta$	0.07(p.u.)*Irating
Derived	current_L1b	$z_{42} = i_{L1,b}(t) = yeq\_real \times x(t) - beq\_real + \eta$	0.07(p.u.)*Irating
Derived	current_L1c	$z_{43} = i_{L1,c}(t) = yeq\_real \times x(t) - beq\_real + \eta$	0.07(p.u.)*Irating
Pseudo	current_L1n	$z_{44} = 0 = yeq\_real \times x(t) - beq\_real + \eta$	0.05(p.u.)*Irating
Derived	current_L1am	$z_{45} = i_{L1,a}(t_m) = yeq\_real \times x(t_m) - beq\_real + \eta$	0.07(p.u.)*Irating
Derived	current_L1bm	$z_{46} = i_{L1,b}(t_m) = yeq\_real \times x(t_m) - beq\_real + \eta$	0.07(p.u.)*Irating

Derived	current_L1cm	$z_{47} = i_{L1,c}(t_m) = yeq\_real \times x(t_m) - beq\_real + \eta$	0.07(p.u.)*Irating
Pseudo	current_L1nm	$z_{48} = 0 = yeq\_real \times x(t) - beq\_real + \eta$	0.05(p.u.)*Irating
Virtual	0	$z_{49} \sim z_{75} = 0 = yeq\_real \times x(t) - beq\_real + \eta$	0.05(p.u.)*Irating
Virtual	0	$z_{76} \sim z_{102} = 0 = yeq\_real \times x(t_m) - beq\_real + \eta$	0.05(p.u.)*Irating

Appendix K Microgrid Measurement Data Definition for the Computer Simulation – Island Operation

Note that explanations about the duplicated measurements (actual measurements, derived measurements, virtual measurements, and pseudo measurements) are not repeated. The only difference between the island operation and the grid connected mode operation is the selected standard deviation values. The measurements are listed in

Table 9.

Table 9: Measurements for three-phase microgrid during the island operation for the computer simulation.

Type	Name	Measurement Model	Standard Deviation
Across	voltage_AN	$z_{50} = v_A(t) - v_N(t)$	0.02(p.u.)*Vrating
Across	voltage_BN	$z_{51} = v_B(t) - v_N(t)$	0.02(p.u.)*Vrating
Across	voltage_CN	$z_{52} = v_C(t) - v_N(t)$	0.02(p.u.)*Vrating
Pseudo	voltage_N	$z_{53} = 0 = v_N(t)$	0.07(p.u.) *Vrating
Across	voltage_an	$z_{54} = v_a(t) - v_n(t)$	0.02(p.u.)*Vrating
Across	voltage_bn	$z_{55} = v_b(t) - v_n(t)$	0.02(p.u.)*Vrating
Across	voltage_cn	$z_{56} = v_c(t) - v_n(t)$	0.02(p.u.)*Vrating
Pseudo	voltage_n	$z_{57} = 0 = v_n(t)$	0.07(p.u.) *Vrating
Across	voltage_ANm	$z_{58} = v_A(t_m) - v_N(t_m)$	0.02(p.u.)*Vrating
Across	voltage_BNm	$z_{59} = v_B(t_m) - v_N(t_m)$	0.02(p.u.)*Vrating
Across	voltage_CNm	$z_{60} = v_C(t_m) - v_N(t_m)$	0.02(p.u.)*Vrating
Pseudo	voltage_Nm	$z_{61} = 0 = v_N(t_m)$	0.07(p.u.) *Vrating
Across	voltage_anm	$z_{62} = v_a(t_m) - v_n(t_m)$	0.02(p.u.)*Vrating
Across	voltage_bnm	$z_{63} = v_b(t_m) - v_n(t_m)$	0.02(p.u.)*Vrating
Across	voltage_cnm	$z_{64} = v_c(t_m) - v_n(t_m)$	0.02(p.u.)*Vrating
Pseudo	voltage_nm	$z_{65} = 0 = v_n(t_m)$	0.07(p.u.) *Vrating
Across	voltage_L1an	$z_{66} = v_{L1a}(t) - v_{L1n}(t)$	0.02(p.u.)*Vrating

Across	voltage_L1bn	$z_{67} = v_{L1b}(t) - v_{L1n}(t)$	0.02(p.u.)*Vrating
Across	voltage_L1cn	$z_{68} = v_{L1c}(t) - v_{L1n}(t)$	0.02(p.u.)*Vrating
Pseudo	voltage_L1n	$z_{69} = 0 = v_{L1n}(t)$	0.07(p.u.) *Vrating
Across	voltage_L1anm	$z_{70} = v_{L1a}(t_m) - v_{L1n}(t_m)$	0.02(p.u.)*Vrating
Across	voltage_L1bnm	$z_{71} = v_{L1b}(t_m) - v_{L1n}(t_m)$	0.02(p.u.)*Vrating
Across	voltage_L1cnm	$z_{72} = v_{L1c}(t_m) - v_{L1n}(t_m)$	0.02(p.u.)*Vrating
Pseudo	voltage_L1nm	$z_{73} = 0 = v_{L1n}(t_m)$	0.07(p.u.) *Vrating
Through	current_A	$z_{74} = i_A(t) = yeq\_real \times x(t) - beq\_real + \eta$	0.008(p.u.)*Irating
Through	current_B	$z_{75} = i_B(t) = yeq\_real \times x(t) - beq\_real + \eta$	0.008(p.u.)*Irating
Through	current_C	$z_{76} = i_C(t) = yeq\_real \times x(t) - beq\_real + \eta$	0.008(p.u.)*Irating
Pseudo	current_N	$z_{77} = 0 = yeq\_real \times x(t) - beq\_real + \eta$	0.07(p.u.) *Irating
Through	current_a	$z_{78} = i_a(t) = yeq\_real \times x(t) - beq\_real + \eta$	0.008(p.u.)*Irating
Through	current_b	$z_{79} = i_b(t) = yeq\_real \times x(t) - beq\_real + \eta$	0.008(p.u.)*Irating
Through	current_c	$z_{80} = i_c(t) = yeq\_real \times x(t) - beq\_real + \eta$	0.008(p.u.)*Irating
Pseudo	current_n	$z_{81} = 0 = yeq\_real \times x(t) - beq\_real + \eta$	0.07(p.u.) *Irating
Through	current_Am	$z_{82} = i_A(t_m) = yeq\_real \times x(t_m) - beq\_real + \eta$	0.008(p.u.)*Irating
Through	current_Bm	$z_{83} = i_B(t_m) = yeq\_real \times x(t_m) - beq\_real + \eta$	0.008(p.u.)*Irating
Through	current_Cm	$z_{84} = i_C(t_m) = yeq\_real \times x(t_m) - beq\_real + \eta$	0.008(p.u.)*Irating
Pseudo	current_Nm	$z_{85} = 0 = yeq\_real \times x(t_m) - beq\_real + \eta$	0.07(p.u.) *Irating
Through	current_am	$z_{86} = i_a(t_m) = yeq\_real \times x(t_m) - beq\_real + \eta$	0.008(p.u.)*Irating
Through	current_bm	$z_{87} = i_b(t_m) = yeq\_real \times x(t_m) - beq\_real + \eta$	0.008(p.u.)*Irating
Through	current_cm	$z_{88} = i_c(t_m) = yeq\_real \times x(t_m) - beq\_real + \eta$	0.008(p.u.)*Irating
Pseudo	current_nm	$z_{89} = 0 = yeq\_real \times x(t_m) - beq\_real + \eta$	0.07(p.u.) *Irating
Through	current_L1a	$z_{90} = i_{L1,a}(t) = yeq\_real \times x(t) - beq\_real + \eta$	0.008(p.u.)*Irating
Through	current_L1b	$z_{91} = i_{L1,b}(t) = yeq\_real \times x(t) - beq\_real + \eta$	0.008(p.u.)*Irating
Through	current_L1c	$z_{92} = i_{L1,c}(t) = yeq\_real \times x(t) - beq\_real + \eta$	0.008(p.u.)*Irating
Through	current_L1n	$z_{93} = i_{L1,n}(t) = yeq\_real \times x(t) - beq\_real + \eta$	0.008(p.u.)*Irating
Through	current_L1am	$z_{94} = i_{L1,a}(t_m) = yeq\_real \times x(t_m) - beq\_real + \eta$	0.008(p.u.)*Irating
Through	current_L1bm	$z_{95} = i_{L1,b}(t_m) = yeq\_real \times x(t_m) - beq\_real + \eta$	0.008(p.u.)*Irating
Through	current_L1cm	$z_{96} = i_{L1,c}(t_m) = yeq\_real \times x(t_m) - beq\_real + \eta$	0.008(p.u.)*Irating

Through	current_L1nm	$z_{97} = i_{L1\_n}(t_m) = yeq\_real \times x(t_m) - beq\_real + \eta$	0.008(p.u.)*Irating
Virtual	0	$z_{98} \sim z_{56} = 0 = yeq\_real \times x(t) - beq\_real + \eta$	0.07(p.u.)*Irating
Virtual	0	$z_{57} \sim z_{64} = 0 = yeq\_real \times x(t_m) - beq\_real + \eta$	0.07(p.u.)*Irating

Appendix L Microgrid Measurement Data Definition for the Laboratory Test – Island Operation

Note that explanations about the duplicated measurements (actual measurements, derived measurements, virtual measurements, and pseudo measurements) are not repeated. The only difference between the island operation and the grid connected mode operation is the selected standard deviation values. The measurements are listed in Table 10.

Table 10: Measurements for three-phase microgrid during the island operation for the laboratory test.

Type	Name	Measurement Model	Standard Deviation
Across	voltage_AN	$z_{50} = v_A(t) - v_N(t)$	0.05(p.u.)*Vrating
Across	voltage_BN	$z_{51} = v_B(t) - v_N(t)$	0.05(p.u.)*Vrating
Across	voltage_CN	$z_{52} = v_C(t) - v_N(t)$	0.05(p.u.)*Vrating
Pseudo	voltage_N	$z_{53} = 0 = v_N(t)$	0.01(p.u.) *Vrating
Derived	voltage_an	$z_{54} = v_a(t) - v_n(t)$	0.08(p.u.)*Vrating
Derived	voltage_bn	$z_{55} = v_b(t) - v_n(t)$	0.08(p.u.)*Vrating
Derived	voltage_cn	$z_{56} = v_c(t) - v_n(t)$	0.08(p.u.)*Vrating
Pseudo	voltage_n	$z_{57} = 0 = v_n(t)$	0.01(p.u.)*Vrating
Across	voltage_ANm	$z_{58} = v_A(t_m) - v_N(t_m)$	0.05(p.u.)*Vrating
Across	voltage_BNm	$z_{59} = v_B(t_m) - v_N(t_m)$	0.05(p.u.)*Vrating
Across	voltage_CNm	$z_{60} = v_C(t_m) - v_N(t_m)$	0.05(p.u.)*Vrating
Pseudo	voltage_Nm	$z_{61} = 0 = v_N(t_m)$	0.01(p.u.) *Vrating
Derived	voltage_anm	$z_{62} = v_a(t_m) - v_n(t_m)$	0.08(p.u.)*Vrating
Derived	voltage_bnm	$z_{63} = v_b(t_m) - v_n(t_m)$	0.08(p.u.)*Vrating
Derived	voltage_cnm	$z_{64} = v_c(t_m) - v_n(t_m)$	0.08(p.u.)*Vrating
Pseudo	voltage_nm	$z_{65} = 0 = v_n(t_m)$	0.01(p.u.)*Vrating
Derived	voltage_L1an	$z_{66} = v_{L1a}(t) - v_{L1n}(t)$	0.08(p.u.)*Vrating
Derived	voltage_L1bn	$z_{67} = v_{L1b}(t) - v_{L1n}(t)$	0.08(p.u.)*Vrating
Derived	voltage_L1cn	$z_{68} = v_{L1c}(t) - v_{L1n}(t)$	0.08(p.u.)*Vrating

Pseudo	voltage_L1n	$z_{69} = 0 = v_{L1n}(t)$	0.01(p.u.)*Vrating
Derived	voltage_L1anm	$z_{70} = v_{L1a}(t_m) - v_{L1n}(t_m)$	0.08(p.u.)*Vrating
Derived	voltage_L1bnm	$z_{71} = v_{L1b}(t_m) - v_{L1n}(t_m)$	0.08(p.u.)*Vrating
Derived	voltage_L1cnm	$z_{72} = v_{L1c}(t_m) - v_{L1n}(t_m)$	0.08(p.u.)*Vrating
Pseudo	voltage_L1nm	$z_{73} = 0 = v_{L1n}(t_m)$	0.01(p.u.)*Vrating
Through	current_A	$z_{74} = i_A(t) = yeq\_real \times x(t) - beq\_real + \eta$	0.01(p.u.)*Irating
Through	current_B	$z_{75} = i_B(t) = yeq\_real \times x(t) - beq\_real + \eta$	0.01(p.u.)*Irating
Through	current_C	$z_{76} = i_C(t) = yeq\_real \times x(t) - beq\_real + \eta$	0.01(p.u.)*Irating
Pseudo	current_N	$z_{77} = 0 = yeq\_real \times x(t) - beq\_real + \eta$	0.01(p.u.)*Irating
Derived	current_a	$z_{78} = i_a(t) = yeq\_real \times x(t) - beq\_real + \eta$	0.07(p.u.)*Irating
Derived	current_b	$z_{79} = i_b(t) = yeq\_real \times x(t) - beq\_real + \eta$	0.07(p.u.)*Irating
Derived	current_c	$z_{80} = i_c(t) = yeq\_real \times x(t) - beq\_real + \eta$	0.07(p.u.)*Irating
Pseudo	current_n	$z_{81} = 0 = yeq\_real \times x(t) - beq\_real + \eta$	0.01(p.u.)*Irating
Through	current_Am	$z_{82} = i_A(t_m) = yeq\_real \times x(t_m) - beq\_real + \eta$	0.01(p.u.)*Irating
Through	current_Bm	$z_{83} = i_B(t_m) = yeq\_real \times x(t_m) - beq\_real + \eta$	0.01(p.u.)*Irating
Through	current_Cm	$z_{84} = i_C(t_m) = yeq\_real \times x(t_m) - beq\_real + \eta$	0.01(p.u.)*Irating
Pseudo	current_Nm	$z_{85} = 0 = yeq\_real \times x(t_m) - beq\_real + \eta$	0.01(p.u.)*Irating
Derived	current_am	$z_{86} = i_a(t_m) = yeq\_real \times x(t_m) - beq\_real + \eta$	0.07(p.u.)*Irating
Derived	current_bm	$z_{87} = i_b(t_m) = yeq\_real \times x(t_m) - beq\_real + \eta$	0.07(p.u.)*Irating
Derived	current_cm	$z_{88} = i_c(t_m) = yeq\_real \times x(t_m) - beq\_real + \eta$	0.07(p.u.)*Irating
Pseudo	current_nm	$z_{89} = 0 = yeq\_real \times x(t_m) - beq\_real + \eta$	0.01(p.u.)*Irating
Derived	current_L1a	$z_{90} = i_{L1,a}(t) = yeq\_real \times x(t) - beq\_real + \eta$	0.07(p.u.)*Irating
Derived	current_L1b	$z_{91} = i_{L1,b}(t) = yeq\_real \times x(t) - beq\_real + \eta$	0.07(p.u.)*Irating
Derived	current_L1c	$z_{92} = i_{L1,c}(t) = yeq\_real \times x(t) - beq\_real + \eta$	0.07(p.u.)*Irating
Pseudo	current_L1n	$z_{93} = 0 = yeq\_real \times x(t) - beq\_real + \eta$	0.01(p.u.)*Irating
Derived	current_L1am	$z_{94} = i_{L1,a}(t_m) = yeq\_real \times x(t_m) - beq\_real + \eta$	0.07(p.u.)*Irating
Derived	current_L1bm	$z_{95} = i_{L1,b}(t_m) = yeq\_real \times x(t_m) - beq\_real + \eta$	0.07(p.u.)*Irating
Derived	current_L1cm	$z_{96} = i_{L1,c}(t_m) = yeq\_real \times x(t_m) - beq\_real + \eta$	0.07(p.u.)*Irating
Pseudo	current_L1nm	$z_{97} = 0 = yeq\_real \times x(t) - beq\_real + \eta$	0.01(p.u.)*Irating
Virtual	0	$z_{98} \sim z_{75} = 0 = yeq\_real \times x(t) - beq\_real + \eta$	0.01(p.u.)*Irating
Virtual	0	$z_{76} \sim z_{102} = 0 = yeq\_real \times x(t_m) - beq\_real + \eta$	0.01(p.u.)*Irating

Appendix M Creation of Measurement Models - Microgrid

The creation of the mathematical models of the measurements for the microgrid depicted in Figure 39 is described in this appendix. For the microgrid, the multi phase cable model is combined. The derivation of the multi phase cable model is same as documented in Appendix B. Measurements are composed of actual, virtual, and pseudo measurements. Among them, actual measurement can be obtained from streaming data or saved COMTRADE data. For online protection scheme, streaming data is required. For this thesis, offline protection scheme is applied, so COMTRADE data are utilized. The relationship between measurement data and system states for time t can be obtained from the single device models and pointers as shown in Figure 57. Note that for time t_m, the same logic can be applied. The $Y_{eq,k,i}$ represents the i^{th} line of the admittance matrix of the k^{th} device, the x_k represents the states of the k^{th} device, and the $B_{eq,k,i}$ represents the i^{th} line of the past history value of the k^{th} device.

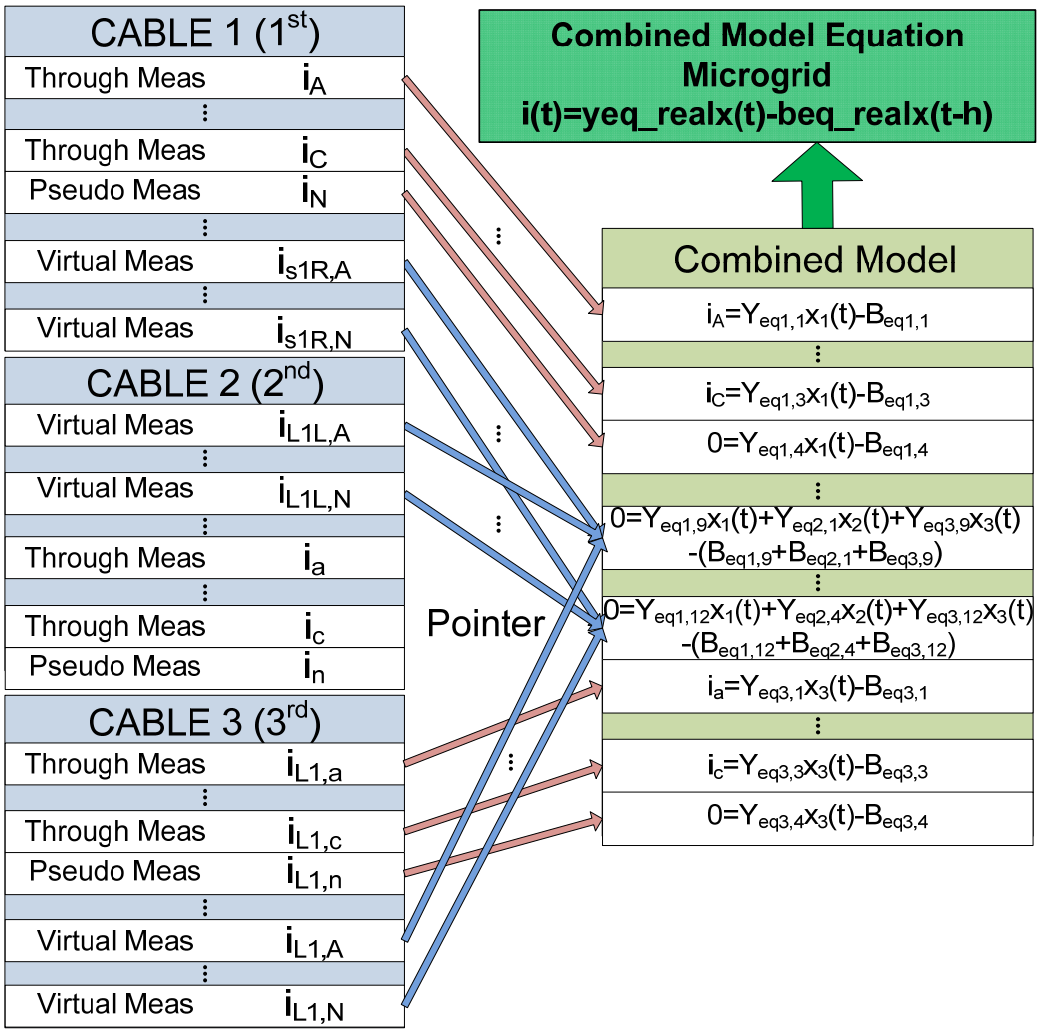

Figure 57: Measurement data and AQCF mapping using pointers – microgrid.

Actual across measurements – For actual across measurements, the model of this measurement type is as follows:

$$V^{m}(t) = v_i(t) - v_n(t) + \eta \,,$$

where $V^{m}(t)$ are the measurement values.

Actual through measurements – For actual through measurements, the model of this measurement type is i[th] row of the combined model equation as follows:

$$I^m(t) = yeq\_real \times x(t) - beq\_real + \eta ,$$

where $I^m(t)$ are the measurement values.

Derived across measurements – For derived across measurements, the model of this measurement type is as follows:

$$V^m(t) = v_i(t) - v_n(t) + \eta ,$$

where $V^m(t)$ are the derived measurement values.

Derived through measurements – For derived through measurements, the model of this measurement type is i[th] row of the combined model equation as follows:

$$I^m(t) = yeq\_real \times x(t) - beq\_real + \eta ,$$

where $I^m(t)$ are the derived measurement values.

Pseudo measurements – The pseudo measurements of the microgrid model can be divided into two groups as follows:

(a) Three across neutral voltage measurements as follows:

$$0 = v_n(t) + \eta .$$

(b) Three through neutral current measurements as follows:

i[th] row of the combined model equation.

$$I^m(t) = yeq\_realV(t) - beq\_real + \eta,$$

Virtual measurements – The model of this measurement type is ith row of the combined model equation:

$$0 = yeq\_real \times x(t) - beq\_real + \eta.$$

The internal measurement model can be obtained by selecting proper ith row of the multi phase cable model equation.

For a composite node that two or more devices are connected, the virtual measurement model is obtained by application of the connectivity constraints among component objects. For electrical circuits, the connectivity constraints are obtained by applying Kirchoff's current law at each node of the system. For example, the row of virtual measurement model that represents the first load node is obtained by summing the ith row of the combined model equation of the connected single devices, multi phase cable one, multi phase cable two, and multiphase cable three as shown in Figure 57.

Appendix N Results Graphs of the DSE-based Protection Scheme Simulation Results – Distribution System

The result graphs of the simulation of the fault condition on the distribution system are depicted in this appendix Figure 58 to Figure 74 as follows: a) confidence level, computation time, and residual, b) external states and some of internal states for time t and t_m, and c) measurement data, estimated measurement data, residual, and normalized residual of actual measurement, virtual measurement, and pseudo measurement data.

a) Confidence level, computation time, and residual for the internal fault case are depicted in Figure 58.

b) External states and some of internal states for time t and t_m are depicted in Figure 59. Internal states of the single section distribution line and the transformer is not explicitly shown in this appendix.

c) Measurement data, estimated measurement data, residual, and normalized residual of actual measurement, virtual measurement, and pseudo measurement data are illustrated in Figure 60 to Figure 74.

c1) Actual measurement data, estimated measurement data, residual, and normalized residual values for time t and t_m. are depicted in Figure 60 to Figure 65. In more detail, for time t and t_m, across measurement data and estimated measurement data at node RECA3R are compared each other as shown in Figure 60. Residual and normalized residual values are also depicted in the same figure. Result graphs of node RECA4L and TL-LOADA3 are depicted in Figure 61 to Figure 62. In addition, through measurement data and estimated measurement data at node RECA3R, RECA4L, and TL-LOADA3 are

compared each other, and the resulting residual and normalized residual values are shown in Figure 63 to Figure 65.

c2) Virtual measurement data, estimated measurement data, residual, and normalized residual values for time t and t_m are depicted in Figure 66 to Figure 71. In more detail, internal virtual measurement data and estimated measurement data of the first single section distribution line model for time t and t_m are compared each other, and the resulting residual and normalized residual values are shown in Figure 66. Result graphs of the second single section distribution line model and the transformer model are depicted in Figure 67 to Figure 70. Moreover, KCL virtual measurement data and estimated measurement data at node TH-LOADA3 for time t and t_m are compared each other, and the resulting residual and normalized residual values are shown in Figure 71.

c3) Pseudo measurement data, estimated measurement data, residual, and normalized residual values for time t and t_m are depicted in Figure 72 to Figure 74. In more detail, pseudo measurement data and estimated measurement data at node RECA3R, RECA4L, and TL-LOADA3 for time t and t_m are compared each other, and the resulting residual and normalized residual values are shown in Figure 72 to Figure 74.

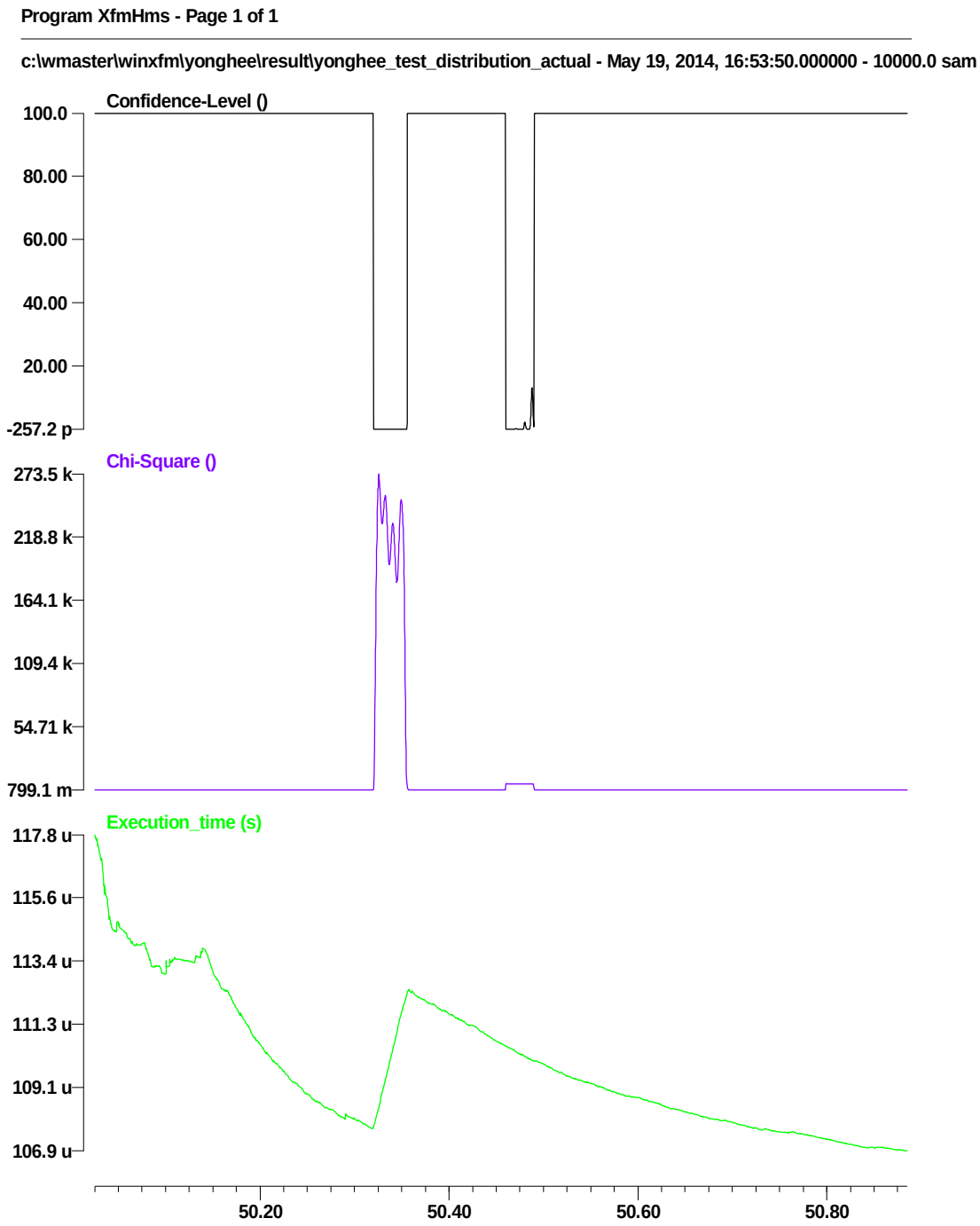

Figure 58: Confidence level, computation time, and residual for the internal fault case on the distribution system.

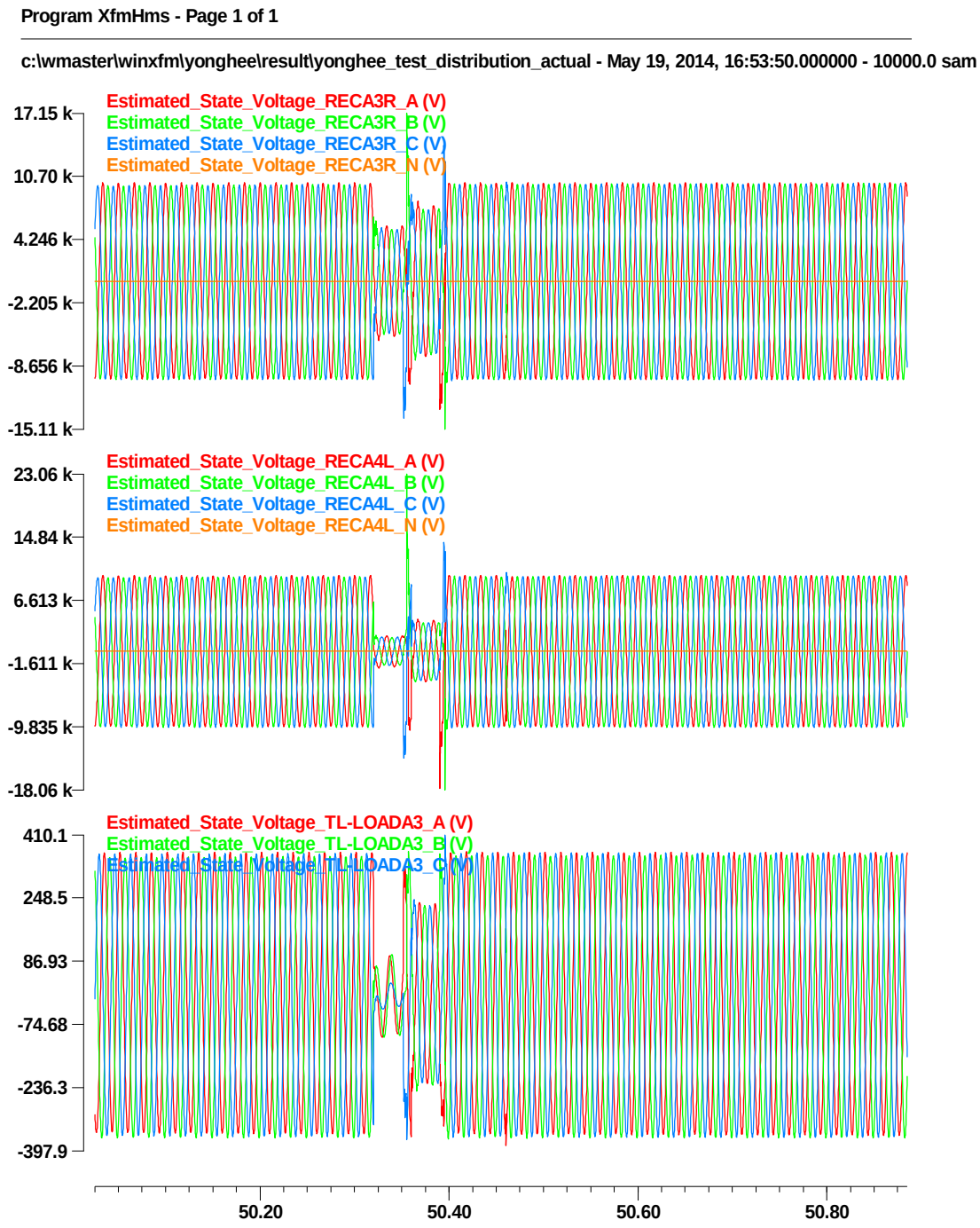

Figure 59: States at node RECA3R, TH-LOADA3, TL-LOADA3, and RECA4L.

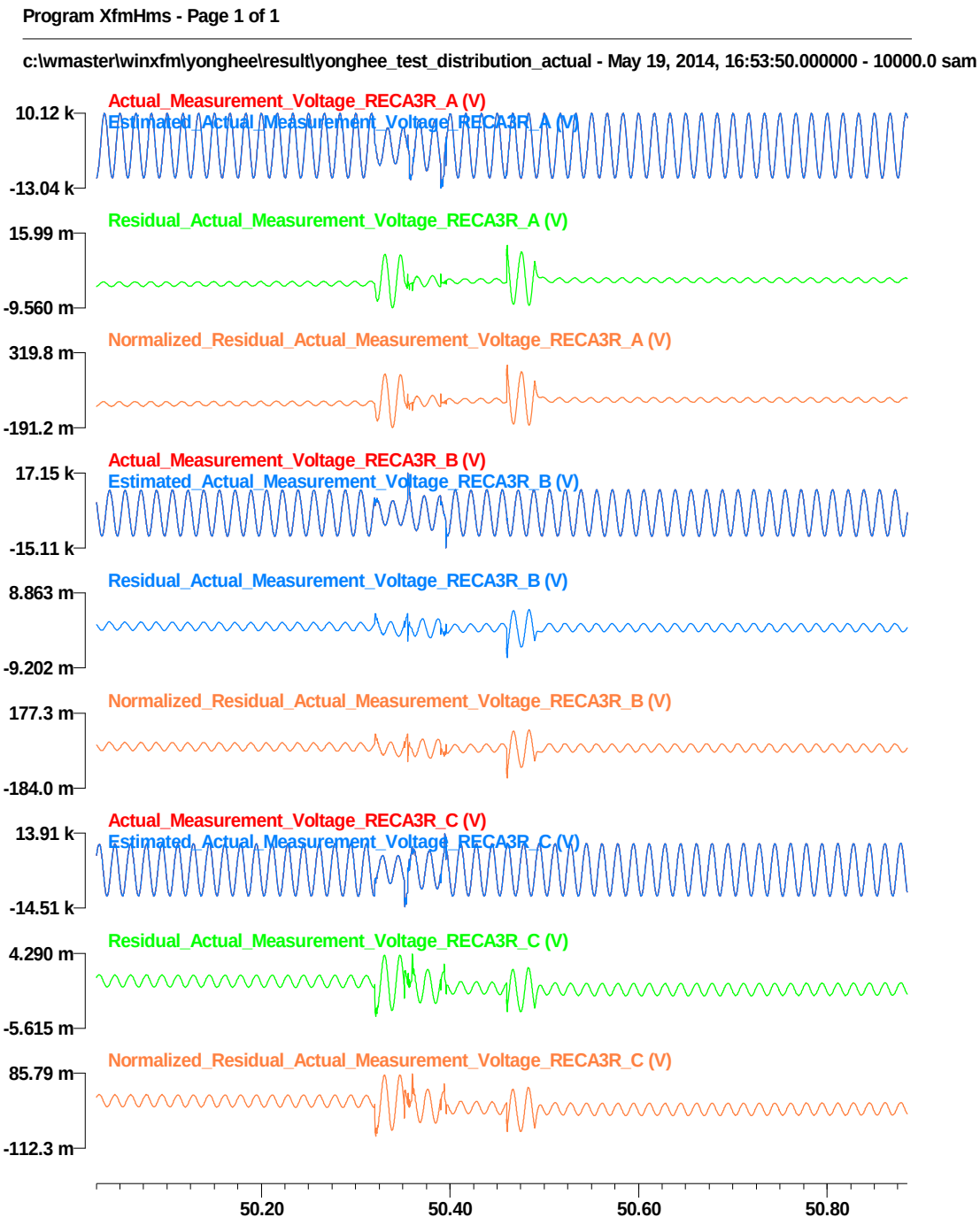

Figure 60: Actual across measurement data, estimated measurement data, residual, and normalized residual at node RECA3R.

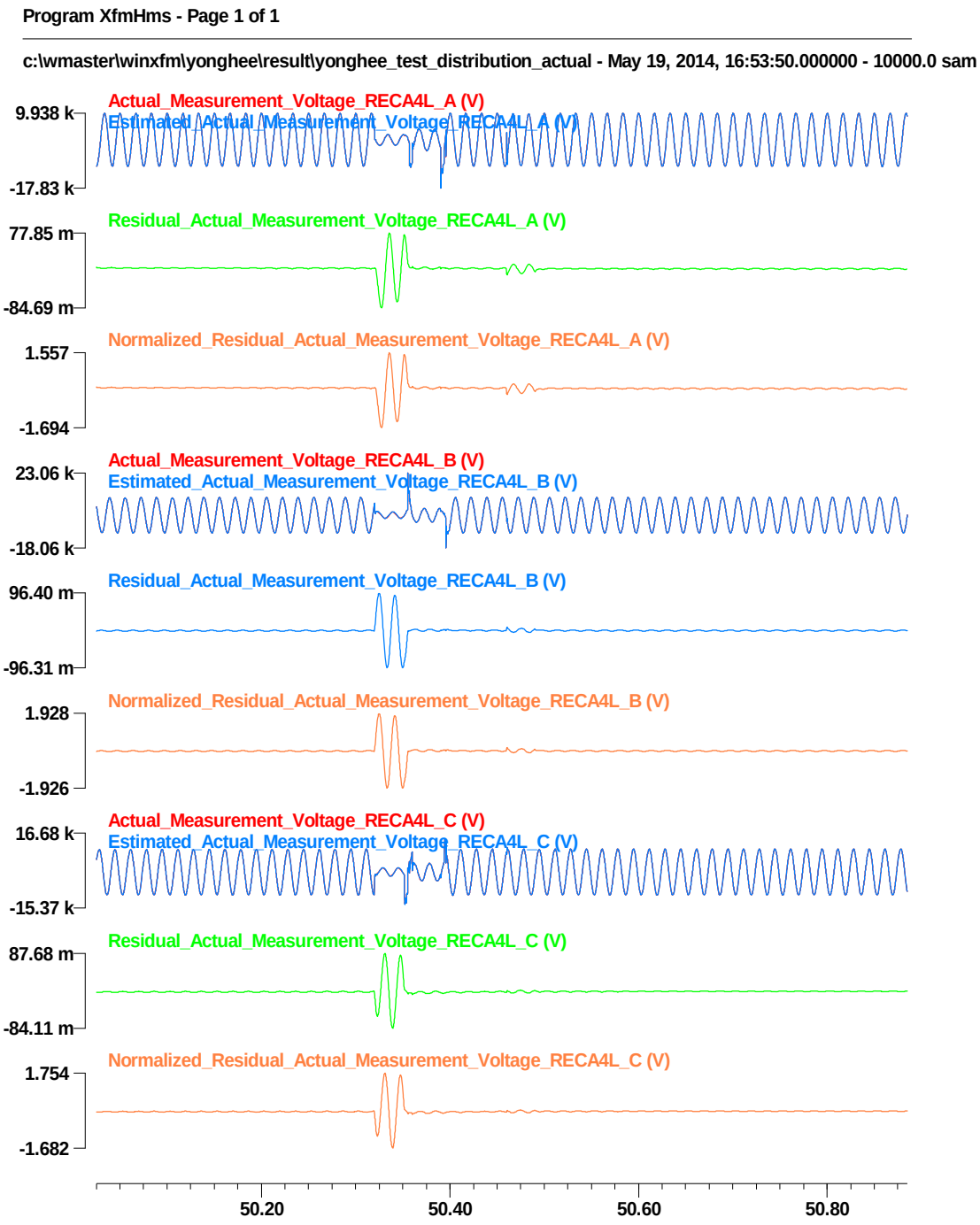

Figure 61: Actual across measurement data at time t, estimated measurement data, residual, and normalized residual at node RECA4L.

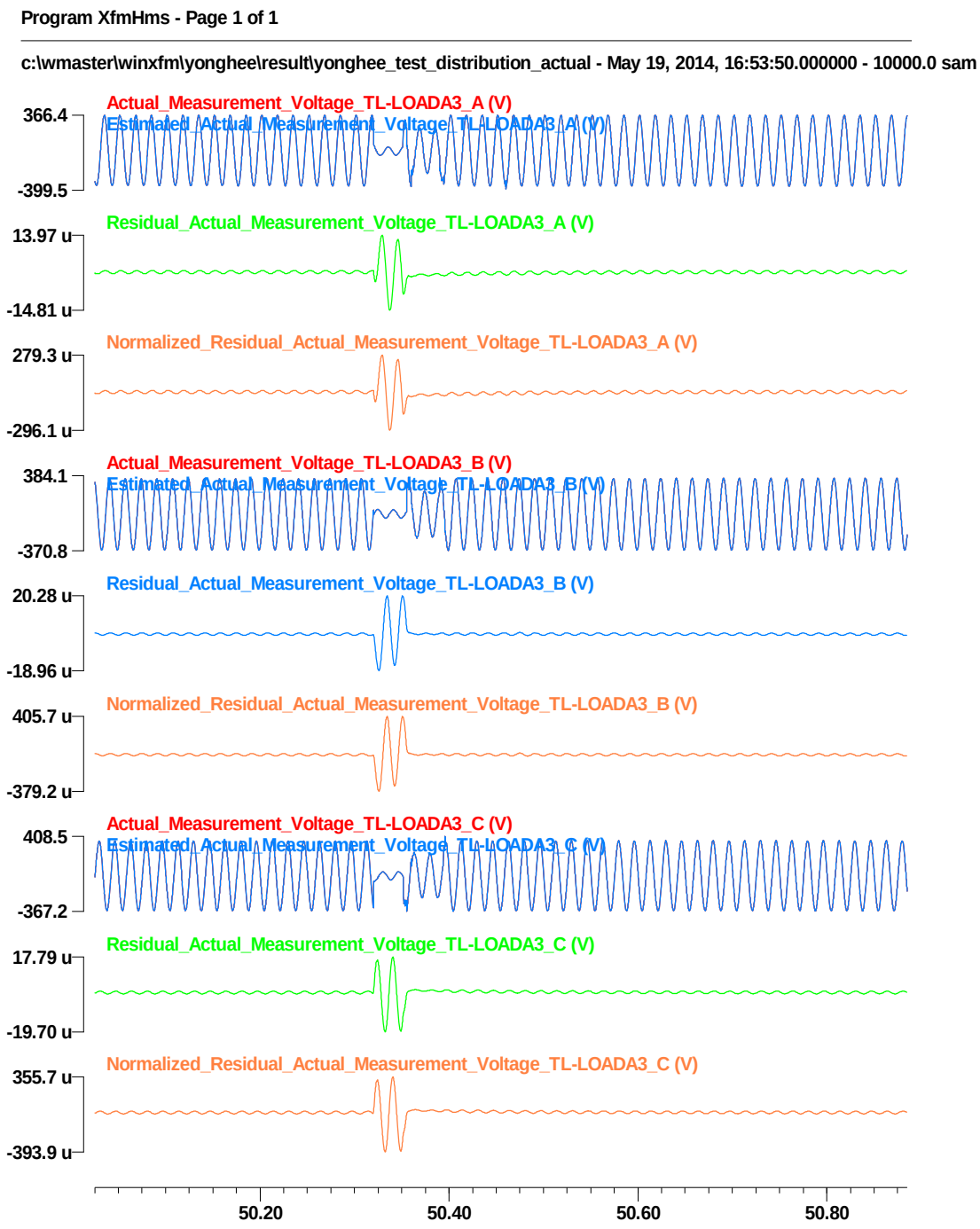

Figure 62: Actual across measurement data at time t, estimated measurement data, residual, and normalized residual at node TL-LOADA3.

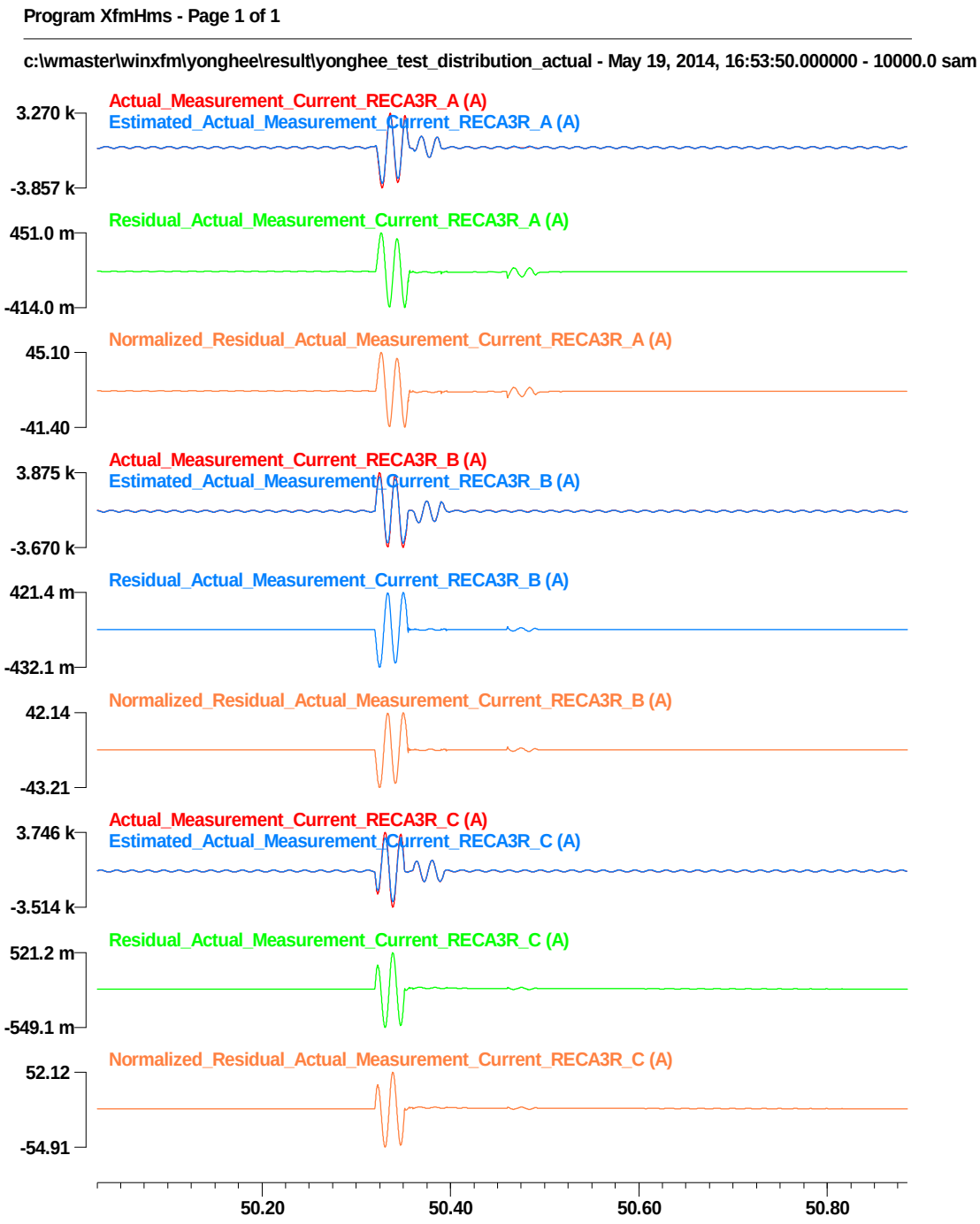

Figure 63: Actual through measurement data at time t, estimated measurement data, residual, and normalized residual at node RECA3R.

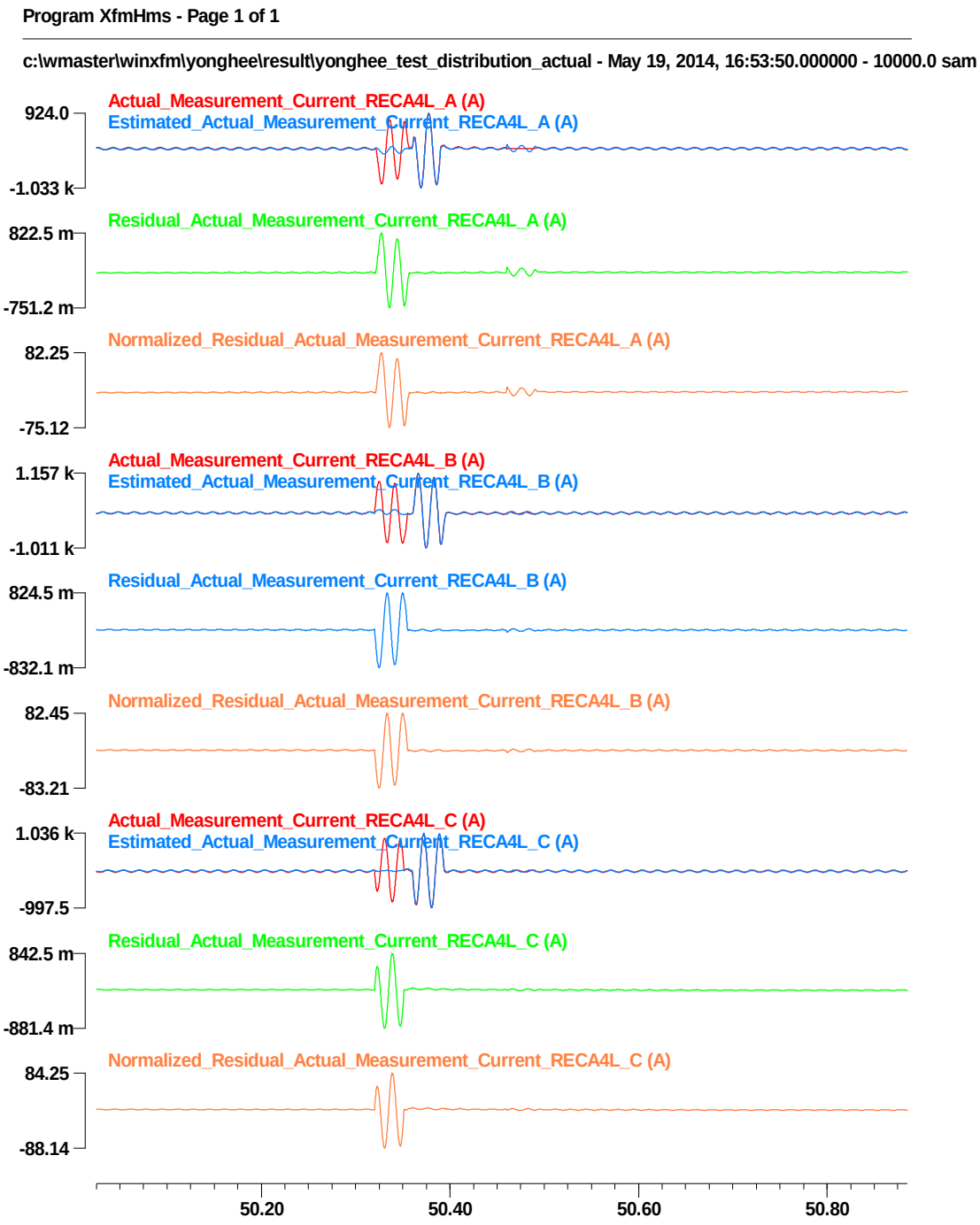

Figure 64: Actual through measurement data at time t, estimated measurement data, residual, and normalized residual at node RECA4L.

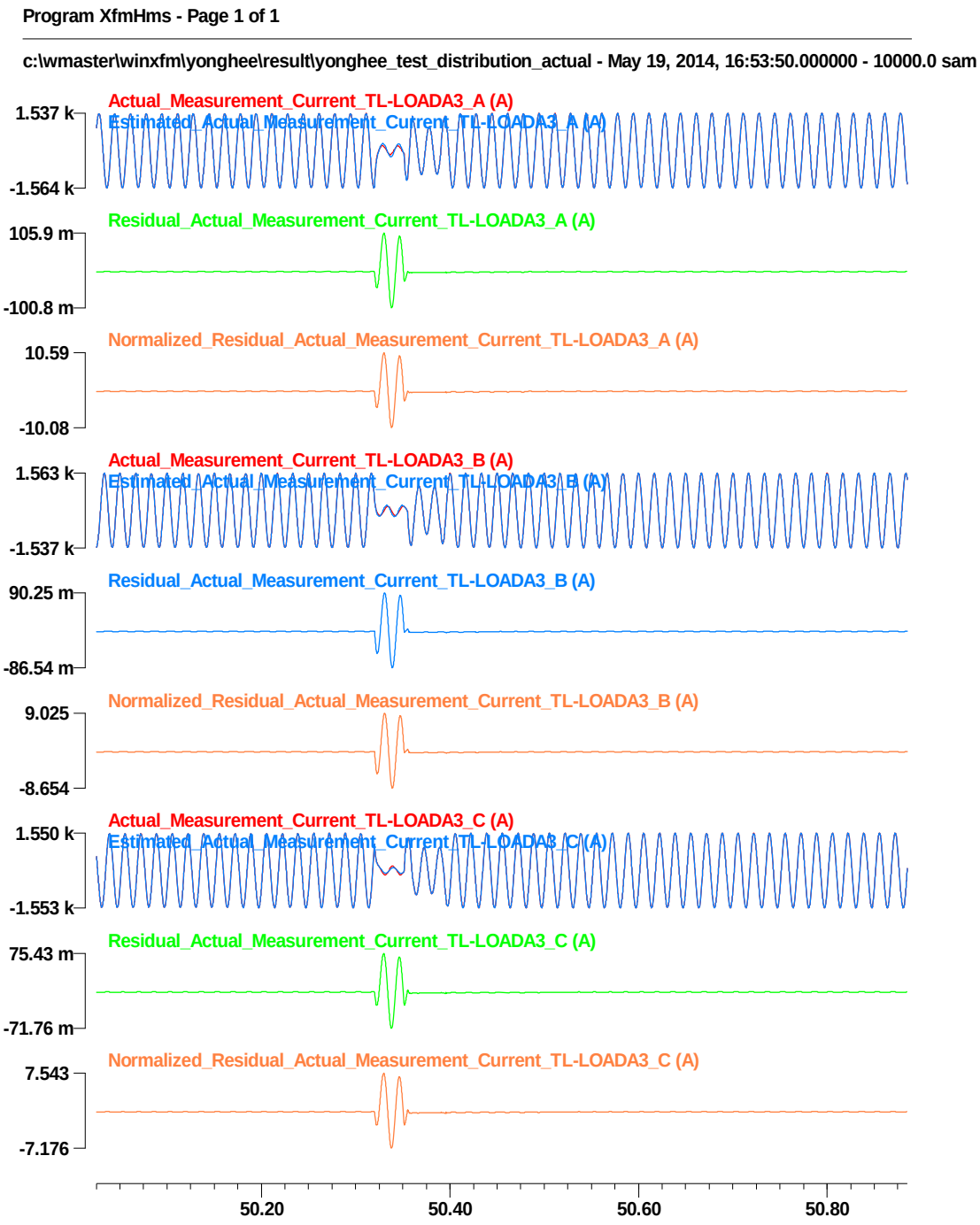

Figure 65: Actual through measurement data at time t, estimated measurement data, residual, and normalized residual at node TL-LOADA3.

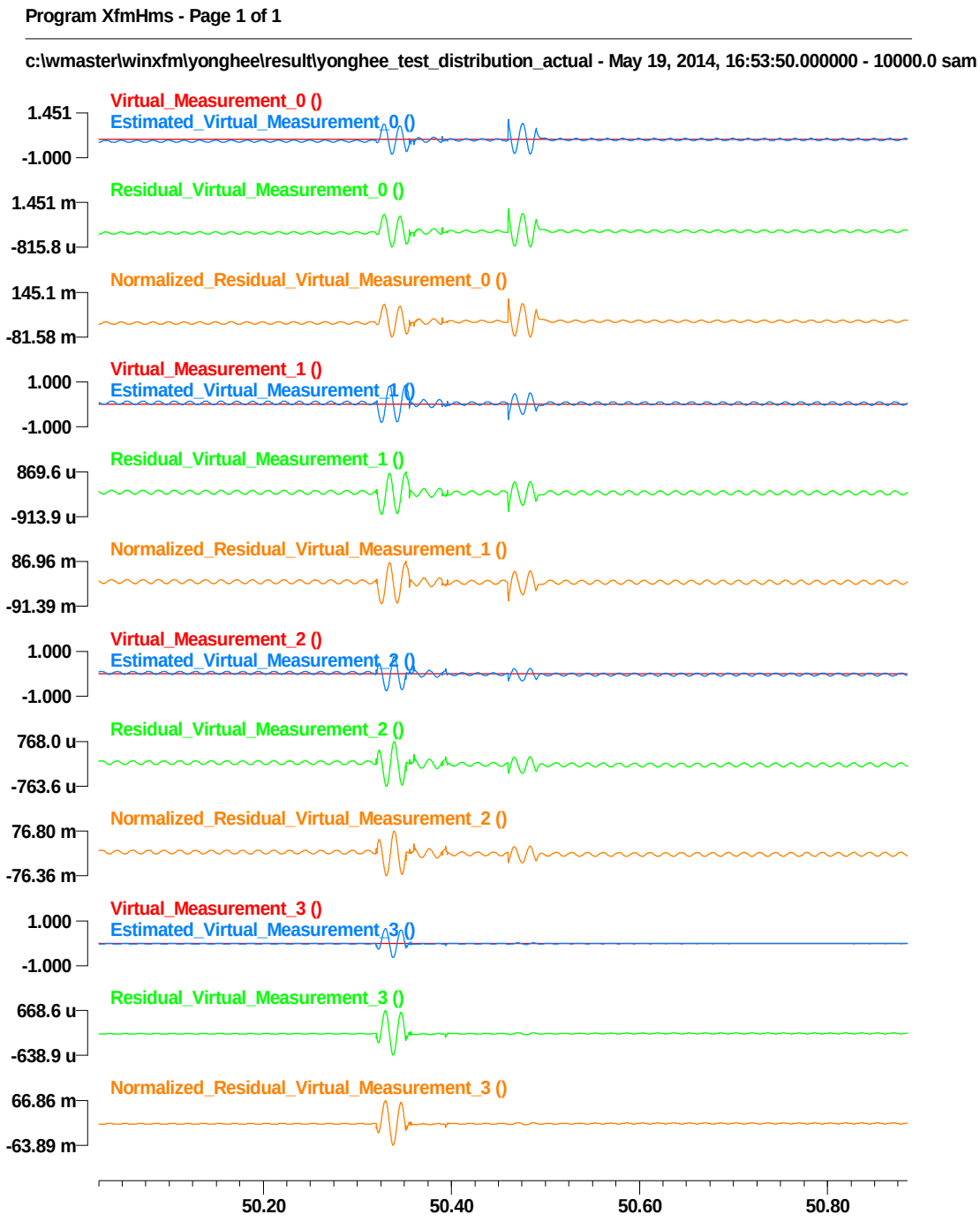

Figure 66: Virtual measurement data at time t, estimated measurement data, residual, and normalized residual of the first line model.

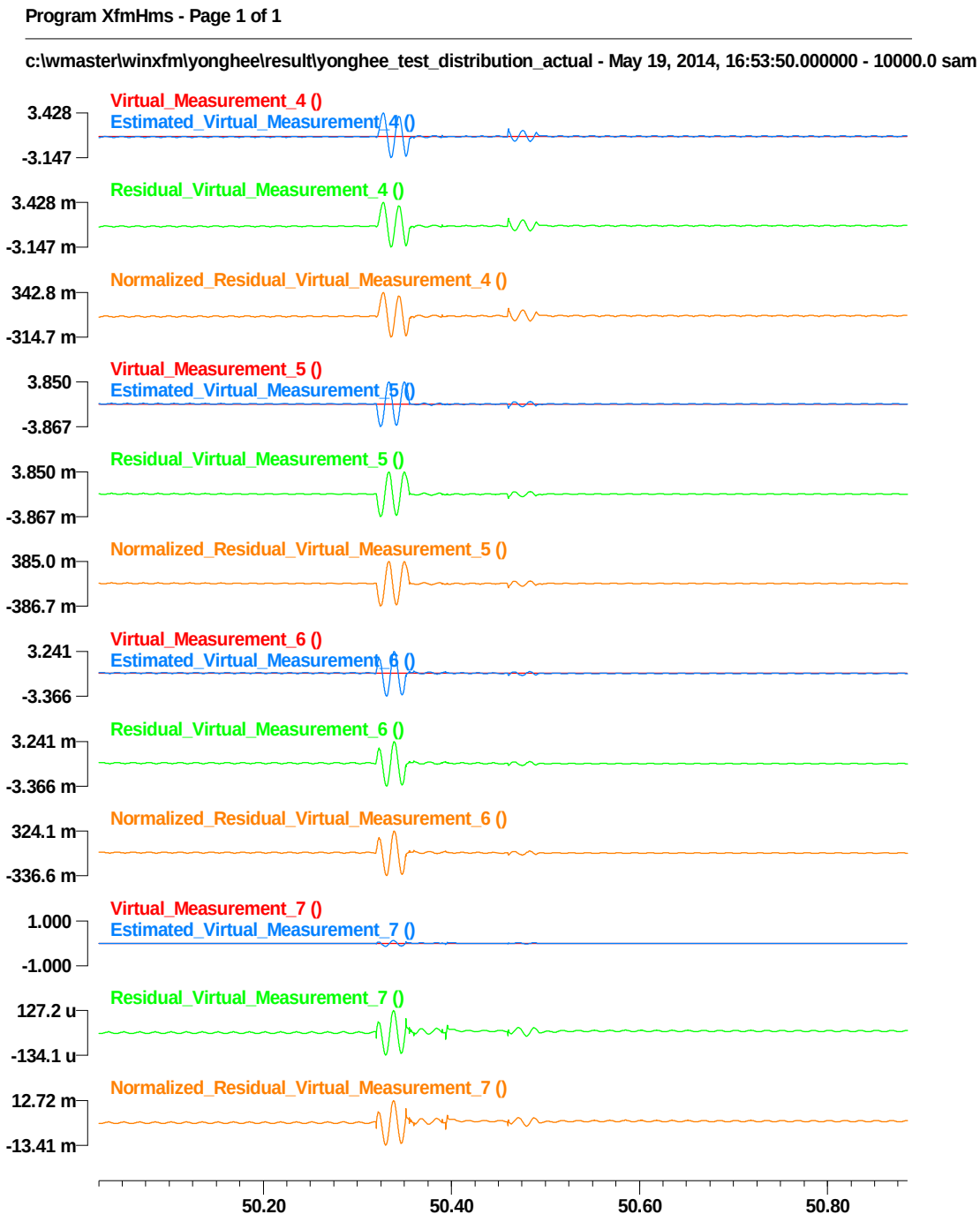

Figure 67: Virtual measurement data at time t, estimated measurement data, residual, and normalized residual of the second line model.

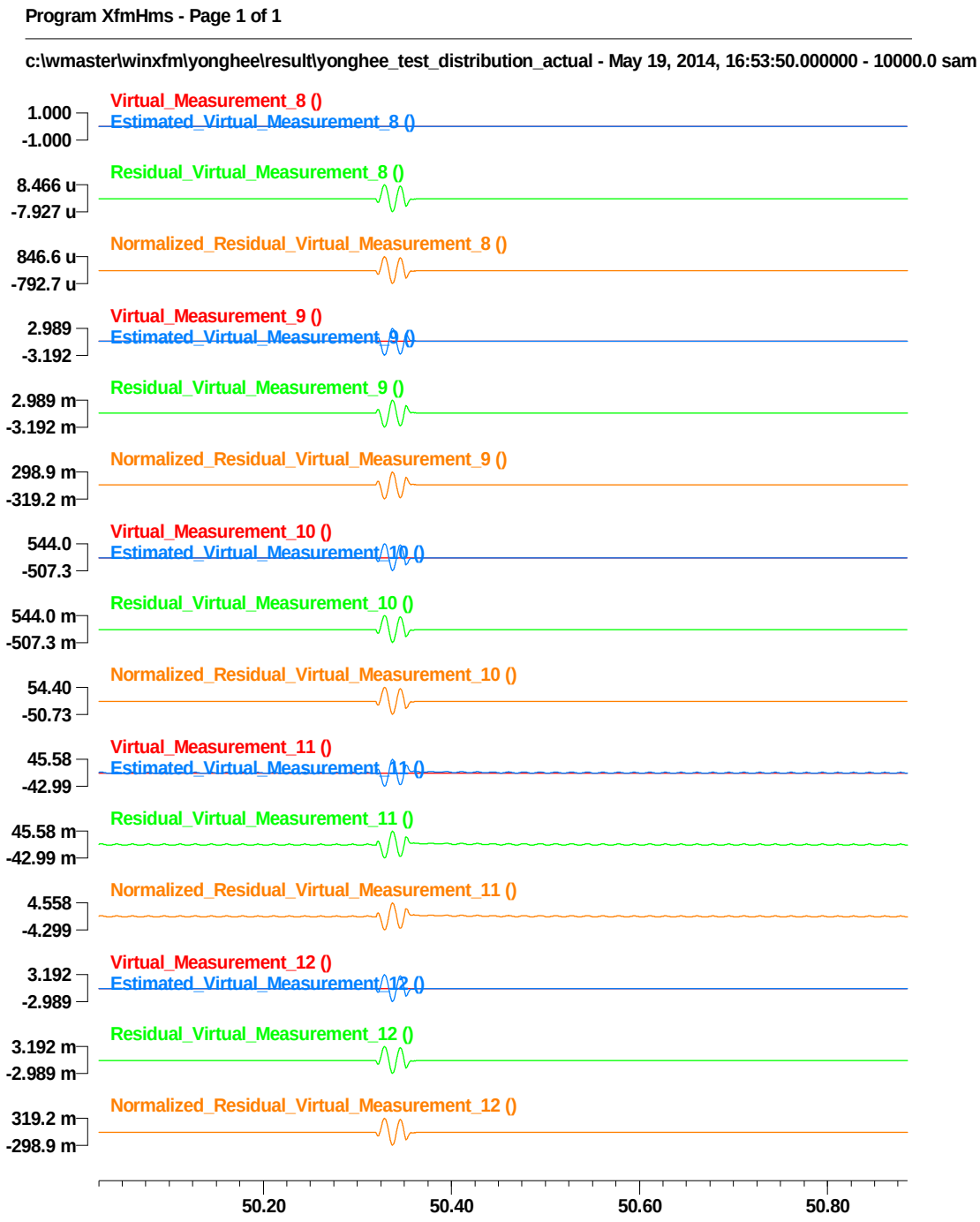

Figure 68: Virtual measurement data (8~12) at time t, estimated measurement data, residual, and normalized residual of the transformer model.

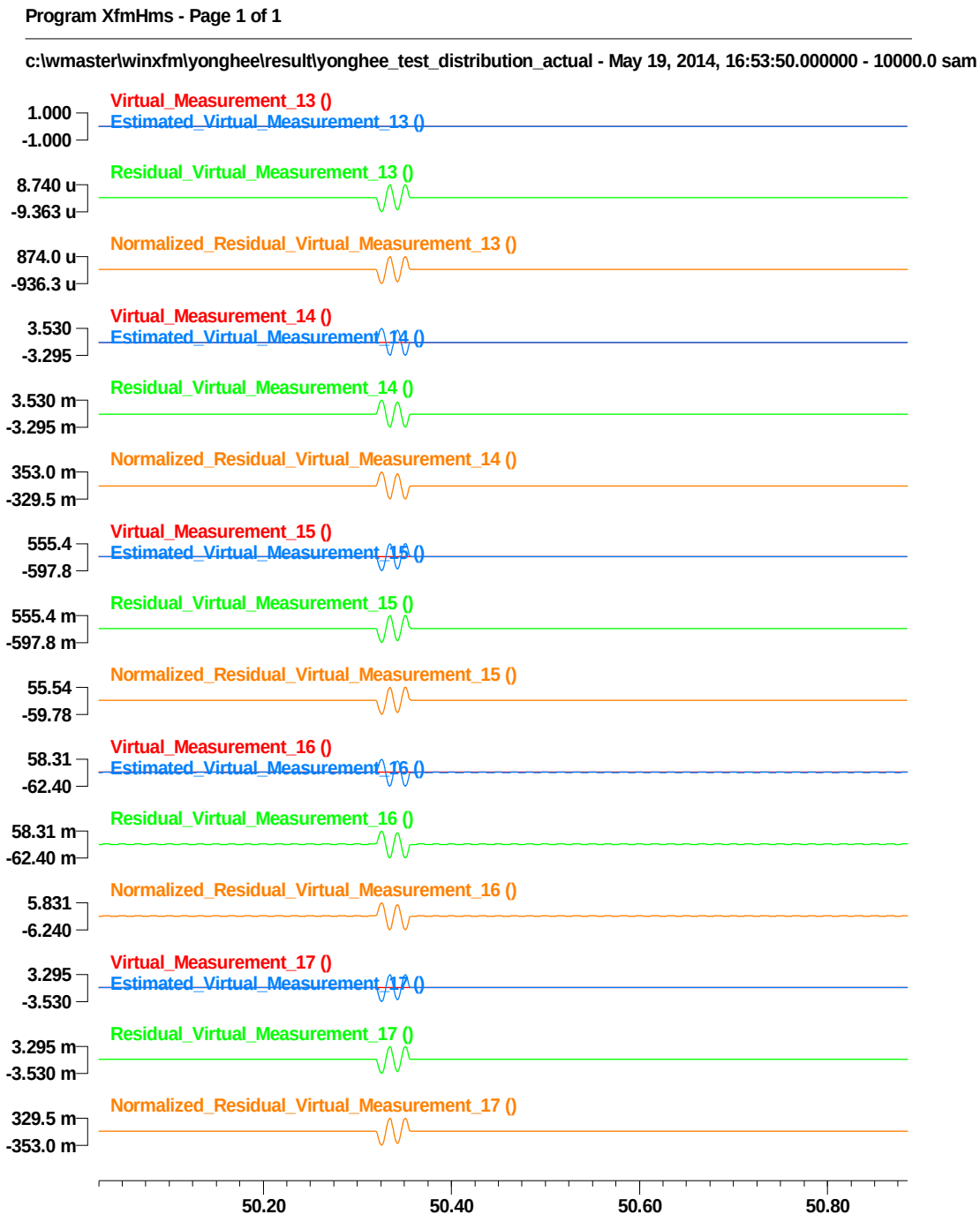

Figure 69: Virtual measurement data (13~17) at time t, estimated measurement data, residual, and normalized residual of the first transformer model.

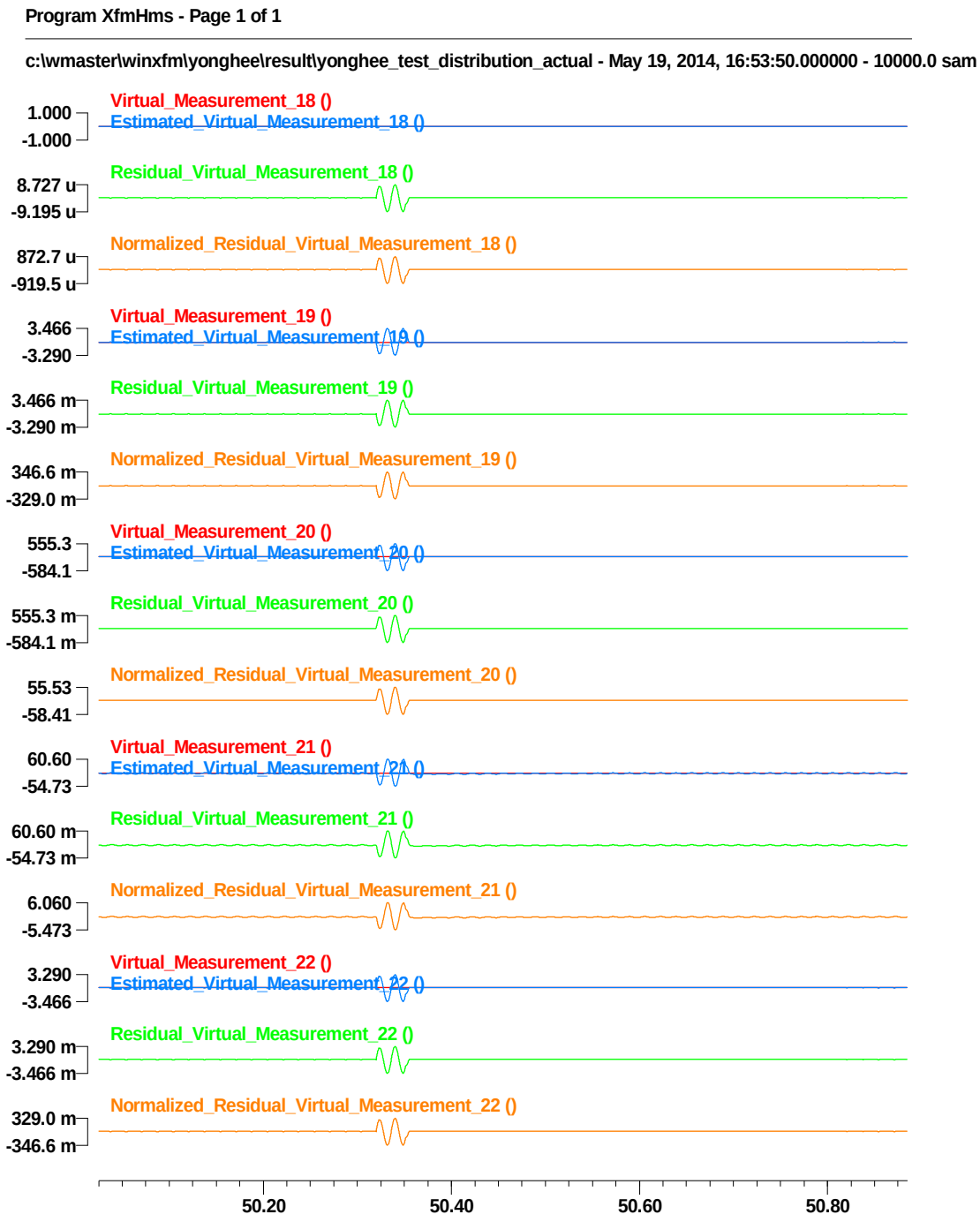

Figure 70: Virtual measurement data (18~22) at time t, estimated measurement data, residual, and normalized residual of the first transformer model.

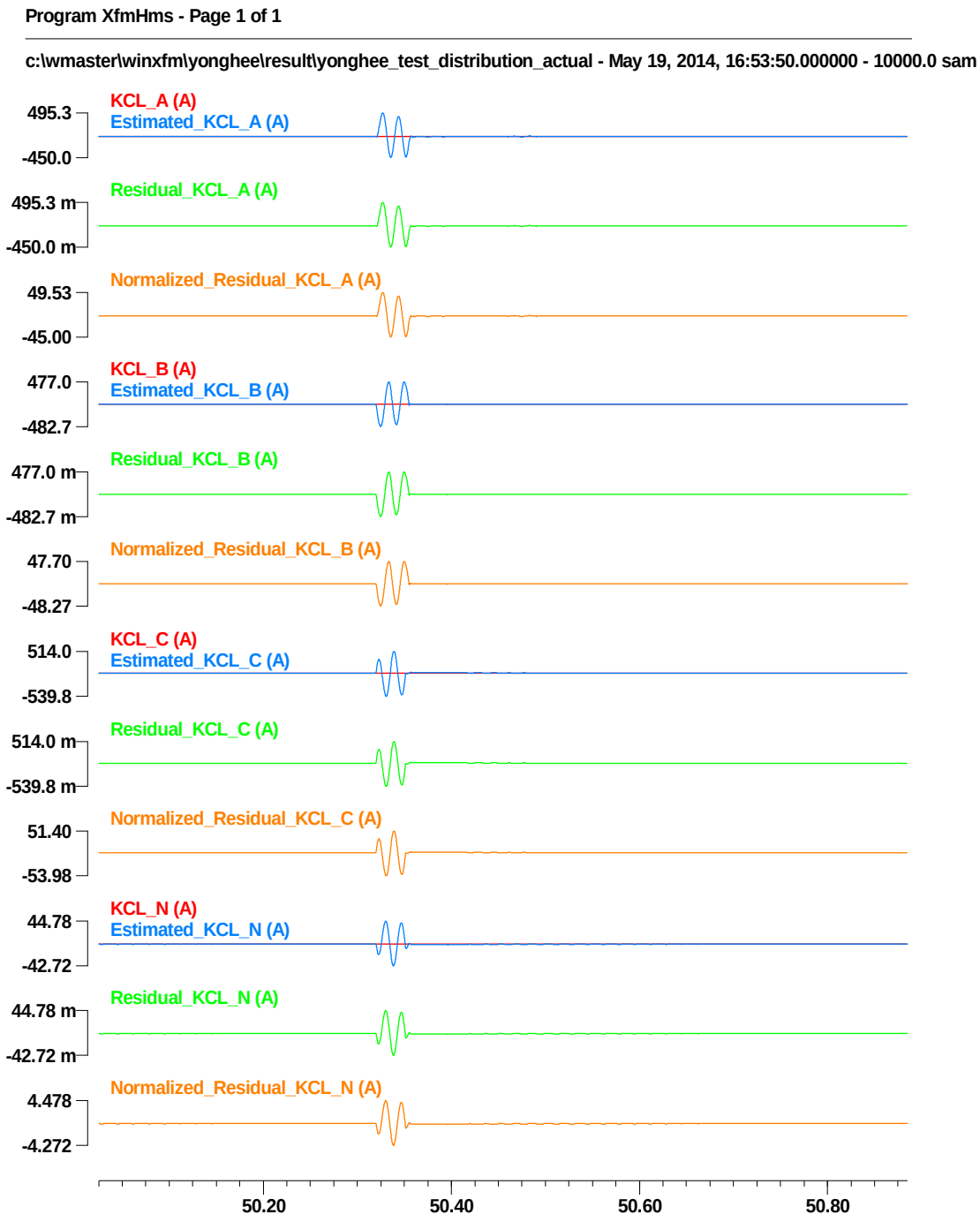

Figure 71: Virtual KCL measurement data at time t, estimated measurement data, residual, and normalized residual at node TH-LOAD3.

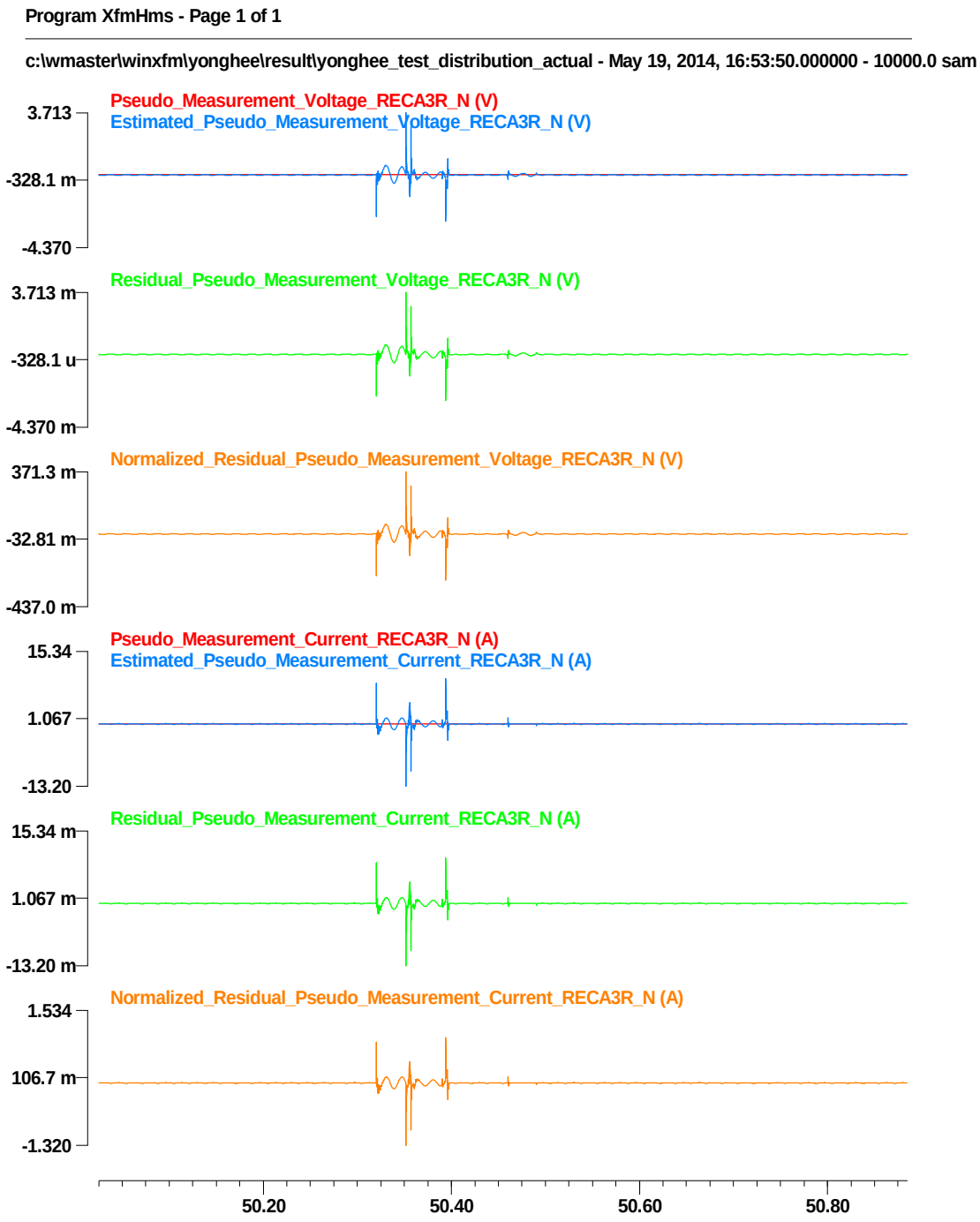

Figure 72: Pseudo measurement data at time t_m, estimated measurement data, residual, and normalized residual at node REC3R.

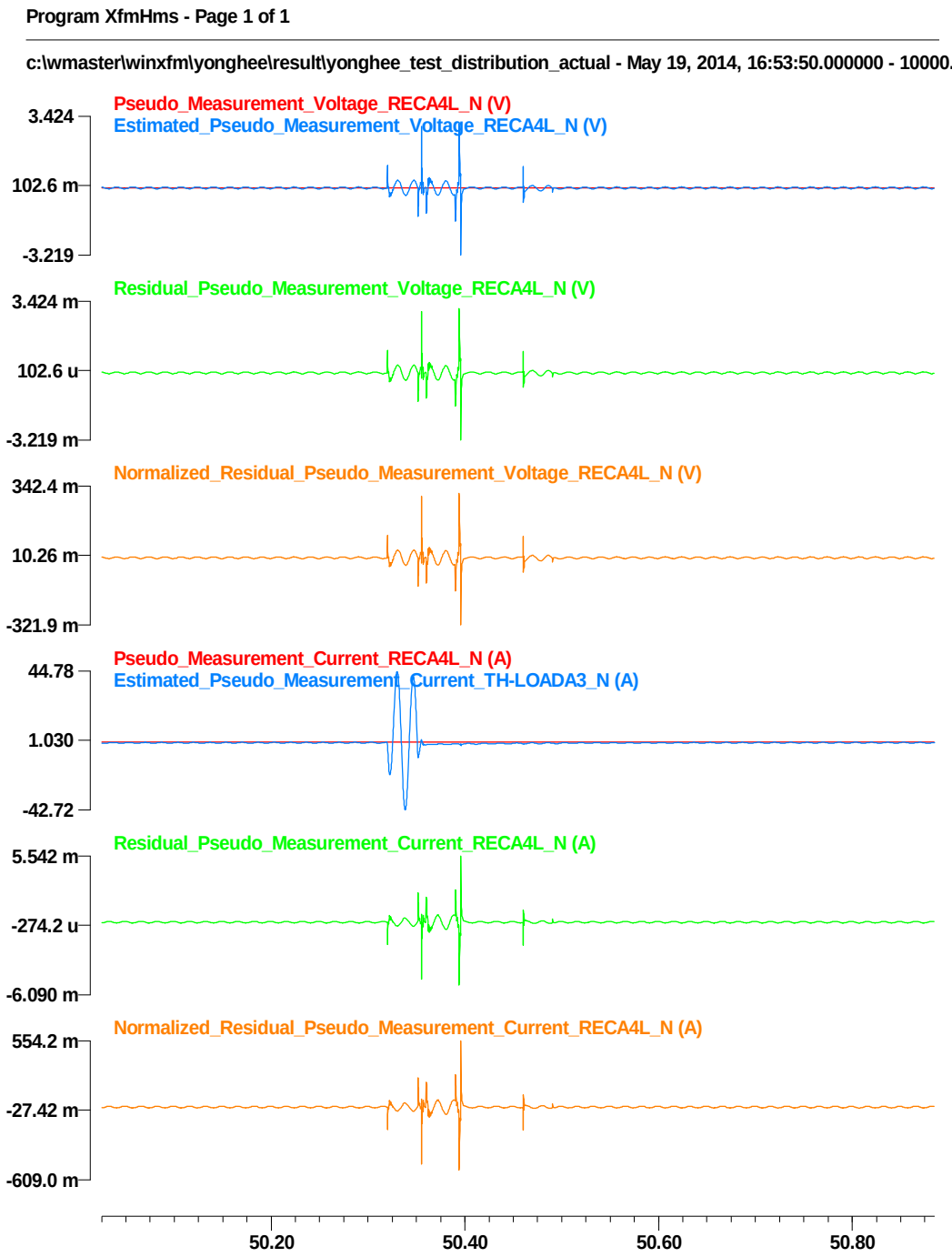

Figure 73: Pseudo measurement data at time t_m, estimated measurement data, residual, and normalized residual at node REC4L.

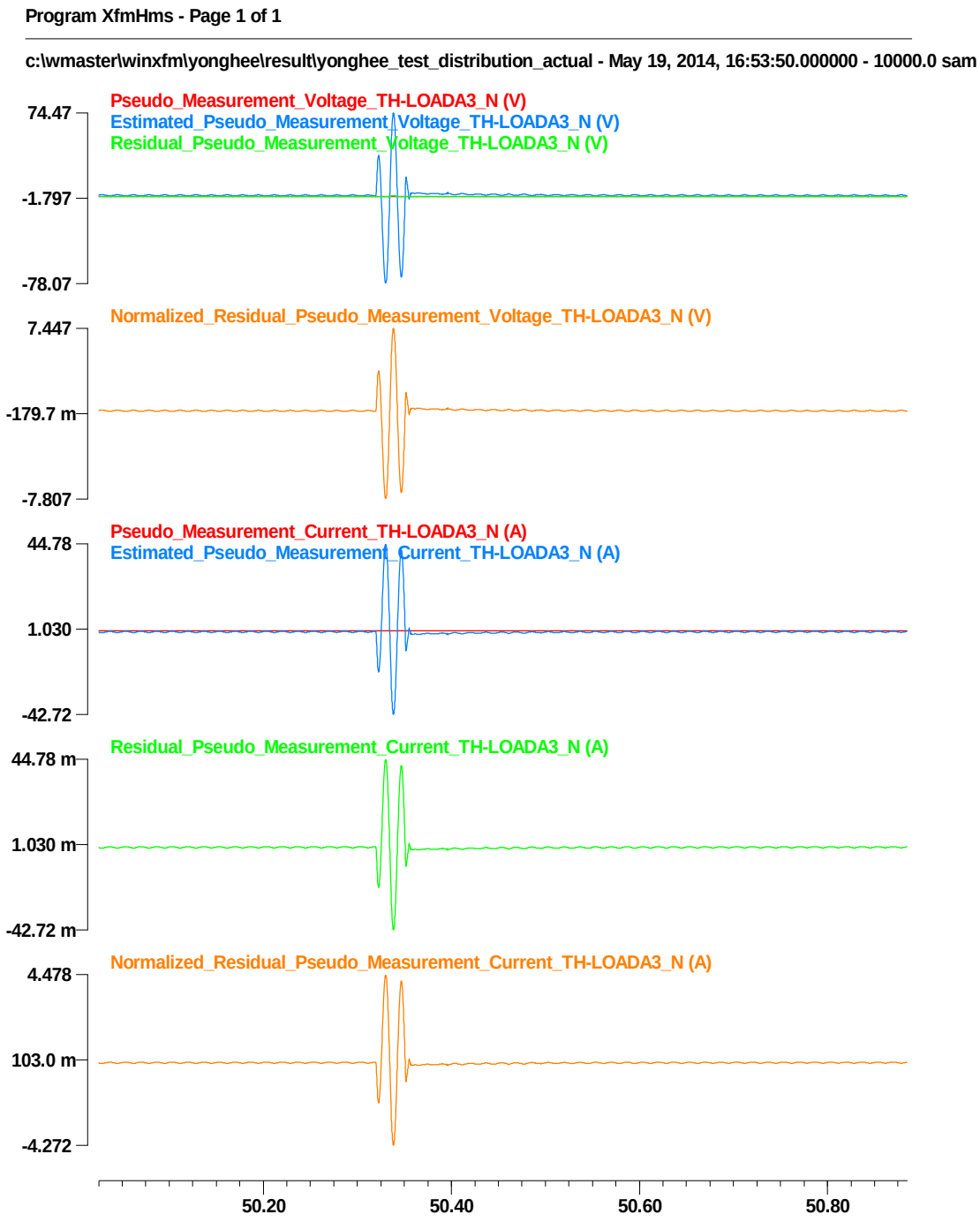

Figure 74: Pseudo measurement data at time t_m, estimated measurement data, residual, and normalized residual at node TH-LOADA3.

Appendix O Results Graphs of the DSE-based Protection Scheme Laboratory Test Results – Distribution System

The experimental results of the fault condition on the microgrid are depicted in this appendix Figure 75 to Figure 91 as follows: a) confidence level, computation time, and residual, b) external states and some of internal states for time t and t_m, and c) measurement data, estimated measurement data, residual, and normalized residual of actual measurement, virtual measurement, and pseudo measurement data.

a) Confidence level, computation time, and residual for the internal fault case are depicted in Figure 75.

b) External states and some of internal states for time t and t_m are depicted in Figure 76. Internal states of the single section distribution line and the transformer is not explicitly shown in this appendix.

c) Measurement data, estimated measurement data, residual, and normalized residual of actual measurement, derived measurements, virtual measurement, and pseudo measurement data are illustrated in Figure 77 to Figure 91.

c1) Actual measurement data, estimated measurement data, residual, and normalized residual values for time t and t_m. are depicted in Figure 77 and Figure 80. In more detail, for time t and t_m, across measurement data and estimated measurement data at node RECA3R are compared each other as shown in Figure 77. Residual and normalized residual values are also depicted in the same figure. In addition, through measurement data and estimated measurement data at node RECA3R, are compared each other, and the resulting residual and normalized residual values are shown in Figure 80.

c2) Derived measurement data, estimated measurement data, residual, and normalized residual values for time t and t_m. are depicted in Figure 78, Figure 79, Figure 81, and Figure 82. In more detail, for time t and t_m, derived across measurement data and estimated measurement data at node RECA4L and TL-LOADA3 are compared each other as shown in Figure 78 and Figure 79, respectively. Residual and normalized residual values are also depicted in the same figure. In addition, derived through measurement data and estimated measurement data at node RECA4L, and TL-LOADA3 are compared each other, and the resulting residual and normalized residual values are shown in Figure 81 and Figure 82.

c3) Virtual measurement data, estimated measurement data, residual, and normalized residual values for time t and t_m are depicted in Figure 83 to Figure 88. In more detail, internal virtual measurement data and estimated measurement data of the first single section distribution line model for time t and t_m are compared each other, and the resulting residual and normalized residual values are shown in Figure 83. Result graphs of the second single section distribution line model and the transformer model are depicted in Figure 84 to Figure 87. Moreover, KCL virtual measurement data and estimated measurement data at node TH-LOADA3 for time t and t_m are compared each other, and the resulting residual and normalized residual values are shown in Figure 88.

c4) Pseudo measurement data, estimated measurement data, residual, and normalized residual values for time t and t_m are depicted in Figure 89 to Figure 91. In more detail, pseudo measurement data and estimated measurement data at node RECA3R, RECA4L, and TL-LOADA3 for time t and t_m are compared each other, and the resulting residual and normalized residual values are shown in Figure 89 to Figure 91.

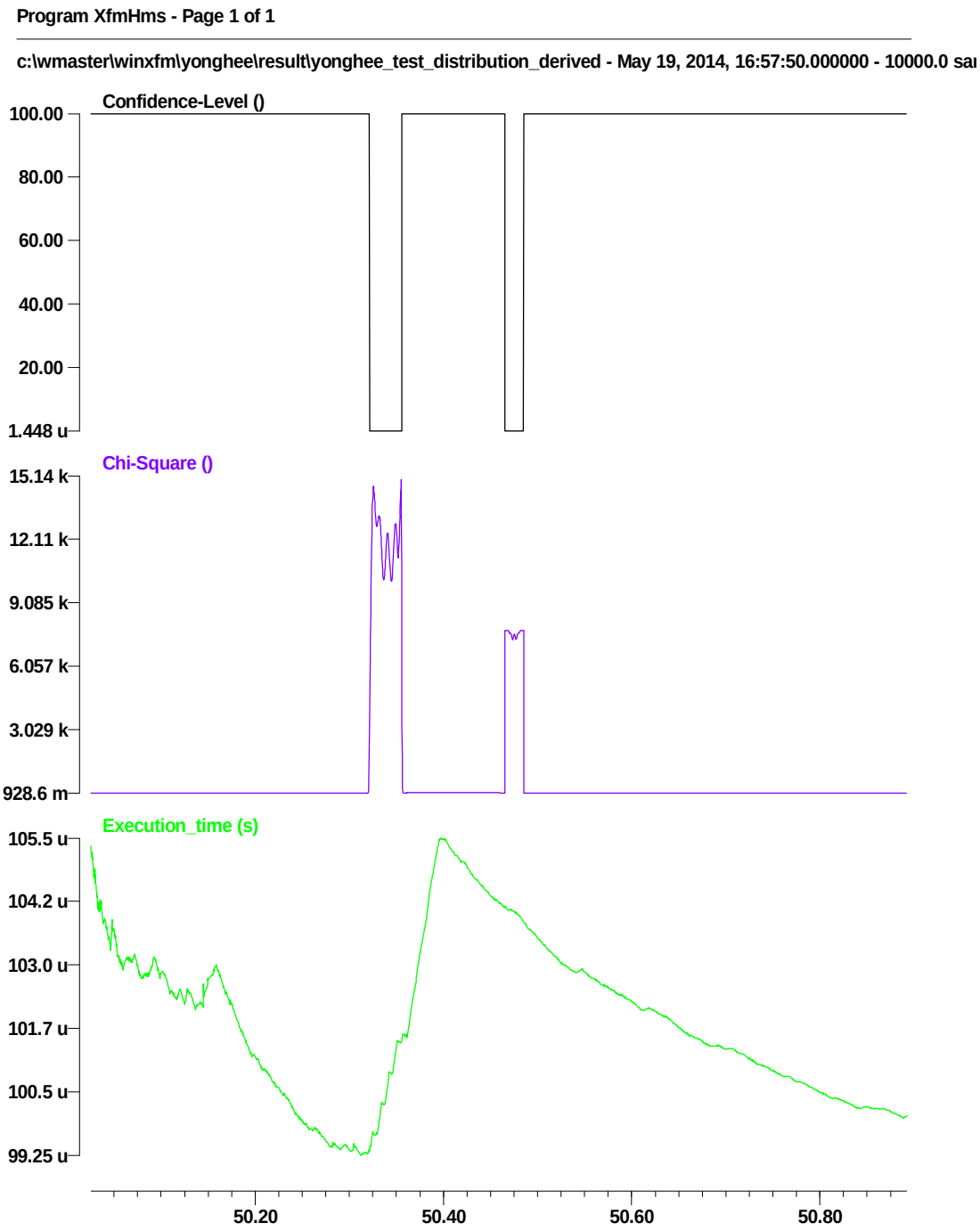

Figure 75: Confidence level, computation time, and residual for the internal fault case on the distribution system.

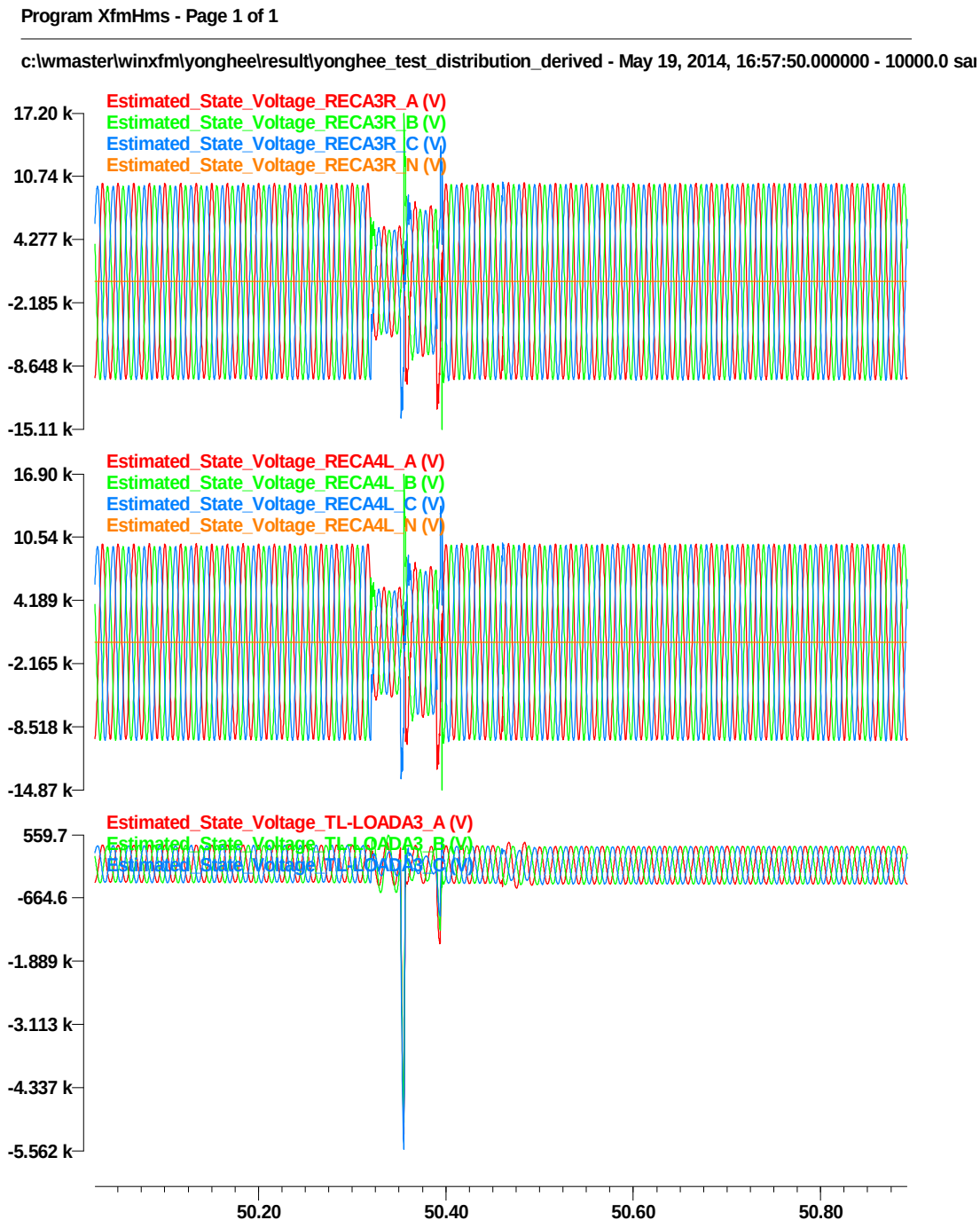

Figure 76: States at node RECA3R, TH-LOADA3, TL-LOADA3, and RECA4L.

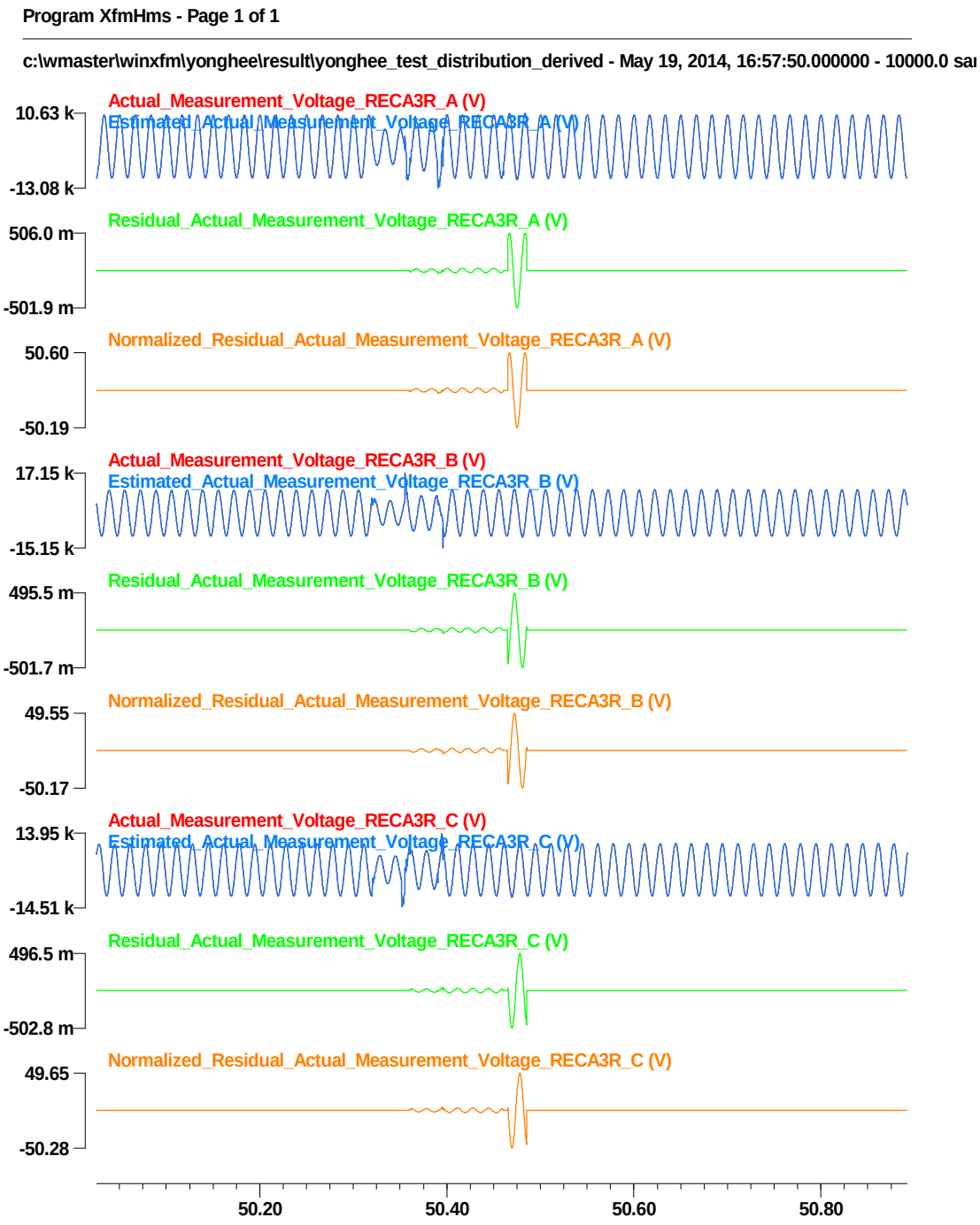

Figure 77: Actual across measurement data, estimated measurement data, residual, and normalized residual at node RECA3R.

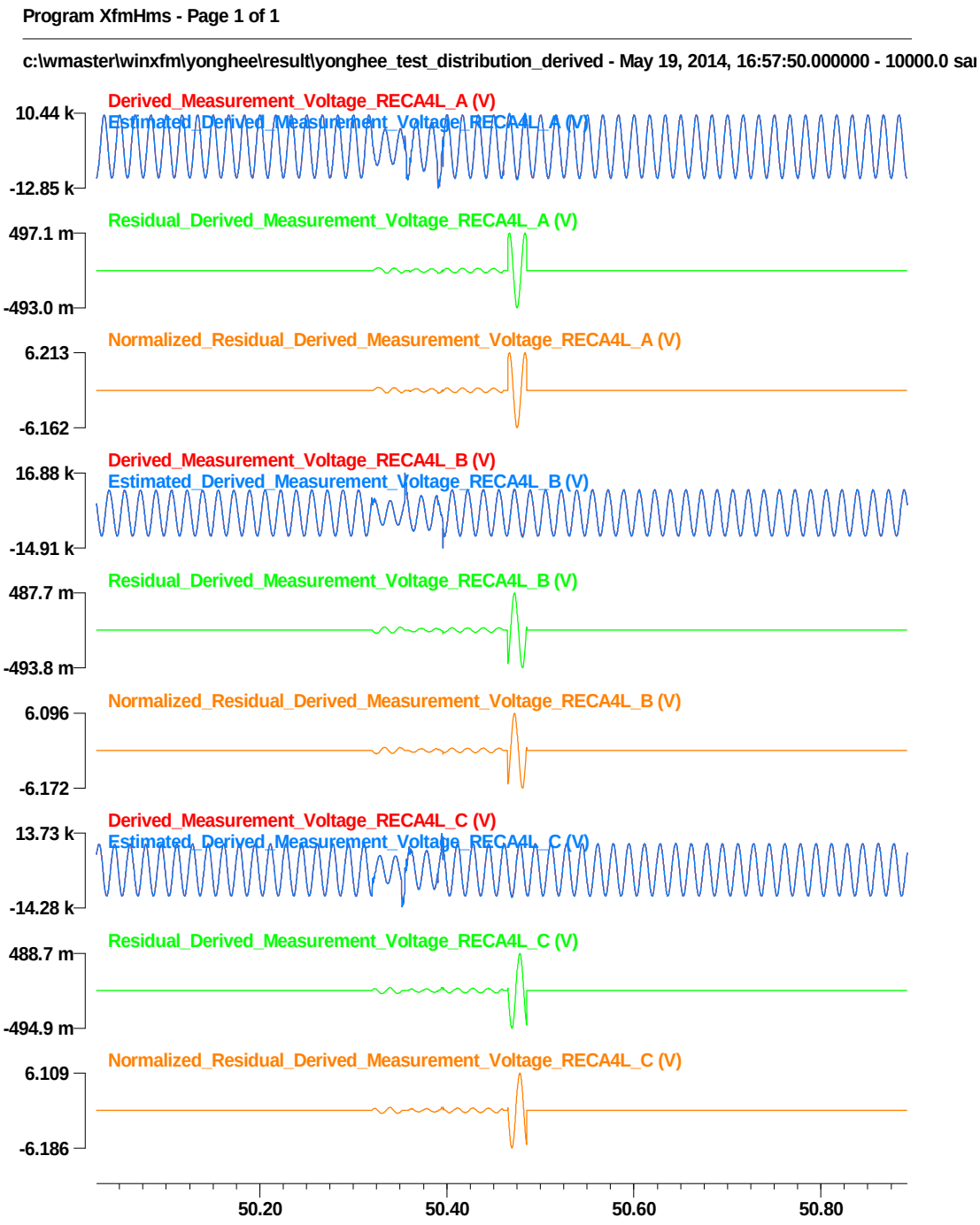

Figure 78: Derived across measurement data at time t, estimated measurement data, residual, and normalized residual at node RECA4L.

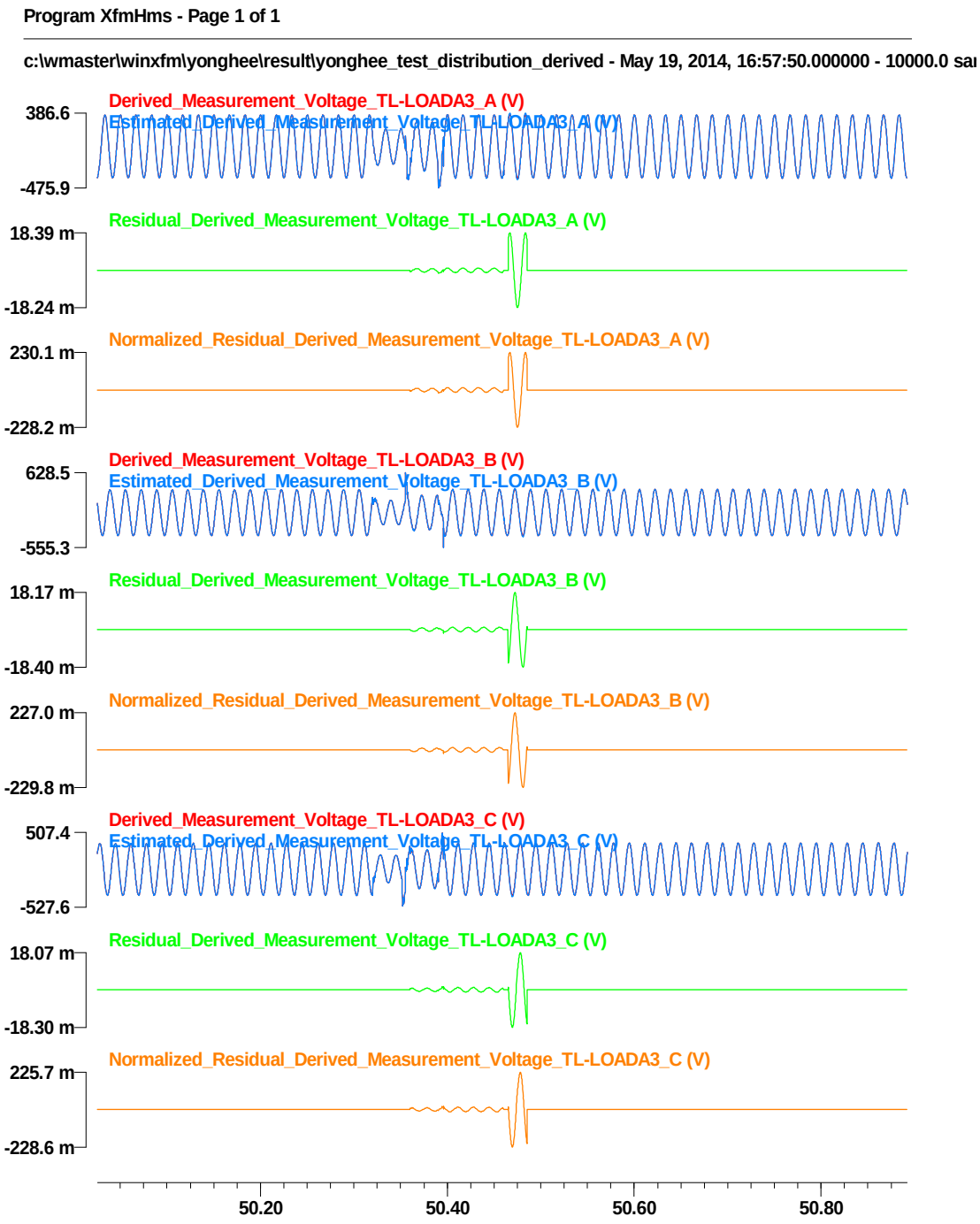

Figure 79: Derived across measurement data at time t, estimated measurement data, residual, and normalized residual at node TL-LOADA3.

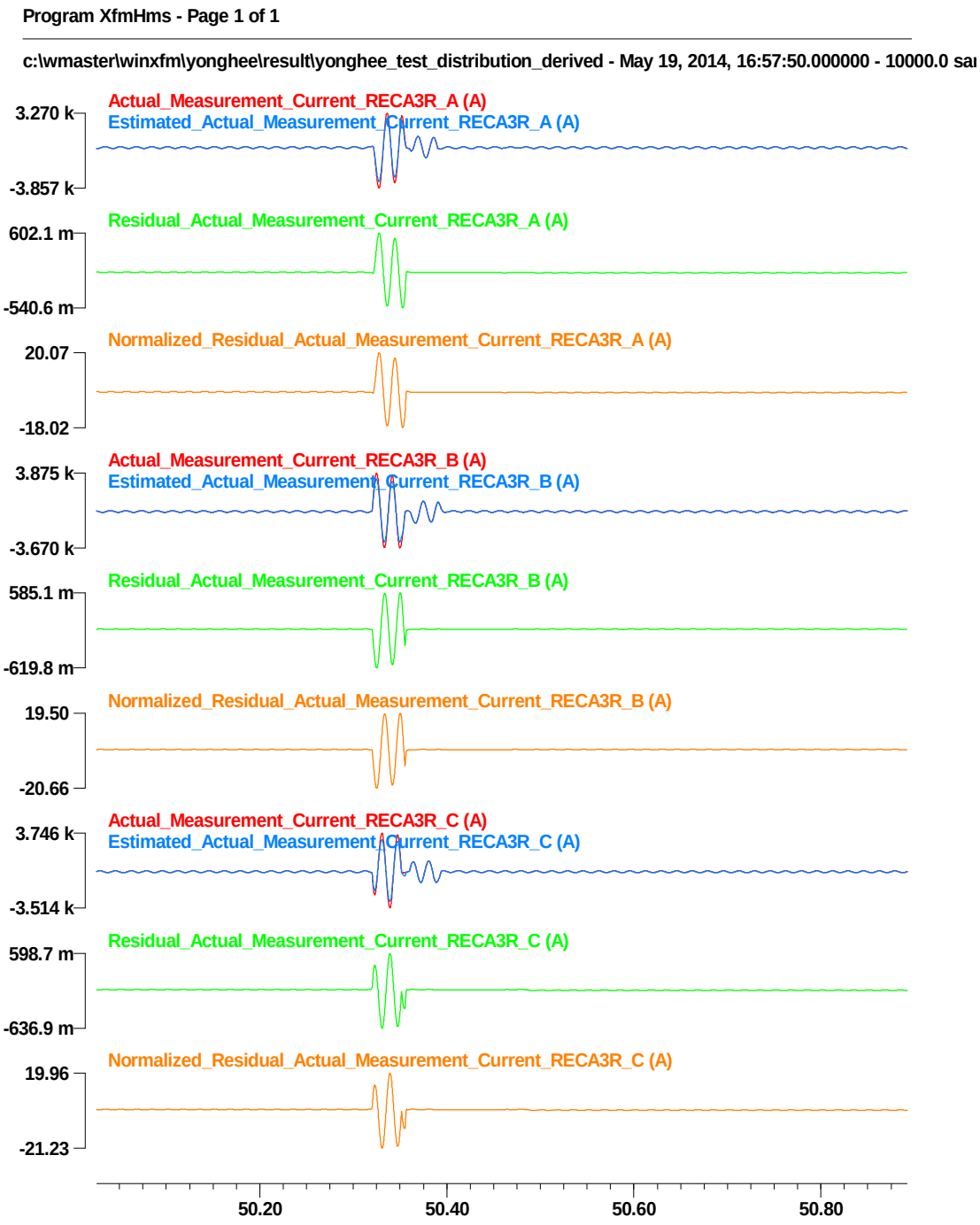

Figure 80: Actual through measurement data at time t, estimated measurement data, residual, and normalized residual at node RECA3R.

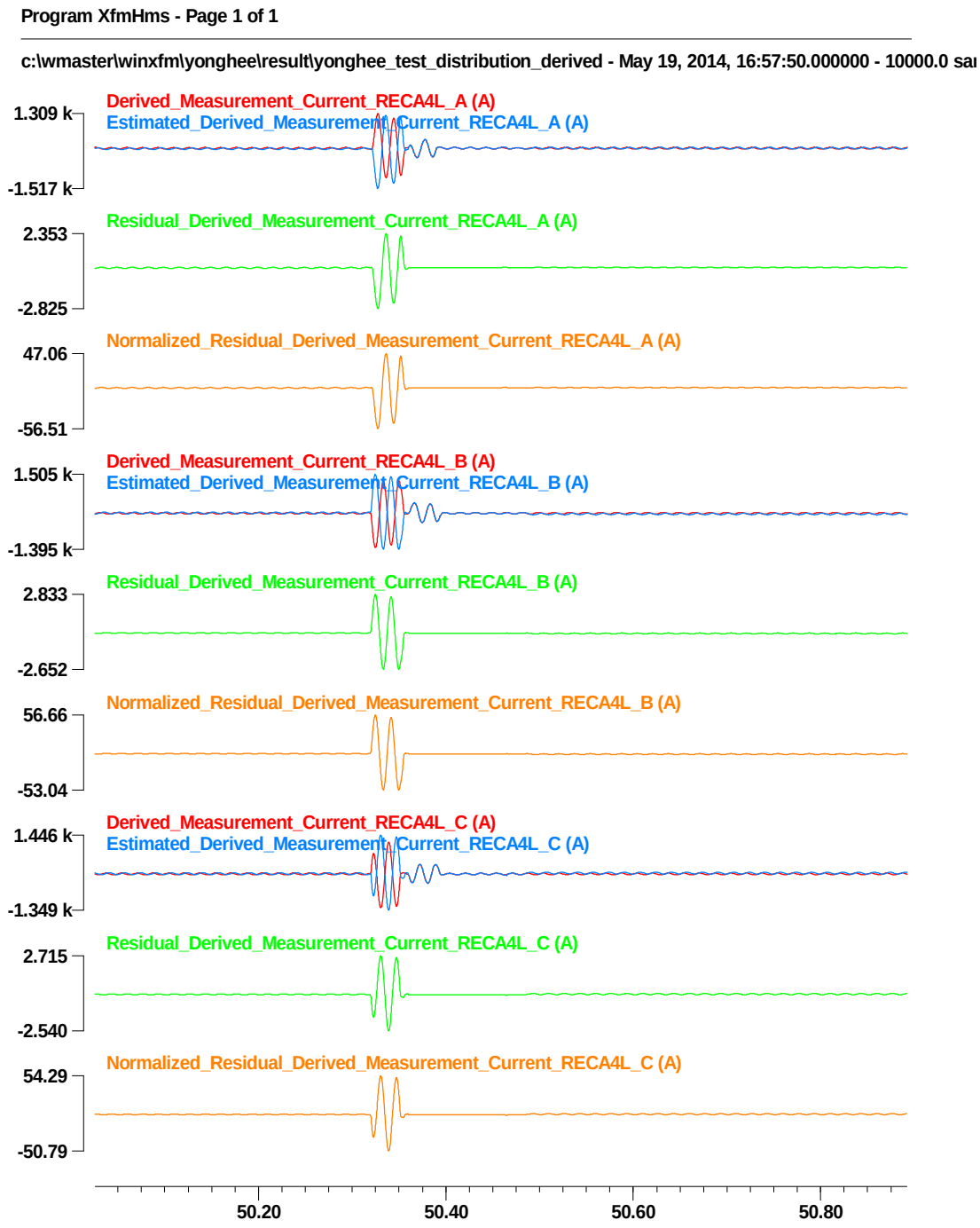

Figure 81: Derived through measurement data at time t, estimated measurement data, residual, and normalized residual at node RECA4L.

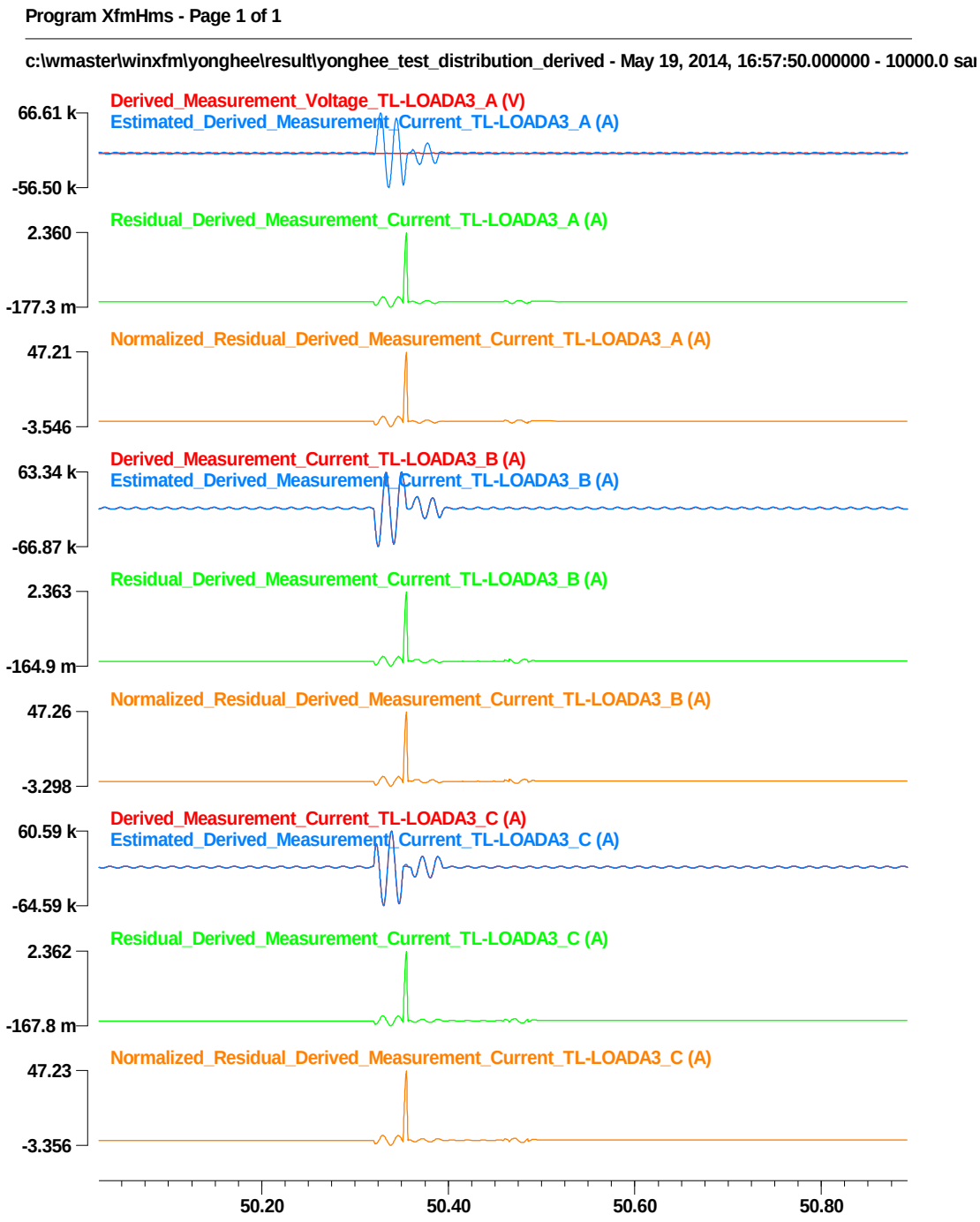

Figure 82: Derived through measurement data at time t, estimated measurement data, residual, and normalized residual at node TL-LOADA3.

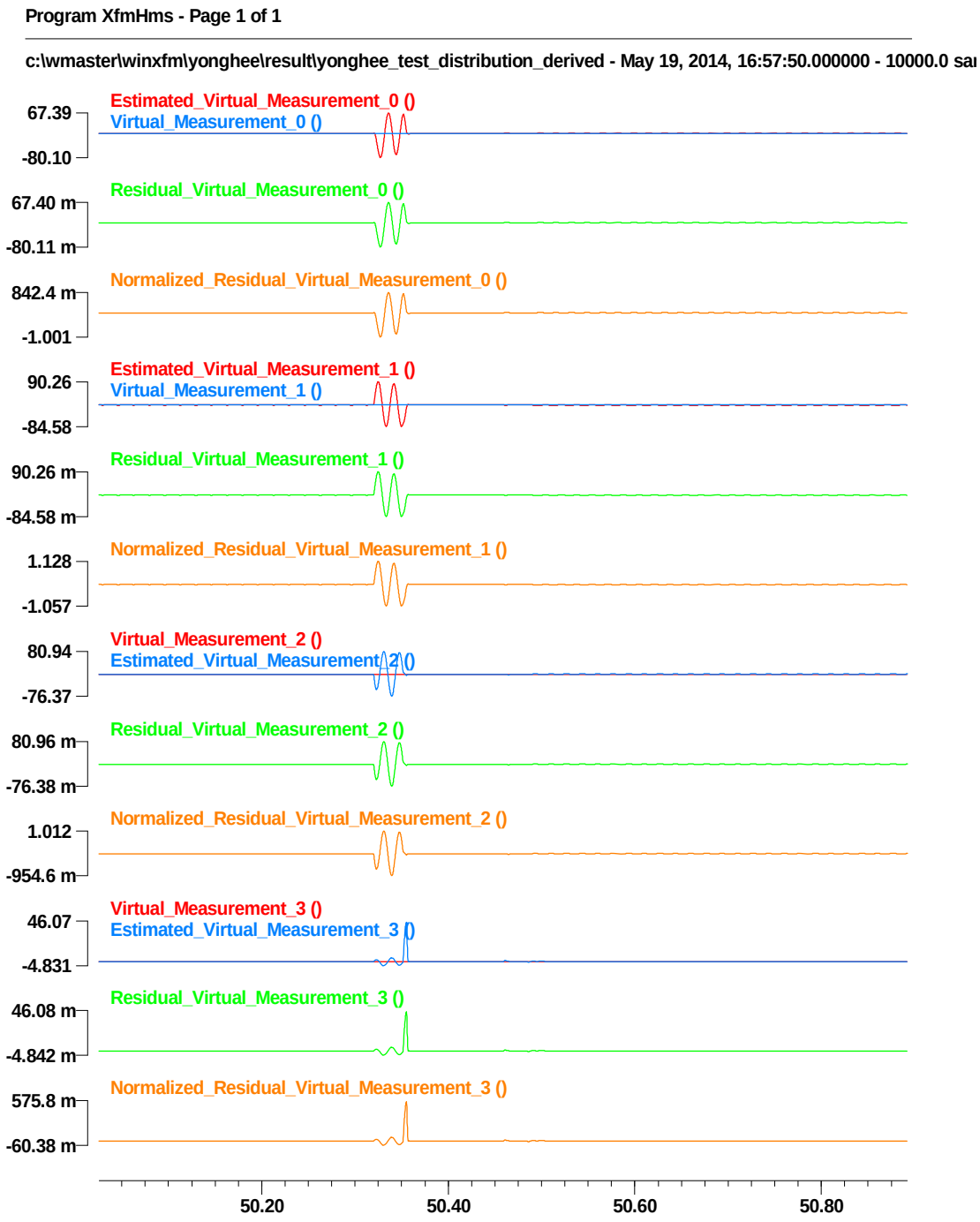

Figure 83: Virtual measurement data at time t, estimated measurement data, residual, and normalized residual of the first line model.

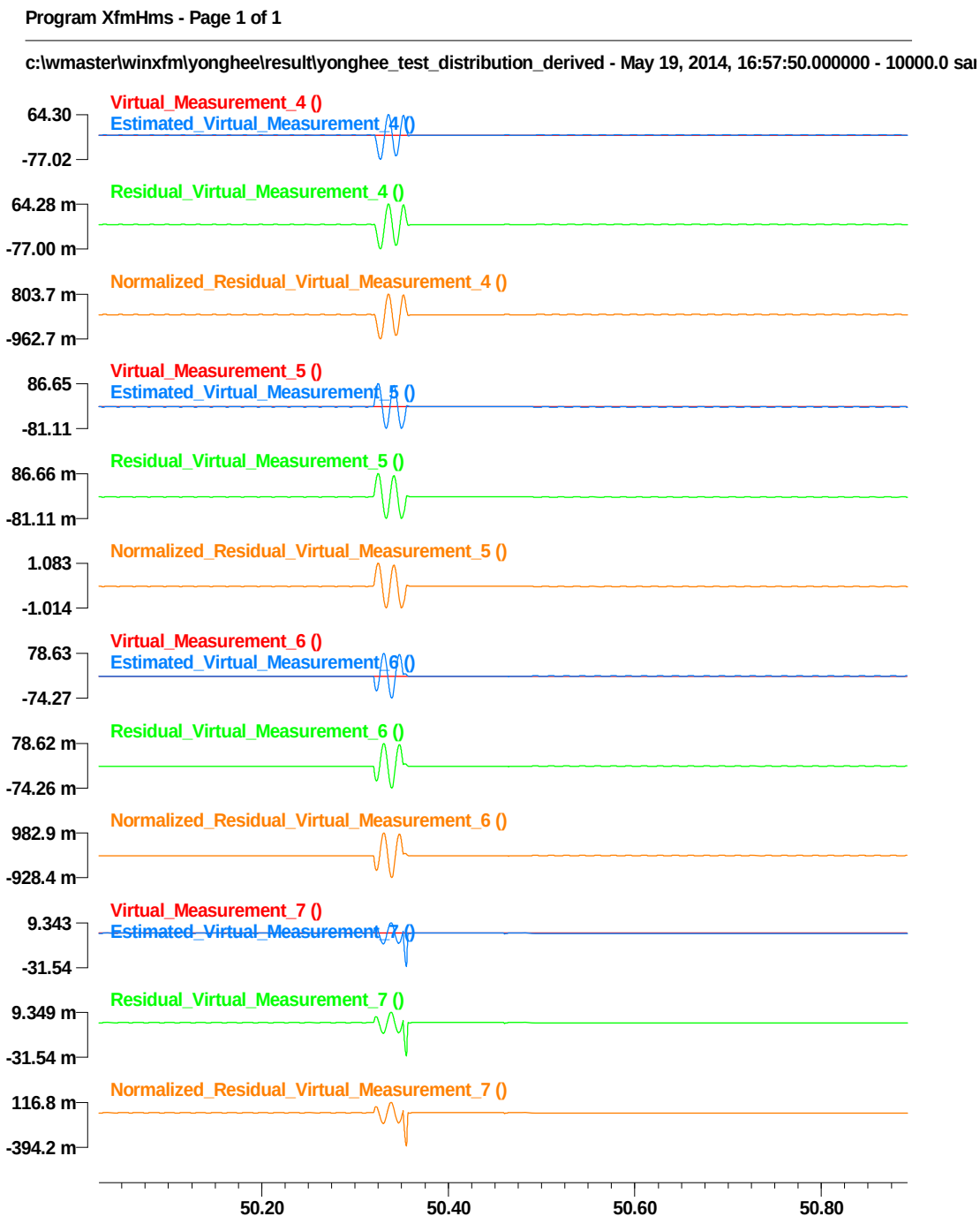

Figure 84: Virtual measurement data at time t, estimated measurement data, residual, and normalized residual of the second line model.

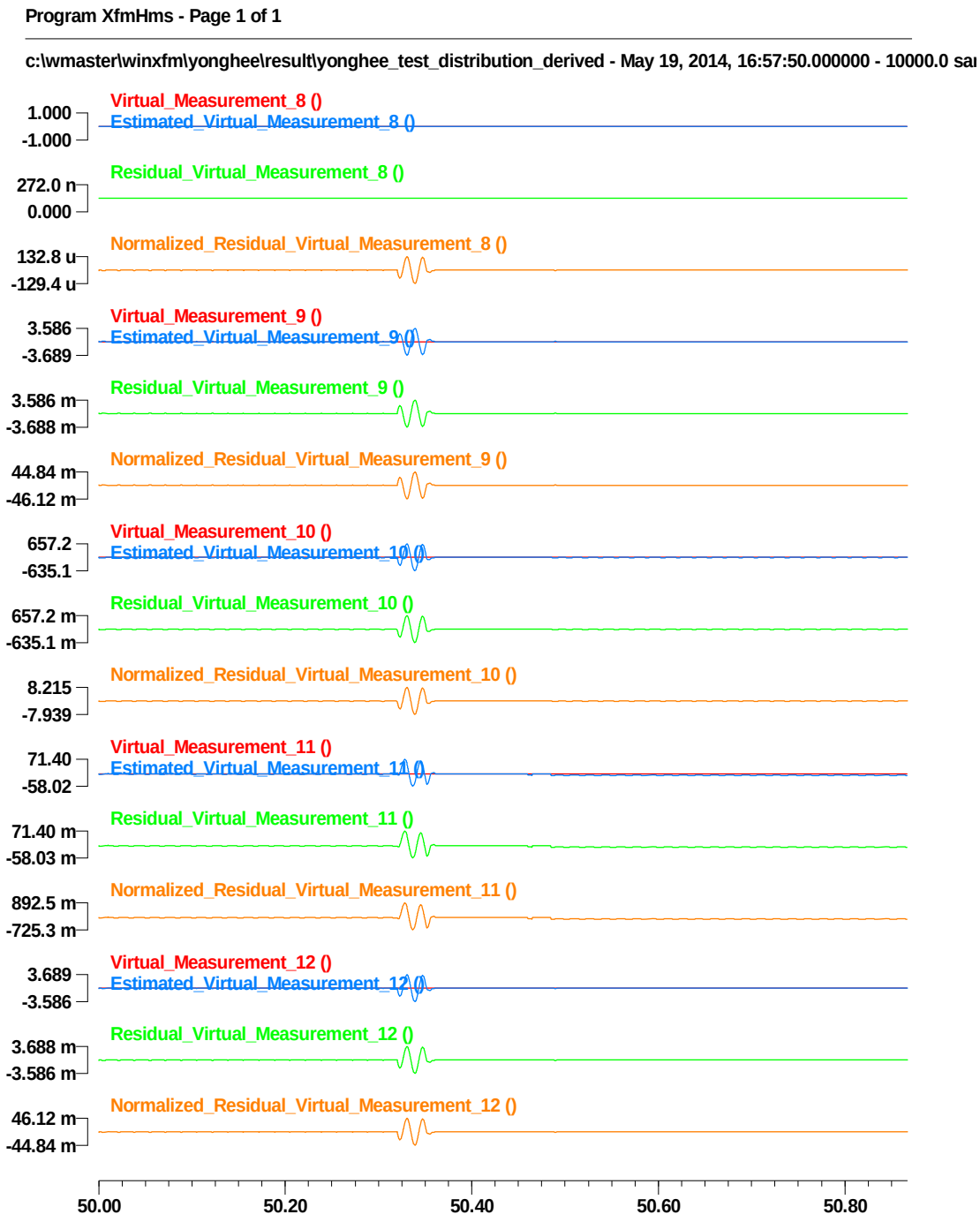

Figure 85: Virtual measurement data (8~12) at time t, estimated measurement data, residual, and normalized residual of the transformer model.

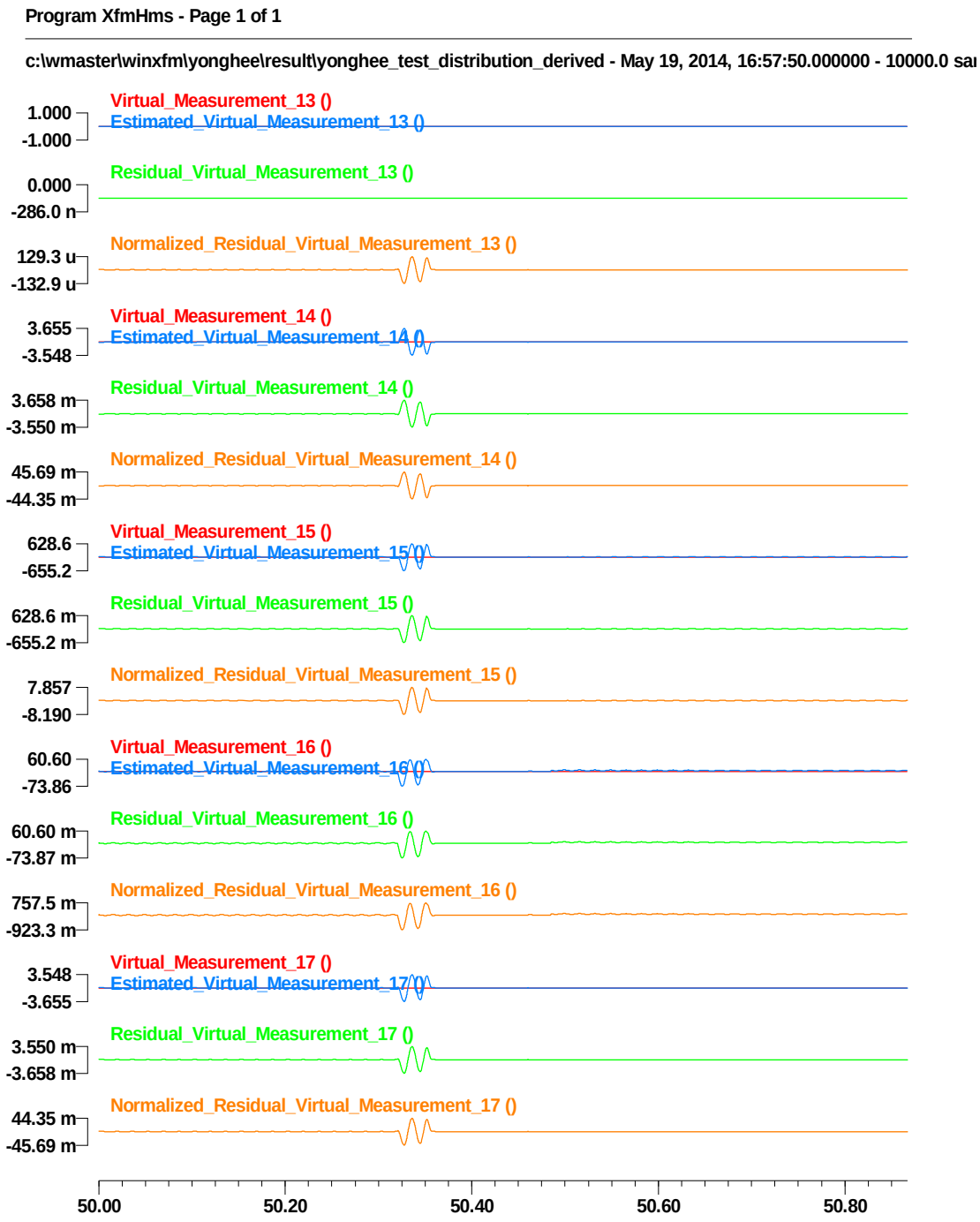

Figure 86: Virtual measurement data (13~17) at time t, estimated measurement data, residual, and normalized residual of the first transformer model.

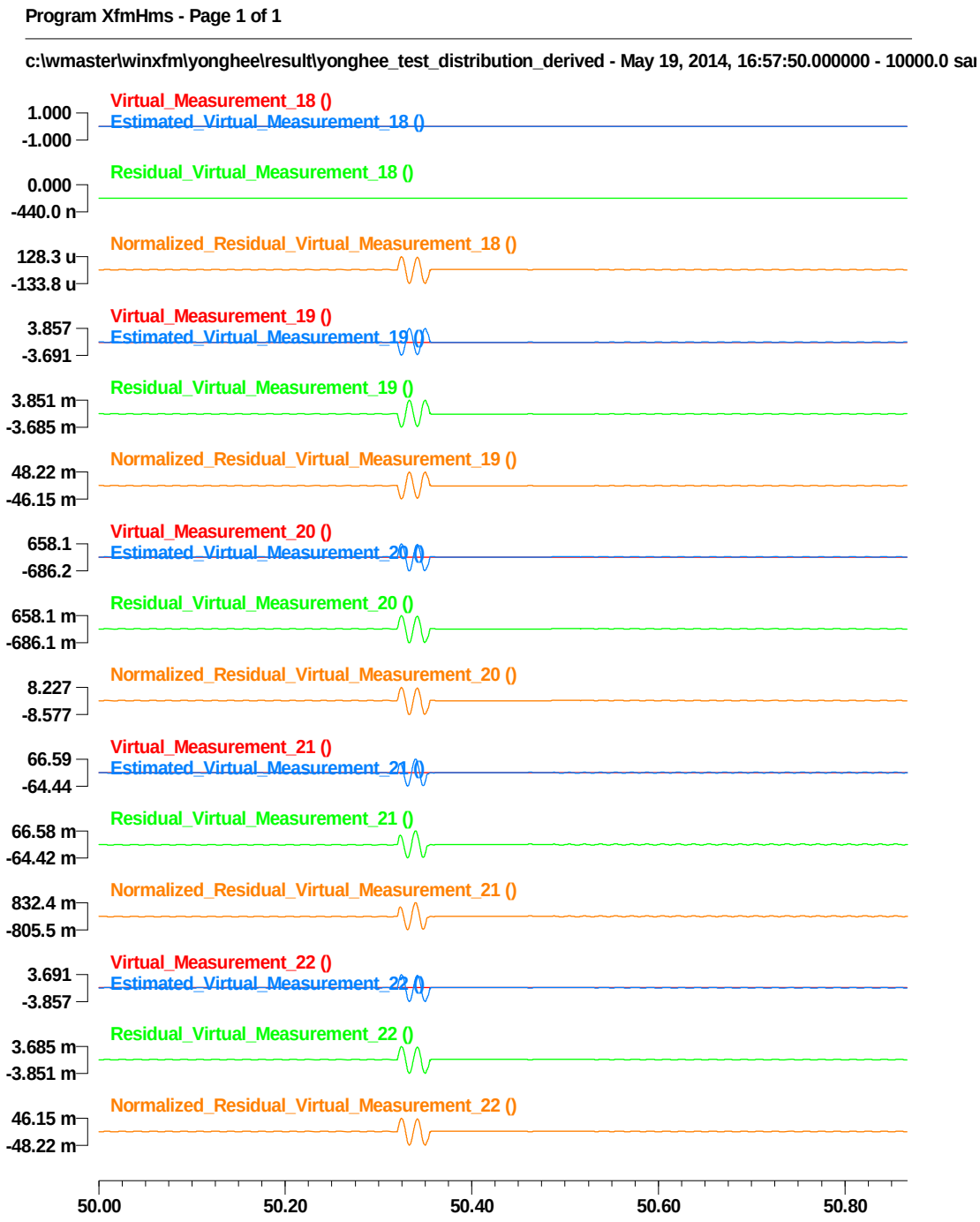

Figure 87: Virtual measurement data (18~22) at time t, estimated measurement data, residual, and normalized residual of the first transformer model.

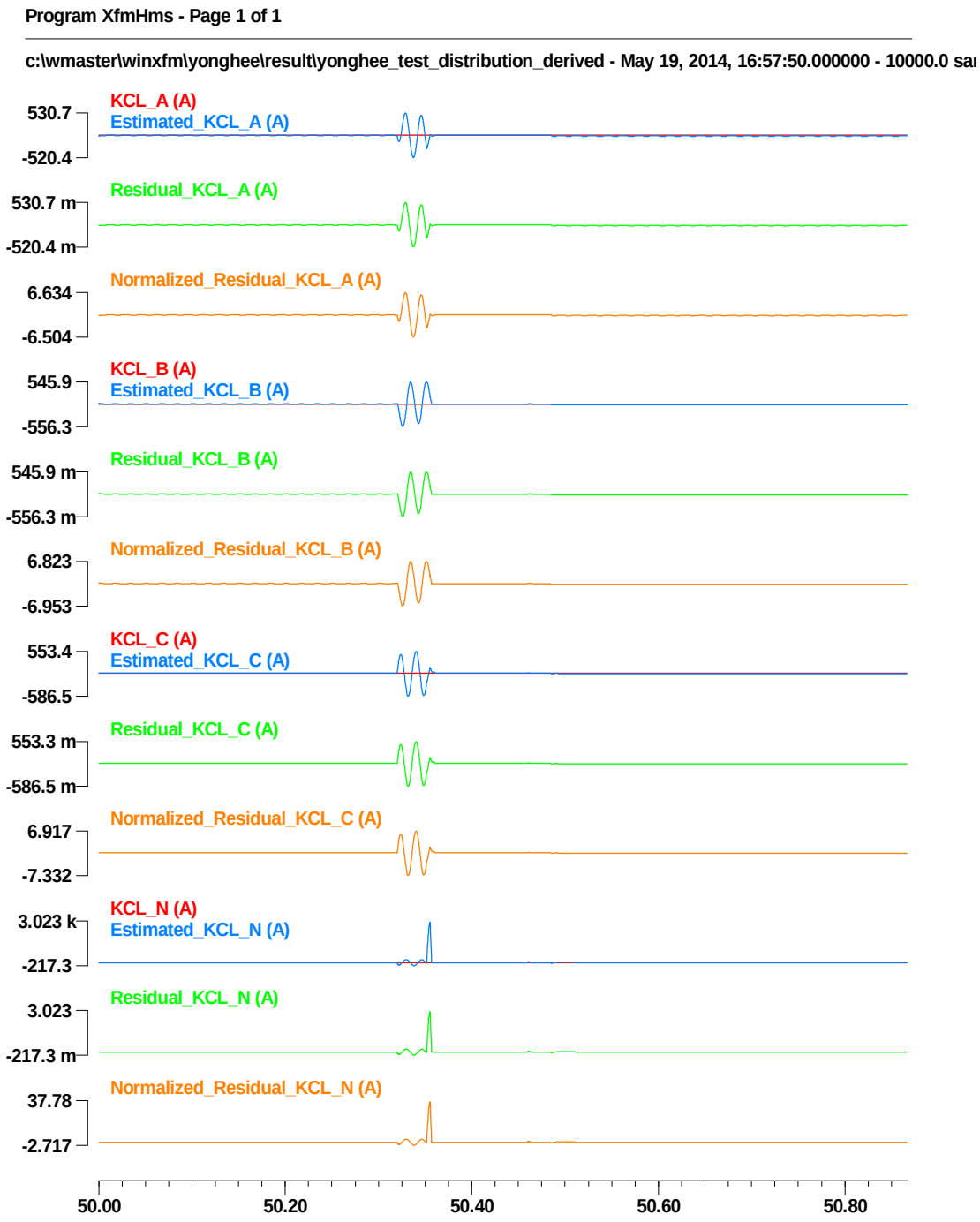

Figure 88: Virtual KCL measurement data at time t, estimated measurement data, residual, and normalized residual at node TH-LOAD3.

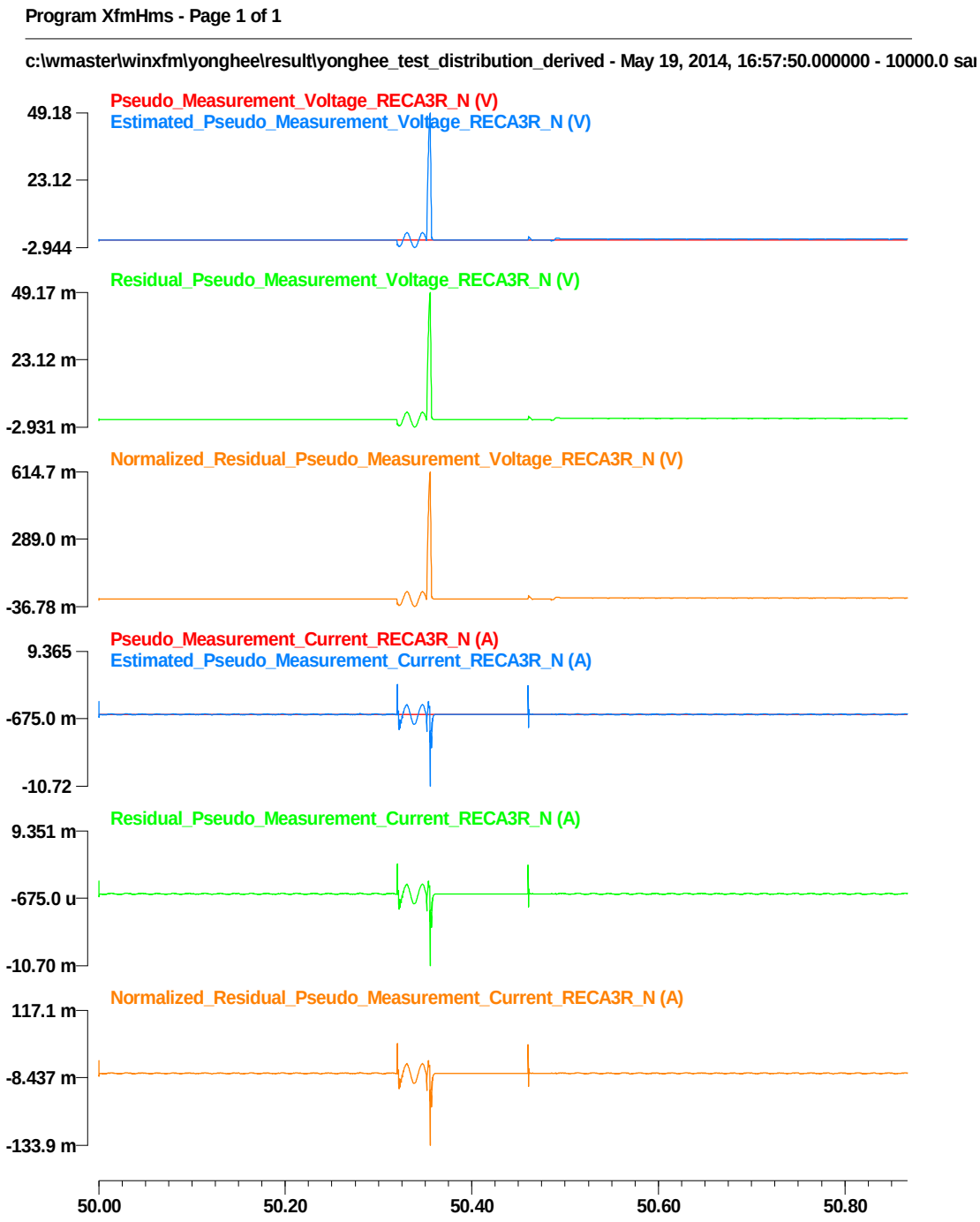

Figure 89: Pseudo measurement data at time t_m, estimated measurement data, residual, and normalized residual at node REC3R.

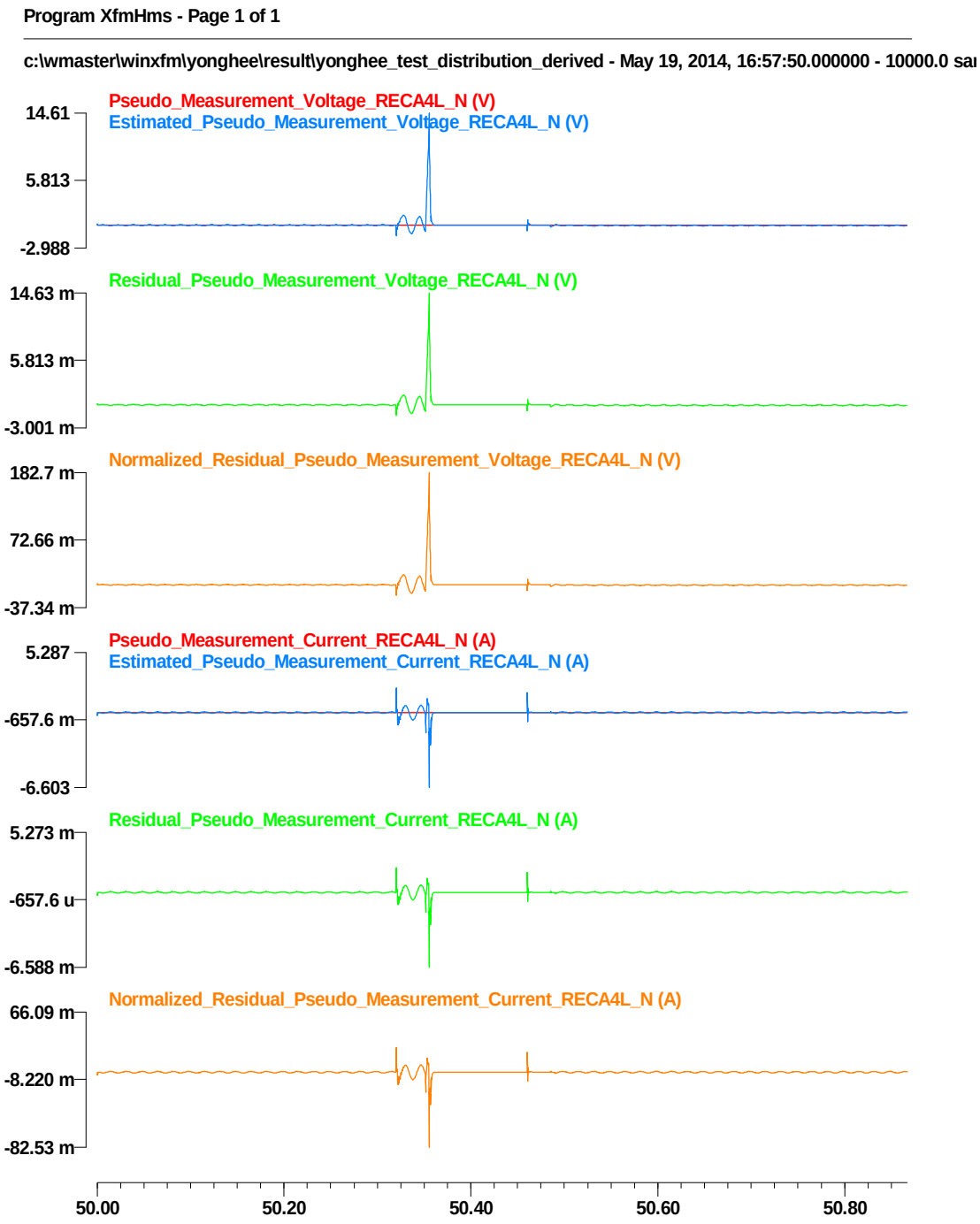

Figure 90: Pseudo measurement data at time t_m, estimated measurement data, residual, and normalized residual at node REC4L.

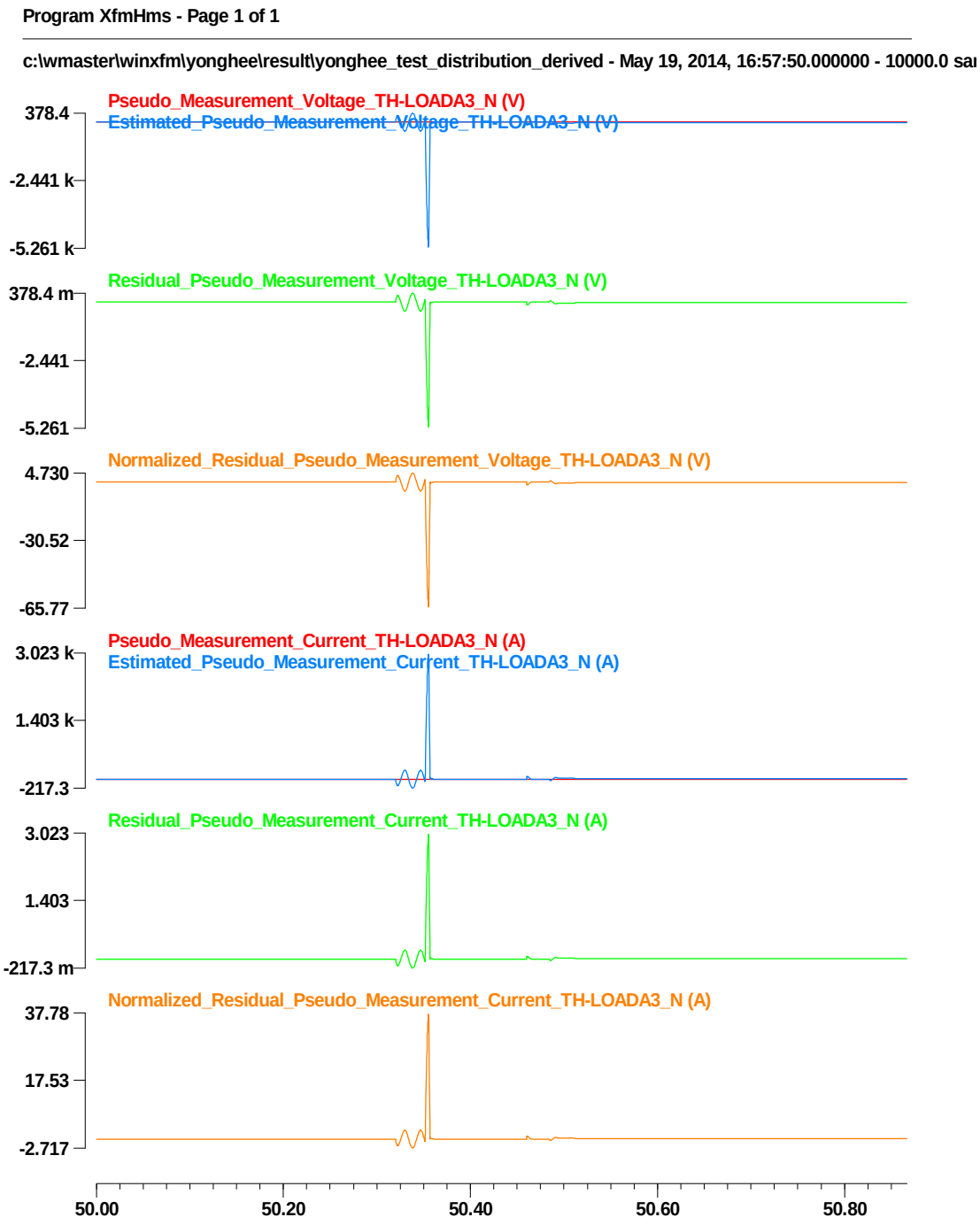

Figure 91: Pseudo measurement data at time t_m, estimated measurement data, residual, and normalized residual at node TH-LOADA3.

Appendix P Results Graphs of the DSE-based Protection Scheme Simulation Results –Microgrid during the Grid-connected Operation

The result graphs of the simulation of the fault condition on the microgrid during the grid-connected operation are depicted in this appendix Figure 92 to Figure 106 as follows: a) confidence level, computation time, and residual, b) external states and some of internal states for time t and t_m, and c) measurement data, estimated measurement data, residual, and normalized residual of actual measurement, virtual measurement, and pseudo measurement data.

a) Confidence level, computation time, and residual for the internal fault case are depicted in Figure 92.

b) External states and some of internal states for time t and t_m are depicted in Figure 93. Internal states of the single section distribution line and the transformer is not explicitly shown in this appendix.

c) Measurement data, estimated measurement data, residual, and normalized residual of actual measurement, virtual measurement, and pseudo measurement data are illustrated in Figure 94 to Figure 106.

c1) Actual measurement data, estimated measurement data, residual, and normalized residual values for time t and t_m. are depicted in Figure 94 to Figure 99. In more detail, for time t and t_m, across measurement data and estimated measurement data at node FEEDER1 are compared each other as shown in Figure 94. Residual and normalized residual values are also depicted in the same figure. Result graphs of node FEEDER2 and M-LOAD1 are depicted in Figure 95 to Figure 96. In addition, through measurement data

and estimated measurement data at node FEEDER1, FEEDER2, and M-LOAD1 are compared each other, and the resulting residual and normalized residual values are shown in Figure 97 to Figure 99.

c2) Virtual measurement data, estimated measurement data, residual, and normalized residual values for time t and t_m are depicted in Figure 100 to Figure 103. In more detail, internal virtual measurement data and estimated measurement data of the first single section distribution line model for time t and t_m are compared each other, and the resulting residual and normalized residual values are shown in Figure 100. Result graphs of the second and the third single section distribution line model and the transformer model are depicted in Figure 101 and Figure 102, respectively. Moreover, KCL virtual measurement data and estimated measurement data at node M-FAC for time t and t_m are compared each other, and the resulting residual and normalized residual values are shown in Figure 103.

c3) Pseudo measurement data, estimated measurement data, residual, and normalized residual values for time t and t_m are depicted in Figure 104 to Figure 106. In more detail, pseudo measurement data and estimated measurement data at node FEEDER1, FEEDER2, and M-LOAD1 for time t and t_m are compared each other, and the resulting residual and normalized residual values are shown in Figure 104 to Figure 106.

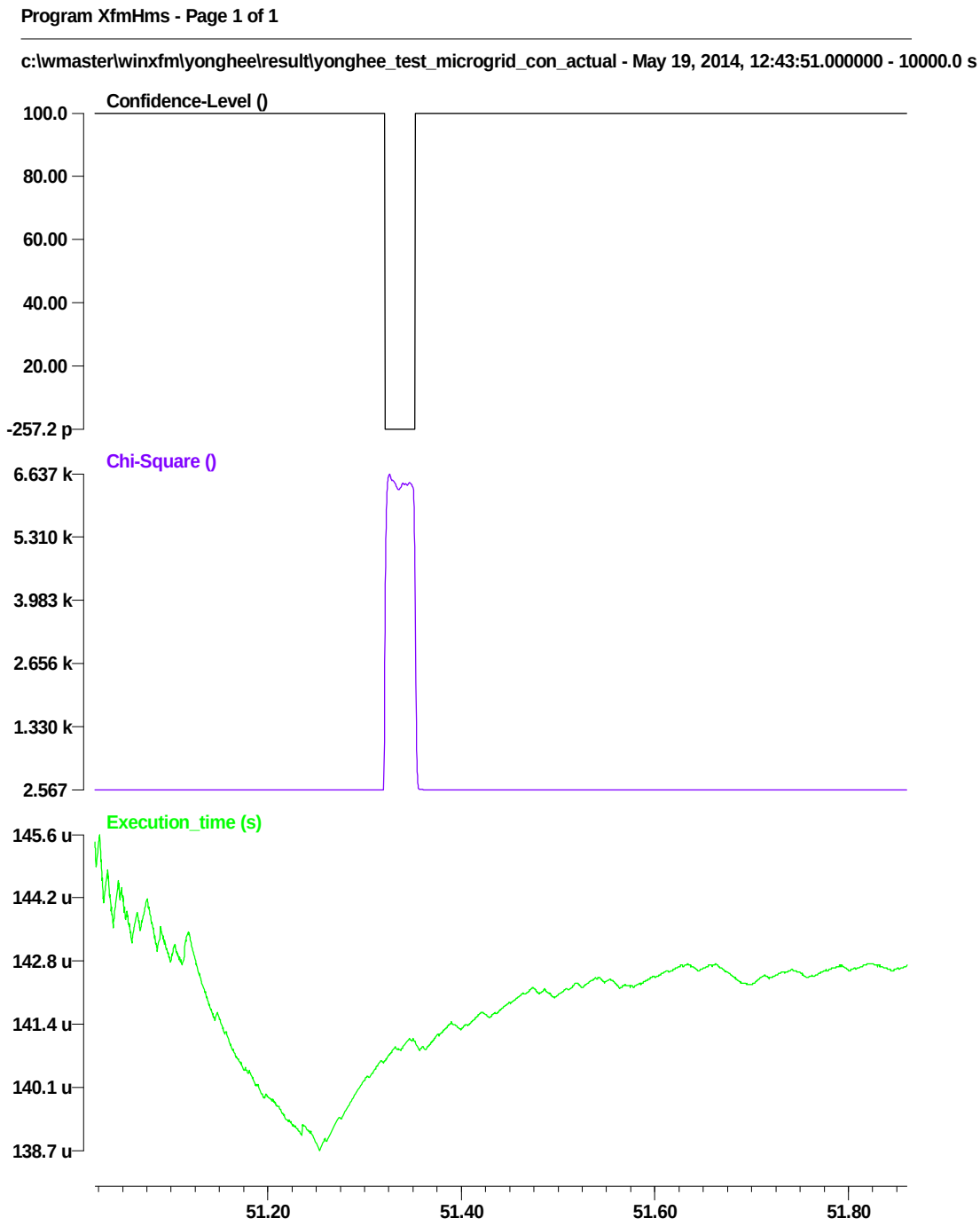

Figure 92: Confidence level, computation time, and residual for the internal fault case on the microgrid during the grid-connected mode.

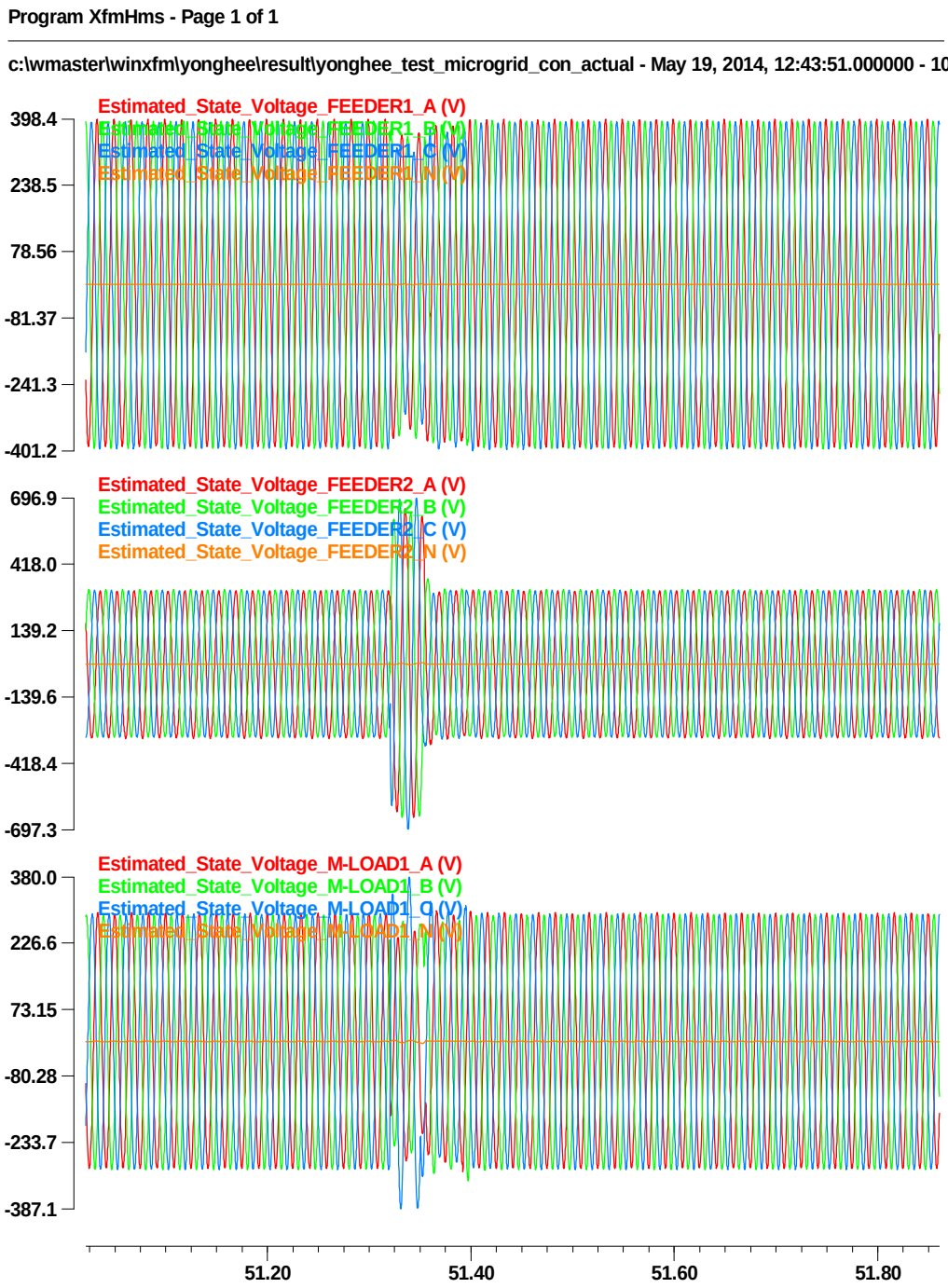

Figure 93: States at node FEEDER1, FEEDER2, and M-LOAD1.

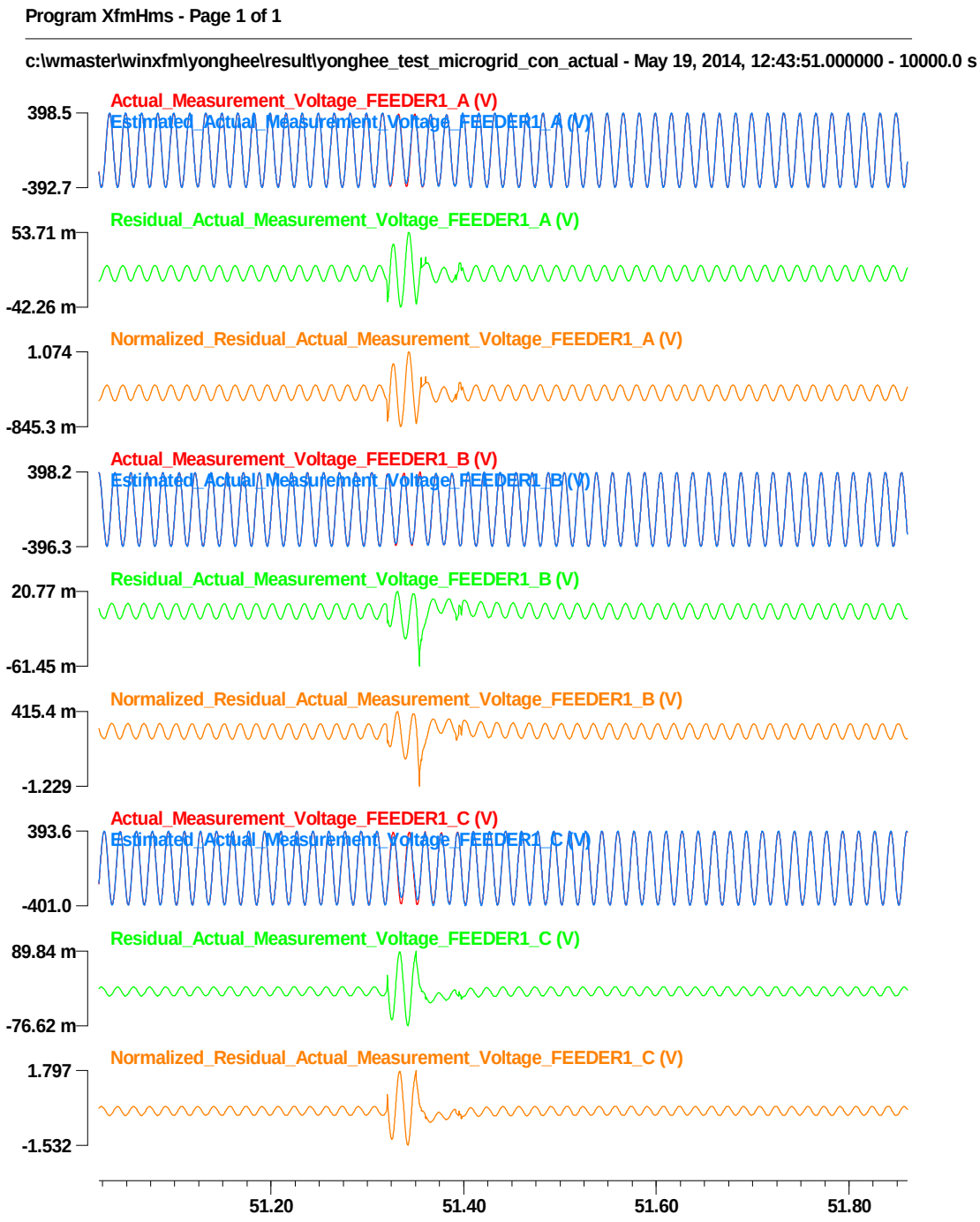

Figure 94: Actual across measurement data, estimated measurement data, residual, and normalized residual at node FEEDER1.

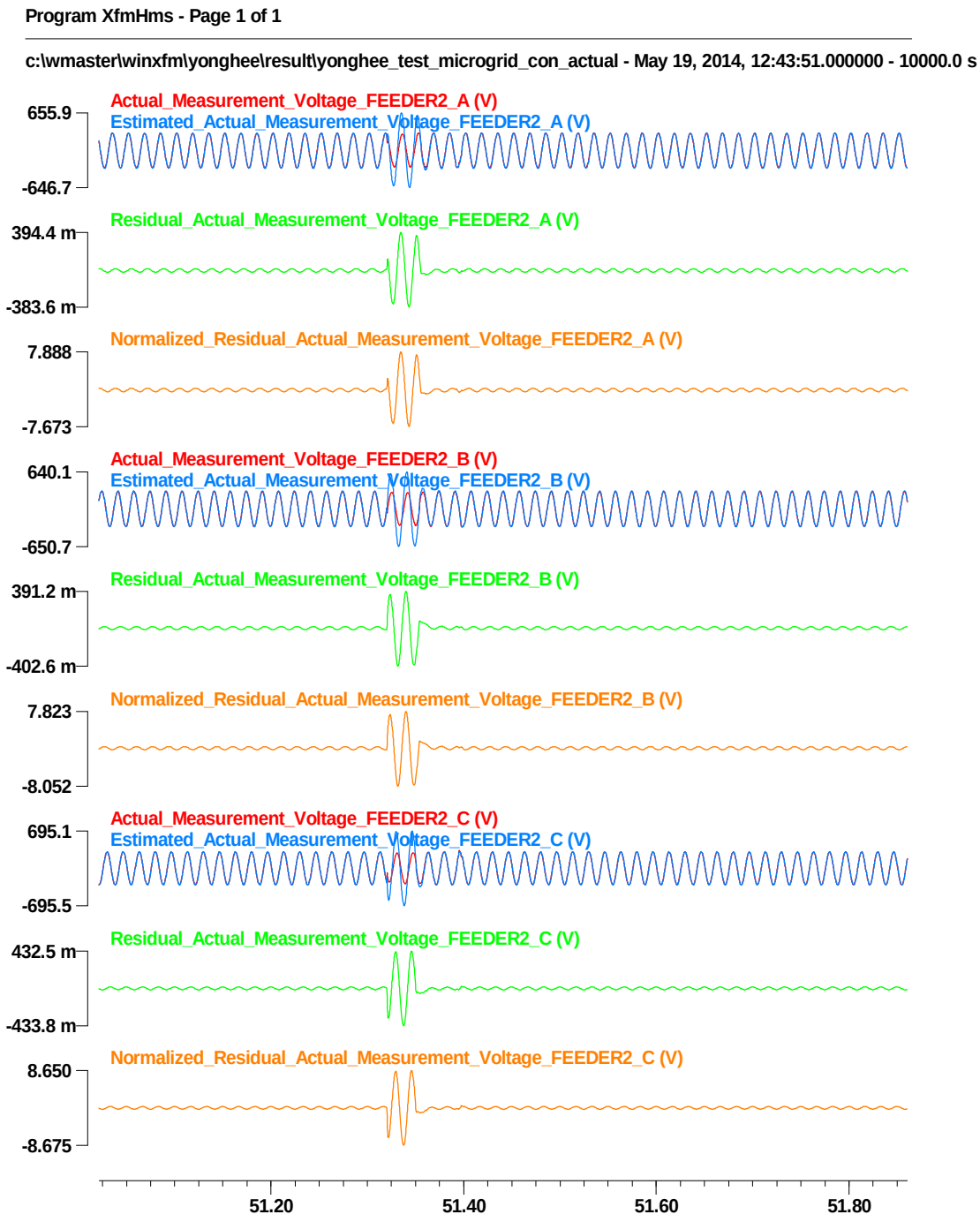

Figure 95: Actual across measurement data at time t, estimated measurement data, residual, and normalized residual at node FEEDER2.

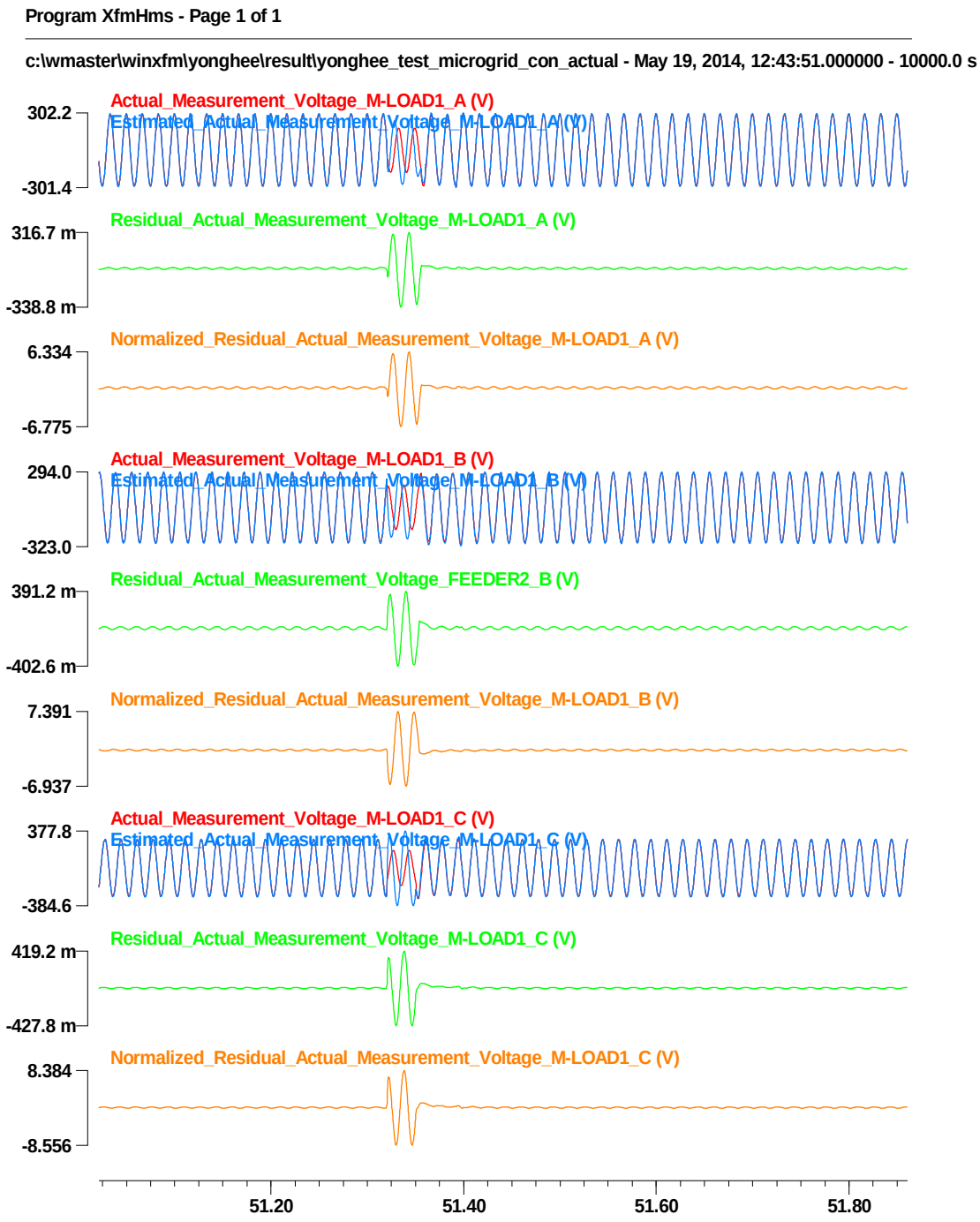

Figure 96: Actual across measurement data at time t, estimated measurement data, residual, and normalized residual at node M-LOAD1.

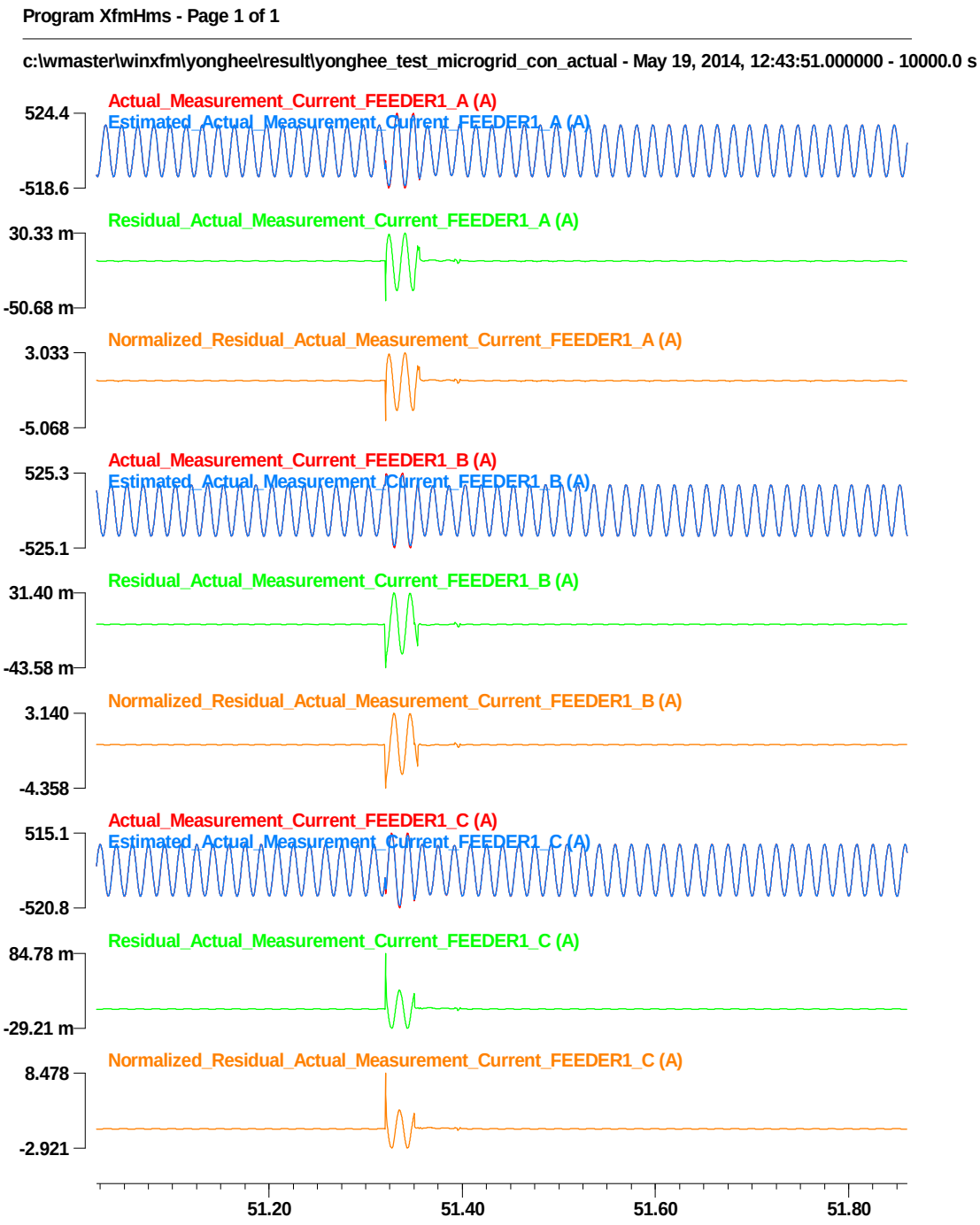

Figure 97: Actual through measurement data at time t, estimated measurement data, residual, and normalized residual at node FEEDER1.

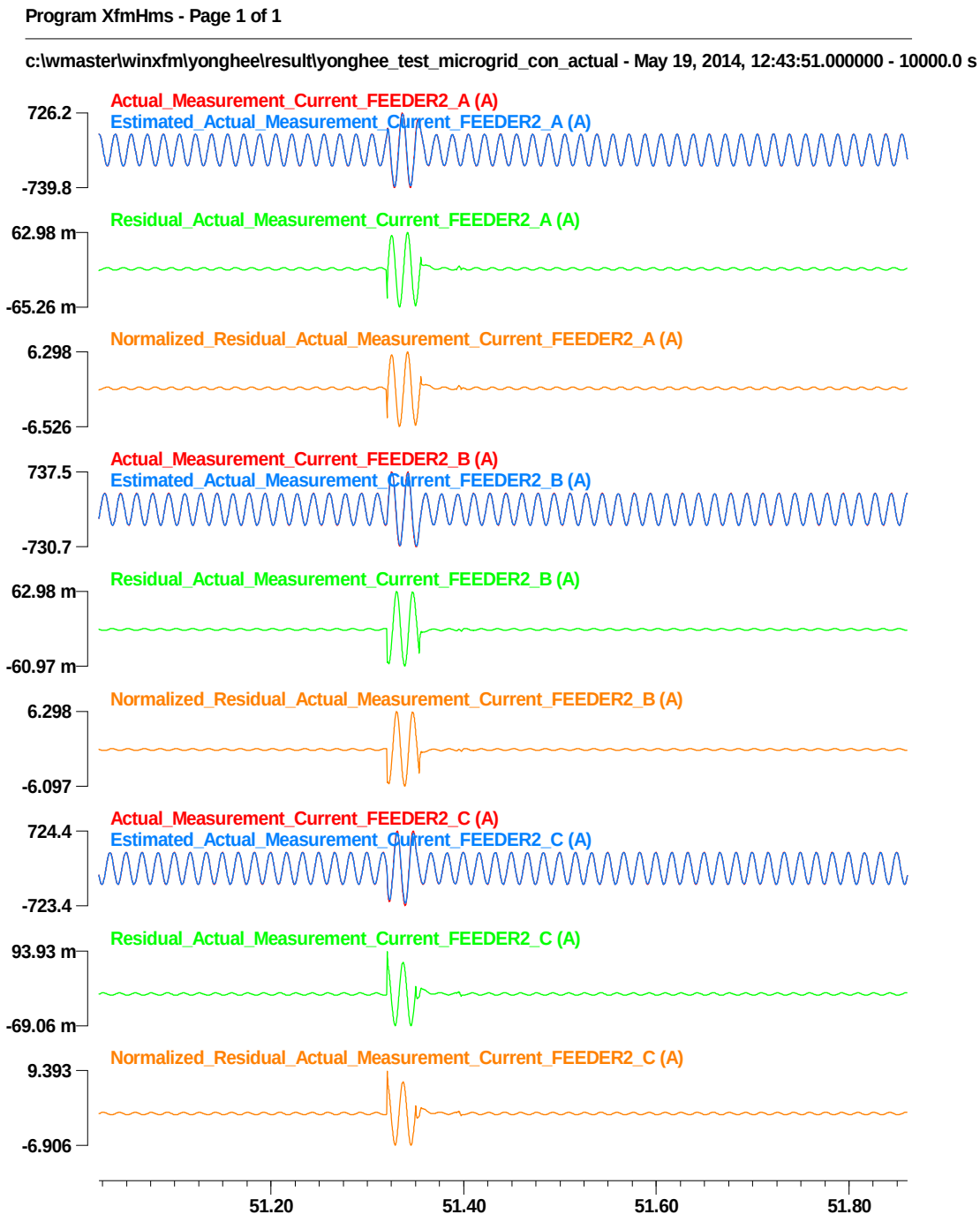

Figure 98: Actual through measurement data at time t, estimated measurement data, residual, and normalized residual at node FEEDER2.

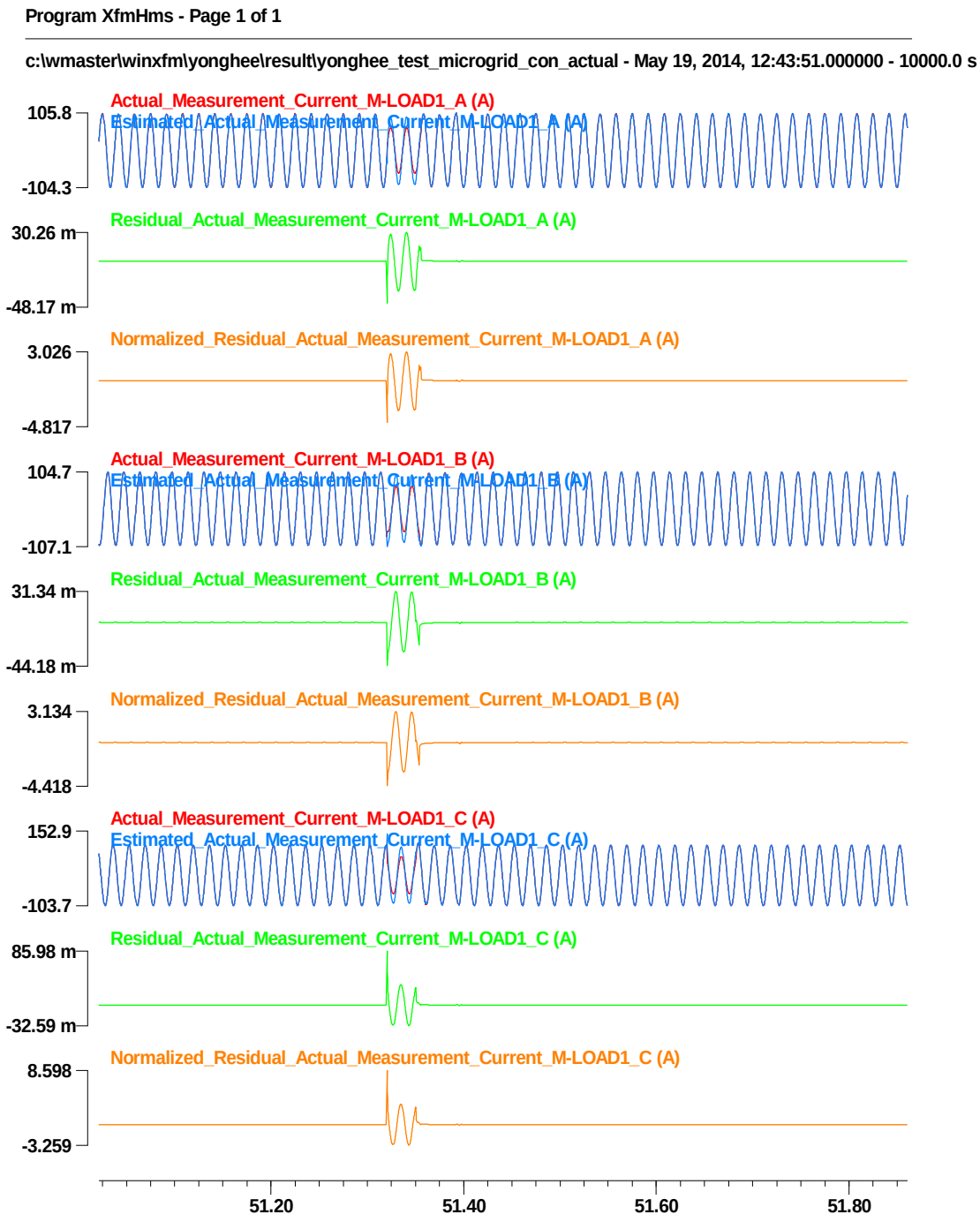

Figure 99: Actual through measurement data at time t, estimated measurement data, residual, and normalized residual at node M-LOAD1.

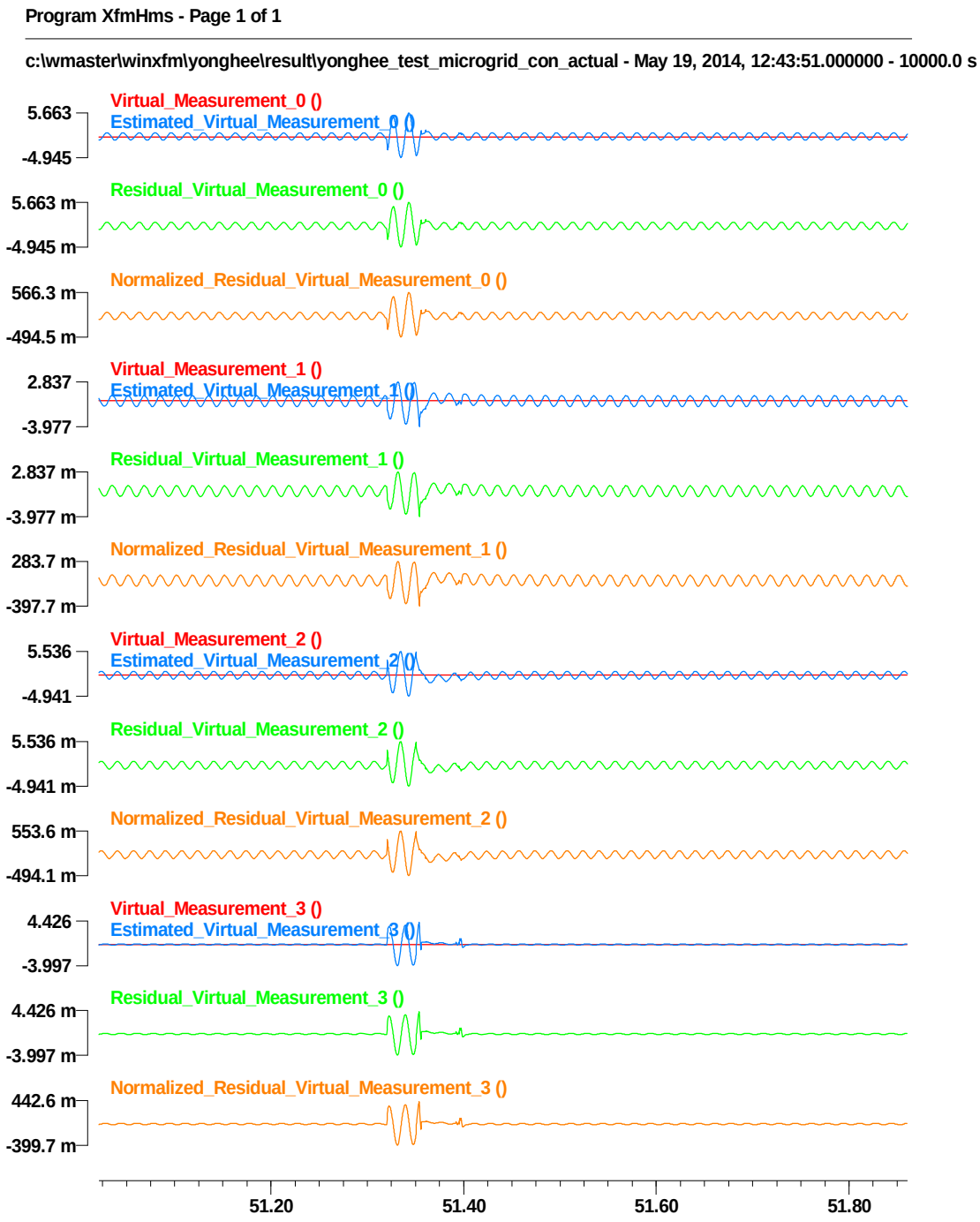

Figure 100: Virtual measurement data at time t, estimated measurement data, residual, and normalized residual of the first line model.

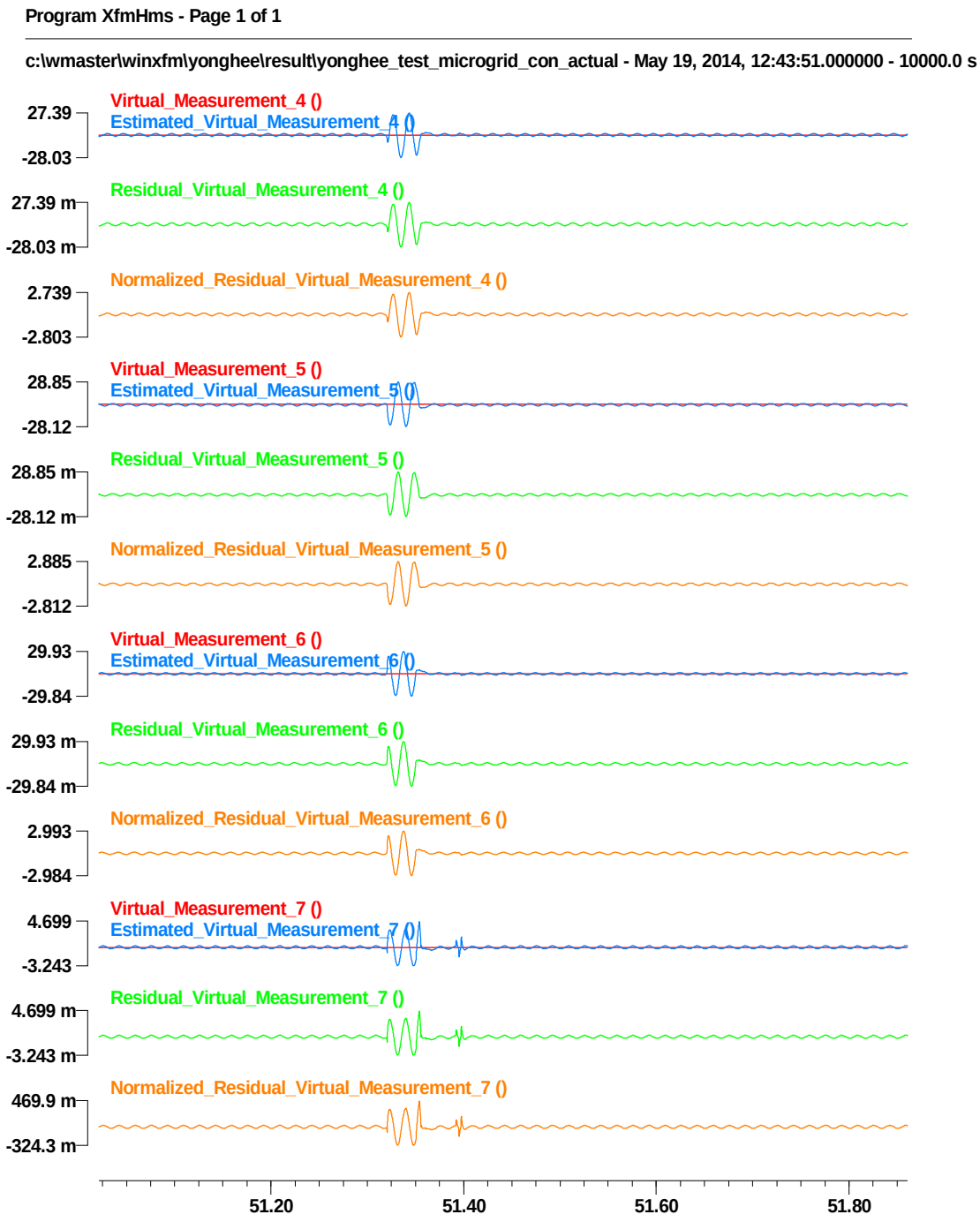

Figure 101: Virtual measurement data at time t, estimated measurement data, residual, and normalized residual of the second line model.

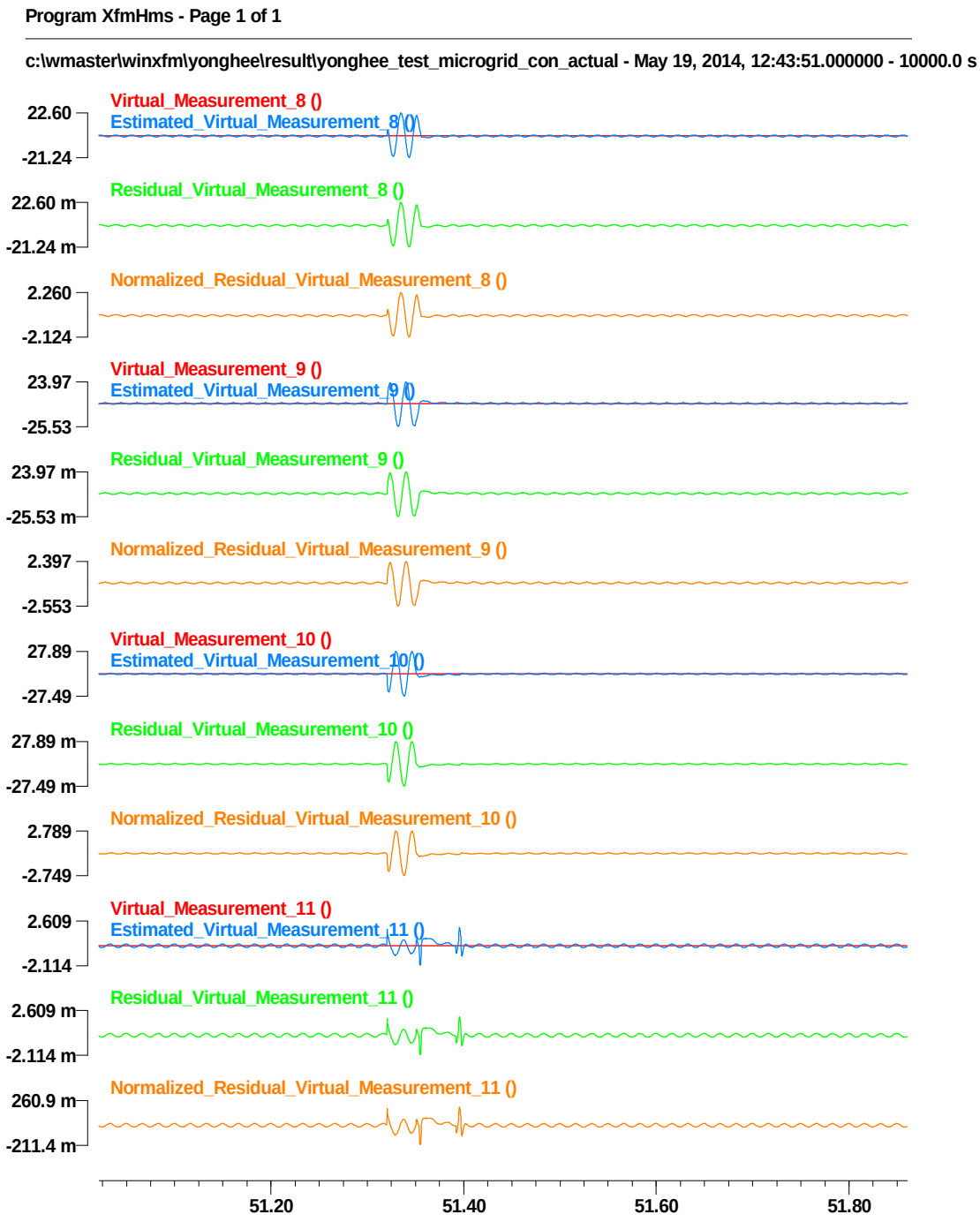

Figure 102: Virtual measurement data at time t, estimated measurement data, residual, and normalized residual of the third line model.

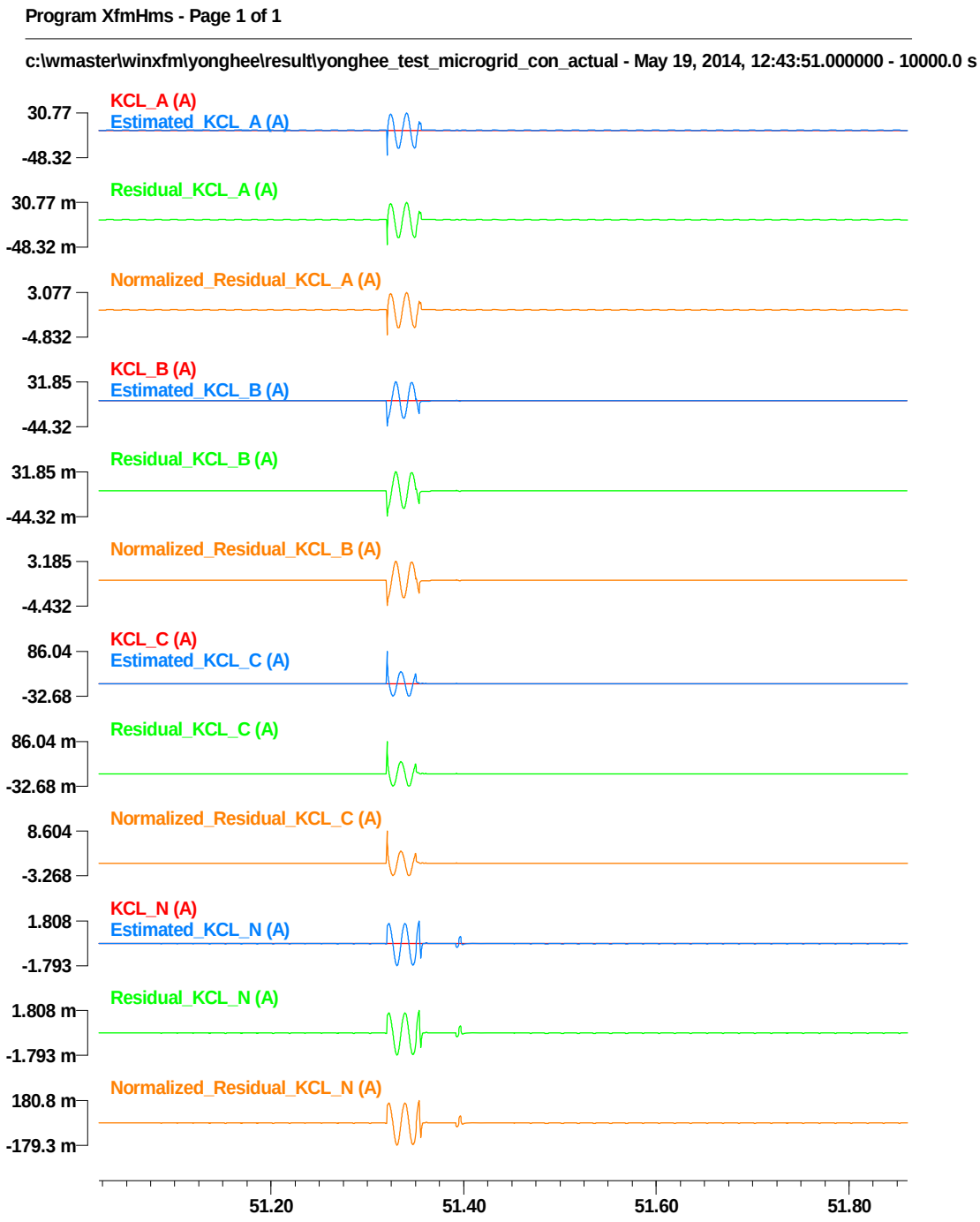

Figure 103: Virtual KCL measurement data at time t, estimated measurement data, residual, and normalized residual at node M-FAC.

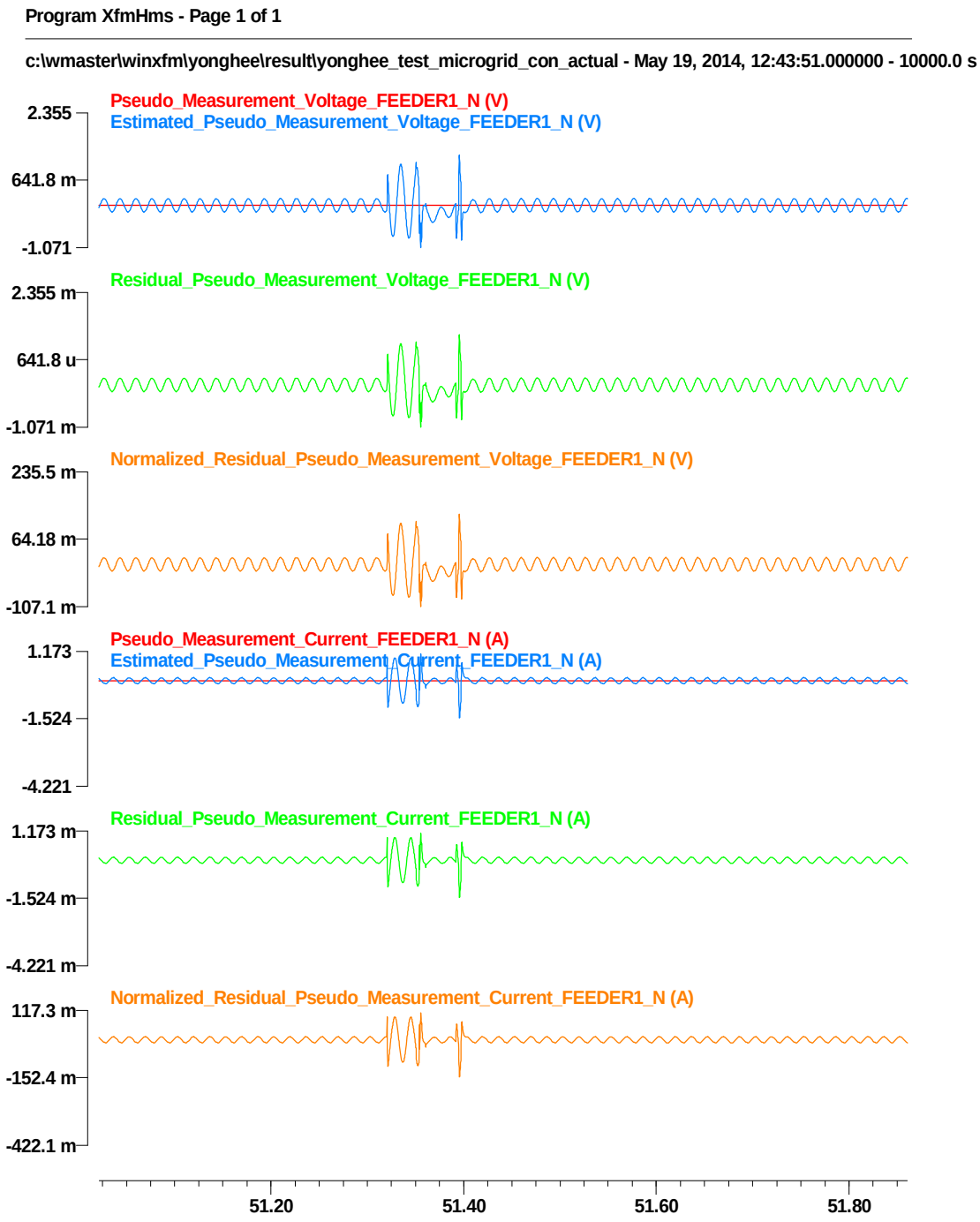

Figure 104: Pseudo measurement data at time t_m, estimated measurement data, residual, and normalized residual at node FEEDER1.

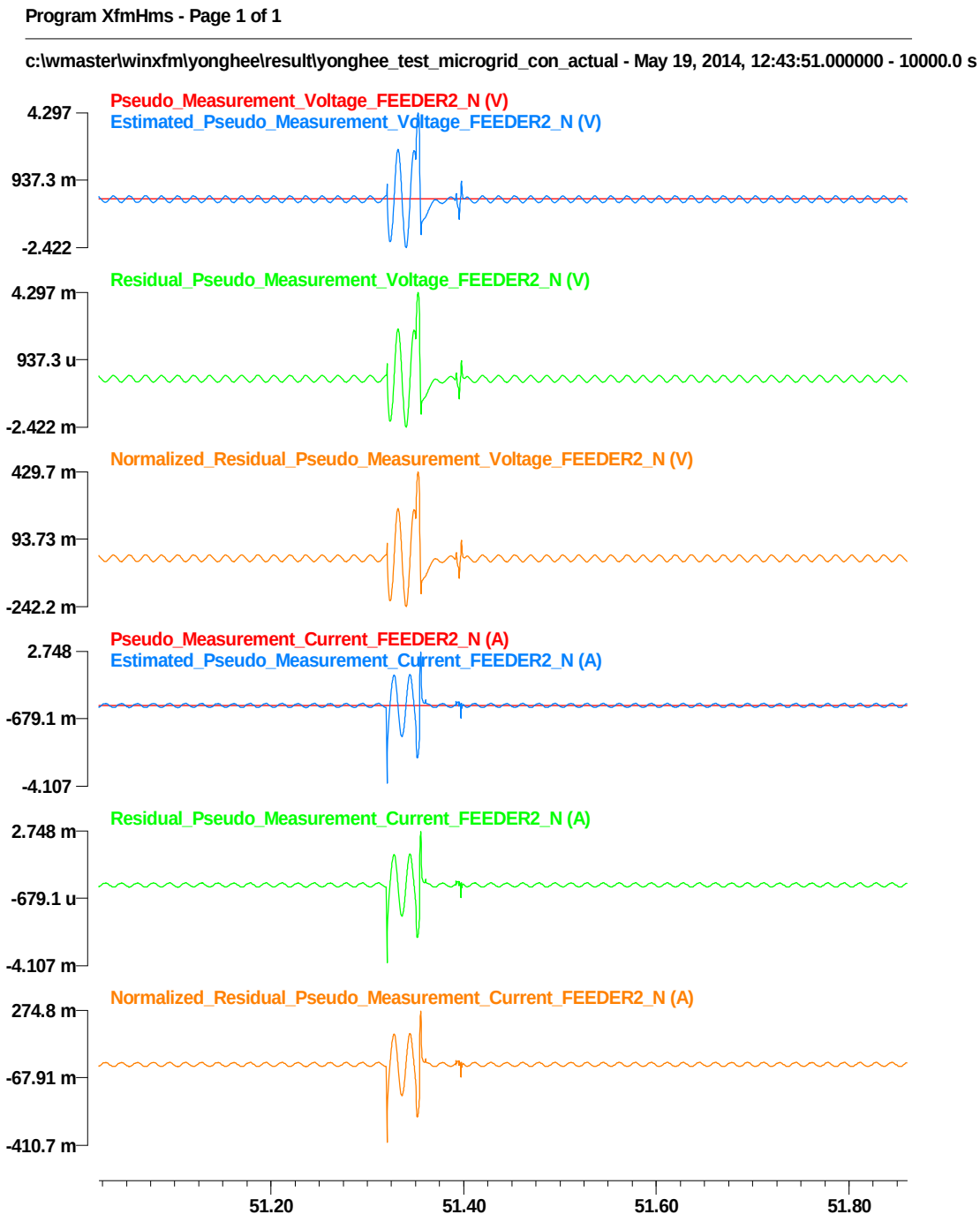

Figure 105: Pseudo measurement data at time t_m, estimated measurement data, residual, and normalized residual at node FEEDER2.

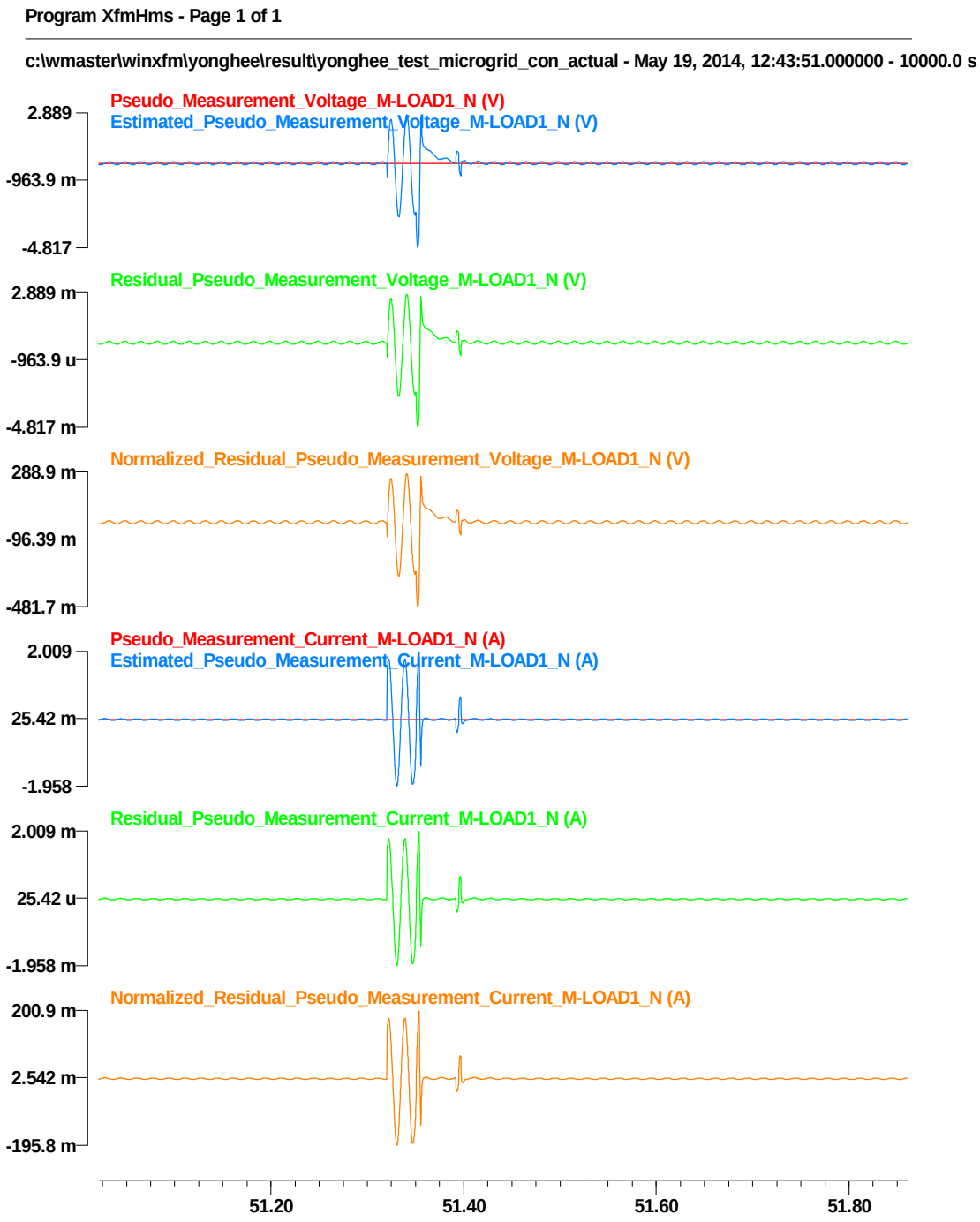

Figure 106: Pseudo measurement data at time t_m, estimated measurement data, residual, and normalized residual at node M-LOAD1.

Appendix Q Results Graphs of the DSE-based Protection Scheme Laboratory Test Results –Microgrid during the Grid-connected Operation

The experimental results of the fault condition on the microgrid during the grid-connected operation are depicted in this appendix Figure 107 to Figure 121 as follows: a) confidence level, computation time, and residual, b) external states and some of internal states for time t and t_m, and c) measurement data, estimated measurement data, residual, and normalized residual of actual measurement, virtual measurement, and pseudo measurement data.

a) Confidence level, computation time, and residual for the internal fault case are depicted in Figure 107.

b) External states and some of internal states for time t and t_m are depicted in Figure 108. Internal states of the single section distribution line and the transformer is not explicitly shown in this appendix.

c) Measurement data, estimated measurement data, residual, and normalized residual of actual measurement, virtual measurement, and pseudo measurement data are illustrated in Figure 109 to Figure 121.

c1) Actual measurement data, estimated measurement data, residual, and normalized residual values for time t and t_m. are depicted in Figure 109 and Figure 112. In more detail, for time t and t_m, across measurement data and estimated measurement data at node FEEDER1 are compared each other as shown in Figure 109. Residual and normalized residual values are also depicted in the same figure. In addition, through measurement data and estimated measurement data at node FEEDER1, are compared

each other, and the resulting residual and normalized residual values are shown in Figure 112.

c2) Derived measurement data, estimated measurement data, residual, and normalized residual values for time t and t_m. are depicted in Figure 110, Figure 111, Figure 113, and Figure 144. In more detail, for time t and t_m, derived across measurement data and estimated measurement data at node FEEDER2 and M-LOAD3 are compared each other as shown in Figure 110 and Figure 111, respectively. Residual and normalized residual values are also depicted in the same figure. In addition, derived through measurement data and estimated measurement data at node FEEDER2 and M-LOAD3 are compared each other, and the resulting residual and normalized residual values are shown in Figure 113 and Figure 144.

c2) Virtual measurement data, estimated measurement data, residual, and normalized residual values for time t and t_m are depicted in Figure 115 to Figure 118. In more detail, internal virtual measurement data and estimated measurement data of the first single section distribution line model for time t and t_m are compared each other, and the resulting residual and normalized residual values are shown in Figure 115. Result graphs of the second and the third single section distribution line model and the transformer model are depicted in Figure 116 and Figure 117, respectively. Moreover, KCL virtual measurement data and estimated measurement data at node M-FAC for time t and t_m are compared each other, and the resulting residual and normalized residual values are shown in Figure 118.

c3) Pseudo measurement data, estimated measurement data, residual, and normalized residual values for time t and t_m are depicted in Figure 119 to Figure 121. In more detail,

pseudo measurement data and estimated measurement data at node FEEDER1, FEEDER2, and M-LOAD1 for time t and t_m are compared each other, and the resulting residual and normalized residual values are shown in Figure 119 to Figure 121.

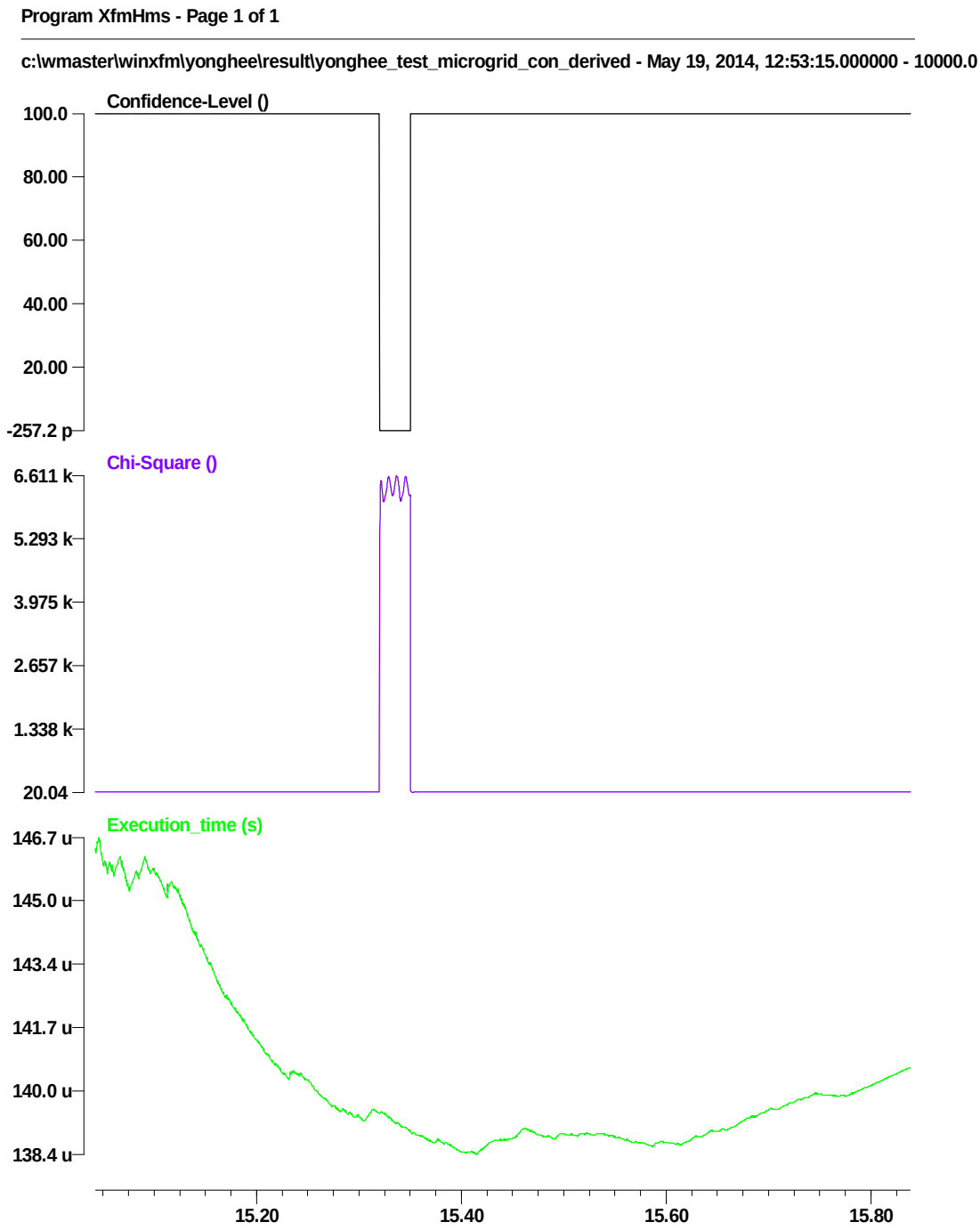

Figure 107: Confidence level, computation time, and residual for the internal fault case on the microgrid during the grid-connected mode.

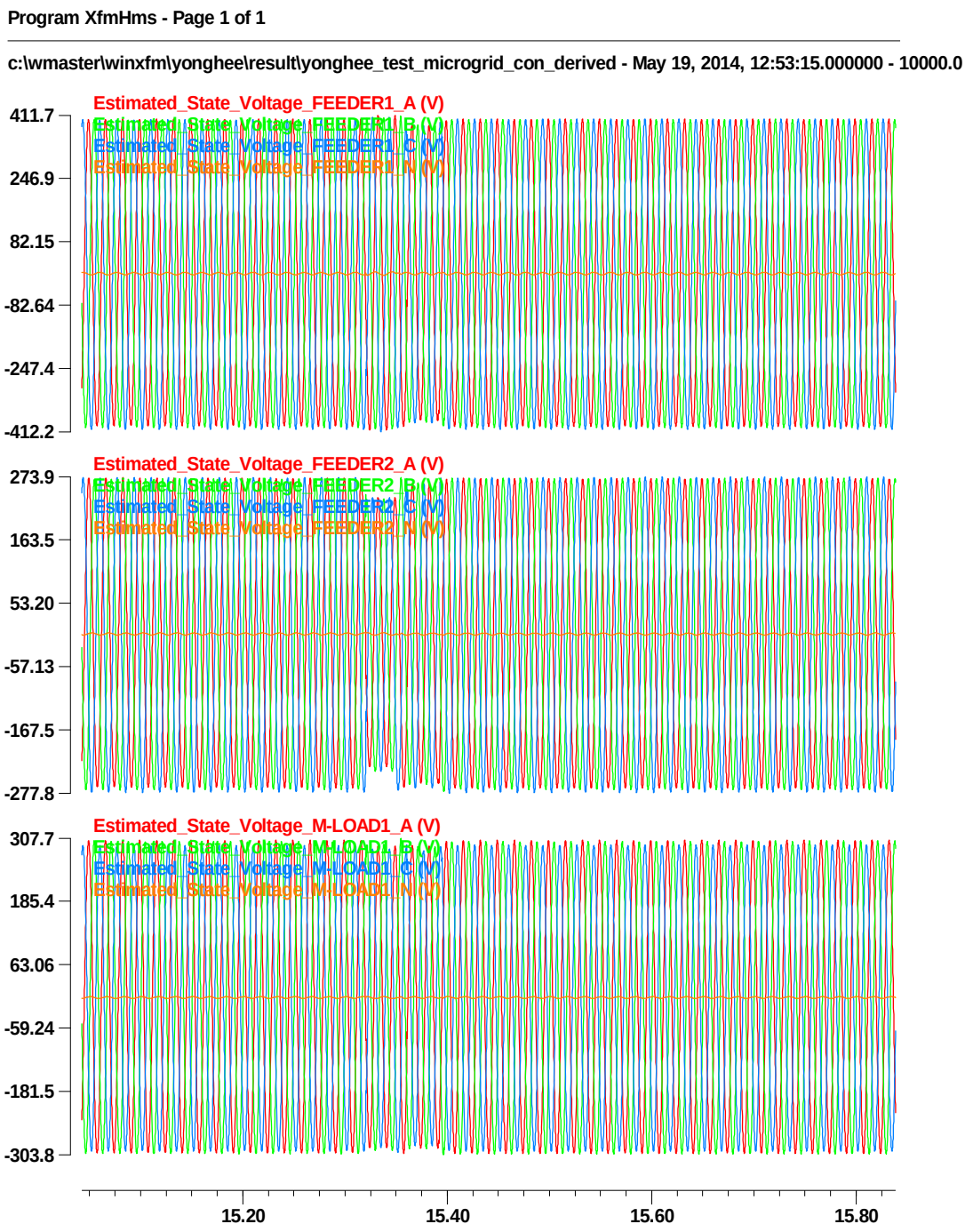

Figure 108: States at node FEEDER1, FEEDER2, and M-LOAD1.

v

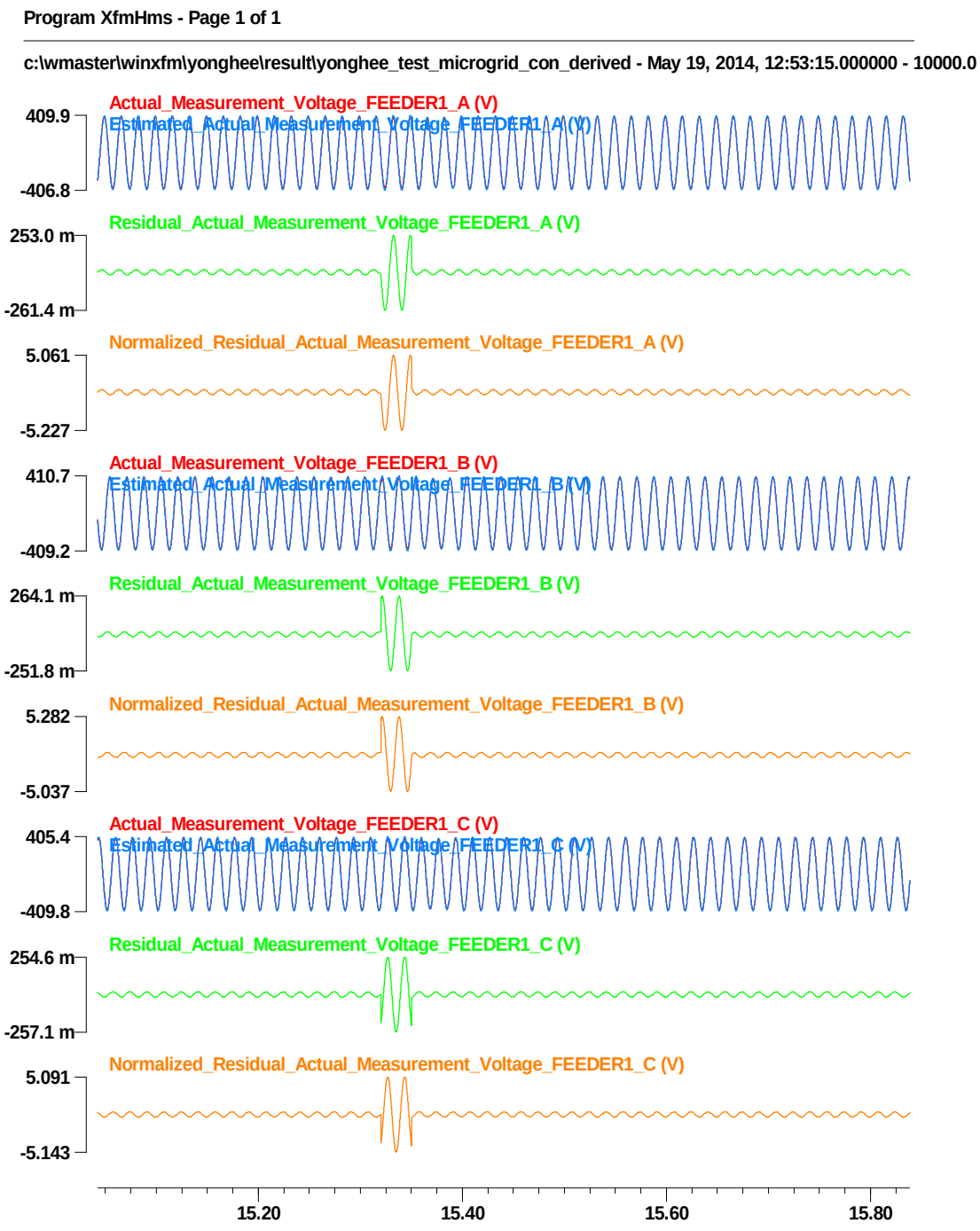

Figure 109: Actual across measurement data, estimated measurement data, residual, and normalized residual at node FEEDER1.

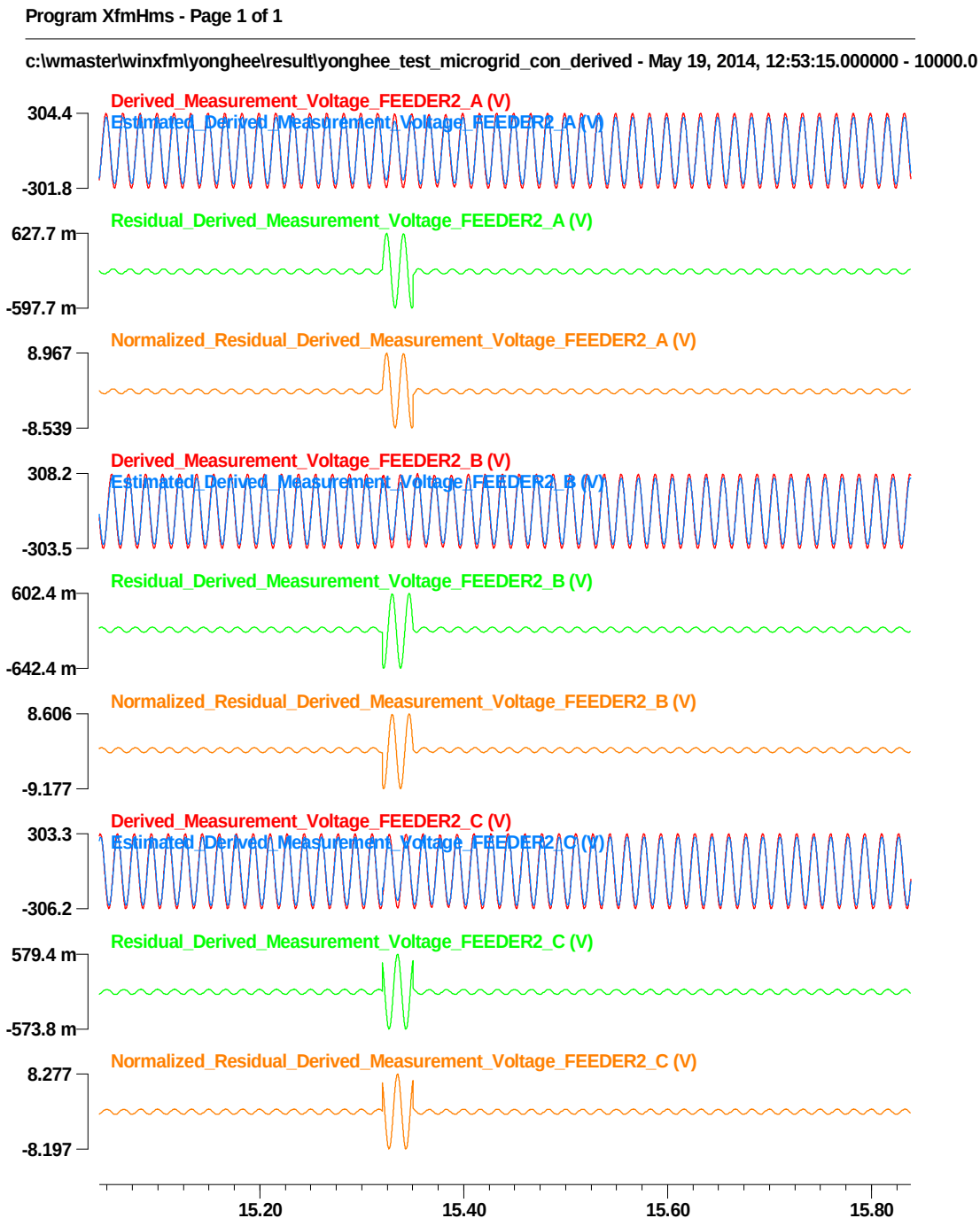

Figure 110: Derived across measurement data at time t, estimated measurement data, residual, and normalized residual at node FEEDER2.

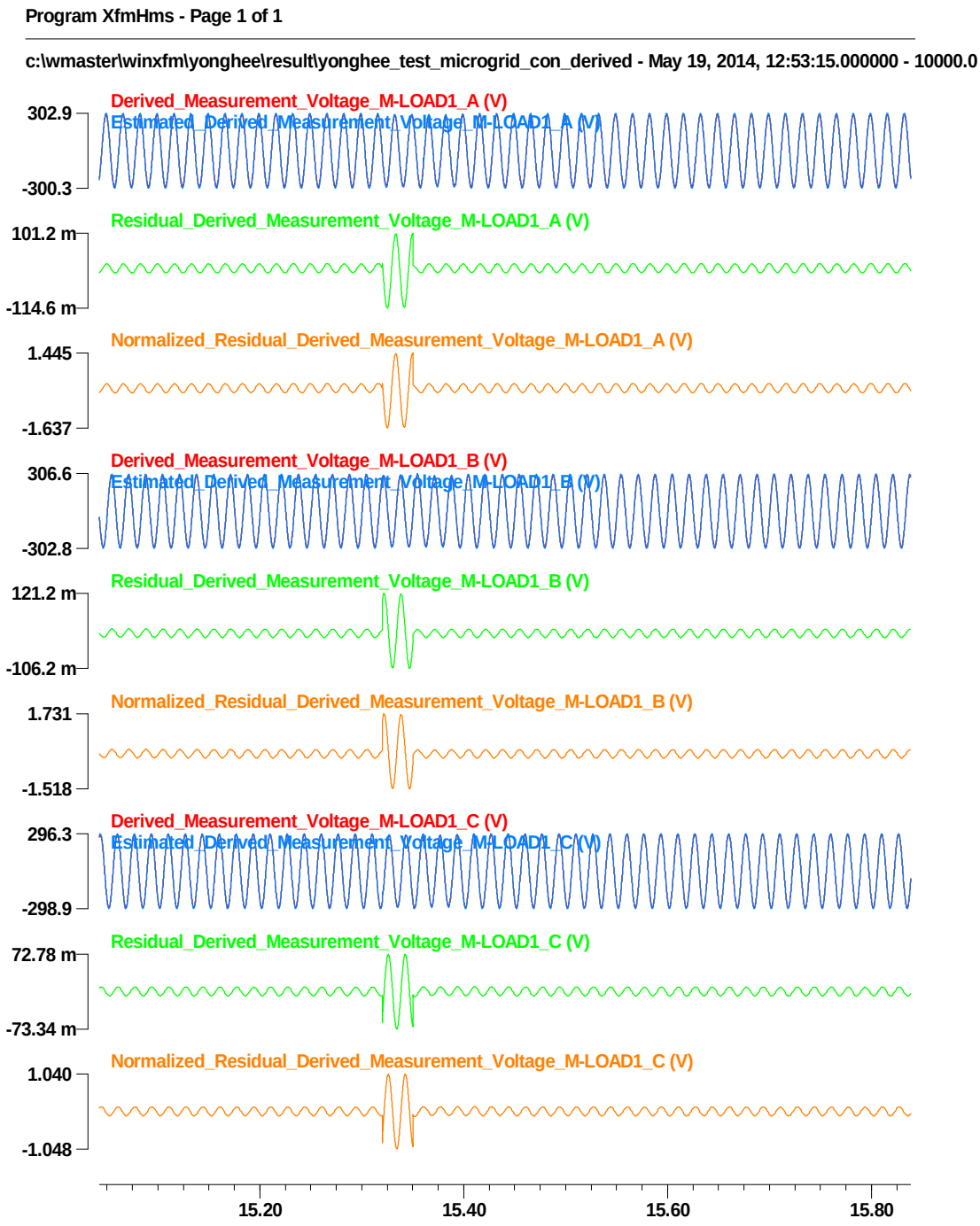

Figure 111: Derived across measurement data at time t, estimated measurement data, residual, and normalized residual at node M-LOAD1.

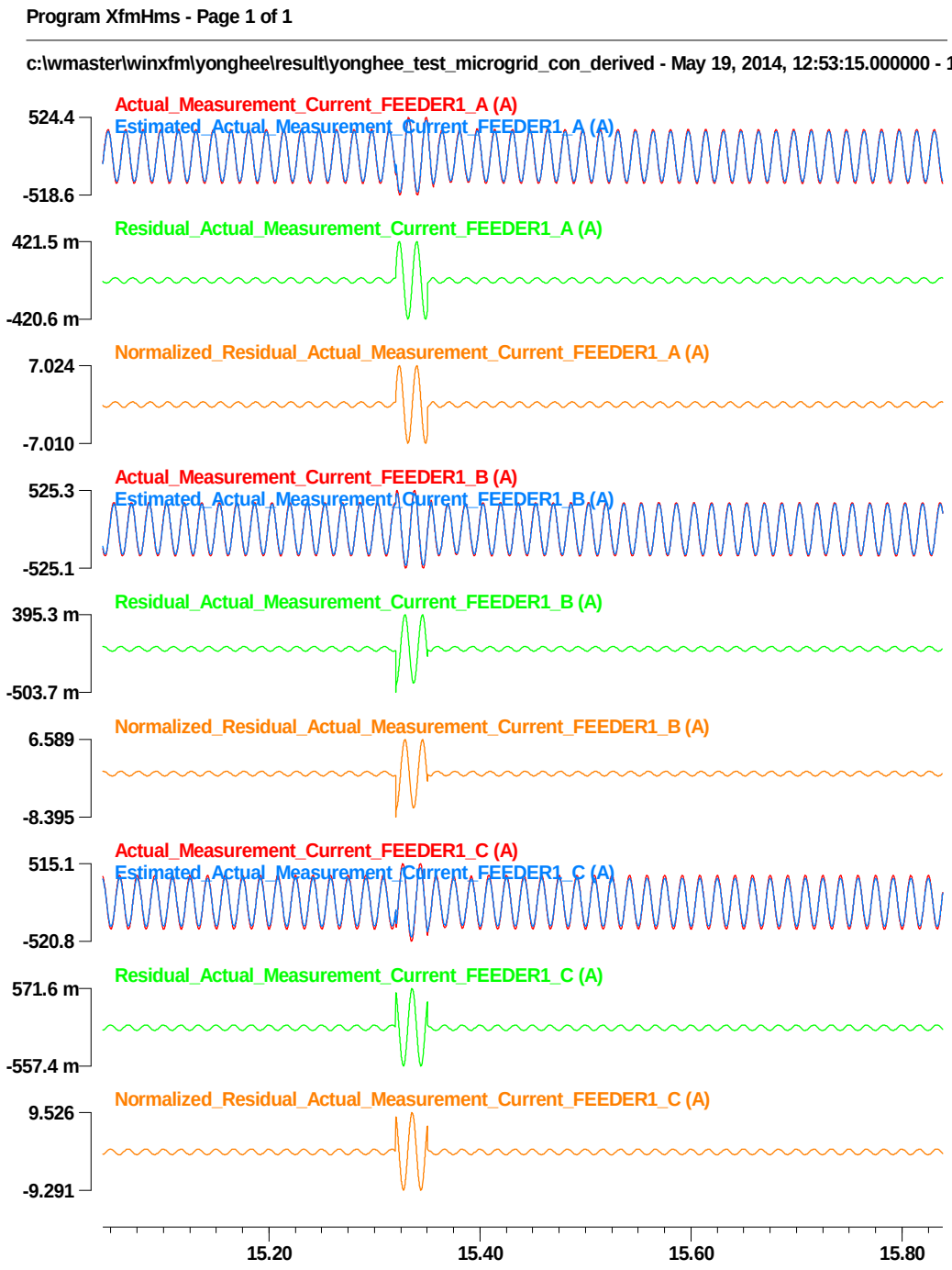

Figure 112: Actual through measurement data at time t, estimated measurement data, residual, and normalized residual at node FEEDER1.

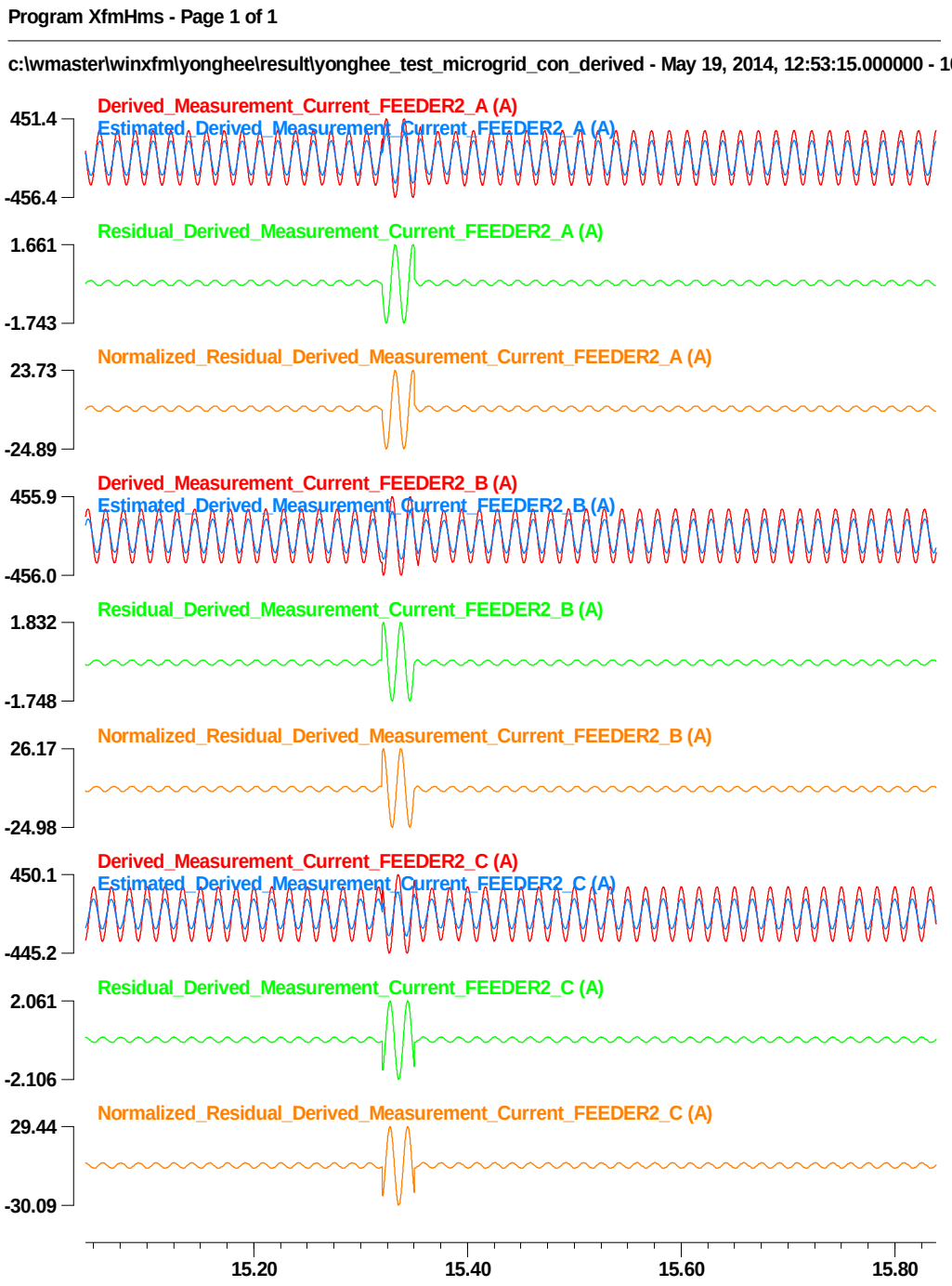

Figure 113: Derived through measurement data at time t, estimated measurement data, residual, and normalized residual at node FEEDER2.

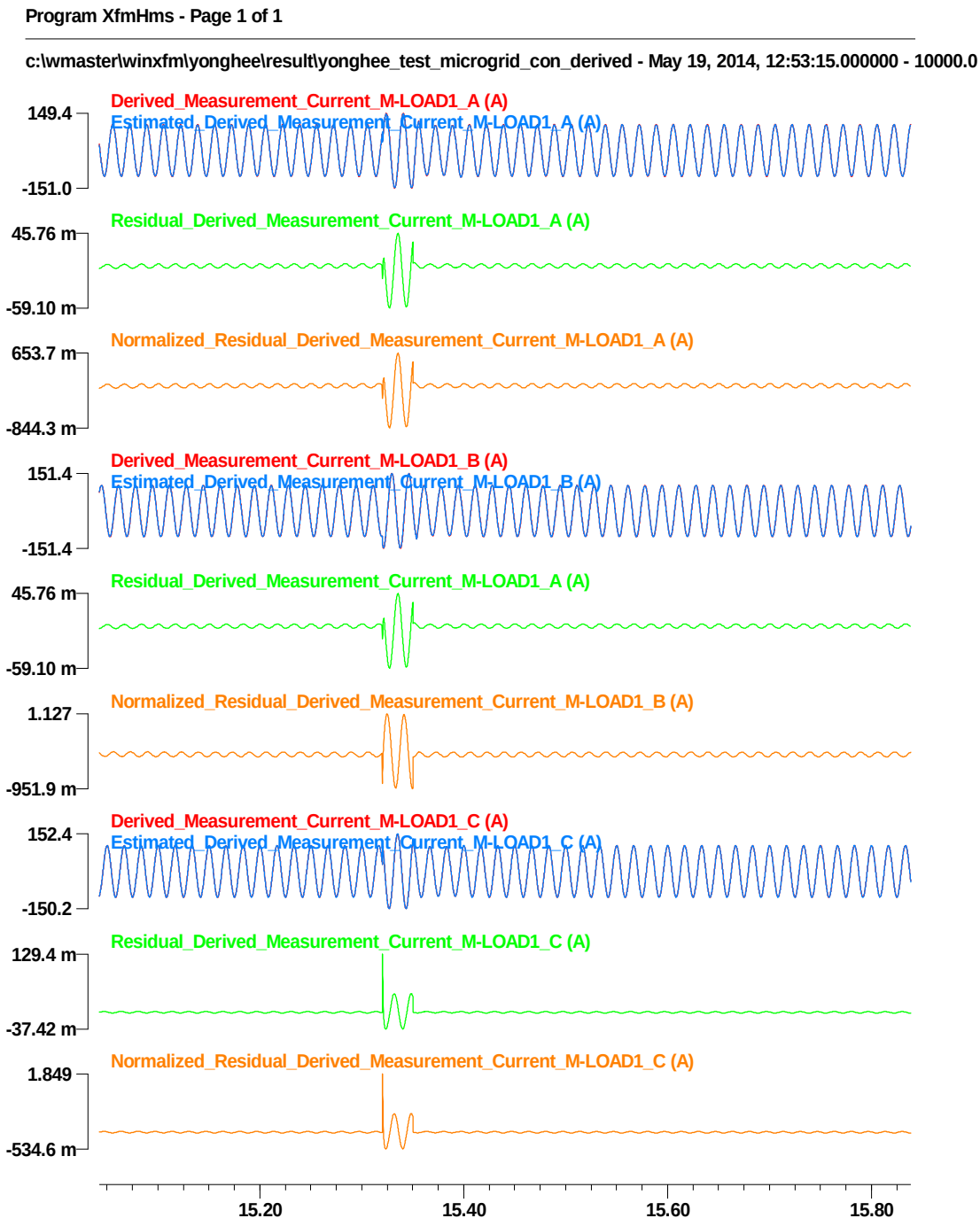

Figure 114: Derived through measurement data at time t, estimated measurement data, residual, and normalized residual at node M-LOAD1.

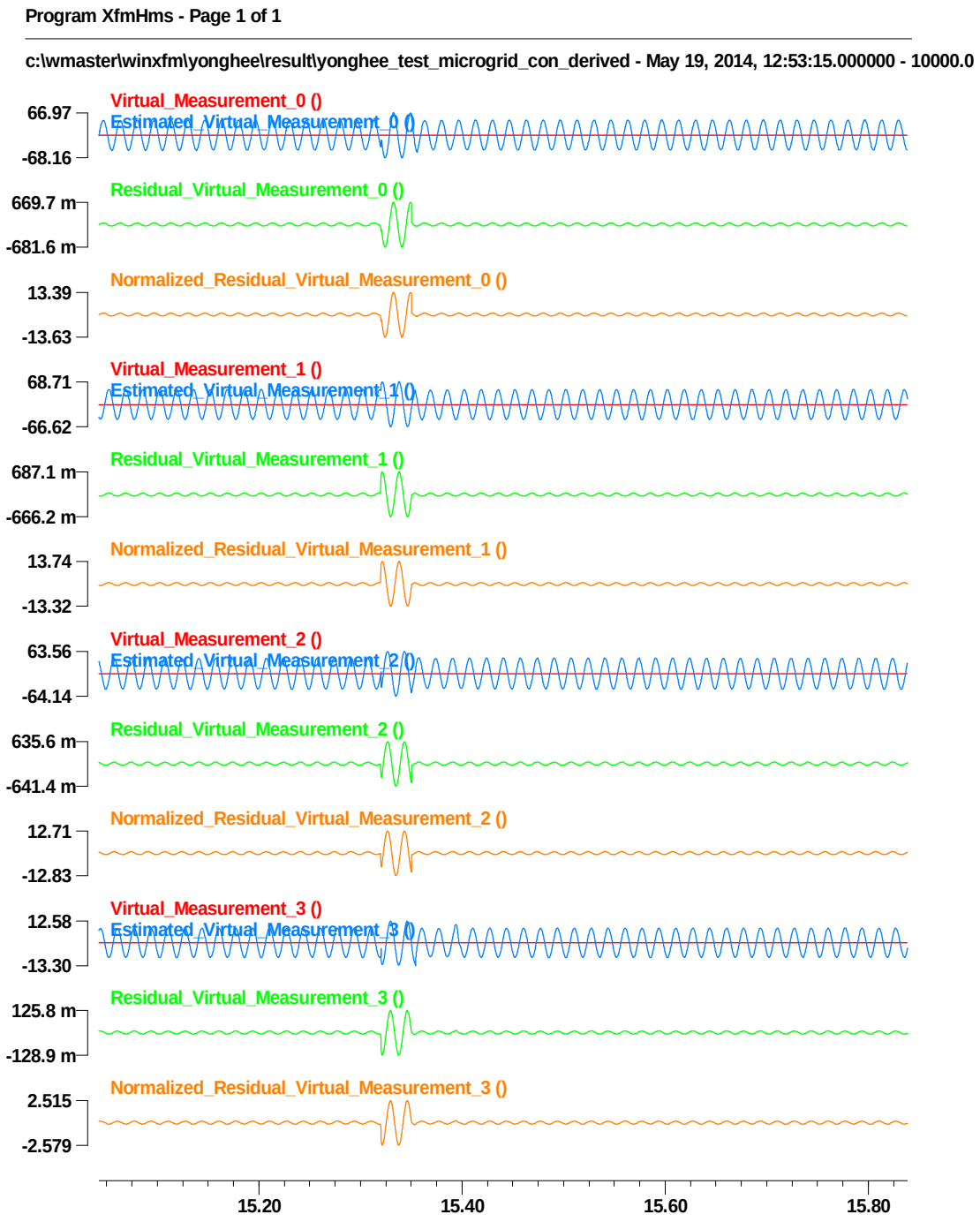

Figure 115: Virtual measurement data at time t, estimated measurement data, residual, and normalized residual of the first line model.

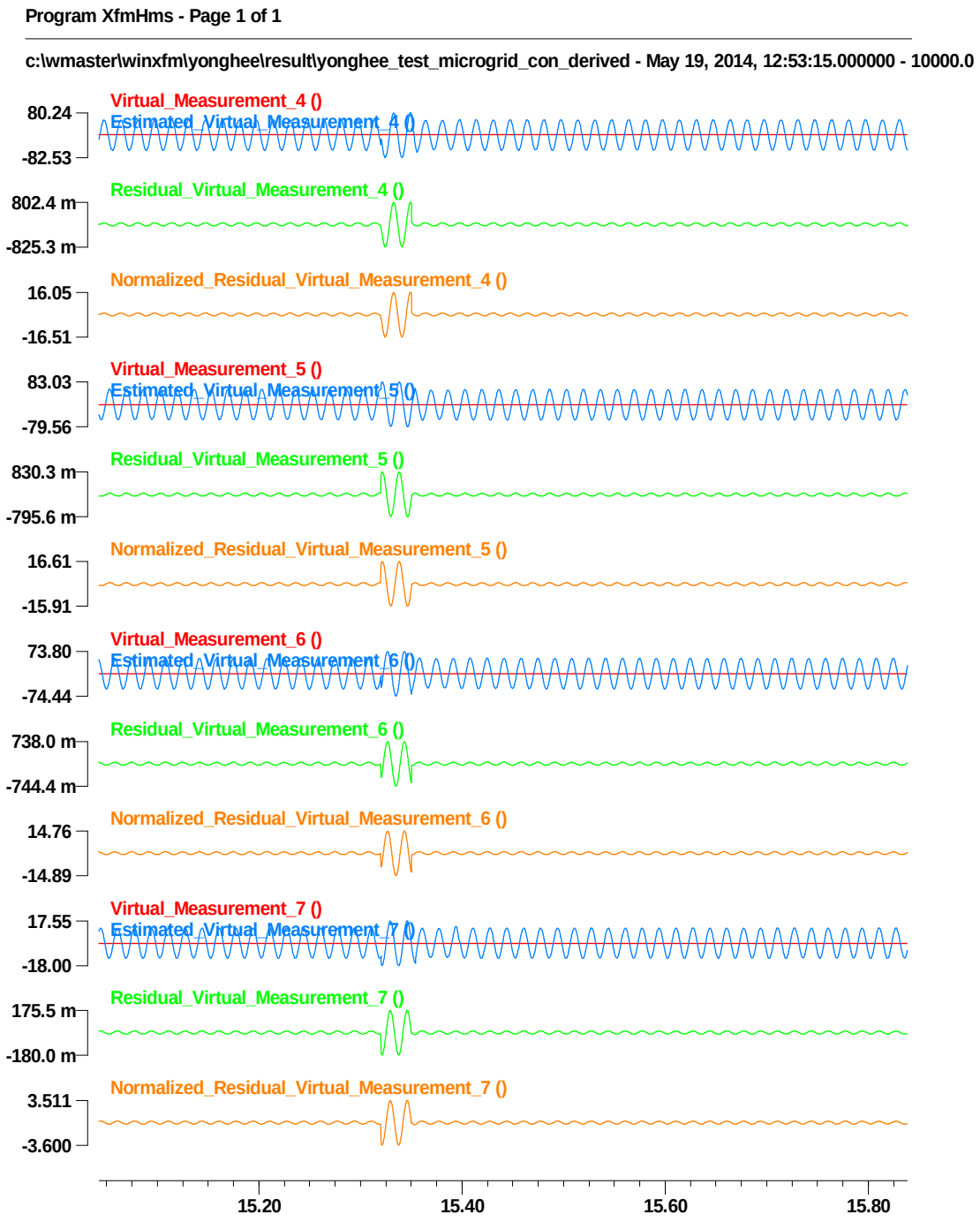

Figure 116: Virtual measurement data at time t, estimated measurement data, residual, and normalized residual of the second line model.

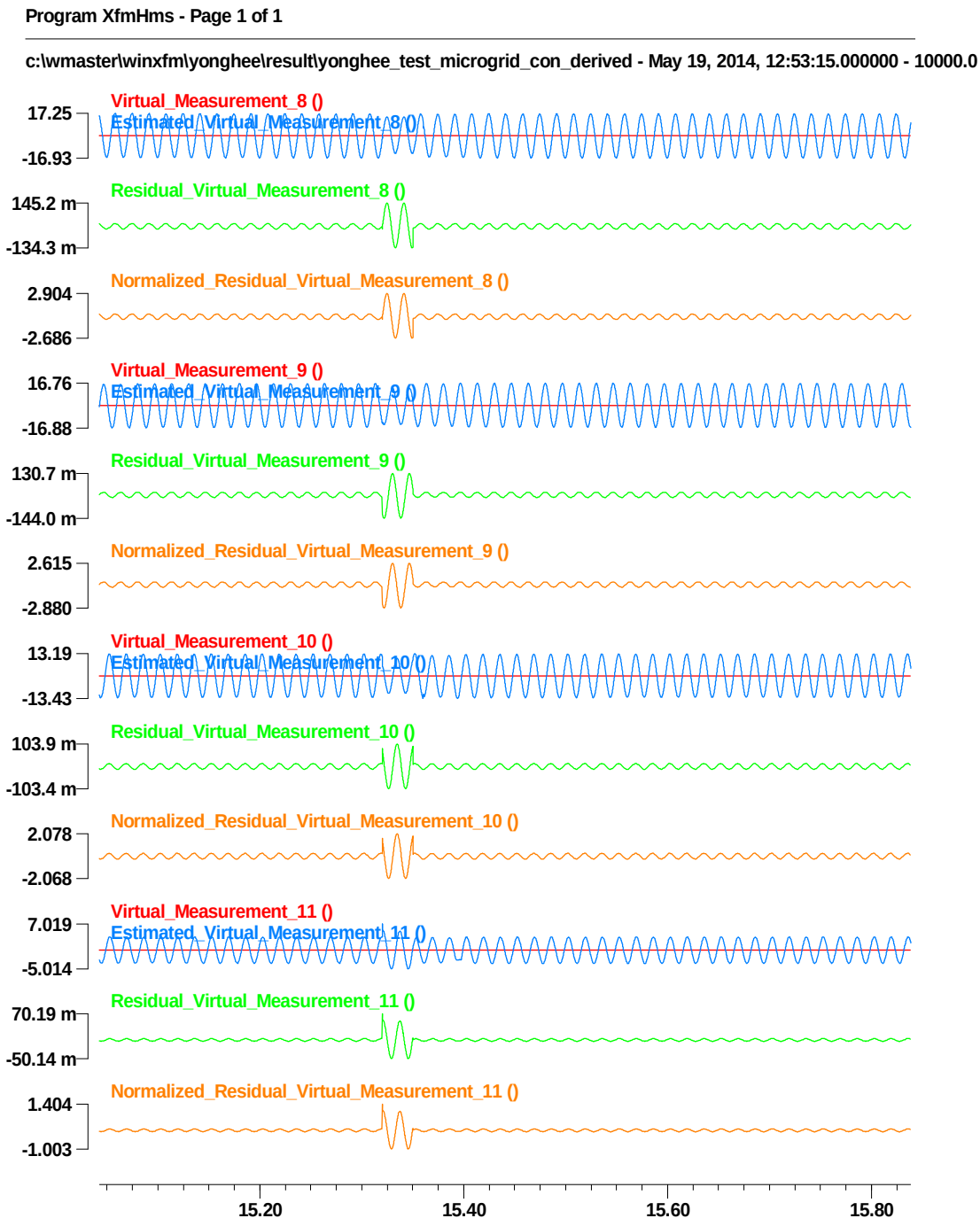

Figure 117: Virtual measurement data at time t, estimated measurement data, residual, and normalized residual of the third line model.

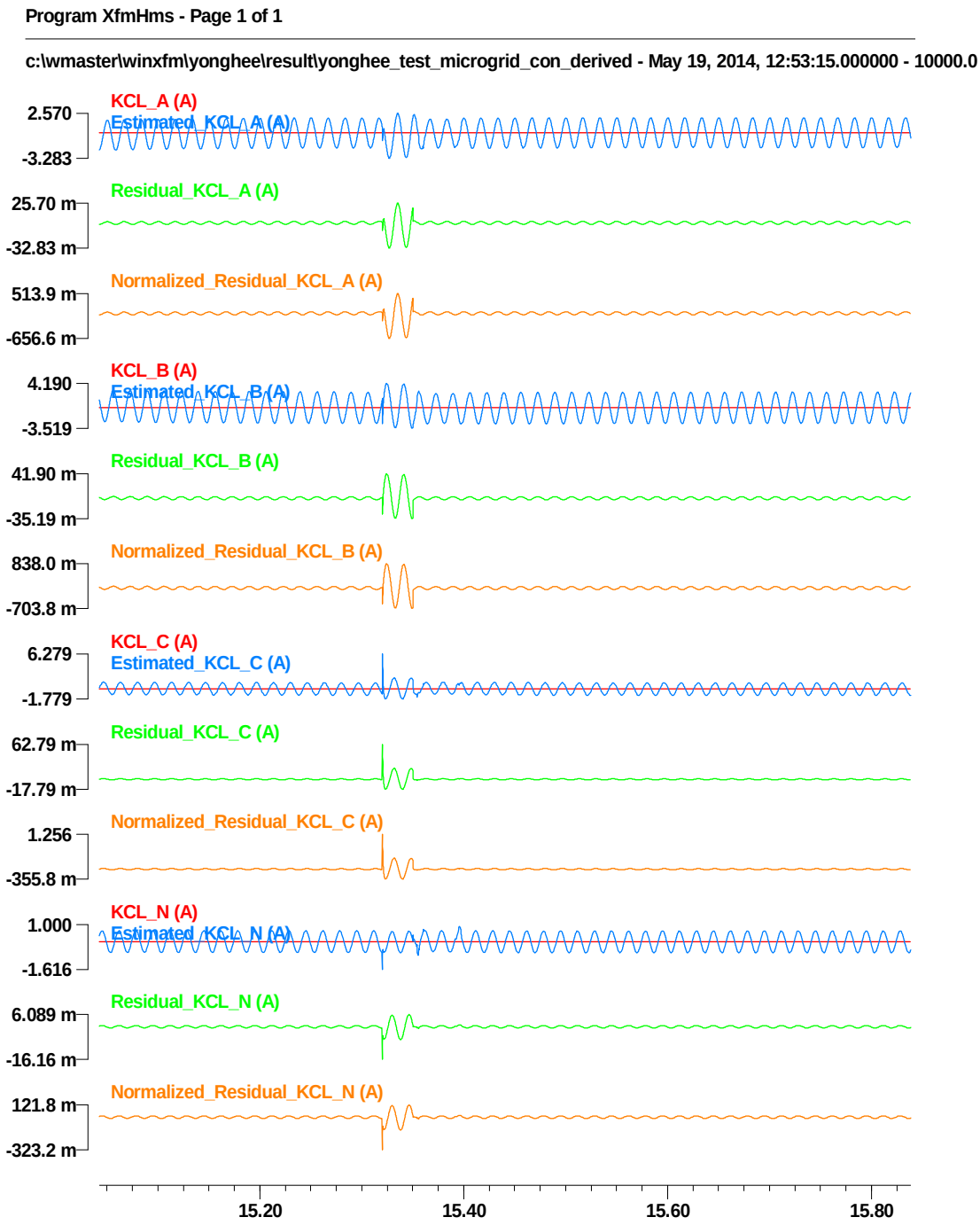

Figure 118: Virtual KCL measurement data at time t, estimated measurement data, residual, and normalized residual at node M-FAC.

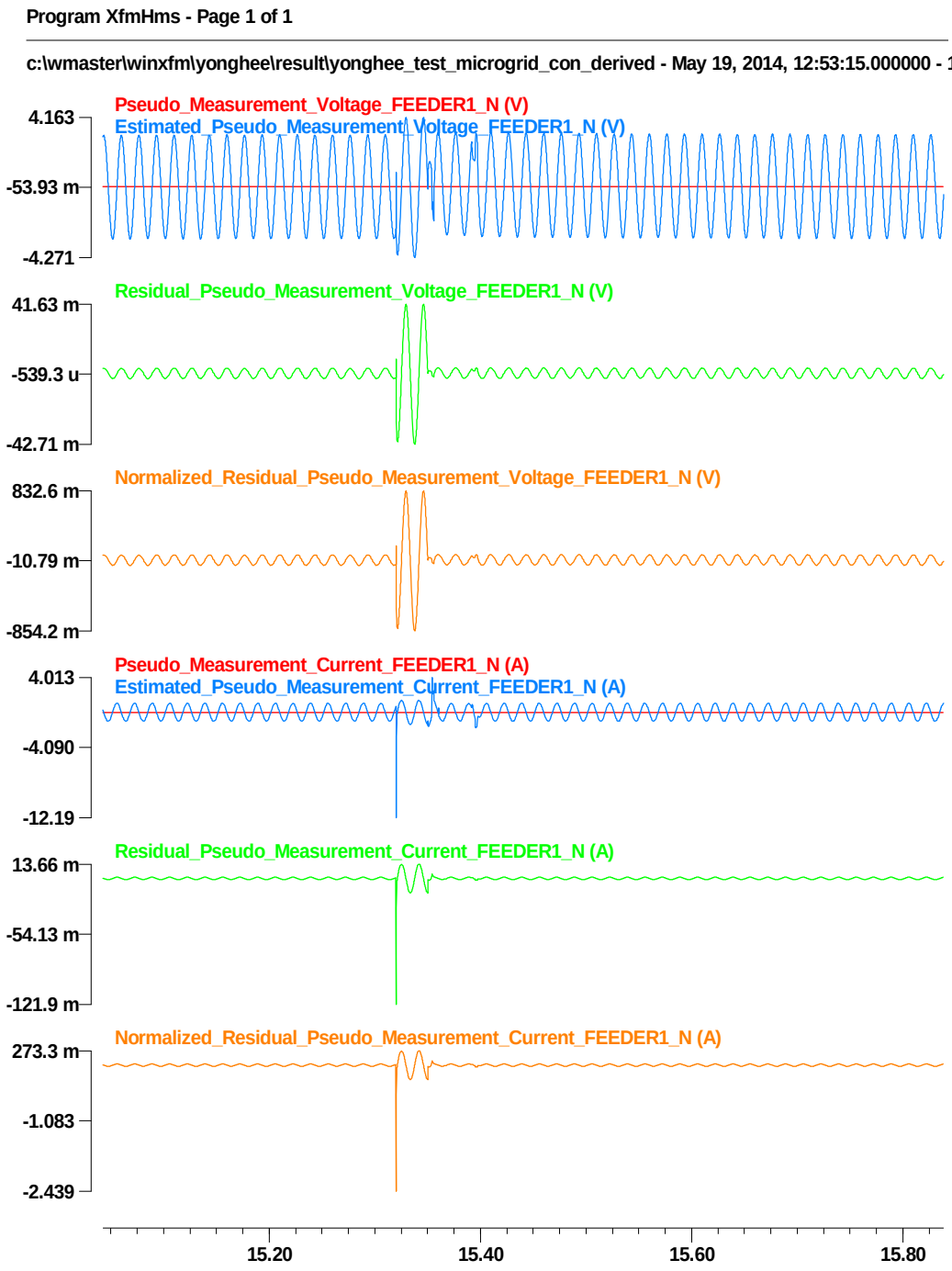

Figure 119: Pseudo measurement data at time t_m, estimated measurement data, residual, and normalized residual at node FEEDER1.

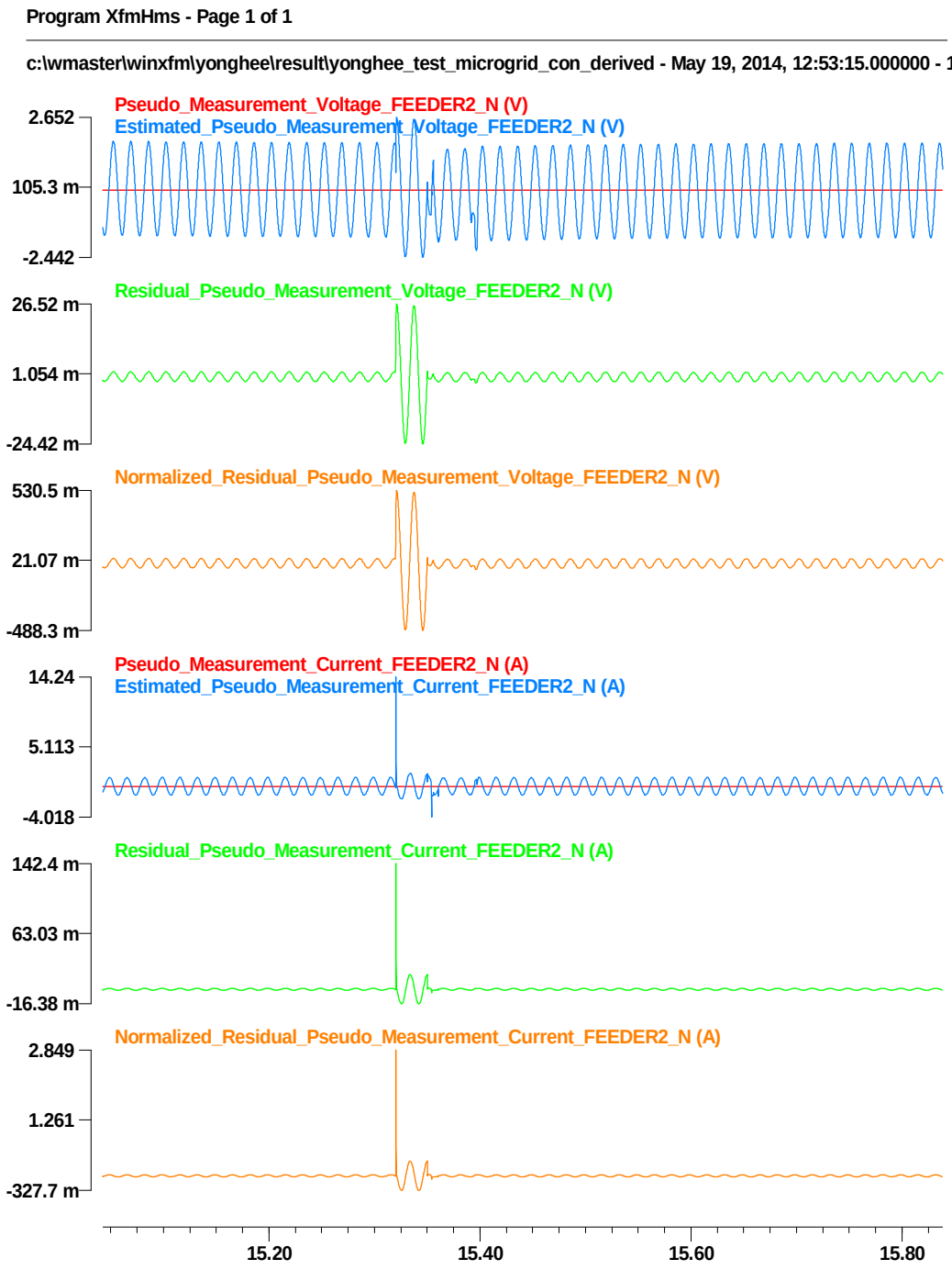

Figure 120: Pseudo measurement data at time t_m, estimated measurement data, residual, and normalized residual at node FEEDER2.

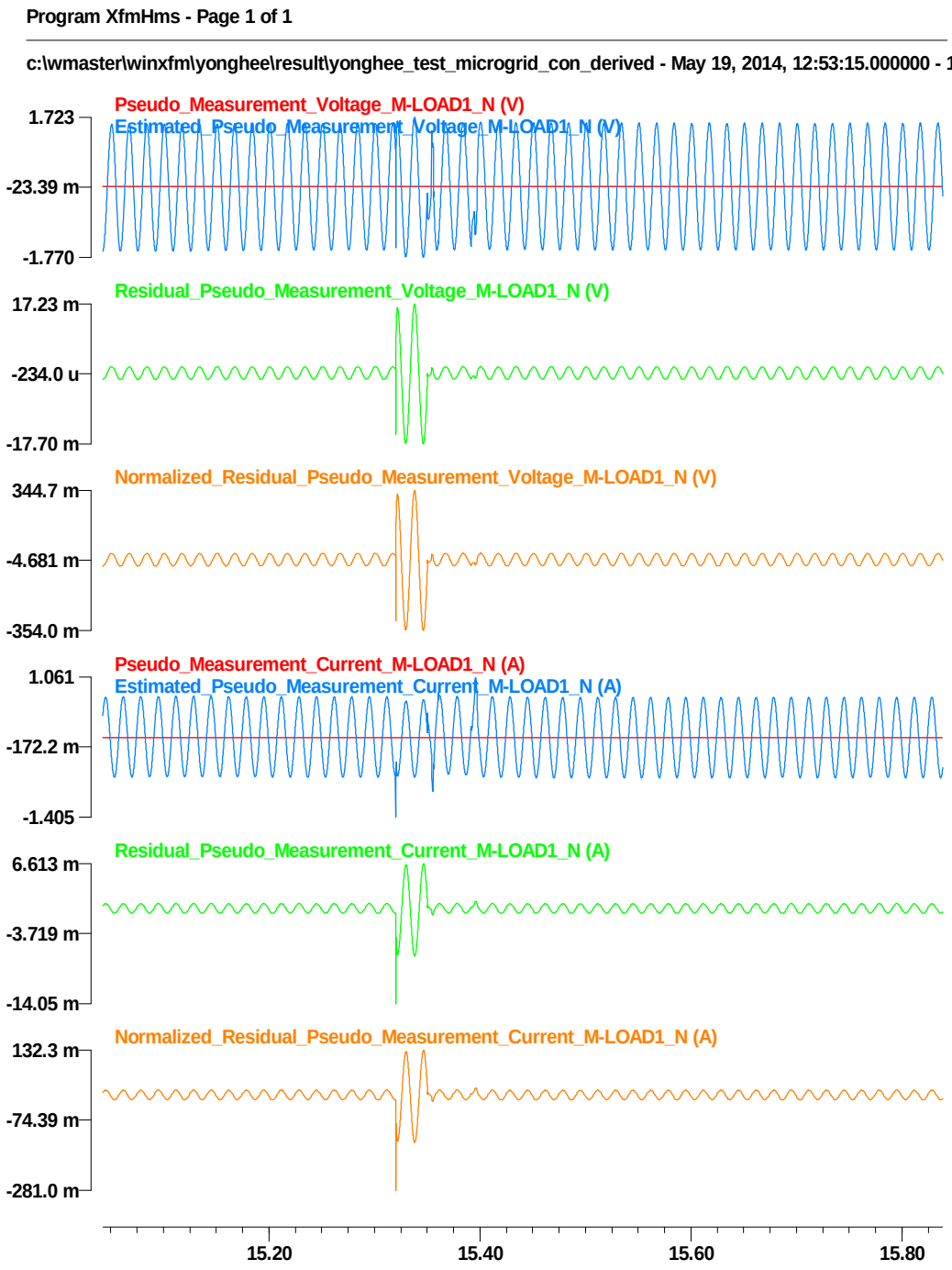

Figure 121: Pseudo measurement data at time t_m, estimated measurement data, residual, and normalized residual at node M-LOAD1.

Appendix R Results Graphs of the DSE-based Protection Scheme Simulation Results –Microgrid during the Island Operation

The result graphs of the simulation of the fault condition on the microgrid during the island operation are depicted in this appendix Figure 122 to Figure 136 as follows: a) confidence level, computation time, and residual, b) external states and some of internal states for time t and t_m, and c) measurement data, estimated measurement data, residual, and normalized residual of actual measurement, virtual measurement, and pseudo measurement data.

a) Confidence level, computation time, and residual for the internal fault case are depicted in Figure 122.

b) External states and some of internal states for time t and t_m are depicted in Figure 123. Internal states of the single section distribution line and the transformer is not explicitly shown in this appendix.

c) Measurement data, estimated measurement data, residual, and normalized residual of actual measurement, virtual measurement, and pseudo measurement data are illustrated in Figure 124 to Figure 136.

c1) Actual measurement data, estimated measurement data, residual, and normalized residual values for time t and t_m. are depicted in Figure 124 to Figure 129. In more detail, for time t and t_m, across measurement data and estimated measurement data at node FEEDER1 are compared each other as shown in Figure 124. Residual and normalized residual values are also depicted in the same figure. Result graphs of node FEEDER2 and M-LOAD1 are depicted in Figure 125 to Figure 126. In addition, through measurement

data and estimated measurement data at node FEEDER1, FEEDER2, and M-LOAD1 are compared each other, and the resulting residual and normalized residual values are shown in Figure 128 to Figure 129.

c2) Virtual measurement data, estimated measurement data, residual, and normalized residual values for time t and t_m are depicted in Figure 130 to Figure 133. In more detail, internal virtual measurement data and estimated measurement data of the first single section distribution line model for time t and t_m are compared each other, and the resulting residual and normalized residual values are shown in Figure 130. Result graphs of the second and the third single section distribution line model and the transformer model are depicted in Figure 131 and Figure 132, respectively. Moreover, KCL virtual measurement data and estimated measurement data at node M-FAC for time t and t_m are compared each other, and the resulting residual and normalized residual values are shown in Figure 133.

c3) Pseudo measurement data, estimated measurement data, residual, and normalized residual values for time t and t_m are depicted in Figure 134 to Figure 136. In more detail, pseudo measurement data and estimated measurement data at node FEEDER1, FEEDER2, and M-LOAD1 for time t and t_m are compared each other, and the resulting residual and normalized residual values are shown in Figure 134 to Figure 136.

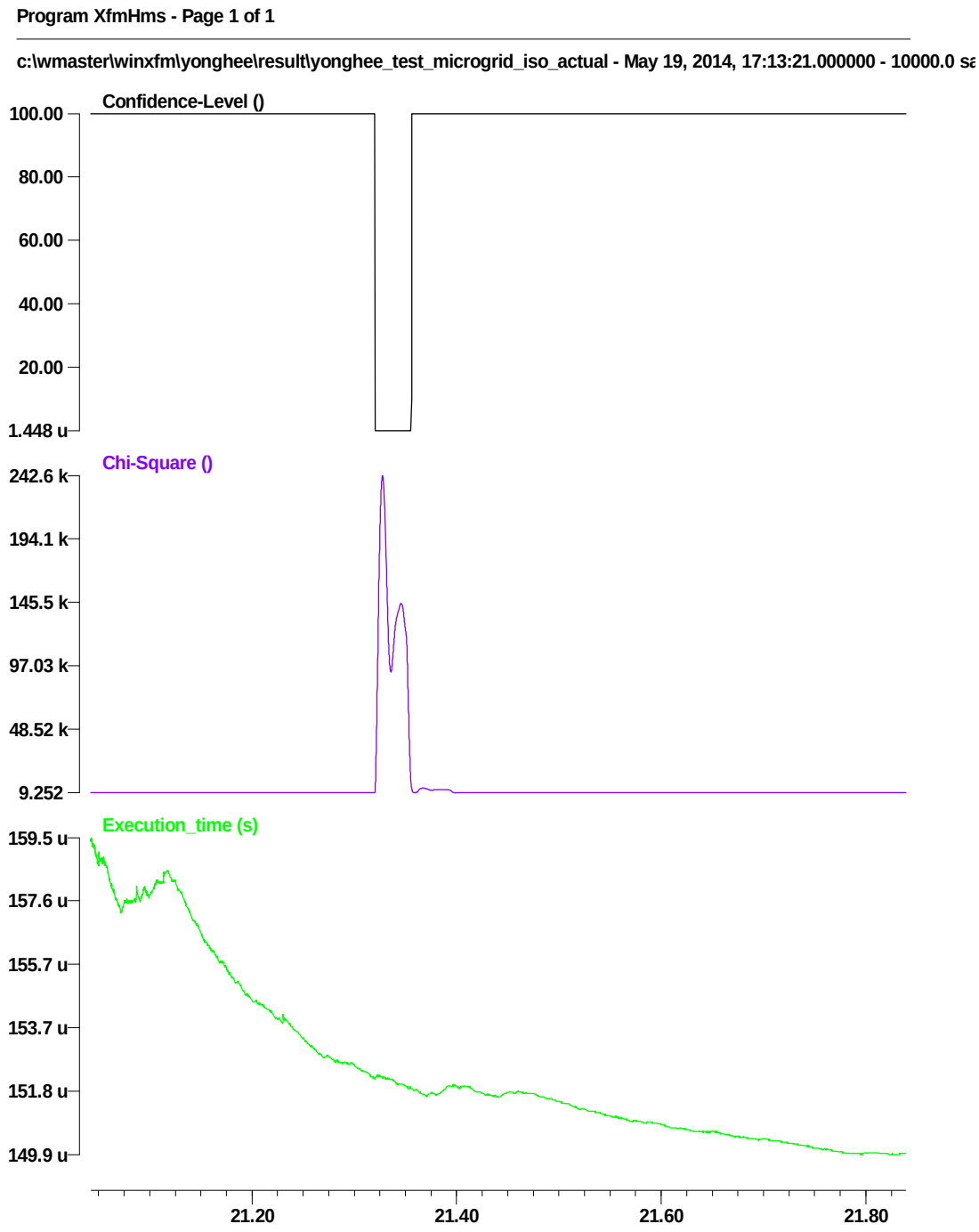

Figure 122: Confidence level, computation time, and residual for the internal fault case on the microgrid during the island mode.

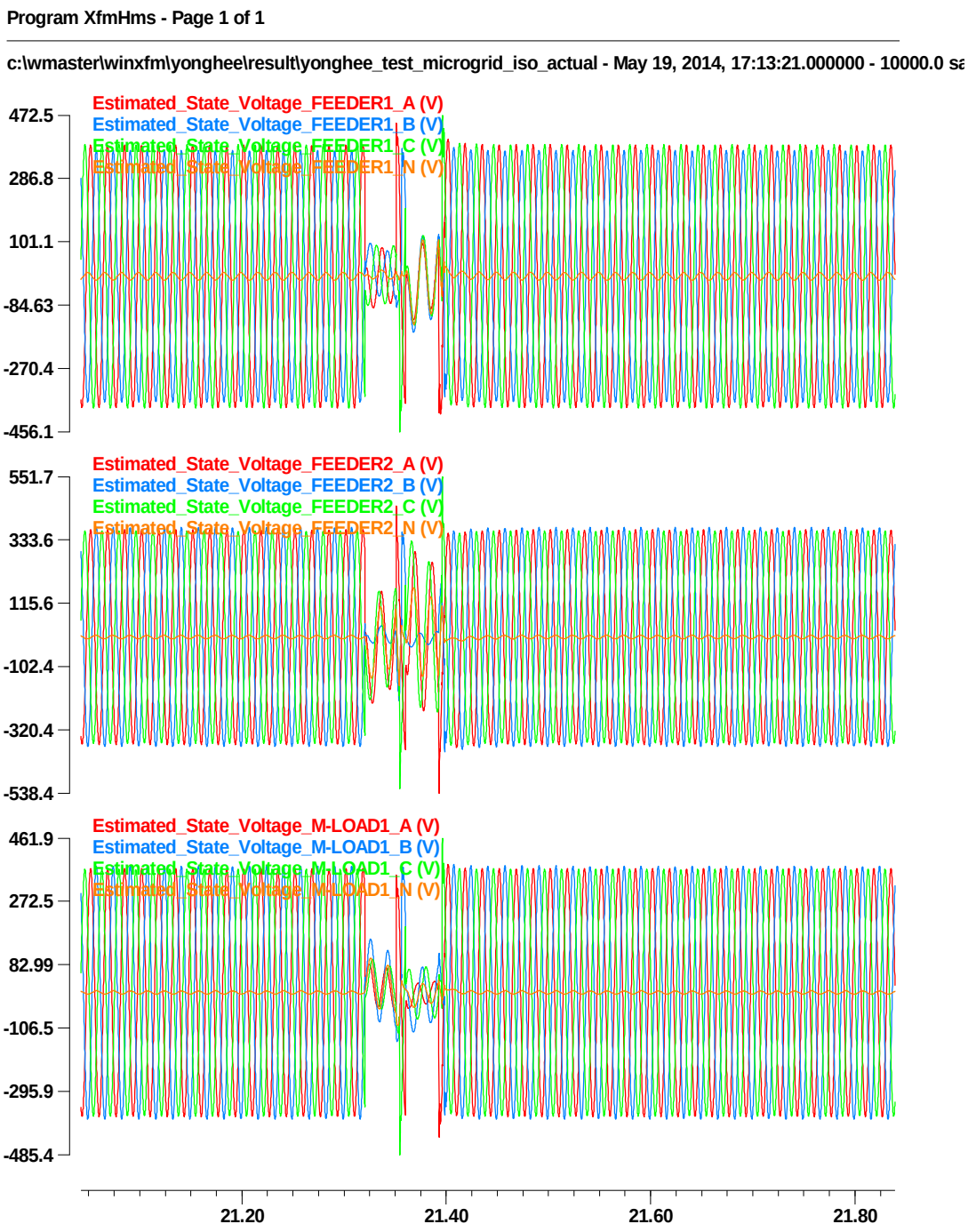

Figure 123: States at node FEEDER1, FEEDER2, and M-LOAD1.

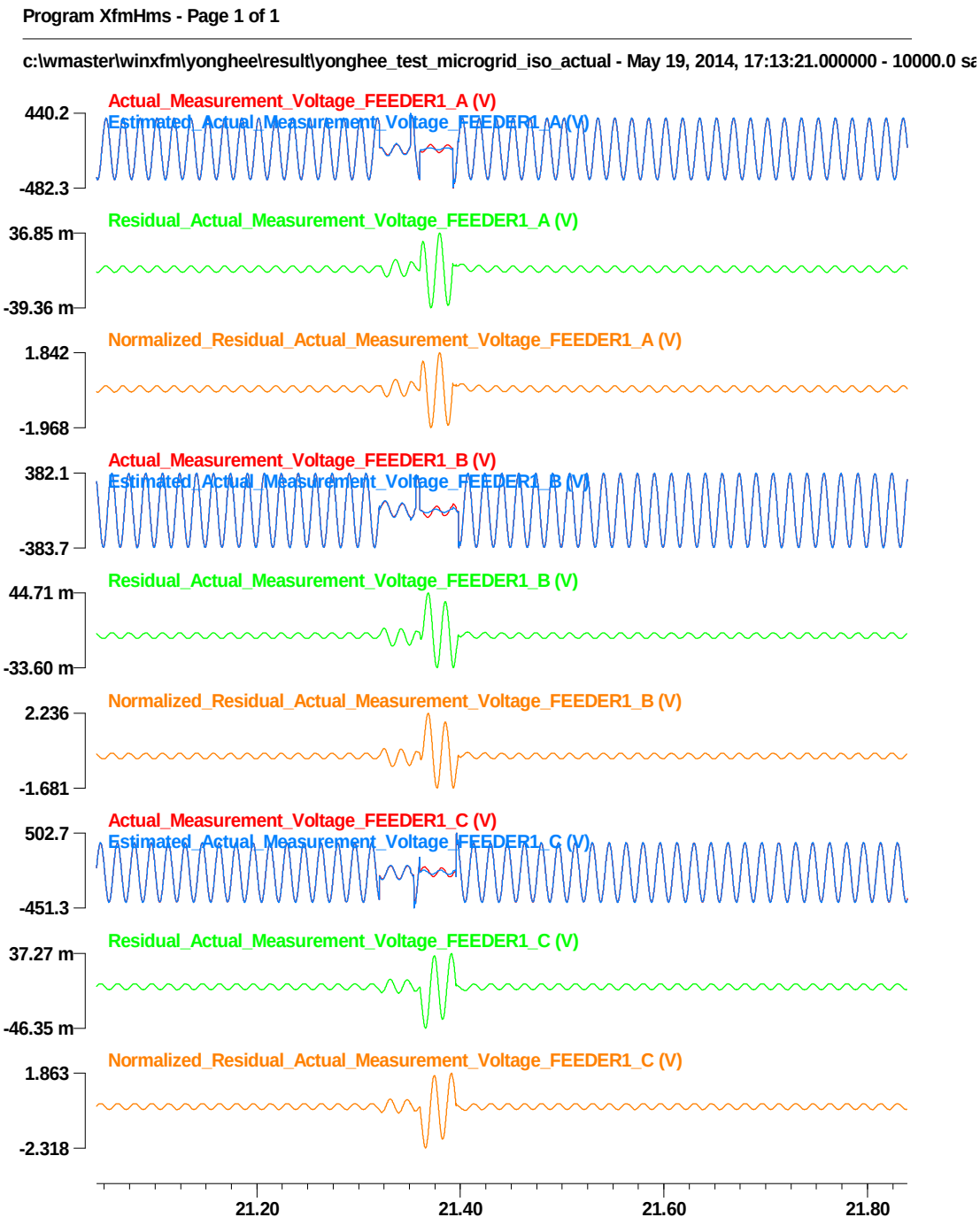

Figure 124: Actual across measurement data, estimated measurement data, residual, and normalized residual at node FEEDER1.

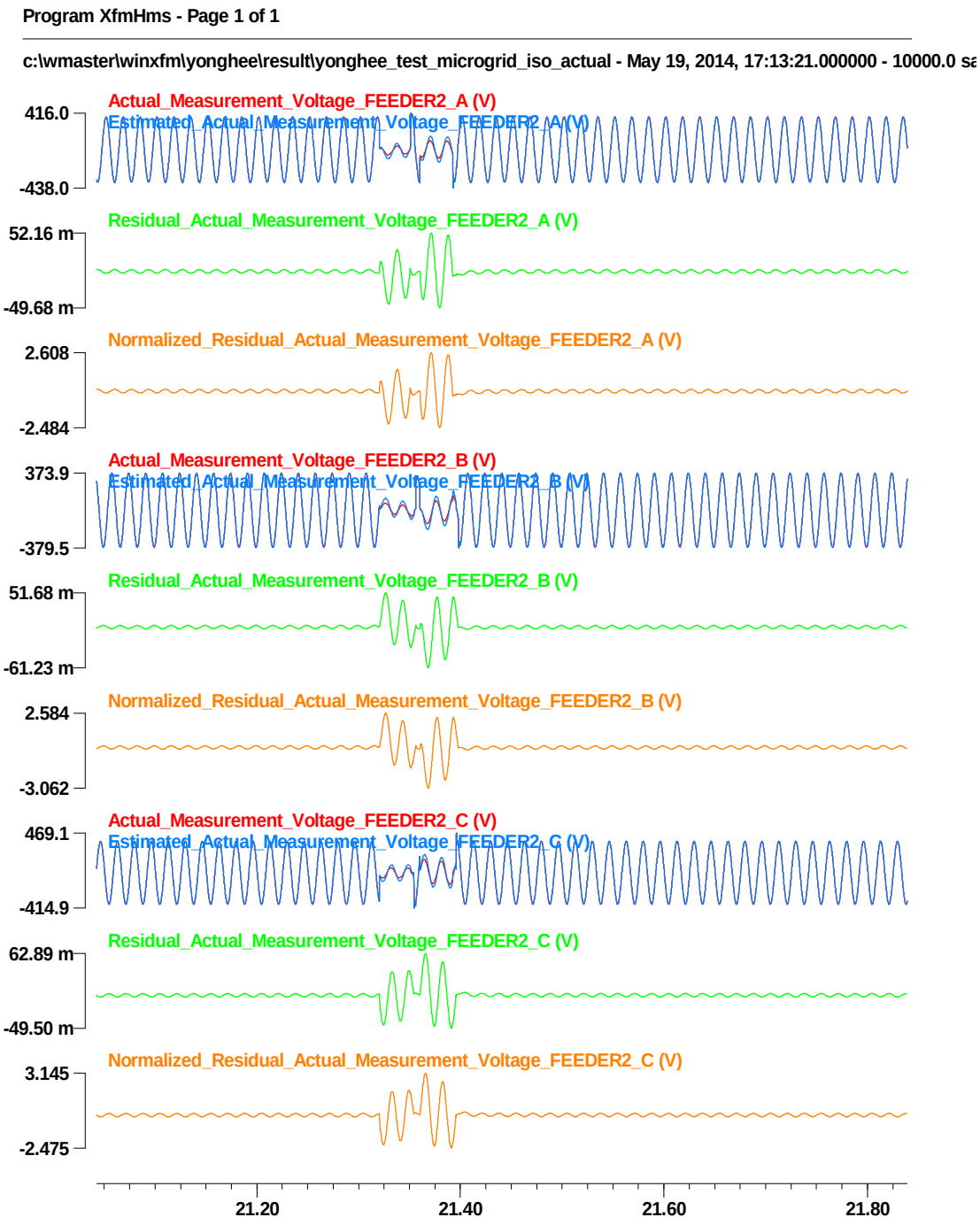

Figure 125: Actual across measurement data at time t, estimated measurement data, residual, and normalized residual at node FEEDER2.

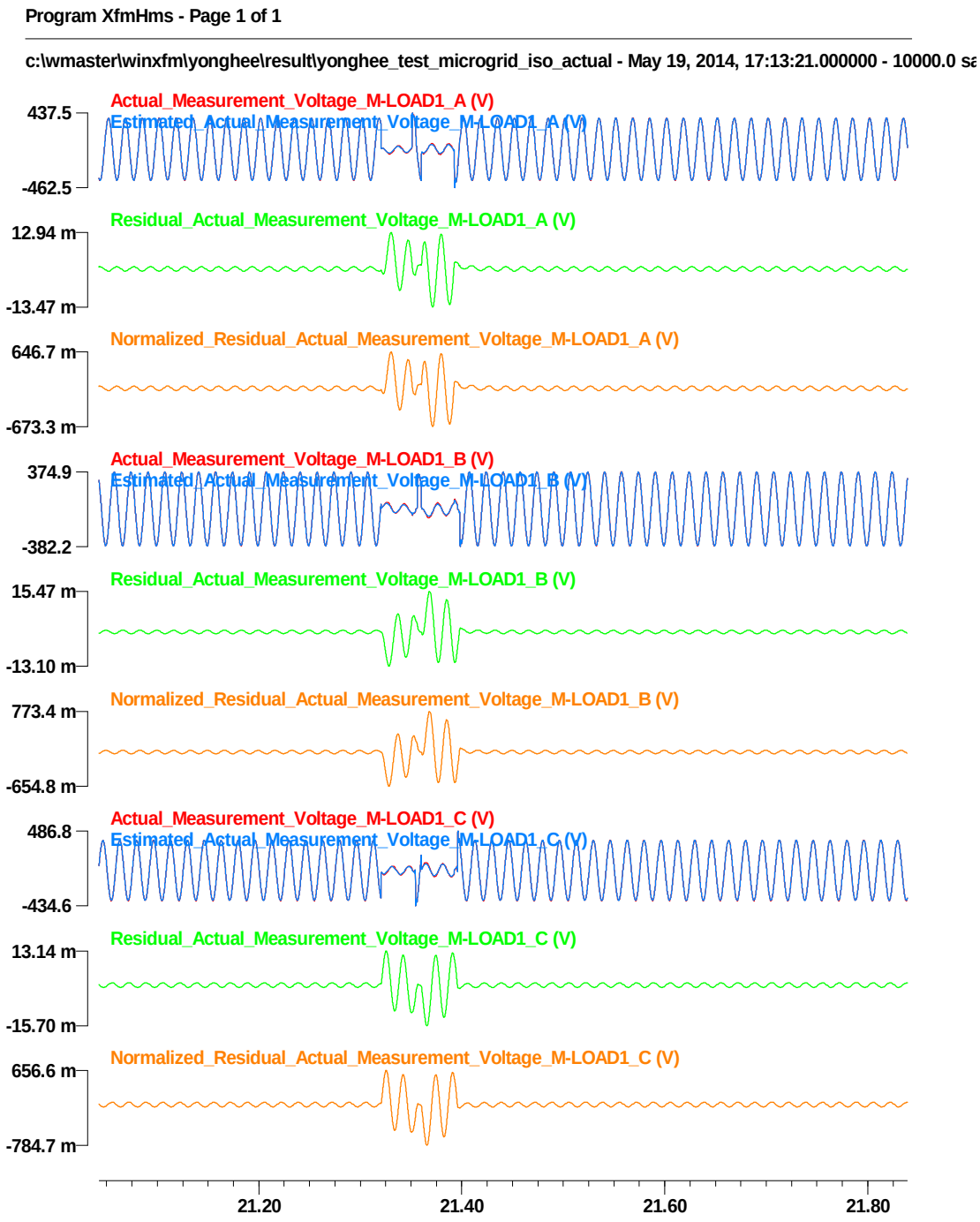

Figure 126: Actual across measurement data at time t, estimated measurement data, residual, and normalized residual at node M-LOAD1.

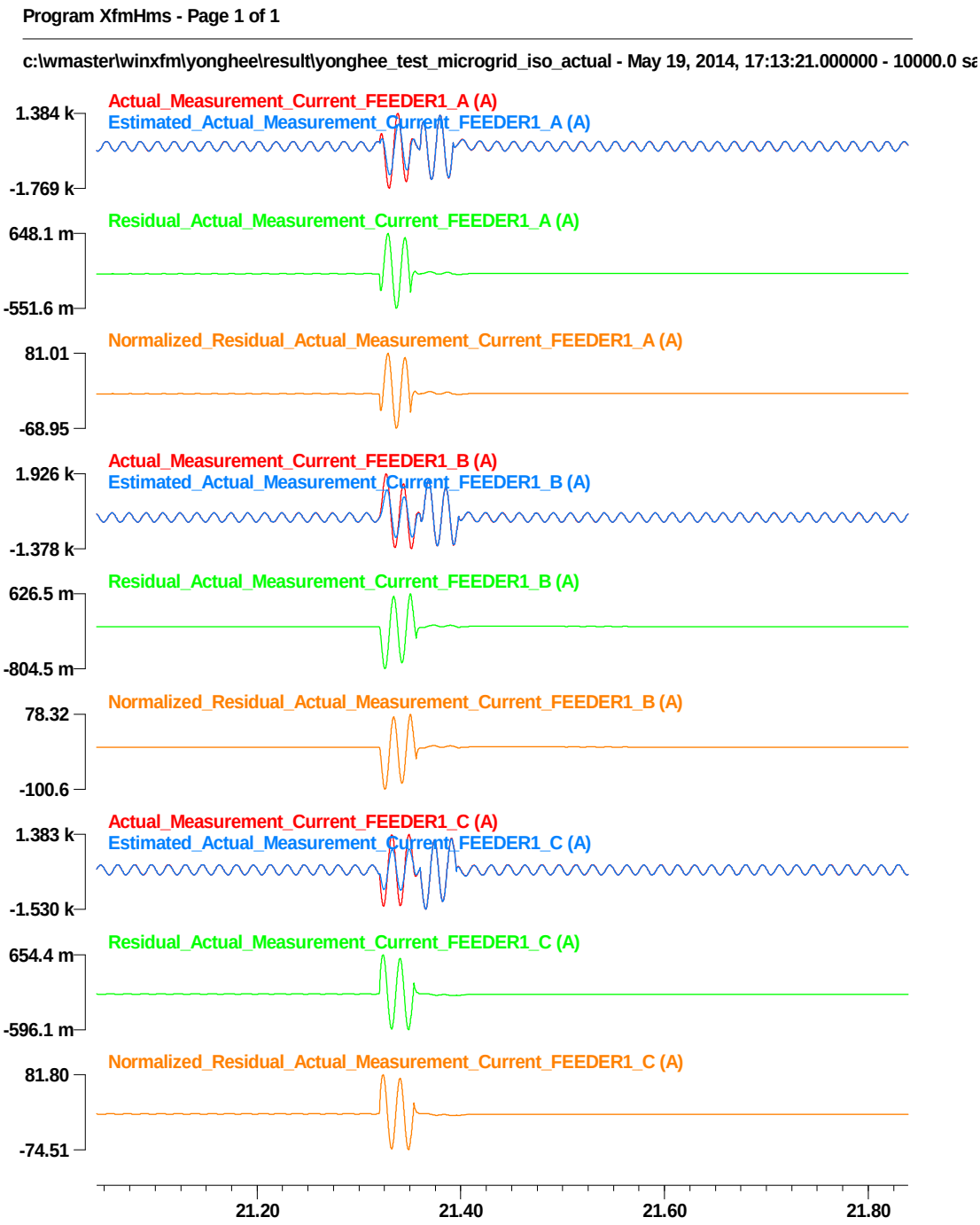

Figure 127: Actual through measurement data at time t, estimated measurement data, residual, and normalized residual at node FEEDER1.

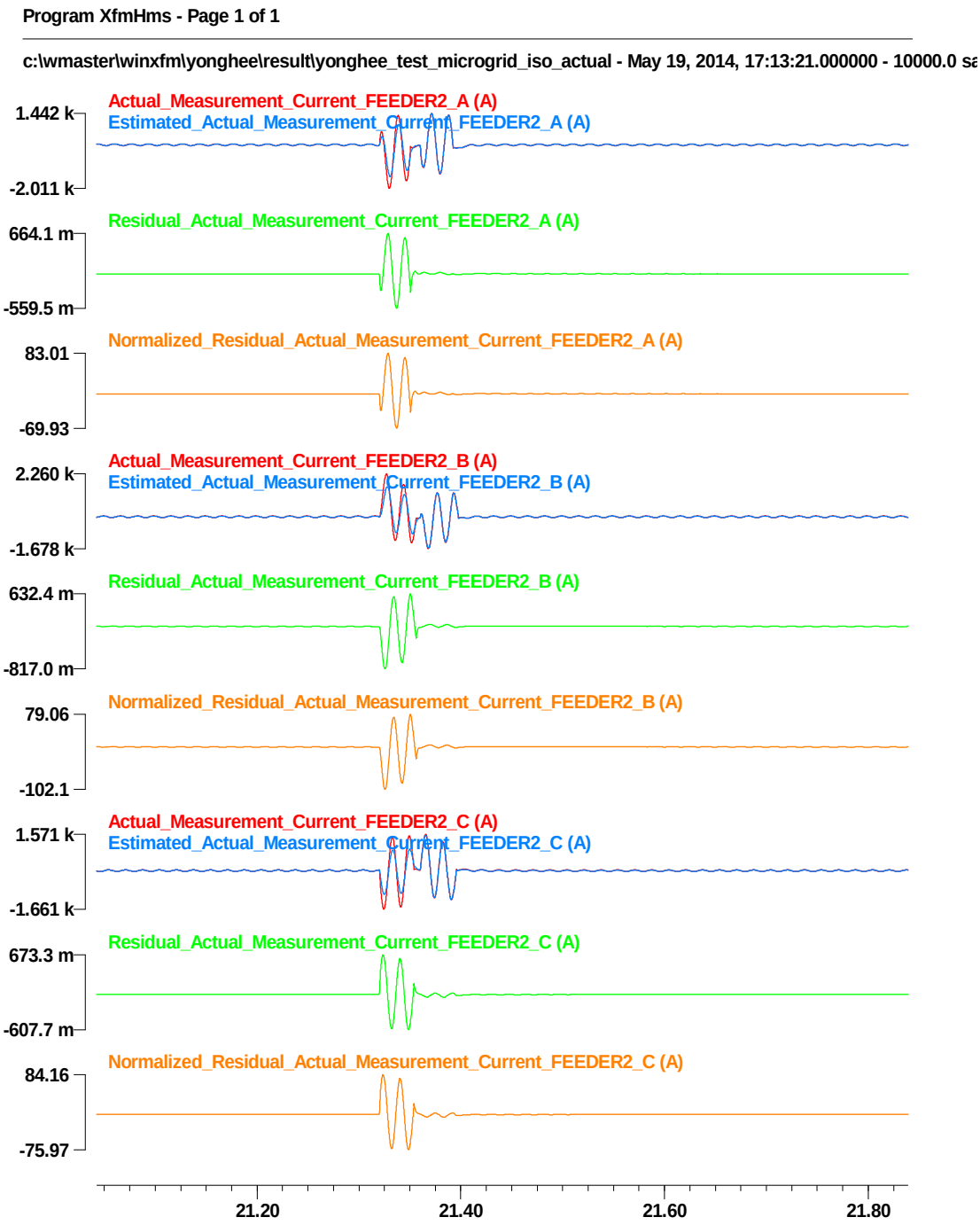

Figure 128: Actual through measurement data at time t, estimated measurement data, residual, and normalized residual at node FEEDER2.

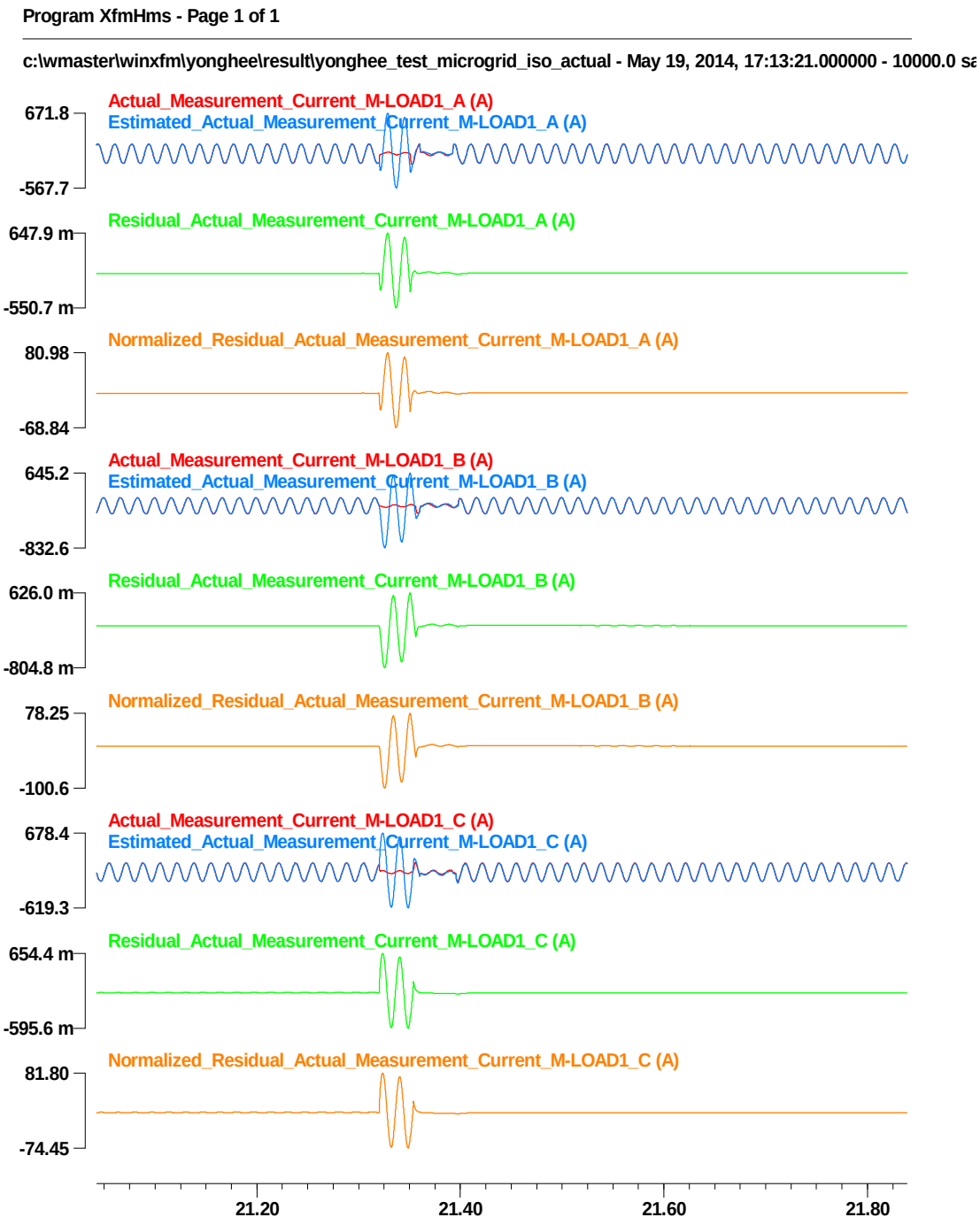

Figure 129: Actual through measurement data at time t, estimated measurement data, residual, and normalized residual at node M-LOAD1.

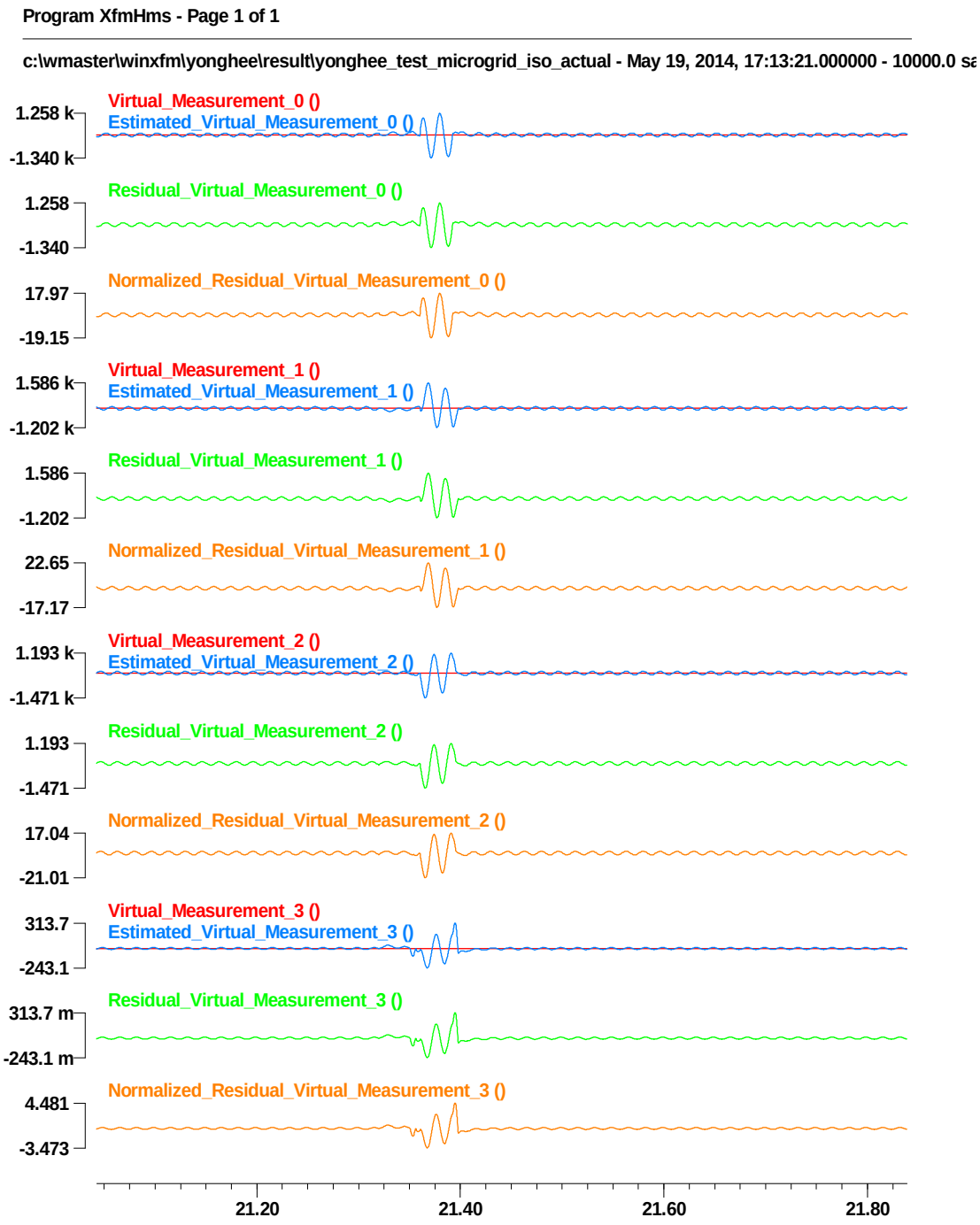

Figure 130: Virtual measurement data at time t, estimated measurement data, residual, and normalized residual of the first line model.

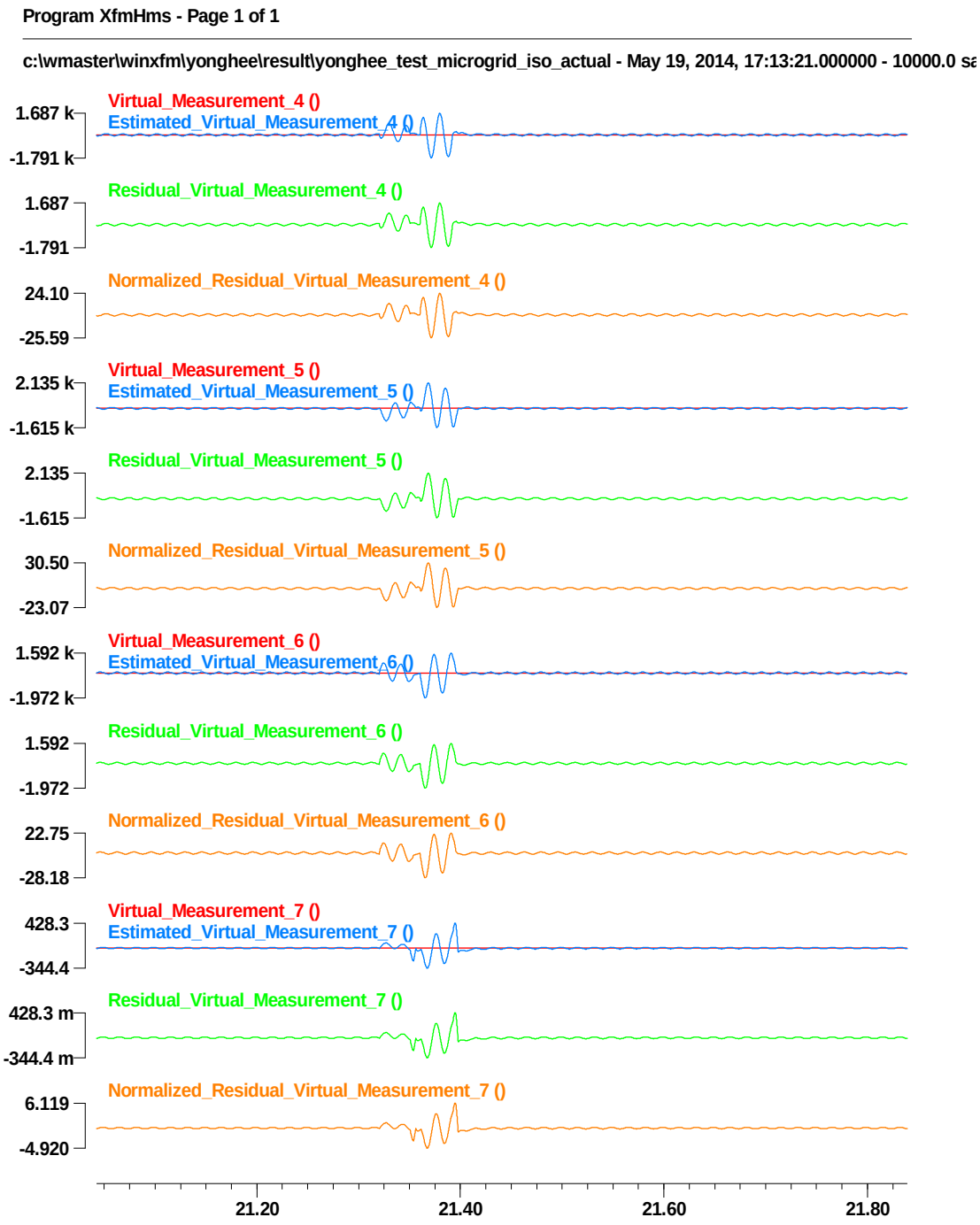

Figure 131: Virtual measurement data at time t, estimated measurement data, residual, and normalized residual of the second line model.

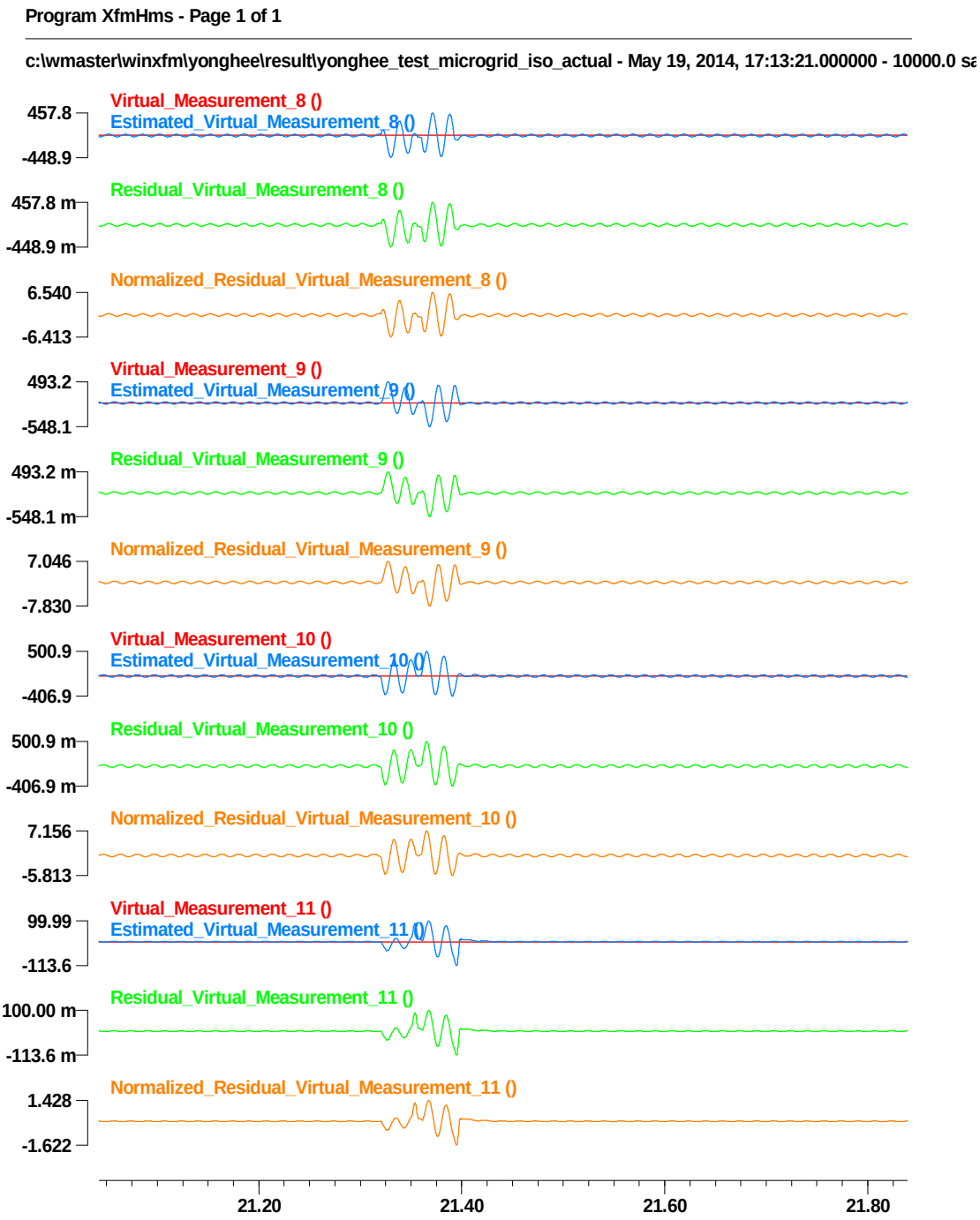

Figure 132: Virtual measurement data at time t, estimated measurement data, residual, and normalized residual of the third line model.

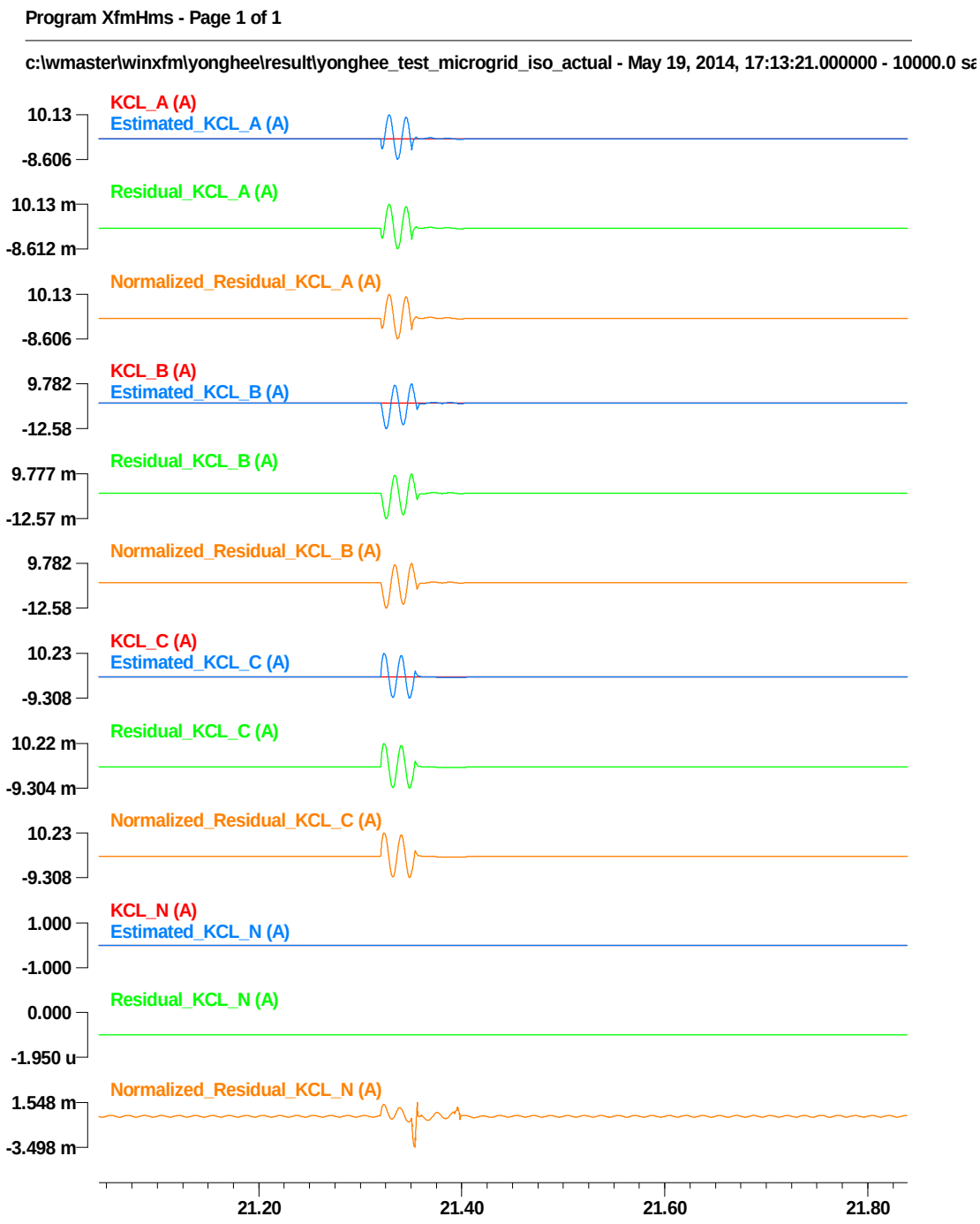

Figure 133: Virtual KCL measurement data at time t, estimated measurement data, residual, and normalized residual at node M-FAC.

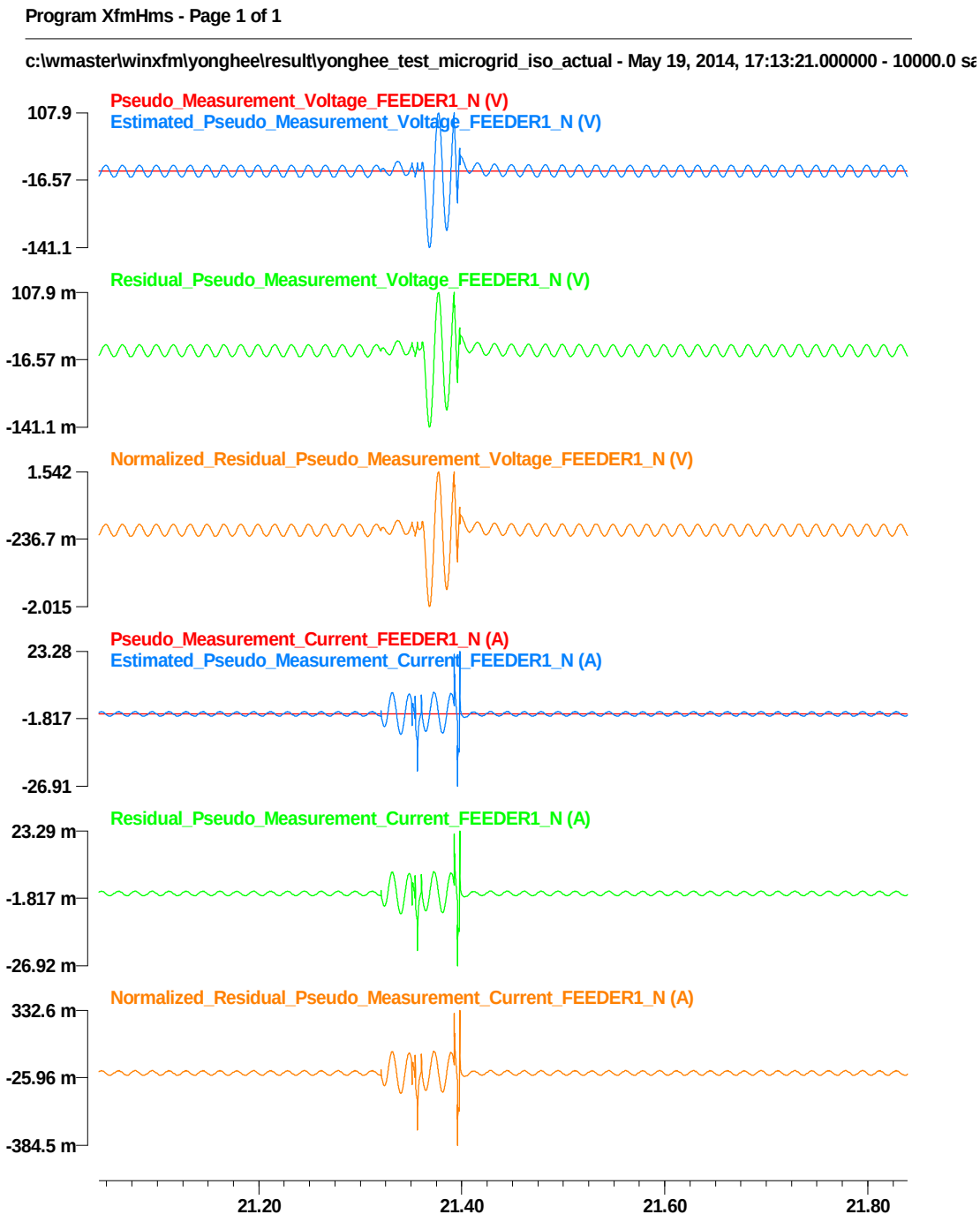

Figure 134: Pseudo measurement data at time t_m, estimated measurement data, residual, and normalized residual at node FEEDER1.

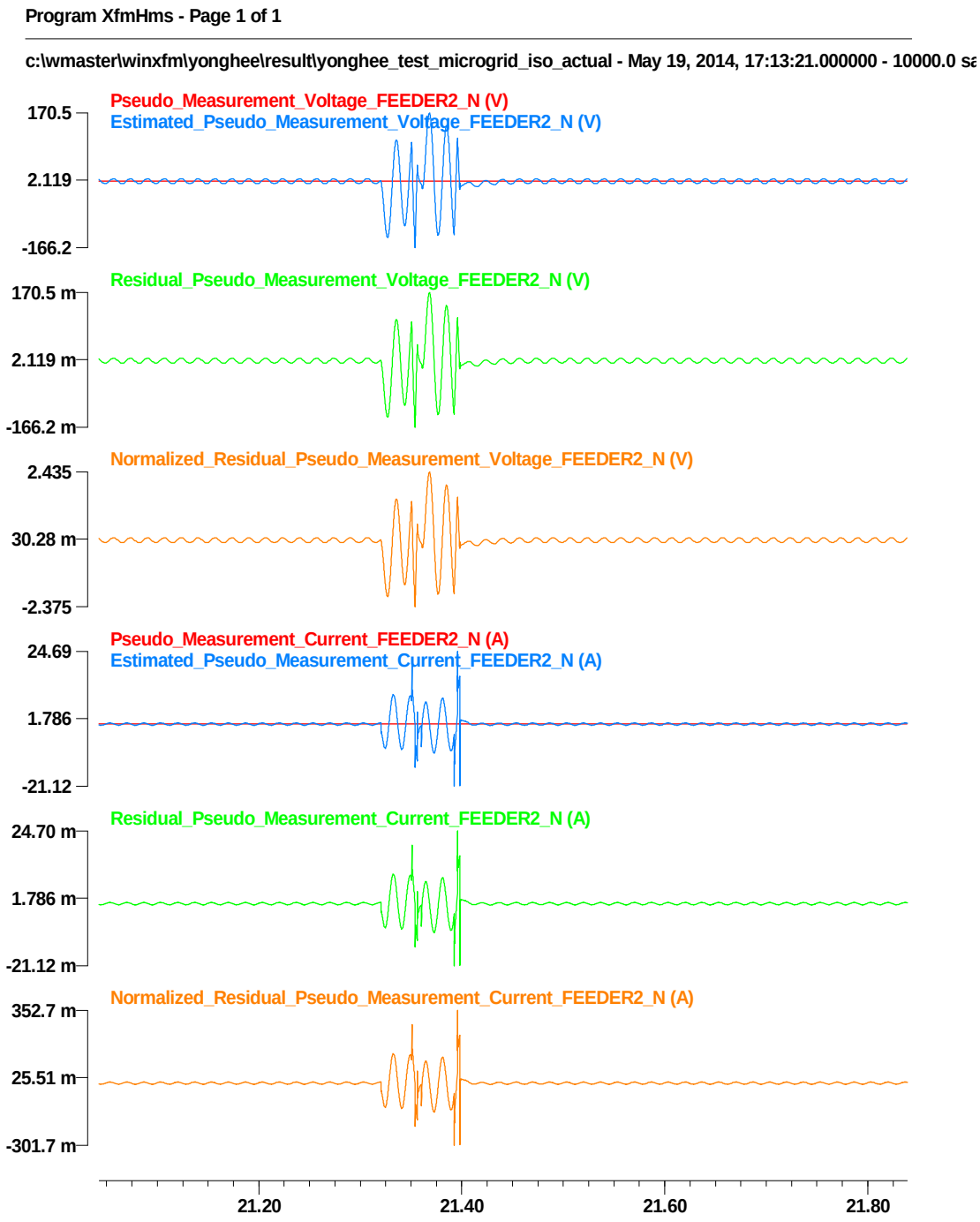

Figure 135: Pseudo measurement data at time t_m, estimated measurement data, residual, and normalized residual at node FEEDER2.

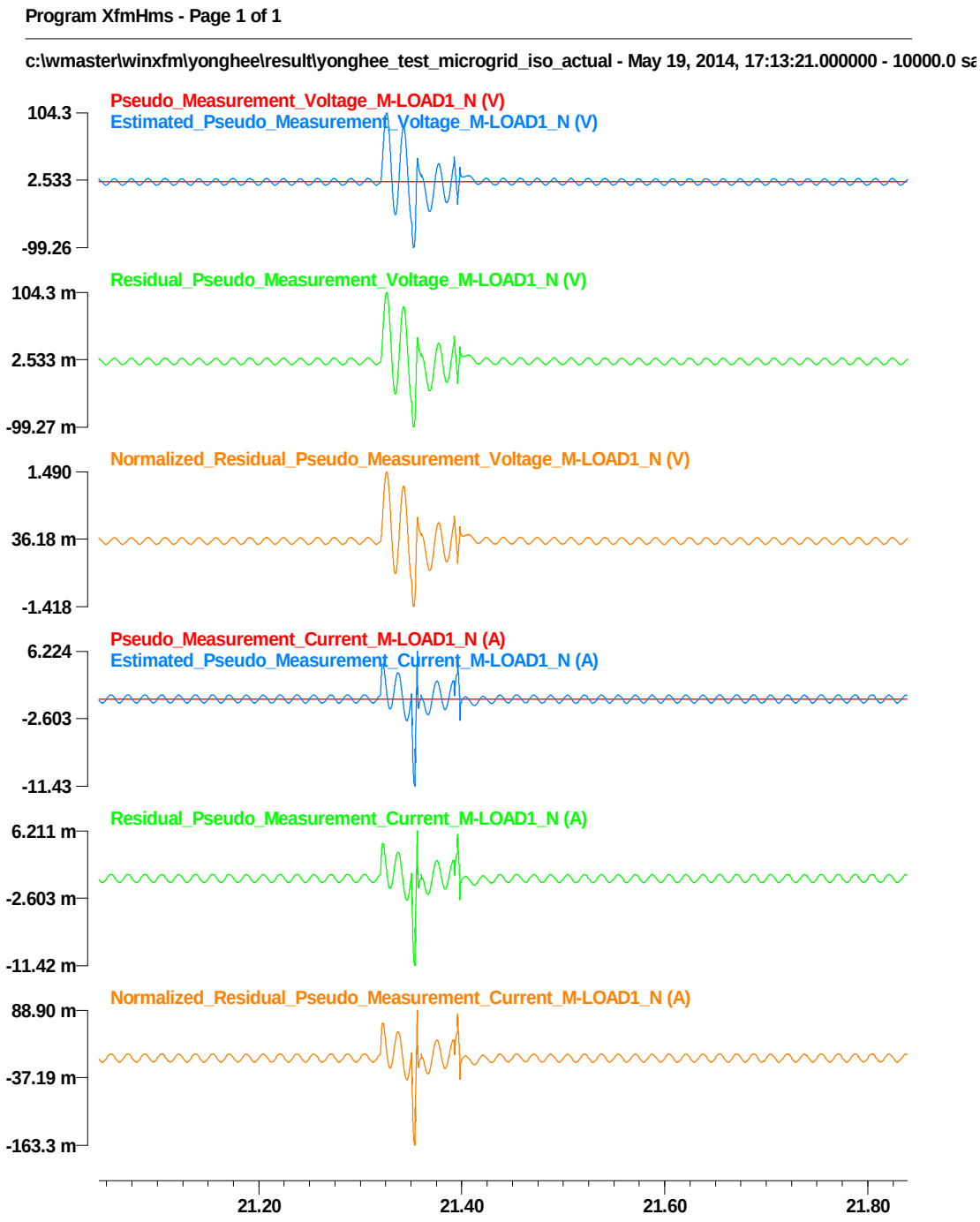

Figure 136: Pseudo measurement data at time t_m, estimated measurement data, residual, and normalized residual at node M-LOAD1.

Appendix S Results Graphs of the DSE-based Protection Scheme Laboratory Test Results –Microgrid during Islanding Operation

The experimental result graphs of the fault condition on the microgrid during the island operation are depicted in this appendix Figure 137 to Figure 151 as follows: a) confidence level, computation time, and residual, b) external states and some of internal states for time t and t_m, and c) measurement data, estimated measurement data, residual, and normalized residual of actual measurement, virtual measurement, and pseudo measurement data.

a) Confidence level, computation time, and residual for the internal fault case are depicted in Figure 137.

b) External states and some of internal states for time t and t_m are depicted in Figure 138. Internal states of the single section distribution line and the transformer is not explicitly shown in this appendix.

c) Measurement data, estimated measurement data, residual, and normalized residual of actual measurement, virtual measurement, and pseudo measurement data are illustrated in Figure 139 to Figure 151.

c1) Actual measurement data, estimated measurement data, residual, and normalized residual values for time t and t_m. are depicted in Figure 139 and Figure 142. In more detail, for time t and t_m, across measurement data and estimated measurement data at node FEEDER1 are compared each other as shown in Figure 139. Residual and normalized residual values are also depicted in the same figure. In addition, through measurement data and estimated measurement data at node FEEDER1, are compared

each other, and the resulting residual and normalized residual values are shown in Figure 142.

c2) Derived measurement data, estimated measurement data, residual, and normalized residual values for time t and t_m. are depicted in Figure 140, Figure 141, Figure 143, and Figure 144. In more detail, for time t and t_m, derived across measurement data and estimated measurement data at node FEEDER2 and M-LOAD3 are compared each other as shown in Figure 140 and Figure 141, respectively. Residual and normalized residual values are also depicted in the same figure. In addition, derived through measurement data and estimated measurement data at node FEEDER2 and M-LOAD3 are compared each other, and the resulting residual and normalized residual values are shown in Figure 143 and Figure 144.

c2) Virtual measurement data, estimated measurement data, residual, and normalized residual values for time t and t_m are depicted in Figure 145 to Figure 148. In more detail, internal virtual measurement data and estimated measurement data of the first single section distribution line model for time t and t_m are compared each other, and the resulting residual and normalized residual values are shown in Figure 145. Result graphs of the second and the third single section distribution line model and the transformer model are depicted in Figure 146 and Figure 147, respectively. Moreover, KCL virtual measurement data and estimated measurement data at node M-FAC for time t and t_m are compared each other, and the resulting residual and normalized residual values are shown in Figure 148.

c3) Pseudo measurement data, estimated measurement data, residual, and normalized residual values for time t and t_m are depicted in Figure 149 to Figure 151. In more detail,

pseudo measurement data and estimated measurement data at node FEEDER1, FEEDER2, and M-LOAD1 for time t and t_m are compared each other, and the resulting residual and normalized residual values are shown in Figure 149 to Figure 151.

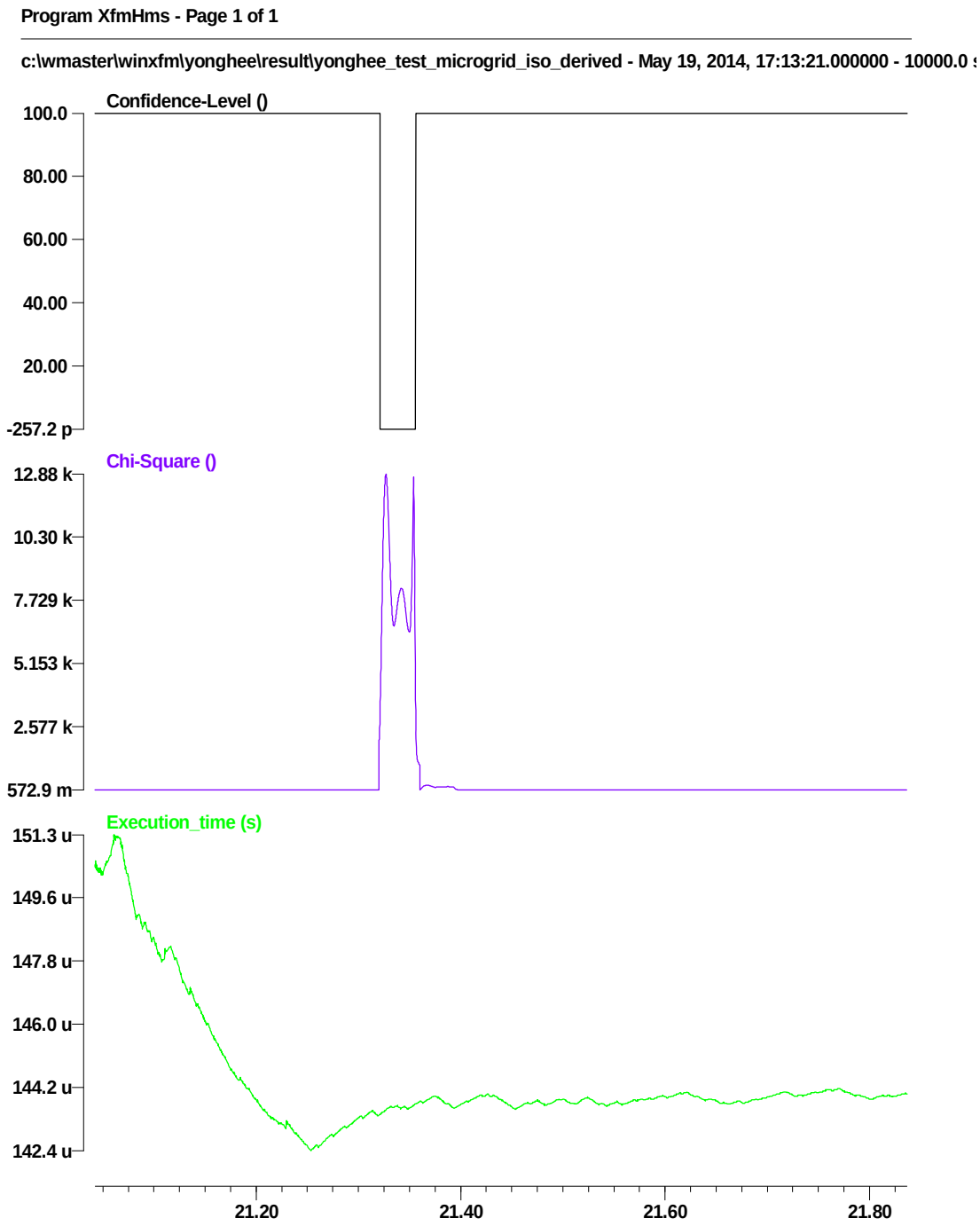

Figure 137: Confidence level, computation time, and residual for the internal fault case on the microgrid during the island mode.

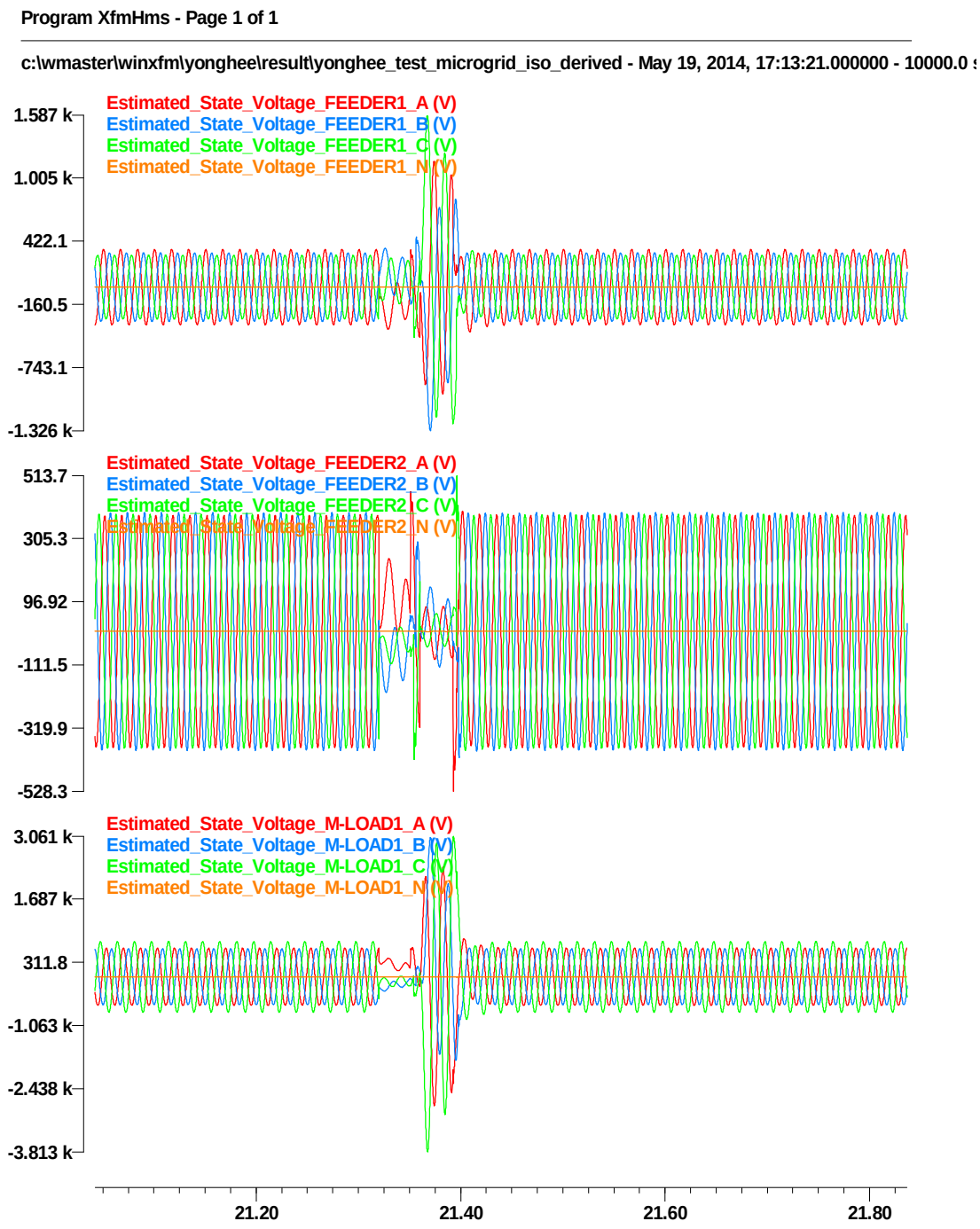

Figure 138: States at node FEEDER1, FEEDER2, and M-LOAD1.

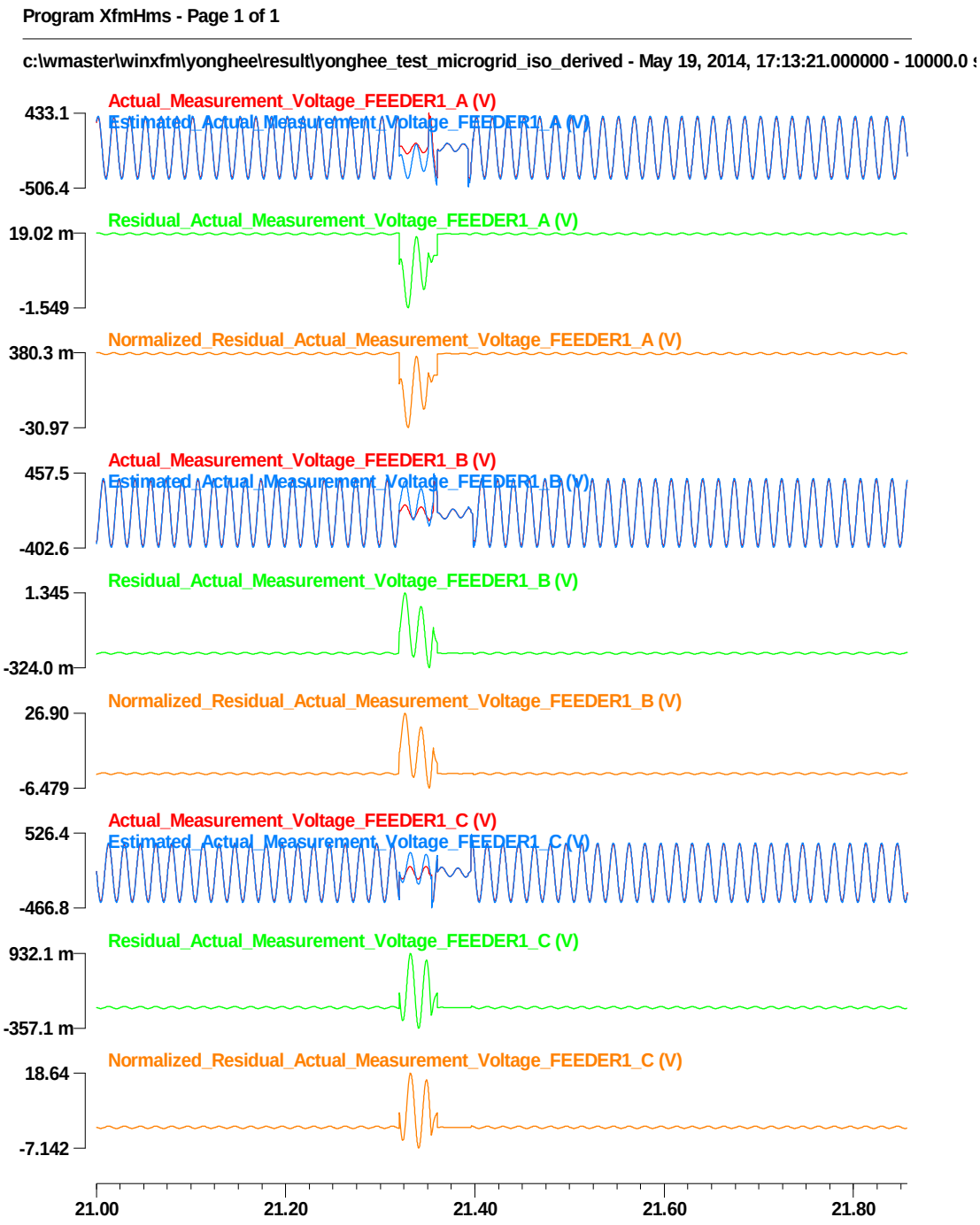

Figure 139: Actual across measurement data, estimated measurement data, residual, and normalized residual at node FEEDER1.

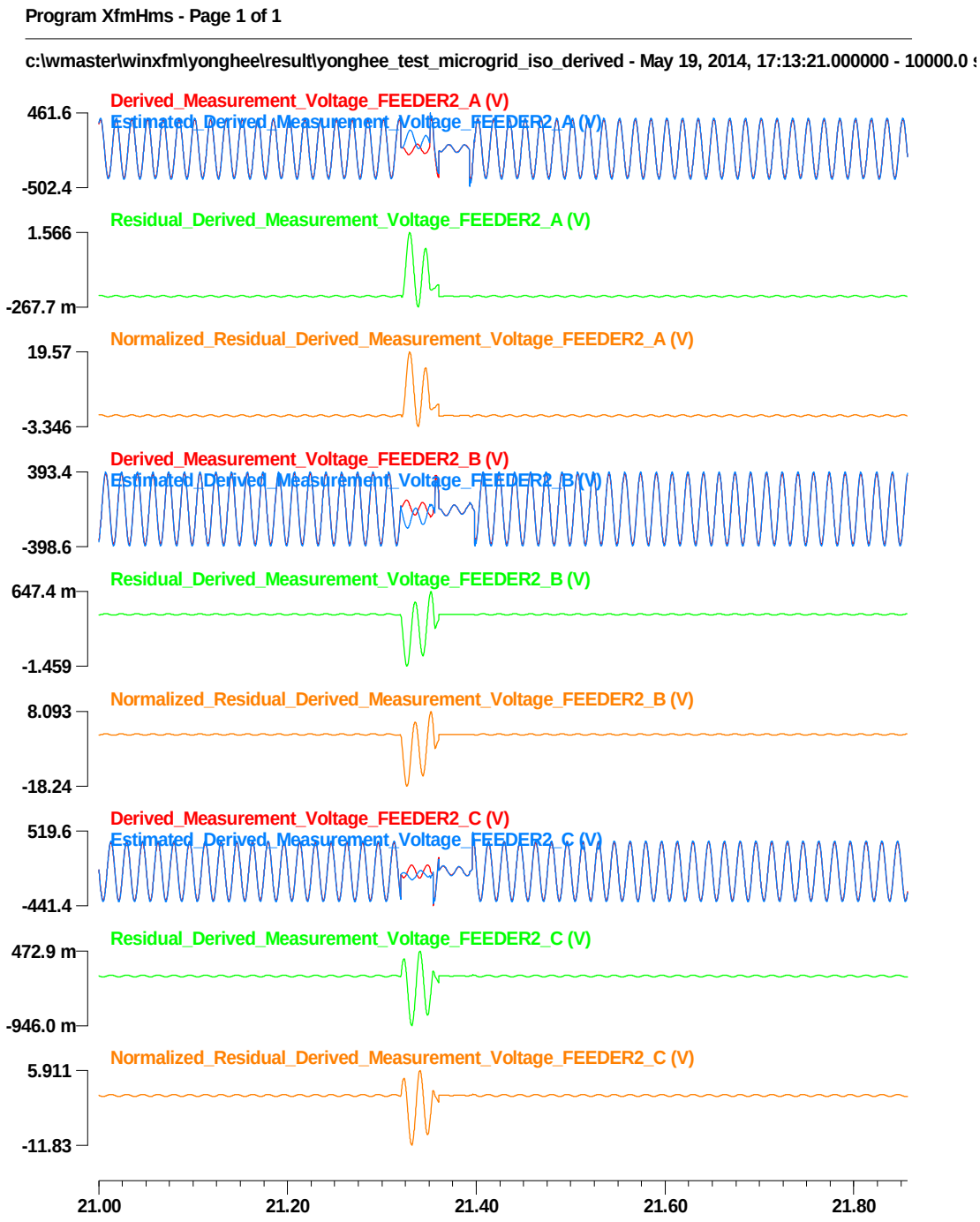

Figure 140: Derived across measurement data at time t, estimated measurement data, residual, and normalized residual at node FEEDER2.

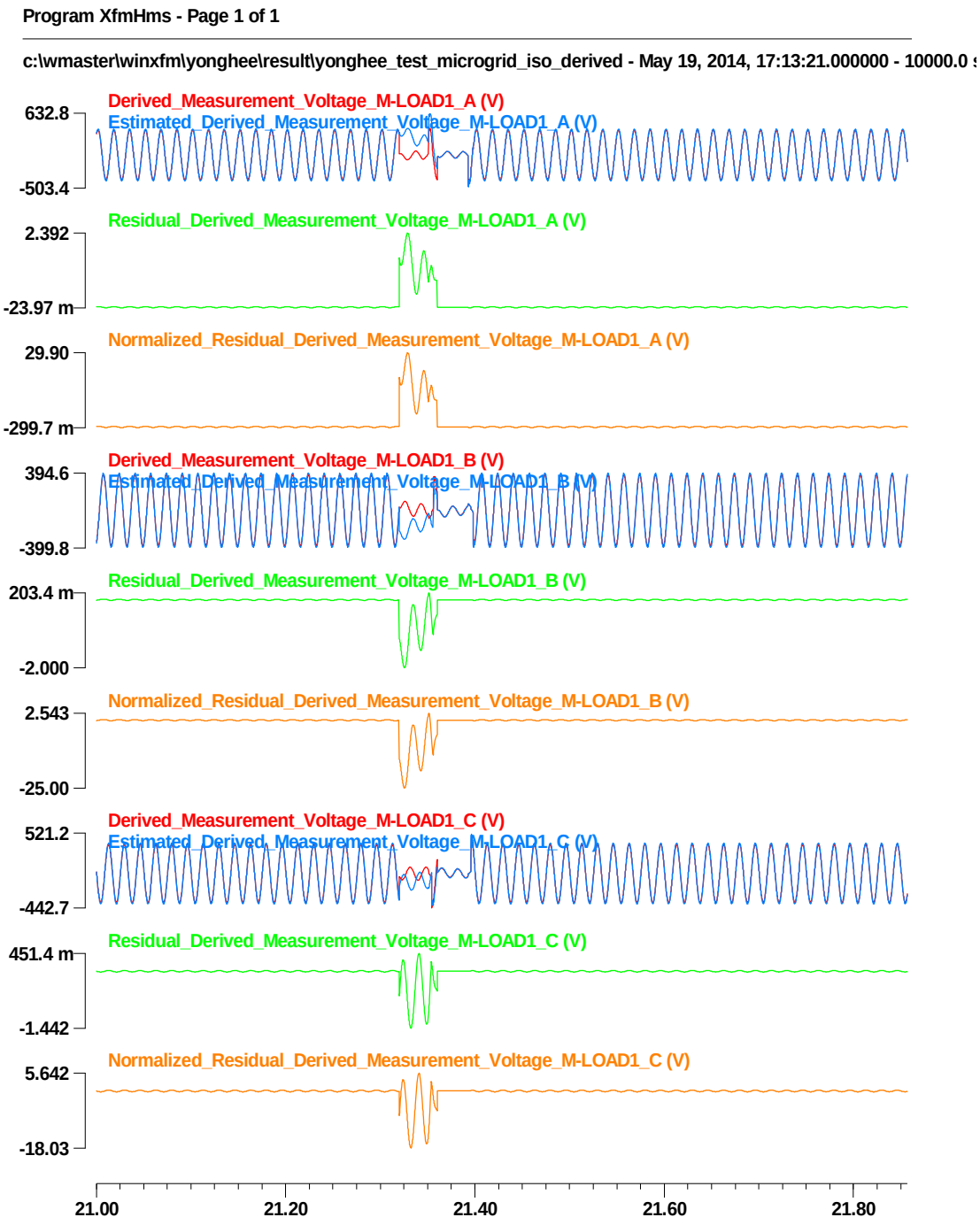

Figure 141: Derived across measurement data at time t, estimated measurement data, residual, and normalized residual at node M-LOAD1.

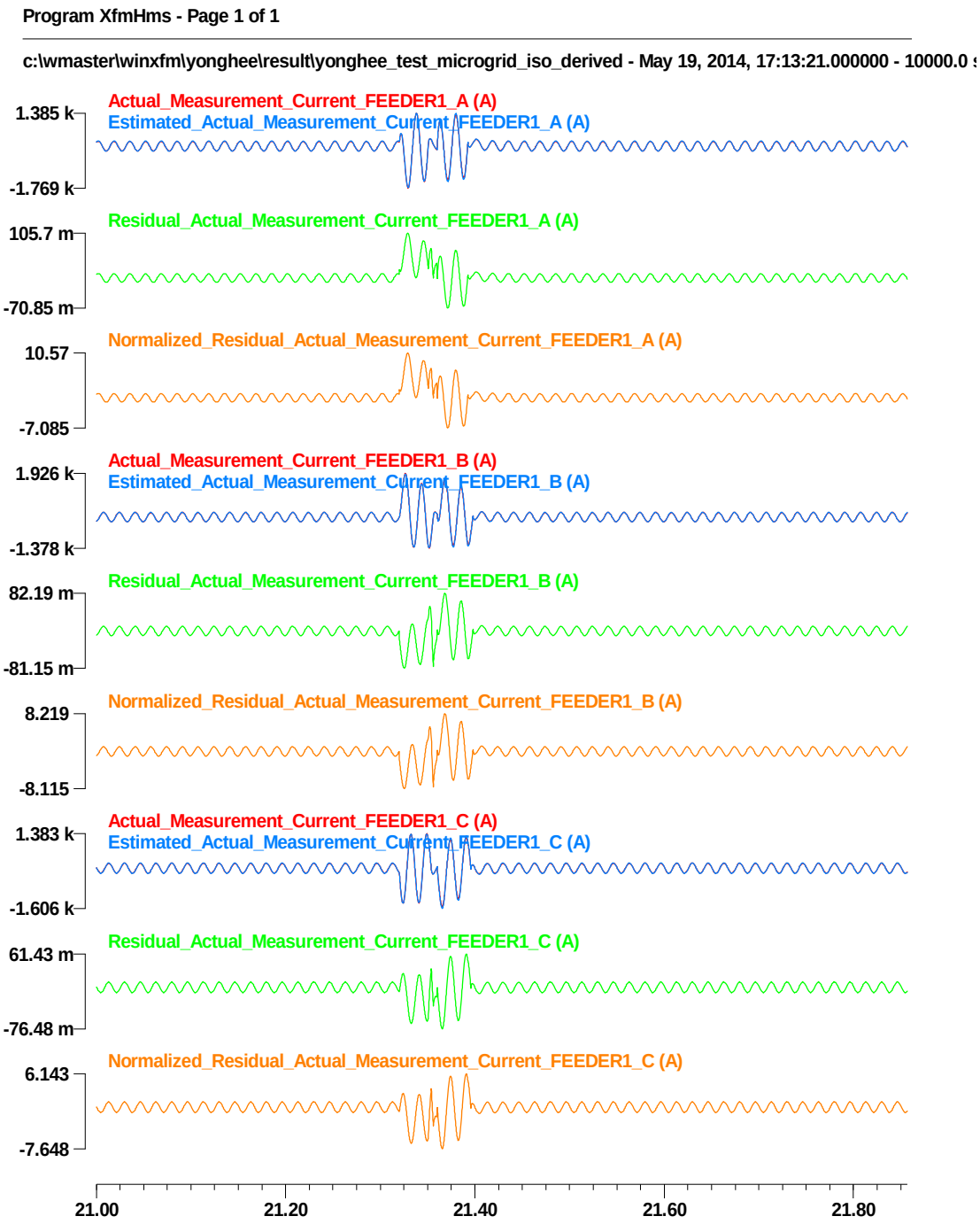

Figure 142: Actual through measurement data at time t, estimated measurement data, residual, and normalized residual at node FEEDER1.

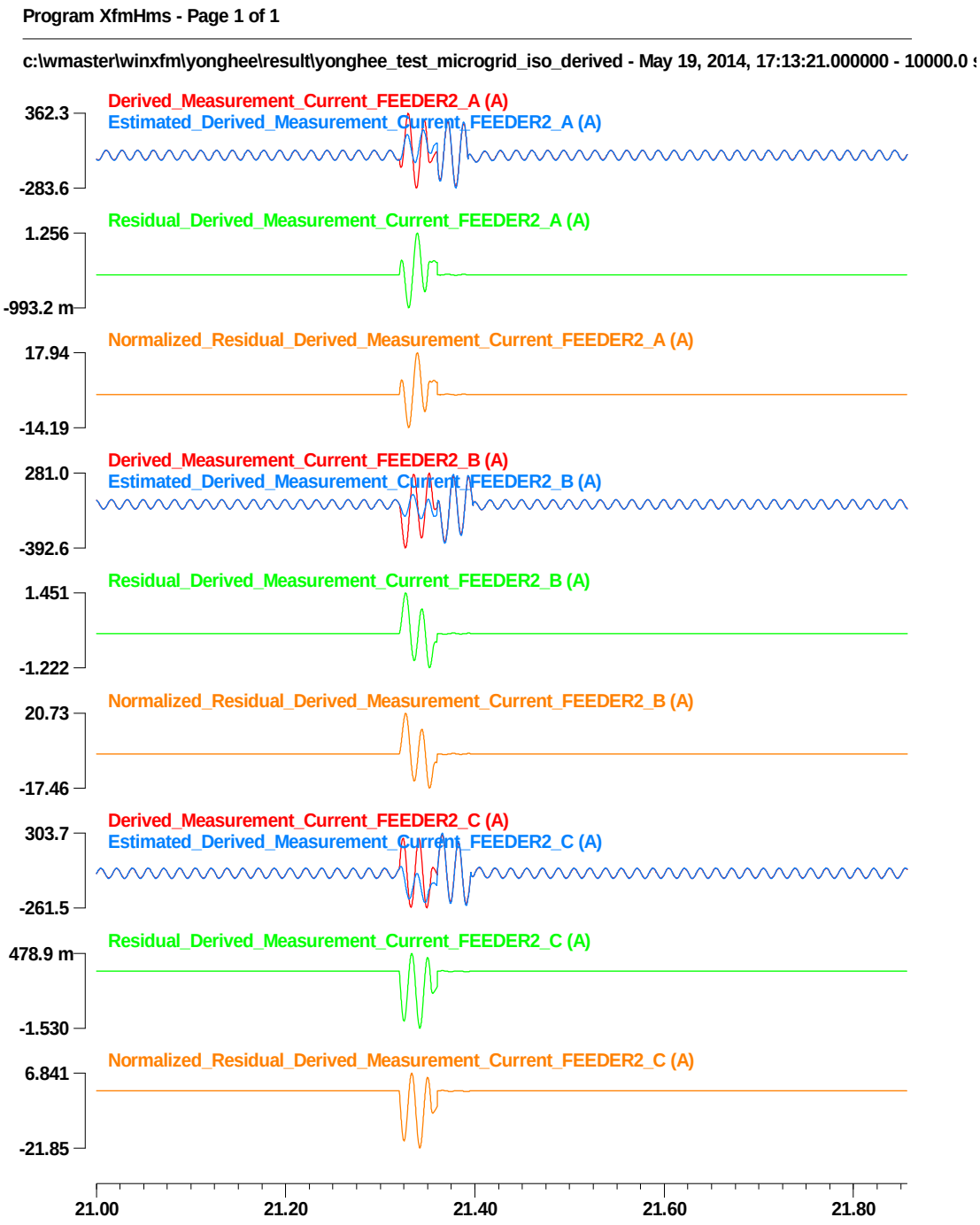

Figure 143: Derived through measurement data at time t, estimated measurement data, residual, and normalized residual at node FEEDER2.

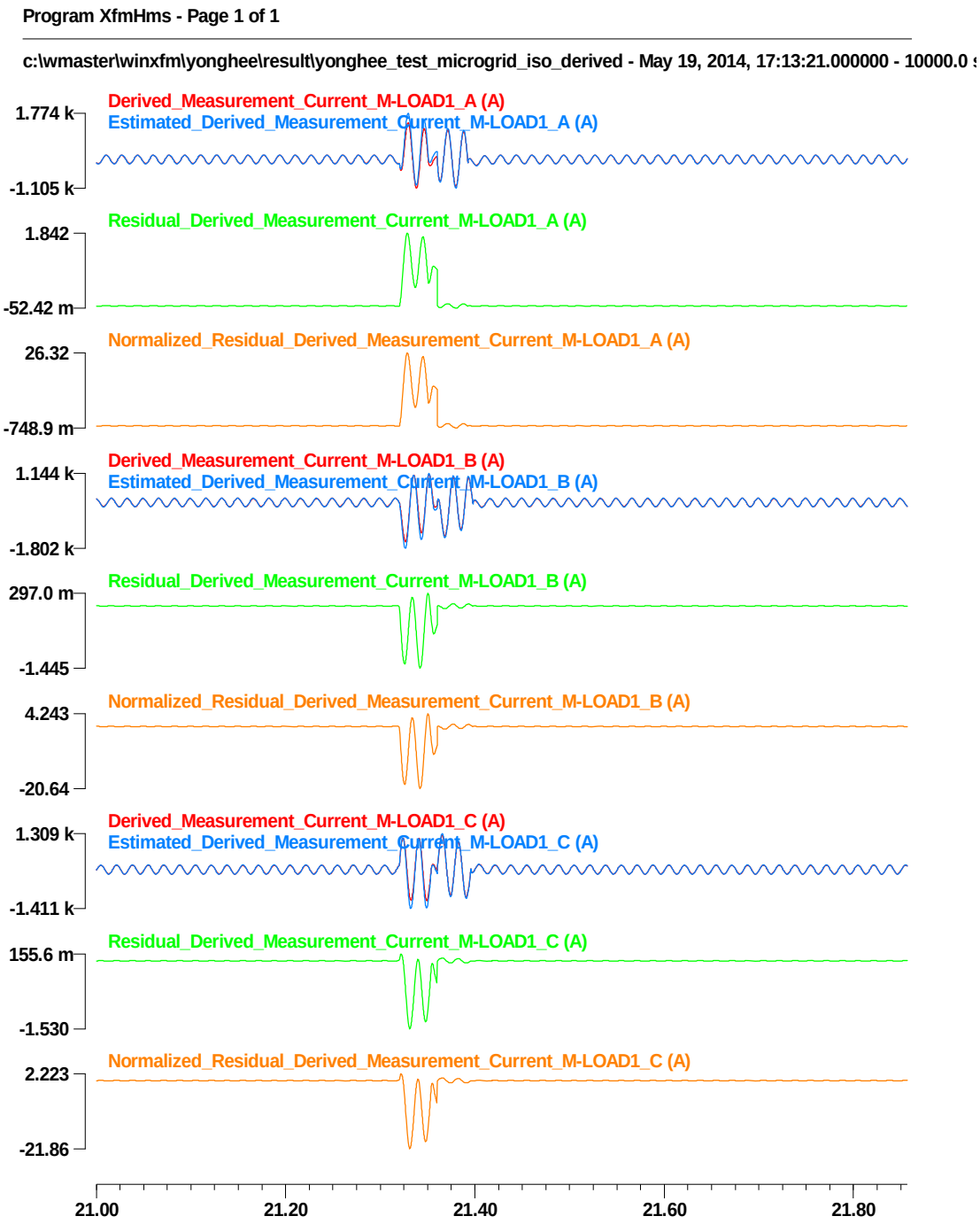

Figure 144: Derived through measurement data at time t, estimated measurement data, residual, and normalized residual at node M-LOAD1.

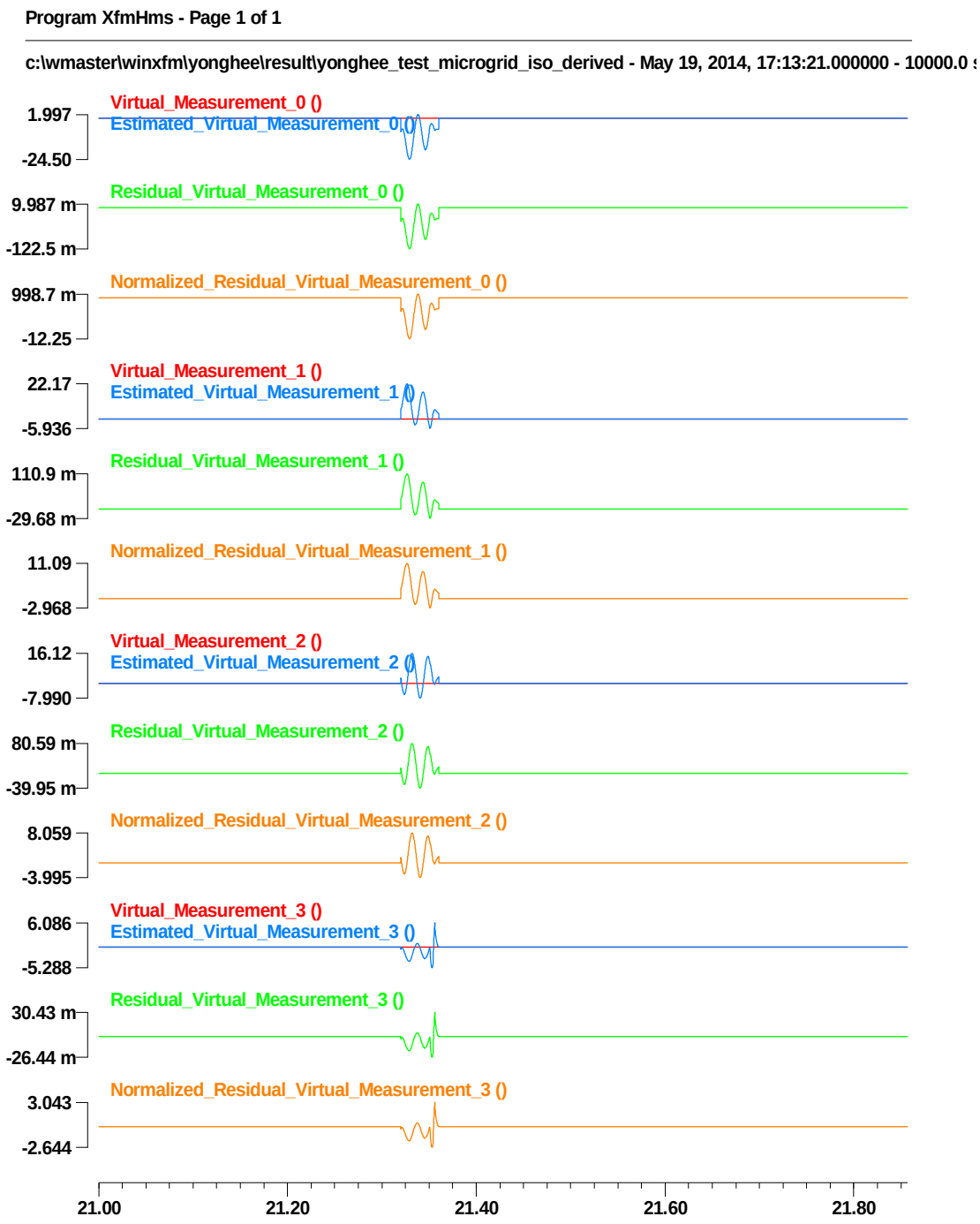

Figure 145: Virtual measurement data at time t, estimated measurement data, residual, and normalized residual of the first line model.

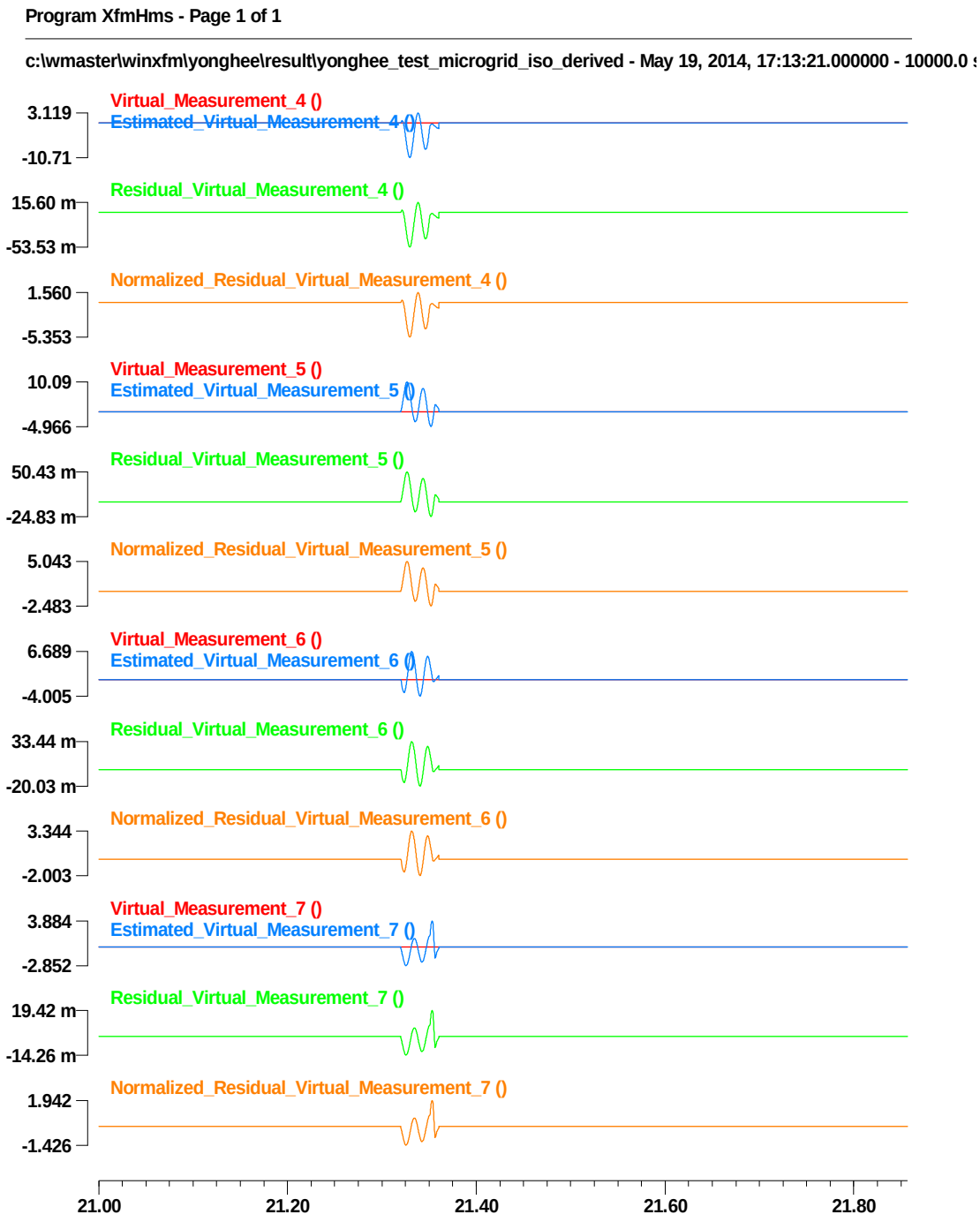

Figure 146: Virtual measurement data at time t, estimated measurement data, residual, and normalized residual of the second line model.

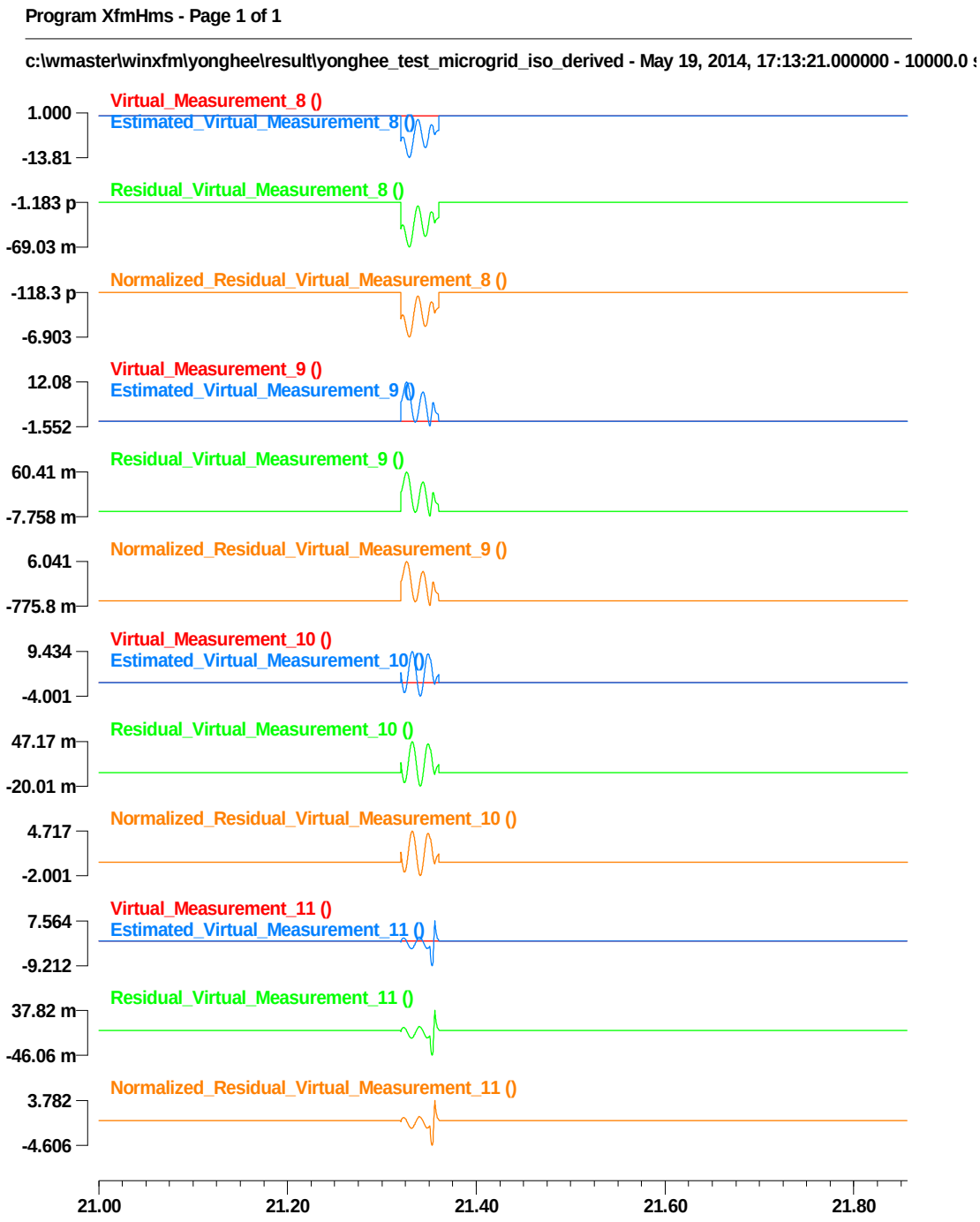

Figure 147: Virtual measurement data at time t, estimated measurement data, residual, and normalized residual of the third line model.

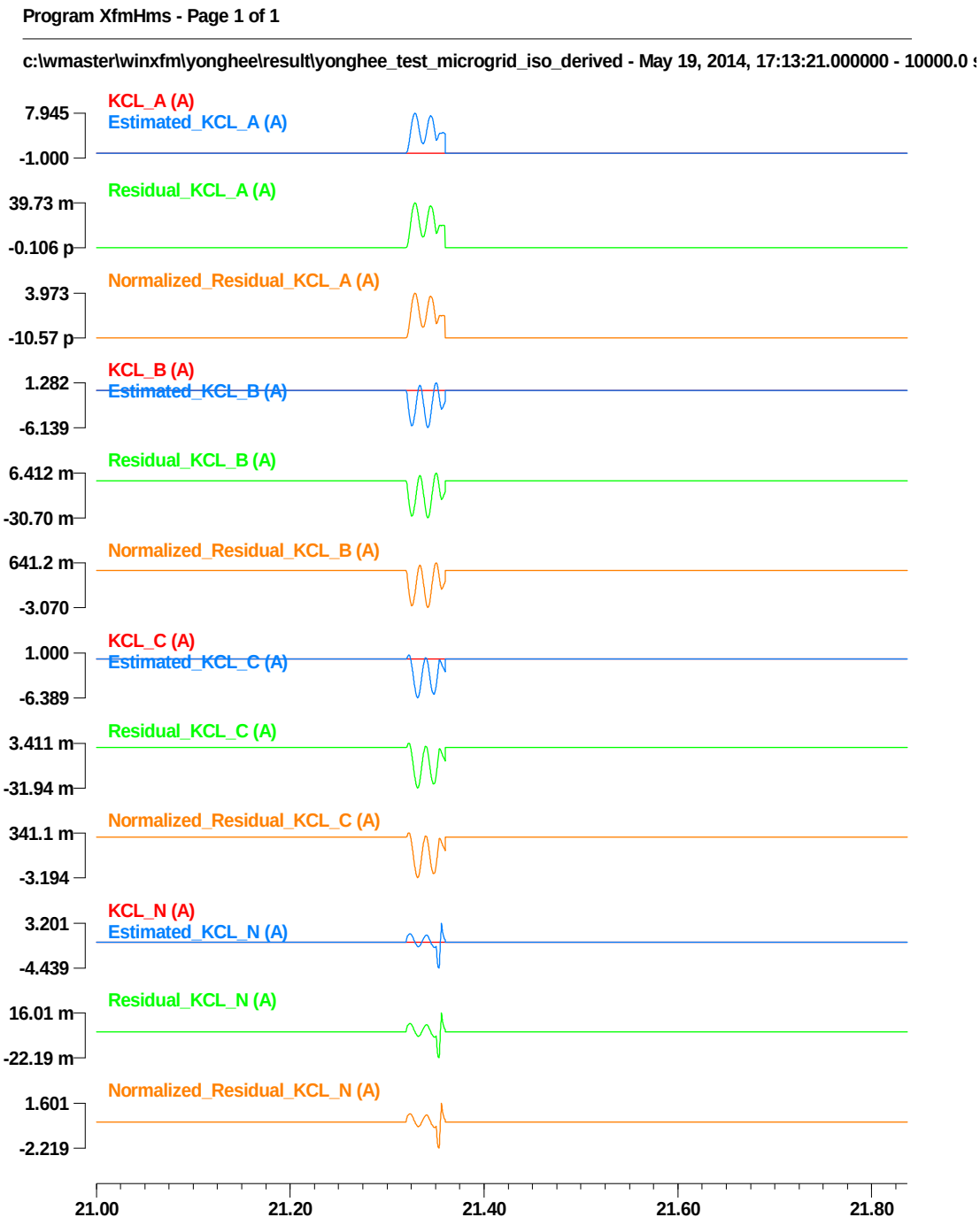

Figure 148: Virtual KCL measurement data at time t, estimated measurement data, residual, and normalized residual at node M-FAC.

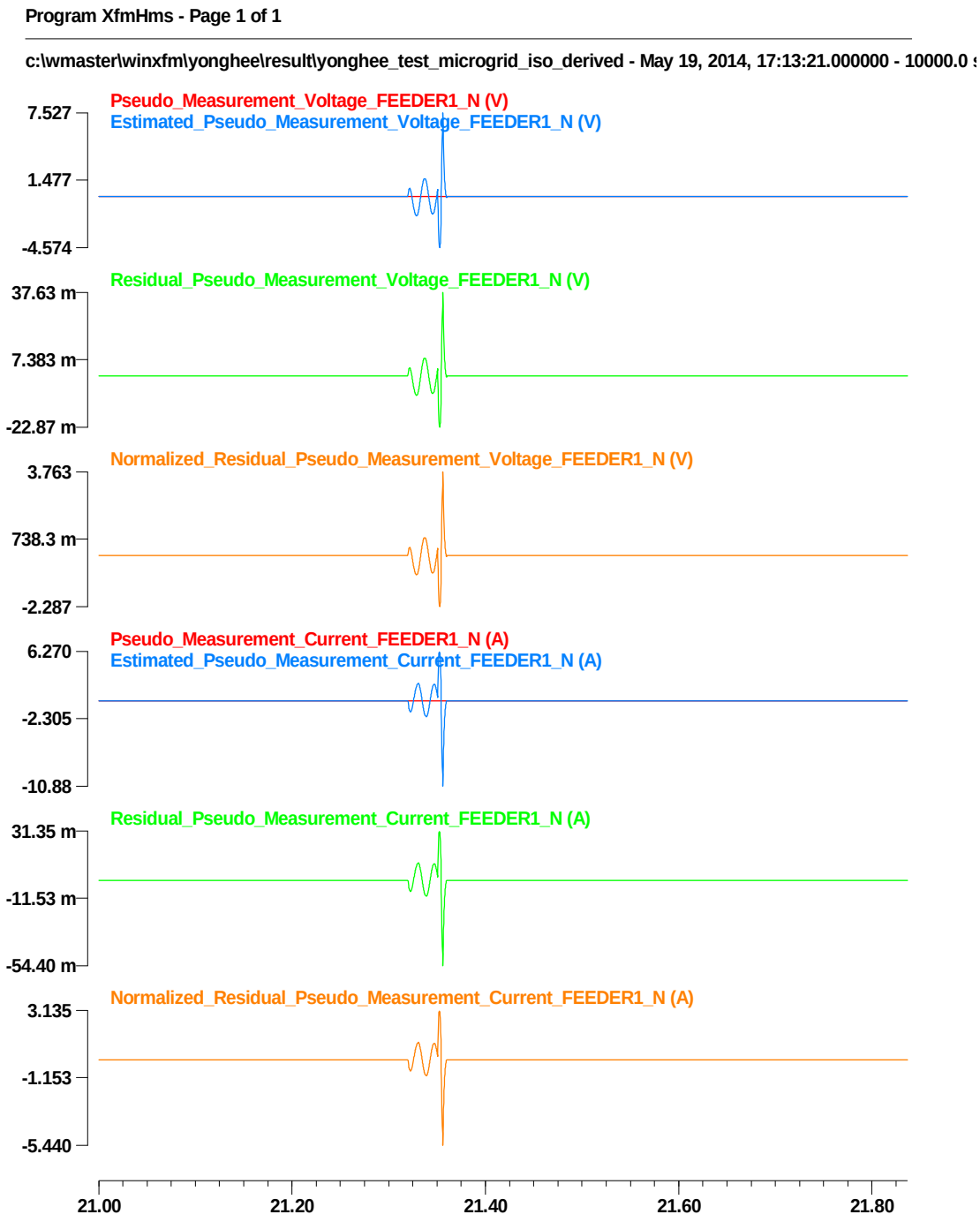

Figure 149: Pseudo measurement data at time t_m, estimated measurement data, residual, and normalized residual at node FEEDER1.

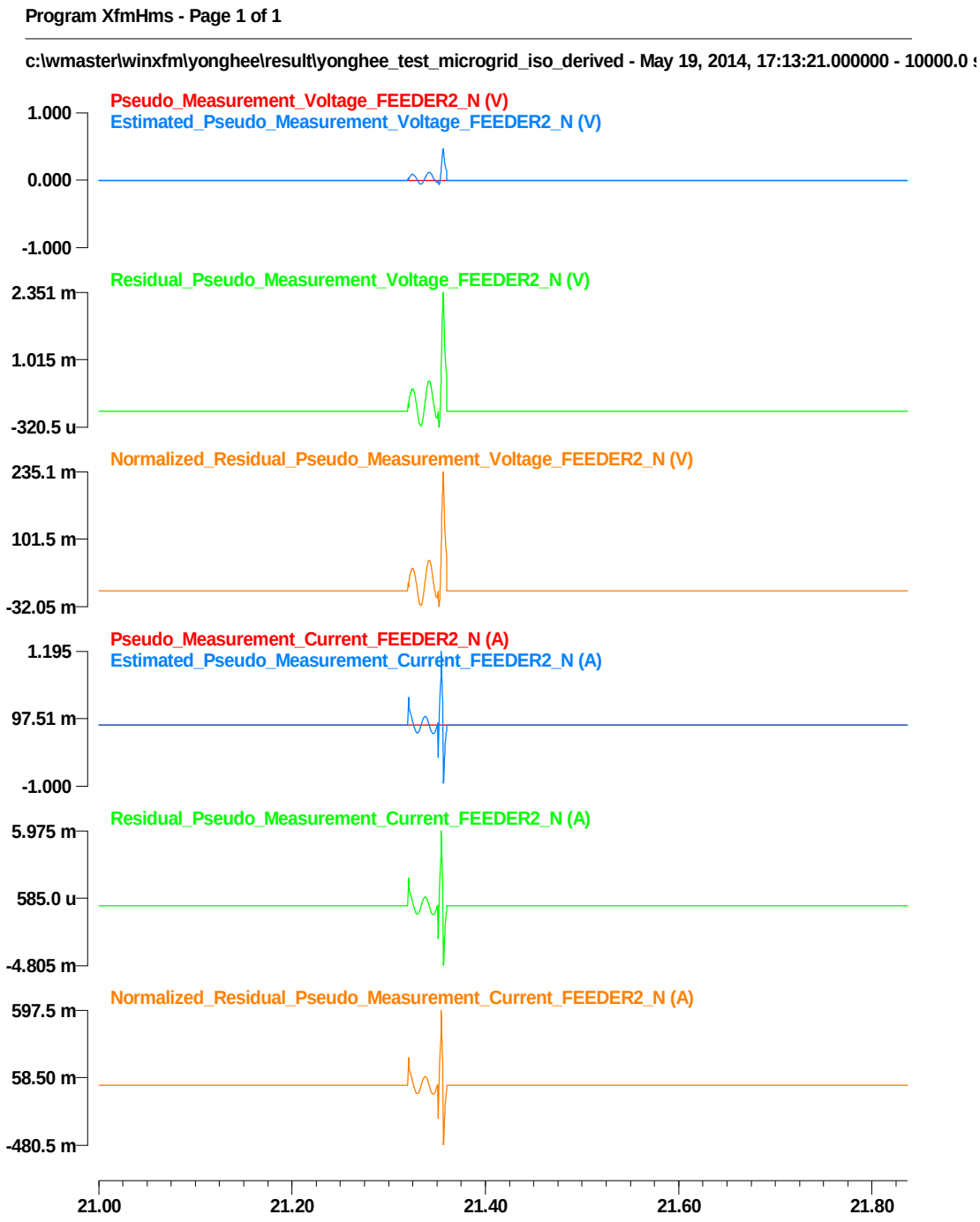

Figure 150: Pseudo measurement data at time t_m, estimated measurement data, residual, and normalized residual at node FEEDER2.

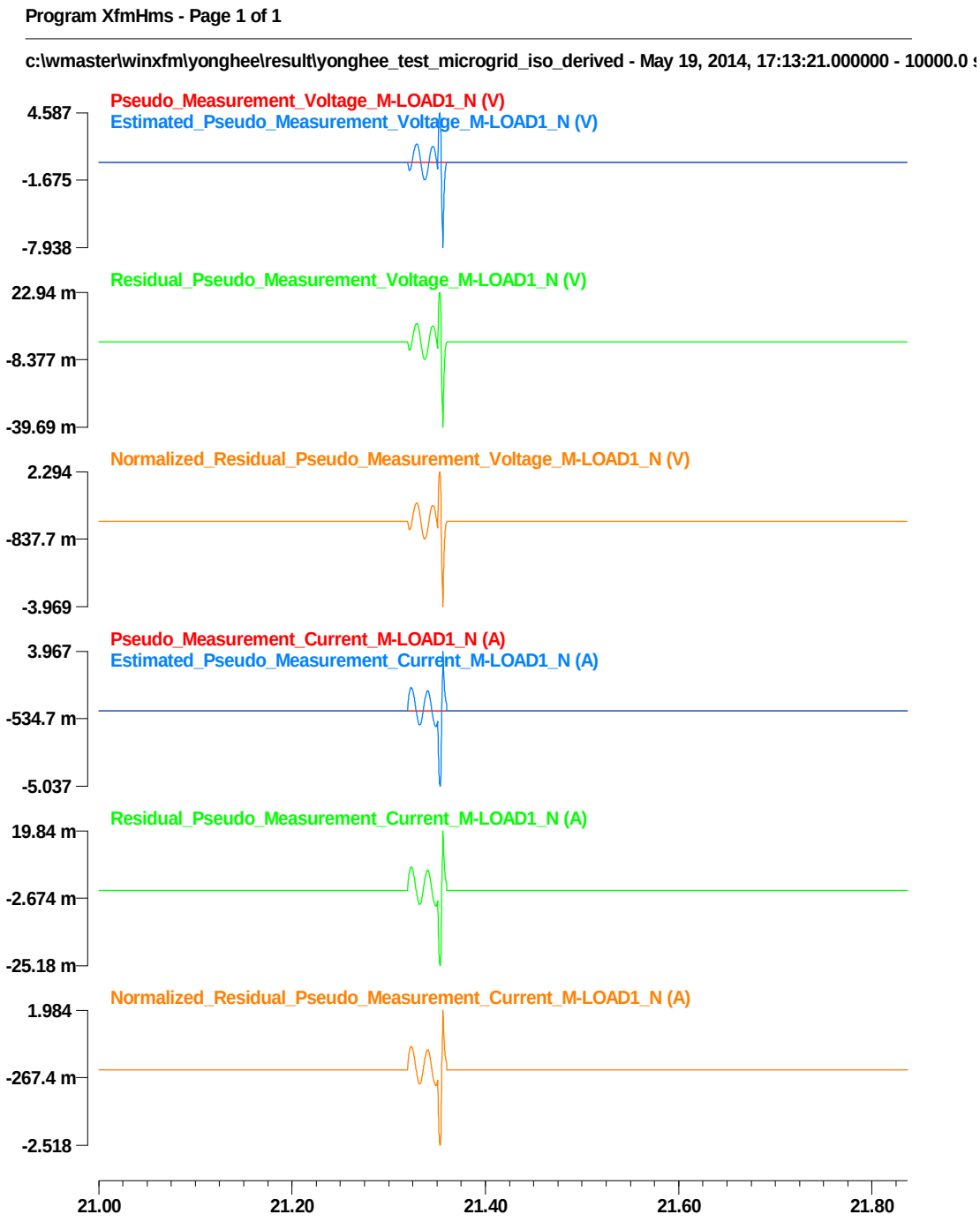

Figure 151: Pseudo measurement data at time t_m, estimated measurement data, residual, and normalized residual at node M-LOAD1.

REFERENCES

[1] *Electrical Distribution System Protection*, 2nd ed. Cooper Power Systems, 2005.

[2] J. L. McElray, Sr. and V. Gharpure, "Loop control schemes increase restoration," in *Transmission and Distribution Conference and Exposition, 2001 IEEE/PES*, 2001, pp. 171-176 vol.1.

[3] H. B. Puttgen, P. R. MacGregor, and F. C. Lambert, "Distributed generation: Semantic hype or the dawn of a new era?," *Power and Energy Magazine, IEEE,* vol. 1, pp. 22-29, 2003.

[4] J. Morren and S. W. H. de Haan, "Impact of distributed generation units with power electronic converters on distribution network protection," in *Developments in Power System Protection, 2008. DPSP 2008. IET 9th International Conference on*, 2008, pp. 664-669.

[5] C. A. Plet, M. Graovac, T. C. Green, and R. Iravani, "Fault response of grid-connected inverter dominated networks," in *Power and Energy Society General Meeting, 2010 IEEE*, 2010, pp. 1-8.

[6] N. R. Friedman, "Distributed Energy Resources Interconnection Systems: Technology Review and Research Needs," Sep 2002.

[7] "IEEE Recommended Practice for Utility Interface of Photovoltaic (PV) Systems," *IEEE Std 929-2000,* p. i, 2000.

[8] "IEEE Guide for Interfacing Dispersed Storage and Generation Facilities With Electric Utility Systems," *ANSI/IEEE Std 1001-1988,* p. 0_1, 1989.

[9] A. M. Massoud, S. Ahmed, S. J. Finney, and B. W. Williams, "Inverter-based versus synchronous-based distributed generation; fault current limitation and protection issues," in *Energy Conversion Congress and Exposition (ECCE), 2010 IEEE*, 2010, pp. 58-63.

[10] A. Min Cheol and K. Tae Kuk, "Proof-of-Concept of a Smart Fault Current Controller With a Superconducting Coil for the Smart Grid," *Applied Superconductivity, IEEE Transactions on,* vol. 21, pp. 2201-2204, 2011.

[11] W. El-Khattam and T. S. Sidhu, "Restoration of Directional Overcurrent Relay Coordination in Distributed Generation Systems Utilizing Fault Current Limiter," *Power Delivery, IEEE Transactions on,* vol. 23, pp. 576-585, 2008.

[12] G. T. Heydt, A. Bose, Y. Zhang, and A. P. S. Meliopoulos, "New Implications of Power System Fault Current Limits," *Power Systems Engineering Research Center (PSERC),* Oct 2005.

[13] A. Girgis and S. Brahma, "Effect of distributed generation on protective device coordination in distribution system," in *Power Engineering, 2001. LESCOPE '01. 2001 Large Engineering Systems Conference on*, 2001, pp. 115-119.

[14] S. M. Brahma and A. A. Girgis, "Microprocessor-based reclosing to coordinate fuse and recloser in a system with high penetration of distributed generation," in *Power Engineering Society Winter Meeting, 2002. IEEE*, 2002, pp. 453-458 vol.1.

[15] "IEEE Application Guide for IEEE Std 1547, IEEE Standard for Interconnecting Distributed Resources with Electric Power Systems," in *IEEE Std 1547.2-2008*, ed, 2009, pp. 1-207.

[16] C. L. Smallwood, "Distributed generation in autonomous and nonautonomous micro grids," in *Rural Electric Power Conference, IEEE*, 2002, pp. D1-D1_6.

[17] W. E. Feero, D. C. Dawson, and J. Stevens, "Protection Issues of the MicroGrid Concept," Mar 2002.

[18] I. Ohshima, M. Sakurai, and A. Fujisawa, "Switch (Sectionalizer) for Distribution Automation System," *Third International Conference on Future Trends in Distribution Switchgear,* vol. 318, pp. 95-99, 1990.

[19] G. Benmouyal, M. Meisinger, J. Burnworth, W. A. Elmore, K. Freirich, P. A. Kotos, P. R. Leblanc, P. J. Lerley, J. E. McConnell, J. Mizener, J. Pinto de Sa, R. Ramaswami, M. S. Sachdev, W. M. Strang, J. E. Waldron, S. Watansiriroch, and S. E. Zocholl, "IEEE standard inverse-time characteristic equations for overcurrent relays," *Power Delivery, IEEE Transactions on,* vol. 14, pp. 868-872, 1999.

[20] R. Nylen, "Auto-reclosing," *ASEA Journal, Relay Division,* pp. 127-132, June 1979.

[21] J. M. Gers and E. J. Holmes, *Protection of Electricity Distribution Networks (2nd Edition)*: Institution of Engineering and Technology.

[22] D. M. Farmer and K. H. Hoffman, "Application of Sectionalizers on Distribution Systems," in *Rural Electric Power Conference, 2007 IEEE*, 2007, pp. A2-A2-7.

[23] Q. C. Yuan, Y. Zeng, and Y. X. Wu, "A novel scheme for automatic loop-reconfiguration following a fault," *Powercon '98: 1998 International Conference on Power System Technology - Proceedings, Vols 1 and 2,* pp. 255-259, 1998.

[24] K. Clark, "Distribution automation to improve circuit reliability," *2004 57th Annual Conference for Protective Relay Engineers,* pp. 91-96, 2004.

[25] S. R. Southerlin, "New distribution automation switchgear and its contribution to overhead distribution reliability," in *Electricity Distribution. Part 1: Contributions. CIRED. 14th International Conference and Exhibition on (IEE Conf. Publ. No. 438)*, 1997, pp. 32/1-32/4 vol.4.

[26] E. Bozzetto, M. Calabrese, M. Sanchez, and T. Lucero, "A new methodology for the automatic load recovery in distribution primary feeders," *Proceedings of the 1995 First Ieee International Caracas Conference on Devices, Circuits and Systems,* pp. 348-351, 1995.

[27] D. G. Hart, D. Uy, J. Northcote-Green, C. LaPlace, and D. Novosel, "Automated solutions for distribution feeders," *Ieee Computer Applications in Power,* vol. 13, pp. 25-30, Oct 2000.

[28] T. A. Short, *Electric Power Distribution Handbook*: CRC Press, 2004.

[29] S. Conti, N. Messina, G. Tina, and P. Nicotra, "Automatic control for loop distribution system reconfiguration: reliability and efficiency improvement," in *Electrical and Computer Engineering, 2000 Canadian Conference on*, 2000, pp. 1152-1156 vol.2.

[30] L. A. Kojovic and T. R. Day, "Advanced distribution system automation," *2003 Ieee Pes Transmission and Distribution Conference & Exposition, Vols 1-3, Conference Proceedings,* pp. 348-353, 2003.

[31] A. T. Ohara and C. S. Takiguchi, "Automatic restoration system," *2004 IEEE/PES Transmission & Distribution Conference & Exposition: Latin America,* pp. 681-685, 2004.

[32] C. A. McCarthy, "New Technology for Looped Distribution Feeders," *2008 Ieee/Pes Transmission and Distribution Conference and Exposition: Latin America, Vols 1 and 2,* pp. 846-850, 2008.

[33] F. Goodman and C. McCarthy, "Applications assessment of pulse closing technology," in *Electricity Distribution - Part 1, 2009. CIRED 2009. 20th International Conference and Exhibition on*, 2009, pp. 1-4.

[34] M. Butts, J. Spare, and R. Brown, "Practical and Verifiable Reliability Improvement at the Baltimore Gas and Electric Company," Feb 2006.

[35] T. Taylor, T. Fahey, T. Royster, and D. Engler, "New recloser functionality enhances feeder automation," *2008 Ieee/Pes Transmission & Distribution Conference & Exposition, Vols 1-3,* pp. 1142-1149, 2008.

[36] B. D. Russell, "Detection of Downed Conductors on Utility Distribution Systems," *IEEE Tutorial Course,* Feb 1990.

[37] W. A. Elmore, "Protective Relaying Theory and Application", second ed. New York: Marcel Dekker. p. 112

[38] H. Calhoun, M. T. Bishop, C. H. Eichler, and R. E. Lee, "Development and Testing of an Electro-Mechanical Relay to Detect Fallen Distribution Conductors," *Power Apparatus and Systems, IEEE Transactions on,* vol. PAS-101, pp. 1643-1650, 1982.

[39] J. Carr, "Detection of High Impedance Faults on Multi-Grounded Primary Distribution Systems," *Power Apparatus and Systems, IEEE Transactions on,* vol. PAS-100, pp. 2008-2016, 1981.

[40] B. M. Aucoin,B. D. Russell, "Distribution High Impedance Fault Detection Utilizing High Frequency Current Components," *Power Apparatus and Systems, IEEE Transactions on,* vol. PAS-101, pp. 1596-1606, 1982.

[41] C. Benner, P. Carswell, and B. Don Russell, "Improved algorithm for detecting arcing faults using random fault behavior," *Electric Power Systems Research,* vol. 17, pp. 49-56, 1989.

[42] B. D. Russell, R. P. Chinchali, and C. J. Kim, "Behaviour of low frequency spectra during arcing fault and switching events," *Power Delivery, IEEE Transactions on,* vol. 3, pp. 1485-1492, 1988.

[43] B. D. Russell,R. P. Chinchali, "A digital signal processing algorithm for detecting arcing faults on power distribution feeders," *Power Delivery, IEEE Transactions on,* vol. 4, pp. 132-140, 1989.

[44] K. Wook Hyun, L. Gi Wen, P. Young Moon, Y. Man Chul, and Y. Myeong Ho, "High impedance fault detection utilizing incremental variance of normalized even order harmonic power," *Power Delivery, IEEE Transactions on,* vol. 6, pp. 557-564, 1991.

[45] D. I. Jeerings,J. R. Linders, "Unique aspects of distribution system harmonics due to high impedance ground faults," *Power Delivery, IEEE Transactions on,* vol. 5, pp. 1086-1094, 1990.

[46] M. Michalik, M. ukowicz, W. Rebizant, L. Seung-Jae, and K. Sang-Hee, "New ANN-Based Algorithms for Detecting HIFs in Multigrounded MV Networks," *Power Delivery, IEEE Transactions on,* vol. 23, pp. 58-66, 2008.

[47] M. Michalik, W. Rebizant, M. Lukowicz, L. Seung-Jae, and K. Sang-Hee, "High-impedance fault detection in distribution networks with use of wavelet-based algorithm," *Power Delivery, IEEE Transactions on,* vol. 21, pp. 1793-1802, 2006.

[48] F. G. Jota,P. R. S. Jota, "High-impedance fault identification using a fuzzy reasoning system," *Generation, Transmission and Distribution, IEE Proceedings-,* vol. 145, pp. 656-661, 1998.

[49] "Protection, Automation, and Bay Control System." available online: https://www.selinc.com/SEL-451/

[50] "High Impedance Fault Detection Technology," *Report of PSRC Working Group D15,* March 1 1996.

[51] A. C. Westrom, A. P. S. Meliopoulos, G. J. Cokkinides, and A. H. Ayoub, "Open conductor detector system," *Power Delivery, IEEE Transactions on,* vol. 7, pp. 1643-1651, 1992.

[52] E. C. Senger, W. Kaiser, J. C. Santos, P. M. S. Burt, and C. V. S. Malagodi, "Broken conductors protection system using carrier communication," *Power Delivery, IEEE Transactions on,* vol. 15, pp. 525-530, 2000.

[53] L. Garcia-Santander, P. Bastard, M. Petit, I. Gal, E. Lopez, and H. Opazo, "Down-conductor fault detection and location via a voltage based method for radial distribution networks," *Generation, Transmission and Distribution, IEE Proceedings-,* vol. 152, pp. 180-184, 2005.

[54] R. Benato, R. Caldon, and S. Corsi, "Protection requirements in distribution systems with high penetration of DG and possibility of intentional islanding," in *Electricity Distribution, 2005. CIRED 2005. 18th International Conference and Exhibition on*, 2005, pp. 1-4.

[55] P. Mahat, C. Zhe, B. Bak-Jensen, and C. L. Bak, "A Simple Adaptive Overcurrent Protection of Distribution Systems With Distributed Generation," *Smart Grid, IEEE Transactions on,* vol. 2, pp. 428-437, 2011.

[56] H. Al-Nasseri, M. A. Redfern, and F. Li, "A voltage based protection for micro-grids containing power electronic converters," in *Power Engineering Society General Meeting, 2006. IEEE*, 2006, p. 7 pp.

[57] O. C. Montero-Hernandez and P. N. Enjeti, "A fast detection algorithm suitable for mitigation of numerous power quality disturbances," in *Industry Applications Conference, 2001. Thirty-Sixth IAS Annual Meeting. Conference Record of the 2001 IEEE*, 2001, pp. 2661-2666 vol.4.

[58] T. Loix, T. Wijnhoven, and G. Deconinck, "Protection of microgrid with a high penetration of inverter-coupled energy sources," in *Integration of Wide-Scale Renewable Resources Into the Power Delivery System, 2009 CIGRE/IEEE PES Joint Symposium*, 2009, pp. 1-6.

[59] M. A. Zamani, T. S. Sidhu, and A. Yazdani, "A Protection Strategy and Microprocessor-Based Relay for Low-Voltage Microgrid," *Power Delivery, IEEE Transactions on,* vol. 26, pp. 1873-1883, 2011.

[60] J. G. Andrichak and S. C. Patel, "Polarizing Sources for Directional Ground Relays."

[61] J. Roberts and A. Guzmán, "Directional Element Design and Evaluation," Aug 2006.

[62] J. Horak, "Directional overcurrent relaying (67) concepts," in *Protective Relay Engineers, 2006. 59th Annual Conference for*, 2006, p. 13 pp.

[63] S. Conti and S. Nicotra, "Procedures for fault location and isolation to solve protection selectivity problems in MV distribution networks with dispersed generation," *Electric Power Systems Research,* vol. 79, pp. 57-64, 2009.

[64] H. Nikkhajoei and R. H. Lasseter, "Microgrid Protection," in *Power Engineering Society General Meeting, 2007. IEEE*, 2007, pp. 1-6.

[65] S. M. Brahma and A. A. Girgis, "Development of adaptive protection scheme for distribution systems with high penetration of distributed generation," *Power Delivery, IEEE Transactions on,* vol. 19, pp. 56-63, 2004.

[66] R. Wernsing, J. Hubertus, M. Duffy, G. Hataway, D. Conner, and E. Nelson, "Implementation of an innovative advanced loop scheme to provide distribution reliability improvement," in *Rural Electric Power Conference (REPC), 2010 IEEE*, 2010, pp. B2-B2-8.

[67] A. Oudalova and A. Fidigatti, "Adaptive Network Protection in Microgrid," *Journal of DER,* vol. 5, 2009.

[68] S. Yong and T. Michalak, "Optimizing system coordination and overcurrent protection with zone selective interlocking," in *Textile, Fiber and Film Industry Technical Conference, 1990., IEEE 1990 Annual*, 1990, pp. 9/1-9/6.

[69] A. P. S. Meliopoulos, *Power System Modeling, Analysis and Control*.

[70] B. K. Zhenyu Huang, Vahid Madani, Ken Martin, Sakis Meliopoulos, Damir Novosel, and Jerry Stenbakken, "Performance Evaluation of Phasor Measurement Systems."

[71] "Guide on PMU-PDC and PDC-PDC Communication (DRAFT)."

[72] "IEC 61850 - Communication Networks and Systems in Substations."

[73] A. P. S. Meliopoulos, G. Cokkinides, H. Renke, E. Farantatos, C. Sungyun, L. Yonghee, and Y. Xuebei, "Smart Grid Technologies for Autonomous Operation and Control," *Smart Grid, IEEE Transactions on,* vol. 2, pp. 1-10, 2011.

[74] A. P. Meliopoulos, G. J. Cokkinides, and G. K. Stefopoulos, "Improved Numerical Integration Method for Power/Power Electronic Systems Based on Three-Point Collocation," in *Proc. the 44th IEEE Conference on Decision and Control, and European Control Conference*, 2005, pp. 6780-6787.

[75] A. P. Meliopoulos, G. J. Cokkinides, and G. K. Stefopoulos, "Quadratic Integration Method," in *Proceedings of the 2005 International Power System Transients Conference (IPST 2005)*, Montreal, Canada, 2005.

[76] A. P. Meliopoulos, G. Cokkinides, R. Huang, E. Farantatos, S. Choi, Y. Lee , "Wide Area Dynamic Monitoring and Stability Controls", IREP Symposium 2010, Bulk Power System Dynamics and Control VIII, Buzios, Brazil, August 1-6, 2010.

[77] A. P. Sakis Meliopoulos and George Cokkinides, *Power System Relaying: An Introduction*, *Book in Preparation*, 980 pages.

[78] A. P. Sakis Meliopoulos, George Cokkinides, Renke Huang, EvangelosFarantatos, Sungyun Choi, Yonghee Lee and Xuebei Yu, "Smart Grid Technologies for Autonomous Operation and Control", *IEEE Transactions on Smart Grid*, Vol 2, No 1, March 2011.